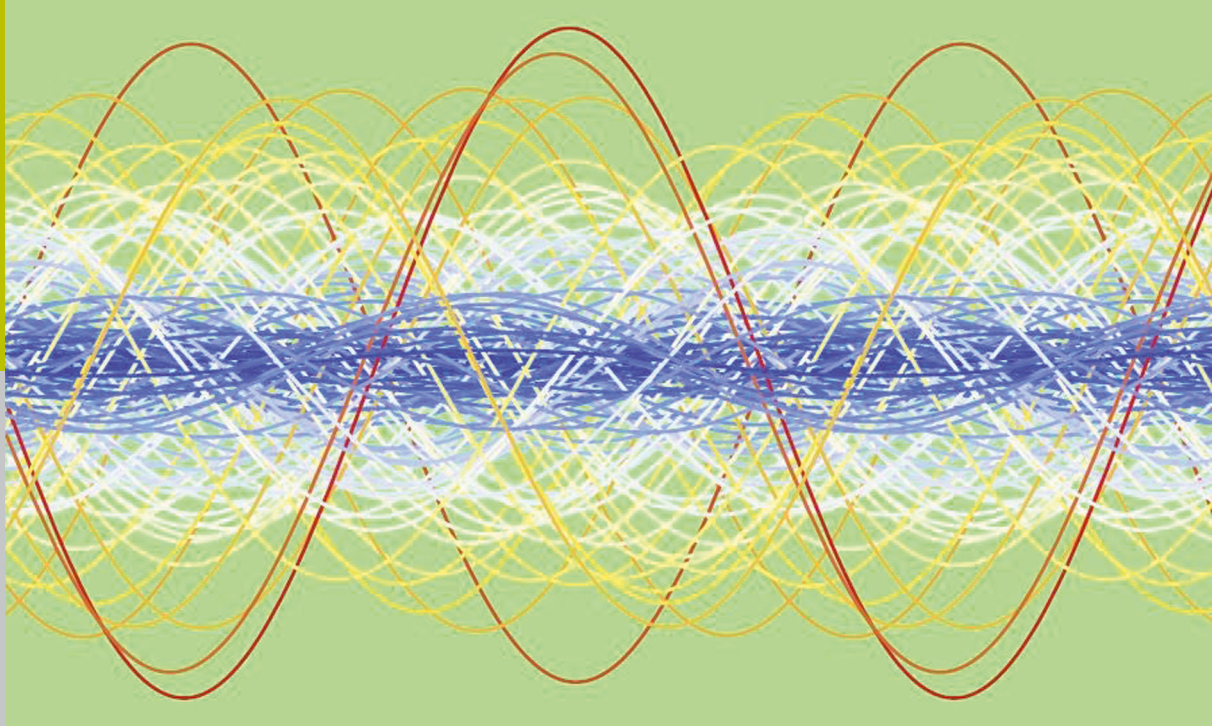


Beam Cooling at COSY and HESR

Theory and Simulation – Part 1 Theory

Hans Stockhorst, Takeshi Katayama and Rudolf Maier



Schlüsseltechnologien /
Key Technologies
Band / Volume 120
ISBN 978-3-95806-127-9

Forschungszentrum Jülich GmbH
Institut für Kernphysik
Kernphysikalische Großgeräte (IKP-4)

Beam Cooling at COSY and HESR

Theory and Simulation – Part 1 Theory

Hans Stockhorst, Takeshi Katayama and Rudolf Maier

Schriften des Forschungszentrums Jülich
Reihe Schlüsseltechnologien / Key Technologies

Band / Volume 120

ISSN 1866-1807

ISBN 978-3-95806-127-9

Bibliographic information published by the Deutsche Nationalbibliothek.
The Deutsche Nationalbibliothek lists this publication in the Deutsche
Nationalbibliografie; detailed bibliographic data are available in the
Internet at <http://dnb.d-nb.de>.

Publisher and
Distributor: Forschungszentrum Jülich GmbH
Zentralbibliothek
52425 Jülich
Tel: +49 2461 61-5368
Fax: +49 2461 61-6103
Email: zb-publikation@fz-juelich.de
www.fz-juelich.de/zb

Cover Design: Grafische Medien, Forschungszentrum Jülich GmbH

Printer: Grafische Medien, Forschungszentrum Jülich GmbH

Copyright: Forschungszentrum Jülich 2016

Schriften des Forschungszentrums Jülich
Reihe Schlüsseltechnologien / Key Technologies, Band / Volume 120

ISSN 1866-1807
ISBN 978-3-95806-127-

The complete volume is freely available on the Internet on the Jülicher Open Access Server (JuSER) at www.fz-juelich.de/zb/openaccess.



This is an Open Access publication distributed under the terms of the [Creative Commons Attribution License 4.0](#), which permits unrestricted use, distribution, and reproduction in any medium, provided the original work is properly cited.

Preface

1 THE ACCELERATION FACILITIES HESR AND COSY	1
1.1 HESR.....	1
1.2 COSY.....	4
2 STOCHASTIC MOMENTUM COOLING.....	7
2.1 Introduction	7
2.2 The Fokker-Planck Equation.....	9
2.3 System Transfer Function	13
2.3.1 Phase Shifter.....	16
2.3.2 Pickup and Kicker Response.....	18
2.3.3 Notch Filter Transfer Function.....	22
2.4 TOF and Filter Cooling	25
2.4.1 Coherent Beam Response.....	25
2.4.2 Incoherent Beam Response	30
2.4.2.1 Schottky Noise	32
2.4.2.2 Thermal Noise	42
2.5 Palmer Cooling	44
2.5.1 Coherent Response (Palmer).....	45
2.5.2 Incoherent Beam Response	45
2.5.2.1 Schottky Noise (Palmer)	45
2.5.2.2 Thermal Noise (Palmer).....	46
2.6 Summary of Drift Terms	46
2.6.1 Drift Terms Filter and TOF Cooling	46
2.6.2 Drift Term Palmer Cooling	47
2.7 Summary of Diffusion Terms and Noise Power	47
2.7.1 Diffusion Terms of Filter and TOF Cooling	47

2.7.2	Diffusion Terms Palmer Cooling	48
2.8	Discussion of Momentum Cooling Techniques.....	49
2.8.1	Filter Cooling	49
2.8.2	Time-Of-Flight Cooling (TOF).....	54
2.9	Momentum Cooling Acceptance	58
2.10	Open Loop Gain and Beam Feedback.....	58
2.11	Rate Equation for Momentum Cooling.....	83
2.12	Example Antiproton Cooling in the HESR.....	91
3	STOCHASTIC BETATRON COOLING	96
3.1	Coherent Emittance Change	99
3.2	Incoherent Emittance Change.....	102
3.3	Emittance Cooling Rate Equation	107
3.4	Schottky Noise Density.....	110
3.5	Mixing Factor and Noise-to-Signal Ratio.....	117
3.6	Open Loop Gain and Beam Feedback.....	122
3.6.1	Emittance Cooling Rate Including Beam Feedback	124
3.6.2	Transverse Beam Transfer Function	125
3.6.3	Core Cooling Formula.....	133
3.7	Transverse Pickup Impedance and Kicker Sensitivity	140
4	BEAM-TARGET INTERACTION	149
4.1	Beam-Target Interaction of an Ion Beam	153
4.1.1	Hydrogen Target	153
4.1.2	Xenon Target.....	154

4.2	Beam-Target Interaction of an Antiproton Beam.....	155
5	INTRABEAM SCATTERING.....	155
6	SYNCHROTRON PHASE SPACE MOTION.....	161
Appendix A	Autocorrelation Function and Power Density.....	172
Appendix B	Distributions	173
Appendix C	Liouville Operator and Time Evolution.....	177
Appendix D	Transverse Dipole Density with Chromaticity.....	179
References		

Preface

The intention of the theory part of the book is to outline a comprehensives and contiguous description of the stochastic cooling theory which is applied in the cooling simulations to predict the beam properties in internal target experiments at COSY and HESR. The cooling formalism is extended to include the beam-target interaction. The latter is discussed in more detail in chapter 4. The simulations and momentum cooling experiments at COSY with internal targets demonstrate that the mean energy loss due to the beam-target interaction cannot be compensated by a momentum cooling application alone. Instead, an $h = 1$ rf-cavity or a barrier bucket cavity is mandatory to compensate the mean energy loss, specifically for thick targets as they are envisaged in the PANDA experiment at the HESR. Beam dynamics experiments at COSY have proven that stochastic momentum cooling with simultaneously barrier bucket operation behaves similar to stochastic cooling of a DC beam and therefore constitutes the preferable method to compensate the mean energy loss successfully. To investigate the cooling experiments theoretically the Fokker-Planck approach of 1-dimensional momentum cooling as outlined in chapter 2 has been extended to include the beam-target interaction under the assumption that the mean energy loss is compensated. Intrabeam scattering (IBS) caused by small-angle Coulomb scattering in a charged beam is incorporated with an additional diffusion term (chapter 5).

Stochastic betatron cooling is described in chapter 3. The rate equations are extended so as to include the small-angle Coulomb scattering due to the beam-target interaction which leads to a transverse emittance growth with time.

The authors have investigated the beam cooling process in the HESR for these several years, developing the cooling theory and the simulation code and frequently performing the experiment at the COSY to confirm the simulation results and benchmark the computer code. After the intensive work it is now concluded that the stochastic cooling is able to attain the high resolution antiproton beam for the energy range 1 to 14 GeV and will meet the requirements for internal target experiments with heavy ions too.

The aim of the theory part of the book is to present a detailed derivation of the longitudinal and betatron stochastic cooling formalism which is applied in part 2 of the book to determine the cooling predictions for COSY or the HESR including internal targets and Intrabeam Scattering. The derivation includes the beam-target interaction formalism.

Examples are considered which illustrate important quantities in the cooling theory. Electronic power is one essential issue. The task, how to adjust a stochastic cooling system, is envisaged with an open loop gain measurement. The measurement carried out with a network analyzer constitutes a complete knowledge on the cooling system performance.

Despite the fact that we elucidate some important facts in the cooling formalism it is beyond our scope to exemplify and to cover all topics in cooling theory. We rather suggest the reader to consult the references given in this book of the original papers on cooling theory for more details and also on the stochastic cooling history. Also, a recently published work that presents the stochastic cooling systems being installed in different laboratories in the world is strongly recommended.

The authors are indebted to D. Prasuhn, A. Lehrach and COSY colleagues for their support in many aspects. The successful stochastic cooling experiments at COSY are much indebted to the efforts of R. Stassen. The discussion with L. Thorndahl, the late D. Moehl and F. Caspers (CERN) are quite suggestive and helpful for the development of stochastic cooling theory. The discussion of electron cooling with S. Kamerdzhiev, J. Dietrich and V. Parchomchuk (Novosibirsk) are quite useful for the elucidation of the electron cooling process. The lattice design of the HESR is done by B. Lorentz which is fundamental for the present work. The suggestion and advice on the internal target effects by F. Hinterberger (Bonn Univ.) is much useful. M. Steck, B. Franzke and the storage ring group (GSI) have collaborated in the Proof-Of-Principal (POP) experiment for the proposed antiproton beam accumulation scenario and continuously suggested and supported to our work. T. Stoehlker and Y. Litvinov proposed the atomic physics experiments with high energy heavy ion beam in the HESR which opened the new field of utility of the HESR accelerator. Author (T.K.) is much indebted to T. Kikuchi (Nagaoka) to his help and discussion on the simulation method. Author (H.St.) would like to thank his wife Heike for her continuous support and patient understanding during the entire stages of preparation of this book.

H. Stockhorst, T. Katayama and R. Maier

December 2015

1 The Acceleration Facilities HESR and COSY

1.1 HESR

Stochastic cooling techniques [1, 2, 3, 4] will play an essential role in the new High Energy Storage Ring (HESR) [5] at the Facility of Antiproton and Ion Research (FAIR) [6]. This machine is dedicated to the field of high energy antiproton physics with high quality beams over the broad momentum range from 1.5 to $15\text{ GeV}/c$ with up to 10^{11} antiprotons to explore the research areas of hadron structure and quark-gluon dynamics, e.g. non-perturbative QCD, confinement, and chiral symmetry. An important feature of the new facility is the combination of phase space cooled beams with internal targets which opens new capabilities for high precision experiments with relative momentum resolution down to nearly $1 \cdot 10^{-5}$.

International collaborations (e.g. PANDA [7]) with a rich scientific program are working on new experiments with antiprotons in the energy range between the CERN Antiproton Decelerator AD and the Tevatron energies.

Special equipment like a multi-harmonic rf and a barrier bucket cavity as well as stochastic cooling enable the high performance of this antiproton machine which will make high precision experiments feasible that are not possible up to now.

It is therefore mandatory to provide powerful beam cooling systems to counteract beam heating from the beam-target interaction and intrabeam scattering to achieve a high luminosity and a high beam quality. Beam dynamics experiments at COSY [8] and the simulations reveal that beam cooling alone cannot compensate the strong mean energy loss and energy loss straggling in the case of thick targets. It is then essential to utilize the barrier bucket (BB) cavity [9] of the HESR to compensate the strong mean energy loss.

In the first stage the HESR is equipped with a stochastic cooling system working in the frequency range ($2 - 4$) GHz [10]. New high sensitive pickups and kickers using ring-slot couplers have been developed and successfully tested at COSY [11]. A stochastic cooling system that makes use of the new ring-slot couplers has been successfully taken into operation at the NUCLETRON in Dubna [12]. Basic cooling system parameters are listed in Table 1.1.

Since in the Modularized Start Version (MSV) of the Facility for Antiproton and Ion Research (FAIR) [6] the Recuperated Experimental Storage Ring (RESR) and the New

Experimental Storage Ring (NESR) are postponed the accumulation of the beam delivered by the Collector Ring (CR) [13, 14] has to be accomplished in the HESR itself. The well-established stochastic stacking method [4] is however not applicable. Instead a different method using moving barriers and stochastic filter momentum cooling is established [15] to accumulate 10^{10} antiprotons within 1000 s. In a proof-of-principle experiment [16] at the GSI it could be demonstrated that the proposed accumulation scheme is indeed capable to provide the antiproton accumulation.

Furthermore, it was proposed to prove the feasibility of operating the HESR storage ring with heavy ion beams with the special emphasis on the experimental program of the SPARC collaboration [17] at FAIR. The magnetic rigidity range from 5 to 50 Tm allows the storage of typical reference ions such as $^{132}Sn^{50+}$ and $^{238}U^{92+}$ in the kinetic energy range 740 MeV/u (injection energy) up to roughly 5 GeV/u. In simulation studies a bare $^{238}U^{92+}$ beam with $N = 10^8$ ions and a kinetic energy 740 MeV/u is kicked injected from the CR [13, 14] into the HESR. The beam preparation for an internal target experiment at 740 MeV/u has been investigated as well as ion beam acceleration up to 4.5 GeV/u has been studied in detail [18]. Stochastic filter and TOF cooling with the envisaged (2 – 4) GHz system, assisted by a barrier bucket cavity, is applied to compensate the mean energy loss caused by a thick hydrogen target. The simulation proved that the HESR can be operated with heavy ion beams as well as with antiprotons without technical changes or additional cost.

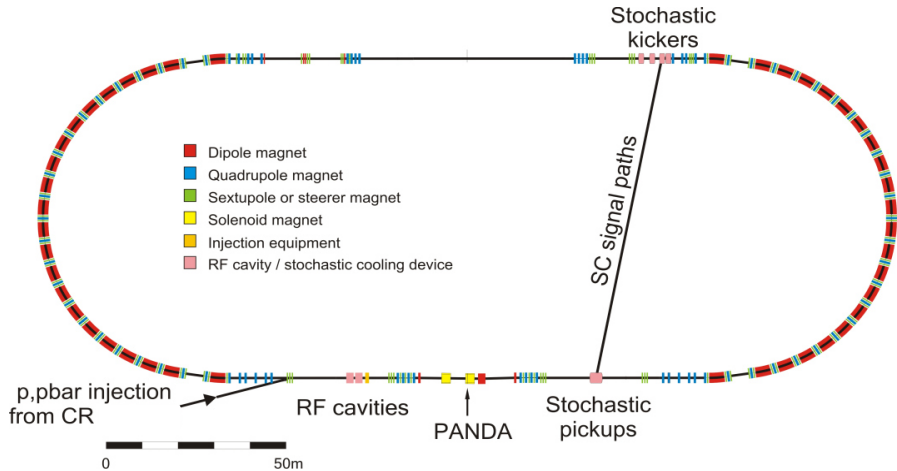


Figure 1.1: Schematic view of the HESR

The HESR ring lattice with zero dispersion in the straights has been optimized for the PANDA internal target experiment and stochastic cooling with a transition gamma $\gamma_{tr} = 6.23$. Zero dispersion at the target as well as at the stochastic pickup and kicker tank locations is essential as will be outlined below. The lattice can however be adjusted for transition gamma values between 6 and 25. This provides the flexibility to adjust the transition energy during acceleration or deceleration so that the transition energy must not be crossed. A schematic drawing of the HESR is shown in Figure 1.1 with the location of the pickup and kicker tanks and important machine parameters are summarized in Table 1.1.

Table 1.1: Main HESR and CAVITY parameters

Parameter	Value	Unit
Ions		
Kinetic energy	165 - 4940	MeV/u
β	0.528 – 0.987	
γ	1.177 – 6.303	
B _p	5 – 50	Tm
Antiprotons		
Kinetic energy	830 – 14081	MeV/u
β	0.848 – 0.998	
γ	1.886 – 16.01	
B _p	5 – 50	Tm
Ring		
Ring length	575	m
Arc length	155.5	m
Straight section	132	m
Transition gamma	6 - 25	
Dipole field	0.17 – 1.7	T
Dipole ramp rate	25	mT/s
Transverse acceptance	15.6 (@ $\gamma_{tr} = 6.23$)	mm mrad
Momentum acceptance	$\pm 2.8 \cdot 10^{-3}$	
BB cavity frequency	5	MHz
Max. BB voltage	2	kV
Max. h = 1 voltage	5	kV

The HESR stochastic cooling system [19] operates in the frequency range 2 – 4 GHz with the future option to be extended up to 6 GHz. The properties of the cooling system as well as the

pickup and kicker characteristics are discussed in chapter 2.3 for momentum cooling and in chapter 3.7 for transverse cooling.

1.2 COSY

COSY [20, 21] is a COoler SYnchrotron and storage ring for medium energy physics. Since its inauguration in 1993 the cooler ring delivers unpolarized or polarized protons and deuterons in the momentum range 270 to 3300 MeV/c. The COSY facility, Figure 1.2, basically consists of an ion source, an injector cyclotron, a 100 m long injection beam line, a 184-m-circumference ring and extraction beam lines. It has an electron cooling system [22] that operates up to 100 keV electron energies which enables to cool proton beams with kinetic energies up to 184 MeV. A stochastic cooling system [23] that operates at momenta between 1500 and 3300 MeV/c is available to increase the phase space density of a proton beam. Just recently a new 2 MeV electron cooler came into operation [24]. Vertically polarized proton beams [25, 26] with a polarization of more than 0.80 are delivered to internal and external experimental areas at different momenta. Additionally, deuteron beams with different combinations of vector and tensor polarization were made available for internal and external experiments.

In internal target experiments at higher proton beam momenta using gas jet targets, pellet targets or internal target storage cells stochastic cooling is mandatory to improve the beam luminosity. A barrier bucket cavity [11] is available to compensate the strong mean energy loss induced by the beam-target interaction.

The COSY lattice [27] is designed to provide flexibility with respect to ion-optical settings in order to fulfill the requirements for internal and external experiments. The lattice allows to shift transition energy upwards during acceleration so that no transition jump is needed. At flat top energy of an experiment the lattice can be tuned to achieve zero dispersion in the 52 m long straight sections.

The COSY stochastic cooling system [23] operates in the frequency range from 1 GHz to 3 GHz divided into two bands, band I (1 - 1.8) GHz and band II (1.8 - 3) GHz. The pickups for the horizontal or vertical plane consist of two 2 m long tanks each containing quarter wave loop couplers for band I and band II mounted on movable bars.

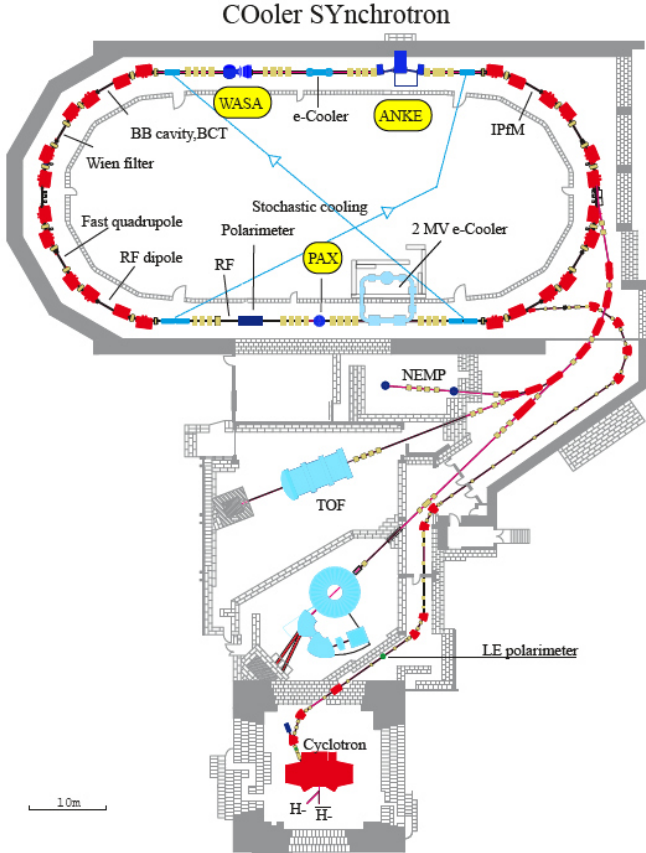


Figure 1.2: Floor plane of the Cooler Synchrotron COSY. Internal and external experiment stations and installations as in the year 2014 are shown. The diagonal signal paths of the stochastic cooling system across the ring from pickup to kicker are visible.

The kickers for horizontal and vertical cooling consist of one 2 m long tank per plane. The pickup and kicker tanks are located in the ring as depicted in the floor plane of COSY, Figure 1.2. The pickups are cryogenically cooled down to nearly 30 K. Uncooled preamplifiers with a noise temperature below 50 K are mounted outside the vacuum tanks. The position of the electrode bars is independently adjustable from 140 mm aperture at injection to 20 mm aperture during cooling. The electrode bars can be adjusted for closed orbit suppression and optimal signal-to-noise ratio. The loop coupler signal combination has been optimized to attain optimal cooling in the whole velocity range $\beta > 0.83$ which corresponds to the proton momentum range 1.5 GeV/c up to 3.3 GeV/c. Presently, vertical beam cooling is carried out

with band I and band II. For horizontal cooling band II is used only. Longitudinal cooling is performed with band I of the horizontal pickup tanks and kicker tank in sum mode. For momentum cooling either TOF or filter cooling with an optical delay line is possible. The installed rf power per cooling plane amounts 500 W. Main properties of the COSY cooling system are summarized in Table 1.2

Table 1.2: Number of loop couplers and cooling bandwidth used for stochastic cooling.

Vertical Cooling	band I + band II
Number of pickup electrodes	112
Number of kicker electrodes	56
Horizontal Cooling	band II
Number of pickup electrodes	64
Number of kicker electrodes	32
Longitudinal Cooling	band I
Number of pickup electrodes	24
Number of kicker electrodes	24
Distance pickup to kicker	≈ 92 m
Power per plane	500 W

During more than 20 years of operation COSY has proven as a reliable machine with valuable benefit for internal and external beam experiments. With the end of 2014 the hadron physics program has been terminated now. The versatility of COSY with its accelerator components and the similarity of the machine to the HESR are now of great advantage for beam dynamics studies in view of the future operation of the HESR. The new 2 MeV electron cooler will be further improved and a combination of electron cooling as well as stochastic cooling will be studied. Preparatory measurements for FAIR, comprising detector tests for the CBM and the PANDA facilities, as well as accelerator equipment investigations have now high priority. In addition, a significant amount of time with polarized deuteron beams for research and development studies for the EDM-project come to the fore.

2 Stochastic Momentum Cooling

2.1 Introduction

The aim of stochastic momentum cooling [1, 2, 3] is to reduce the momentum spread of each individual particle in an ion beam. To follow the beam dynamics of stochastic momentum cooling in detail it is therefore not sufficient to solely deal with equations that describe the time evolution of rms-values as is done in the description of betatron cooling. Instead an equation is necessary to describe the time evolution of the momentum distribution of the beam. Specifically this becomes important if the beam-target interaction that alters the beam momentum distribution is considered when an internal target is inserted in the accelerator ring. Such an equation exists and was first proposed for the description of stochastic momentum cooling [1]. In the next section a graphic description of the Fokker-Planck equation is presented.

Longitudinal stochastic cooling can be utilized by three methods. In the first method (*filter cooling*) a pickup measures the beam current and the discrimination of particles with different momentum deviations is obtained by inserting a notch filter in the signal path before it drives a kicker in sum mode. The advantage of the filter cooling method, preferred for the HESR design, is that it uses a sum mode pickup which is much more sensitive especially for a smaller number of particles as compared to a pickup that measures the beam position. Moreover, due to filtering after the preamplifier the signal-to-noise ratio is much higher even for a low particle number in the ring. As will be demonstrated a further benefit of filter cooling is that the center frequency of the filter can be adjusted to optimize the cooling in the presence of an internal target. The derivative of the pulse signal of a particle delivered by the pickup is at first equally divided into two paths. One path is delayed by the revolution time corresponding to the nominal beam momentum. Then both signals are subtracted and the resulting signal is amplified and fed to the kicker. Thus a particle sees two correcting kicks at the kicker, the first one when it passes from pickup to kicker and the other one from the previous revolution. The two pulses cancel each other exactly if the particle has the nominal revolution frequency (nominal momentum). The cancellation is incomplete for particles that have a momentum deviation resulting in acceleration or deceleration until the particle has the nominal revolution frequency. Consequently, the undesired mixing is larger as compared to that of the Palmer cooling method or the TOF cooling method. In the latter two methods only

the undesired mixing on the way from pickup to kicker is relevant. This may lead to a severe restriction in the practical cooling bandwidth when the filter cooling system is applied to a beam with a large initial momentum spread. The filter cooling method is practical if the longitudinal Schottky bands are well separated in the cooling bandwidth to avoid too much mixing from pickup to kicker. It will be shown later that band overlap occurs only above the maximum considered frequency of the HESR cooling system.

The second momentum cooling method is the Time-Of-Flight (*TOF*) technique which was proposed by W. Kells [28] and first experimentally demonstrated at COSY [8]. The output pulse of a pickup in sum mode is differentiated and sent to the kicker with a delay set to the time of flight from pickup to kicker for the nominal particle. At the kicker the nominal particle then sees the zero crossing of the differentiated pulse at the pickup and is thus not affected while particles which are too slow or too fast receive a correction. This technique can be easily established when in the filter cooling chain the filter is removed. This method has the advantage of a larger cooling acceptance and is used to pre-cool the beam if the initial momentum spread is too large for filter cooling. After sufficient momentum spread reduction with TOF cooling the cooling chain can be switched to the faster filter Cooling technique. This procedure is very effective and needs no additional hardware components and has been successively demonstrated in cooling experiments at COSY [8].

Note that both, filter and TOF cooling needs a 90 degree phase shifter to differentiate the particle pulse delivered at the pickup.

The third method (*Palmer cooling*) uses the fact that the momentum deviation of a particle can be measured directly by a position sensitive pickup located at a point in the ring with high position dispersion. The signal at the output of the pickup averaged over the betatron motion is then proportional to the product $D \cdot \delta$ where D is the dispersion and δ is the relative momentum deviation of a particle. This correction signal is amplified and sent to the kicker operated in sum mode to provide the necessary momentum correction. This cooling technique needs no 90 degree phase shifter.

2.2 The Fokker-Planck Equation

In longitudinal cooling the time evolution of the beam momentum distribution $\Psi(\delta, t)$ is found from (numerically) solving a *Fokker-Planck equation (FPE)*

$$\frac{\partial}{\partial t} \Psi(\delta, t) = -\frac{\partial}{\partial \delta} \Phi(\delta, t) \quad (2.1)$$

with the flux

$$\Phi(\delta, t) = F(\delta) \Psi(\delta, t) - D(\delta, t) \frac{\partial}{\partial \delta} \Psi(\delta, t) \quad (2.2)$$

where δ is the relative momentum deviation of a particle. Appropriate initial and boundary conditions are taken into account. The boundary condition describes the finite momentum acceptance of the accelerator.

The flux $\Phi(\delta, t)$ is determined by two terms. The *drift term* $F(\delta)$ describes the *coherent* cooling effect by the self-interaction of a single particle with its own momentum deviation. The second term describes the *incoherent* beam heating by diffusion and its strength is determined by the *diffusion coefficient* $D(\delta, t)$ which is always positive. Diffusion always leads to a broadening of the beam distribution.

The FPE, eq. (2.1) is nothing else but a continuity equation. To understand how the FPE can describe cooling eq. (2.1) is approximately written as

$$\Psi(\delta, t + \Delta t) \approx \Psi(\delta, t) - \frac{\partial}{\partial \delta} \Phi(\delta, t) \Delta t \quad (2.3)$$

to find the change in the particle density within the time interval Δt . One concludes that the particle density increases for a given momentum deviation in the time interval Δt if the flux has a negative slope. In regions where the flux has a positive slope the density is decreased. This is illustrated graphically in Figure 2.1. The simple sketch in Figure 2.1 shows the cooling of an initial Gaussian beam distribution (red curve) when the drift term is proportional to the momentum deviation, $F(\delta) = -k \cdot \delta$, with a positive constant k . Neglecting the diffusion term and using the drift term only the flux as shown in the figure is easily derived graphically. One clearly sees where the beam density is increased or decreased. As a net result cooling occurs as indicated by the blue curve in the left hand side of the figure. A similar sketch can be drawn for the flux if only the (constant) diffusion term is present. One concludes that the diffusion

term in $\Phi(\delta, t) = D \frac{\partial^2}{\partial \delta^2} \Psi(\delta, t)$ always leads to a broadening of the beam distribution (sketch the second derivative in Figure 2.1).

From eq. (2.2) it follows that cooling only occurs if the coherent term predominates the incoherent one, i.e. the resulting flux has a shape similar to that as shown in Figure 2.1.

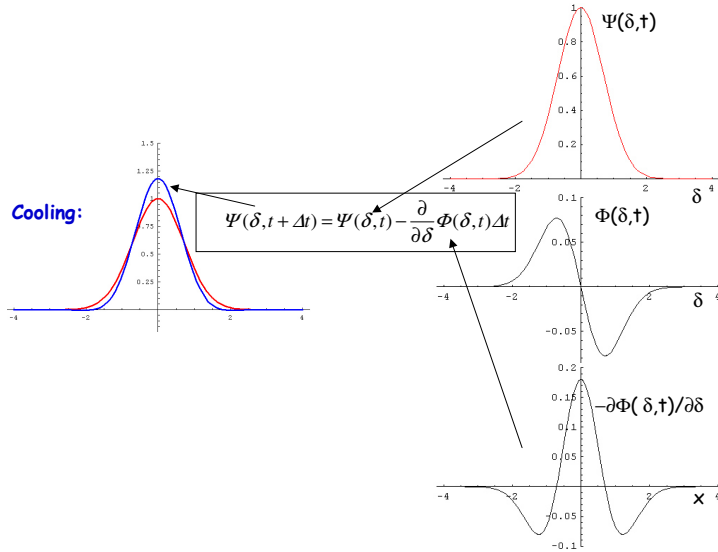


Figure 2.1: Sketch of cooling when the drift term is proportional to the momentum deviation. The flux as shown in the middle of the right hand side is simply proportional to the product of the initial beam distribution (red curve) at time t with $-\delta$. Below the flux its derivative is shown. One clearly sees in which regions the density is increased or decreased. If this curve is added to the initial distribution with an appropriate weight (gain) the beam distribution at time $t + \Delta t$ is found (blue curve). The peak density is increased and the width is reduced.

The rate at which the number of particles $N_{[-\delta, \delta]}(t) = \int_{-\delta}^{\delta} \Psi(\tilde{\delta}, t) d\tilde{\delta}$ with momentum deviations in the interval $[-\delta, \delta]$ changes at time t is given by $\frac{dN_{[-\delta, \delta]}(t)}{dt} = \frac{\partial}{\partial t} \int_{-\delta}^{\delta} \Psi(\tilde{\delta}, t) d\tilde{\delta}$.

Inserting the Fokker Planck equation (2.1) in the previous expression and taking into account

Figure 2.1 we deduce $\frac{dN_{[-\delta, \delta]}(t)}{dt} = -(\Phi(\delta, t) - \Phi(-\delta, t)) = -2\Phi(\delta, t)$. The number of

particles in the considered momentum range increases if $\Phi(\delta, t) < 0$ at the boundary $\delta > 0$, see Figure 2.1. We therefore conclude that the condition of fast cooling is that the flux Φ is maximized. The impact of this requirement on the choice of the cooling system parameters is outlined in the next chapters.

If drift and diffusion balance each other the flux will vanish and cooling stops. An equilibrium distribution is then attained. Note, that reversing the sign in k results in a heating of the beam distribution. The sign is determined by the amplifier gain of the cooling system and the frequency slip factor as shown below.

Both drift and diffusion coefficient are determined by the system layout and were calculated in [29] for a specific design of the cooling system at TARN. Later improvements were given by the authors (H. St. and T. K.) where it is assumed that pickup and kicker structures are designed as quarter wave loop couplers with electronic transfer functions as given in [30]. In this contribution the newly developed pickup and kicker structures designed for the HESR are taken into account. They have been tested successfully at COSY [11] and at the Nucletron ring at Dubna [12].

In the following it is more convenient to write the Fokker Planck equation in the form

$$\frac{\partial}{\partial t} \Psi(\Delta E, t) = -\frac{\partial}{\partial \Delta E} \left[F(\Delta E, t) \Psi(\Delta E, t) - D(\Delta E, t) \frac{\partial}{\partial \Delta E} \Psi(\Delta E, t) \right] \quad (2.4)$$

for the energy density function $\Psi(\Delta E, t)$ where ΔE is the energy deviation per nucleon from the total energy per nucleon $E = \gamma E_0$ of an ion with charge number Z and mass number A . The rest energy is $E_0 = 938.27 \text{ MeV}$ for protons or antiprotons while for heavy ions $E_0 = 931.5 \text{ MeV}$. The kinematic factor of a particle with velocity v is $\gamma = \sqrt{1/(1-\beta^2)}$ with $\beta = v/c$. The energy density function at time t is normalized to the number of ions in the ring $N(t) = \int \Psi(\Delta E, t) d\Delta E$. The center of gravity of the distribution is

$$\mu(t) = \frac{1}{N(t)} \int \Delta E \Psi(\Delta E, t) d\Delta E \quad \text{and the beam variance is given by second moment}$$

$$\sigma_E^2(t) = \frac{1}{N(t)} \int (\Delta E - \mu(t))^2 \Psi(\Delta E, t) d\Delta E.$$

For convenience, if we talk from energy deviation it is meant energy deviation per nucleon henceforth.

The drift term in the FPE

$$F(\Delta E, t) = \frac{\omega_0}{2\pi} \Delta E_c \quad (2.5)$$

depends explicitly on the energy deviation and may depend on time. It is proportional to the energy deviation per nucleon of the particle at the pickup. The drift term describes the coherent cooling and determines the coherent change of the energy deviation per nucleon per second a particle receives at the kicker by its own signal at the pickup. The coherent change of the energy deviation per turn is given by ΔE_c . The angular revolution frequency of the nominal particle with total energy E is denoted by $\omega_0 > 0$.

The diffusion is a result from random energy changes due to noise in the cooling loop and due to the fluctuations in the beam signal at the pickup. The diffusion term is

$$D(\Delta E, t) = \frac{1}{2} \frac{\omega_0}{2\pi} \langle \Delta E_{ic}^2 \rangle \quad (2.6)$$

where $\langle \Delta E_{ic}^2 \rangle$ is the mean square change of the energy deviation of an ion per turn at the kicker.

The diffusion term $D(\Delta E, t)$ describes beam heating by noise. The *diffusion term* $D(\Delta E, t) = D_{th}(\Delta E, t) + D_s(\Delta E, t)$ consists of two parts, beam heating due to thermal noise, $D_{th}(\Delta E, t)$, and Schottky noise, $D_s(\Delta E, t)$. Later we will introduce additional diffusion terms induced by the beam-target interaction and intrabeam scattering of the ions.

When deriving the drift and diffusion terms we deal with fluctuating quantities such as beam signals created by a large number of particles. Thus on a microscopic scale the signals are not well defined. We therefore apply averaging of stochastic quantities. In this context we note that stochastic cooling is a slow process so that the statistics do not significantly change on a short scale. Hence we can apply the mathematical apparatus for stationary statistical processes in which mean values and distribution functions do not depend on time. Furthermore the autocorrelation function of a stationary process only depends on time differences. We

assume that the results still are good approximations when the distributions change slowly as time proceeds during cooling. Partly, important necessary mathematical tools are illustrated in the appendices and for further reading we refer to [31].

2.3 System Transfer Function

The system transfer functions models the electronics which is contained in the signal path of the stochastic cooling system including pickup and kicker structures. In the following we make model assumptions on these devices which allow predicting the behavior analytically. In the numerical cooling model simulations it is however possible to include more refined transfer functions such as a non-linear gain or equalizers to optimized the response of the cooling chain. Details of signal processing can be found in [32].

We first derive the system transfer function of the cooling system for the filter and TOF methods since both techniques apply a pickup and a kicker in sum mode.

The following figures give an overview of the main components in the electronic cooling chain set up for filter cooling, filter-less (TOF cooling) and Palmer cooling. Details are given in the chapters below.

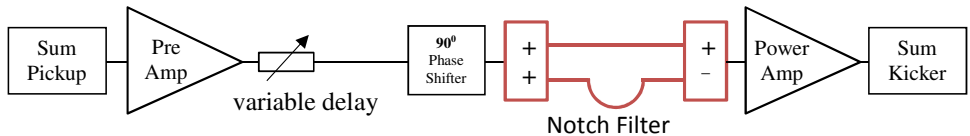


Figure 2.2: Electronic setup for filter cooling. The output signal of the sum-pickup is pre-amplified and after filtering and amplification the signal is fed to the kicker in sum mode. The filtering is accomplished with the notch filter. A 90 degree phase shifter is essential for the correct sign of the momentum correction signal at the kicker. The variable delay in the chain is used to adjust the electronic transit time to the arrival time of the reference particle at the kicker.

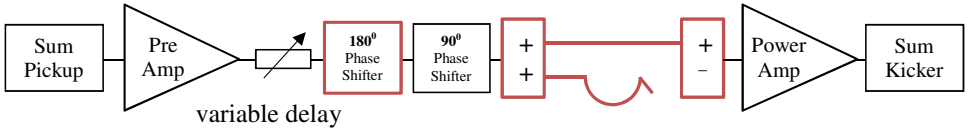


Figure 2.3: Electronic setup for TOF cooling. The output signal of the sum-pickup is first pre-amplified. The delay-path of the notch filter is opened and the 90 degree phase shifter is used to differentiate the pickup output pulse of a particle which is then sent after power amplification to the kicker in sum mode. For the correct sign of the momentum correction signal at the kicker an additional 180 degrees phase shift is applied. The variable delay in the chain is used to adjust the electronic transit time and thereby the zero crossing time of the differentiated pulse to the arrival time of the reference particle at the kicker.

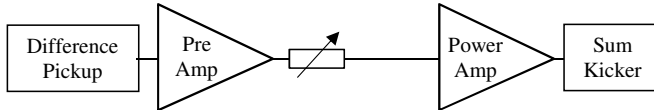


Figure 2.4: Setup for Palmer cooling. A specifically designed horizontal-position-sensitive pickup (Palmer pickup) located in the ring at a large dispersion is used to measure the momentum deviation of a particle.

From signal analysis theory it is known that the transfer function is the Fourier transform of the impulse response of the system and completely describes the steady state of a linear and time-invariant system [32]. The transfer function is a complex function with magnitude and phase in the angular frequency domain.

If the voltage U_K is applied at the kicker the energy change per nucleon of a single ion with charge Ze and mass number A is found from

$$\Delta E(\omega) = \frac{Ze}{A} K_{\parallel}(\omega) U_K(\omega) \quad (2.7)$$

The angular frequency is ω and takes on positive and negative values. The kicker transfer function (or kicker sensitivity) for kicker in sum mode is denoted by $K_{\parallel}(\omega)$. An explicit expression for the HESR structures will be given below.

Since the pickup in both methods, TOF and filter method, measures the beam current the output voltage of the pickup is given by

$$U_p(\omega) = Z_{PL}(\omega)i_b(\omega) \quad (2.8)$$

where the pickup transfer function or coupling impedance is $Z_{PL}(\omega)$ and the beam current is $i_b(\omega)$.

In the model we assume that the amplifiers in the cooling chain are gathered in one group having the transfer function

$$G_A(\omega) = \begin{cases} G_A e^{i\phi_A(\omega)} & n_1\omega_0 \leq |\omega| \leq n_2\omega_0 \\ 0 & \text{elsewhere} \end{cases} \quad (2.9)$$

with constant electronic gain G_A in the cooling bandwidth $W = (n_2 - n_1)\omega_0/(2\pi)$.

The lower and upper harmonic of the cooling system is n_1 and n_2 , respectively. It is assumed that the phase response is linear and an additional adjustable delay line in the cooling loop is included in the phase $\phi_A(\omega) = -\omega T_D$ ($T_D = T_{amp} + T_{delay}$). In the following we use this simplified gain with flat magnitude response and ideal linear phase. However the model can also include non-ideal transfer functions and, if necessary, can include equalizer etc.

In the case of filter cooling the signal path contains a 90 degree phase shifter $P(\omega)$ and the notch filter $H(\omega)$, see Figure 2.2. For TOF cooling the path with the delay line in the notch filter is opened, see Figure 2.7 below and Figure 2.3. Since in TOF cooling no filter is needed this method is also called filter-less momentum cooling [28].

The kicker input voltage is thus the product of the individual transfer functions and yields

$$U_k(\omega) = H(\omega)P(\omega)G_A e^{-i\omega T_D} U_p(\omega) = H(\omega)P(\omega)G_A e^{-i\omega T_D} Z_{PL}(\omega)i_b(\omega)$$

The complete transfer function of the cooling chain may then be written as

$$\Delta E(\omega) = T(\omega)i_b(\omega) \quad (2.10)$$

where

$$T(\omega) = \frac{Ze}{A} K_{\parallel}(\omega) G_A H(\omega) P(\omega) Z_{PL}(\omega) e^{-i\omega T_D} \quad (2.11)$$

is the transfer function of the cooling chain in case of filter cooling. For TOF cooling one has to remove the filter, i.e. set $H(\omega) = 1$.

It is important to note that all transfer functions, specifically $T(\omega)$ obeys the rule $T^*(\omega) = T(-\omega)$ where the star denotes the conjugate complex quantity since the signals in time domain are real quantities.

2.3.1 Phase Shifter

The 90 degree phase shifter is specifically essential to form a derivative of the output pulse of the pickup in the TOF method. It is defined as

$$P(\omega) = i \cdot \text{sign}(\omega) \quad \text{with} \quad \text{sign}(\omega) = \begin{cases} 1, & \omega > 0 \\ -1, & \omega \leq 0 \end{cases} \quad (2.12)$$

where the imaginary unit is $i = \sqrt{-1}$.

The phase shifter has the properties $P^*(\omega) = P(-\omega) = -P(\omega)$.

The corresponding impulse response in time domain is $p(t) = -1/\pi t$ [31]. The response in time domain of the 90 degree phase shifter $U(t)$ to a real signal $I(t)$ is then given by the convolution of the pulse response $p(t)$ with the input signal $I(t)$

$$U(t) = \int_{-\infty}^{\infty} p(\tau) I(t - \tau) d\tau = -\frac{1}{\pi} P \int_{-\infty}^{\infty} \frac{I(t - \tau)}{\tau} d\tau. \quad (2.13)$$

The principal value of the integral is denoted by P .

According to eq. (2.13) the 90 degree phase shifter responds to the input signal $I(t) = \sin(\omega t)$ with the output signal $U(t) = \sin(\omega t + \pi/2) = \cos(\omega t)$ which is proportional to the derivative of the input signal. Similarly, if $I(t) = \cos(\omega t)$, then $U(t) = -\sin(\omega t)$.

To illustrate the signal processing of the 90 degree phase shifter we assume that the pickup pulse of a particle is processed by a lowpass system with bandwidth W . The transfer function is given by $B(\omega) = 1$ for $|\omega| \leq 2\pi W$ and $B(\omega) = 0$ for $|\omega| > 2\pi W$. The time response $b(t)$ of

the lowpass system due to a particle that passes a short pickup is then found with the inverse Fourier transform (Appendix A) of the lowpass transfer function. One obtains

$$b(t) = 2W \frac{\sin(2\pi Wt)}{2\pi Wt} \quad (2.14)$$

and the output voltage, Figure 2.5, is proportional to $b(t)$. Due to the limited bandwidth the short pickup output pulse of a particle is broadened. The time duration T_s of the pickup output signal is defined according to [32] as

$$T_s = \frac{I}{2W} \int_{-\infty}^{\infty} b(t) dt = \frac{I}{2W} B(0) = \frac{I}{2W}. \quad (2.15)$$

The output signal of a short pickup can thus be approximated by a rectangular pulse with duration T_s given by eq. (2.15) as is shown in Figure 2.5.

The output voltage due to the single passage of a particle with charge Ze through a short pickup including the 90 degree phase shifter is then found with an inverse Fourier transformation of $U(\omega) = B(\omega)P(\omega)Z_{PL}(Ze)$ yielding

$$U(t) = -Z_{PL}(Ze) \cdot 2\pi t W^2 \left(\frac{\sin(2\pi Wt)}{2\pi Wt} \right)^2. \quad (2.16)$$

For the present illustration the pickup impedance Z_{PL} has been assumed to be real and constant.

One concludes that the output voltage of the phase shifter can be used to discriminate between particles which are too slow or too fast. This technique will be used in the TOF cooling method. In Figure 2.5 it is seen that the output signal of the phase shifter is alike the derivative of the pickup signal.

Actually, the cooling system is a bandpass system (see eq. (2.9)). However, every bandpass system can be represented by an equivalent lowpass system [32] so that the conclusions drawn in this chapter are still valid for a bandpass system.

In addition a *90 degree* phase shifter is necessary for filter cooling. The necessity is discussed in chapter 2.8.1. A *180 degrees* phase shift of the amplifier provides an electronic gain reversal.

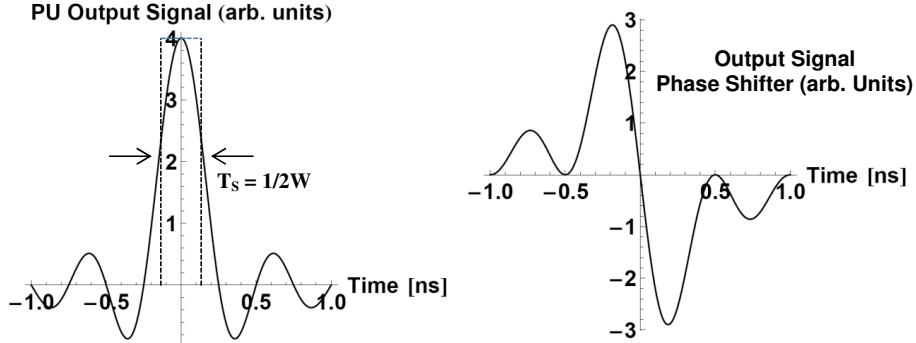


Figure 2.5: The pickup output signal after processing with a bandpass system of bandwidth W , left panel. The output of a *90 degree* phase shifter, right panel, provides a signal which is similar to the derivative of the input pulse. As discussed in the chapter for TOF cooling the output signal allows to discriminate between particles of different energy deviations and provides the correct phase to correct it at the kicker.

2.3.2 Pickup and Kicker Response

In the HESR newly designed ring slot coupler structures for the $(2 - 4)$ GHz system which have been experimentally tested at COSY [11] will come into operation. They provide a high sensitive beam probing and, driven as kicker, can apply effective corrections to the beam momentum. No moving electrode bars and feedthroughs are necessary in this design. The special design of the loop structures covering the whole beam is a fundamental requisite for their high sensitivity and compact construction in the application in the HESR stochastic cooling system.

In our description we adopt the frequency response similar to the quarter wave loop coupling impedance and kicker sensitivity function as outlined in [30], however modified in amplitude and strength according to the new design of the ring-slot coupler structures.

The frequency behaviour of each ring slot coupler cell for the $(2 - 4)$ GHz system operated as kicker is determined from simulations [33] as well as experiments and resulted in

an shunt impedance in the center of the cooling bandwidth, 3 GHz, of $Z_K = 36 \Omega$. The *shunt impedance* is determined from the kicker structure input power

$$P_K = \frac{(A \Delta E / Ze)^2}{2Z_K} \quad (2.17)$$

where $\Delta E / Ze$ is the energy change per nucleon and per charge (the integrated electric peak field) along one structure cell.

According to the reciprocity theorem [30] the *pickup shunt impedance* of one cell is

$$Z_P = \frac{1}{4} Z_K = 9 \Omega. \quad (2.18)$$

It is defined as the output power of the pickup P_p normalized to the squared rms beam current

$$i_{rms}, Z_P = \frac{P_p}{i_{rms}^2}.$$

In the HESR the kicker tank for momentum cooling contains 64 cells which results in a total shunt impedance $Z_K = 64 \cdot 36 \Omega = 2304 \Omega$. There are two pickup tanks each equipped with 64 cells yielding a total pickup shunt impedance of $Z_p = 2 \cdot 64 \cdot 9 \Omega = 1152 \Omega$.

The *pickup coupling impedance* Z_{PL} as used by [30] is defined as the ratio of output rms voltage of the pickup and the rms beam current. Then $U_{rms}^2 = Z_{PL}^2 i_{rms}^2$ and the output power of the pickup delivered into a line with characteristic impedance Z_0 is found with

$$P_p = \frac{U_{rms}^2}{Z_0} = \frac{Z_{PL}^2}{Z_0} \cdot i_{rms}^2 = Z_p \cdot i_{rms}^2.$$

The relation between coupling Z_{PL} and shunt impedance Z_p is then in the center of the cooling bandwidth

$$Z_{PL} = \sqrt{Z_p \cdot Z_0}. \quad (2.19)$$

We find the equivalent coupling impedance $Z_{PL} = 240 \Omega$ in the center of the cooling bandwidth.

The *kicker sensitivity* K_{\parallel} is defined as the ratio of the energy gain a particle of charge Ze receives by the kicker and the applied input voltage U_K ,

$$K_{\parallel} = \frac{\Delta E/(Ze/A)}{U_K}, \quad (2.20)$$

and is a dimensionless quantity. The power relation $\frac{(\Delta E/(Ze/A))^2}{2Z_K} = \frac{U_K^2}{2Z_0}$ holds if the input

power $P_K = \frac{U_K^2}{2Z_0}$ at the kicker entrance with characteristic line impedance Z_0 is matched to

the kicker. This defines the kicker sensitivity in terms of kicker shunt impedance Z_K and characteristic line impedance,

$$K_{\parallel} = \sqrt{\frac{Z_K}{Z_0}}. \quad (2.21)$$

The quantities given in eqs. (2.19) - (2.21) are given at the center frequency of the cooling system bandwidth. For the frequency dependency we adopt the magnitude and phase response of quarter wave loop electrodes as derived in [30]. The frequency behavior of the pickup coupling impedance is then given by

$$Z_{PL}(\omega) = \sqrt{Z_p \cdot Z_0} \sin \theta(\omega) e^{i(\frac{\pi}{2} - \theta(\omega))} \quad (2.22)$$

and the kicker sensitivity is

$$K_{\parallel}(\omega) = \sqrt{\frac{Z_K}{Z_0}} \sin \theta(\omega) e^{i(\frac{\pi}{2} - \theta(\omega))} \quad (2.23)$$

where the phase function $\theta(\omega)$ is

$$\theta(\omega) = \left(\frac{1}{\beta} + \frac{1}{\beta_s} \right) \frac{\omega \ell}{2c} \quad (2.24)$$

with βc the beam velocity and $\beta_s c$ the signal velocity. The loop length of the equivalent quarter wave loop is ℓ . We assume that beam and signal velocity are equal and $\ell = \frac{c}{4f_c}$. The

coupling impedance and the kicker sensitivity is then real in the center ($f_c = 3\text{GHz}$) of the cooling bandwidth W . The phase function reduces to

$$\theta(\omega) = \frac{\pi}{2} \frac{\omega}{\omega_c} \quad (2.25)$$

with $\omega_c = 2\pi f_c$.

The coupling impedance, eq. (2.22), and kicker sensitivity, eq. (2.23), possess the property $Z_{PL}^*(\omega) = Z_{PL}(-\omega)$ and $K_{||}^*(\omega) = K_{||}(-\omega)$.

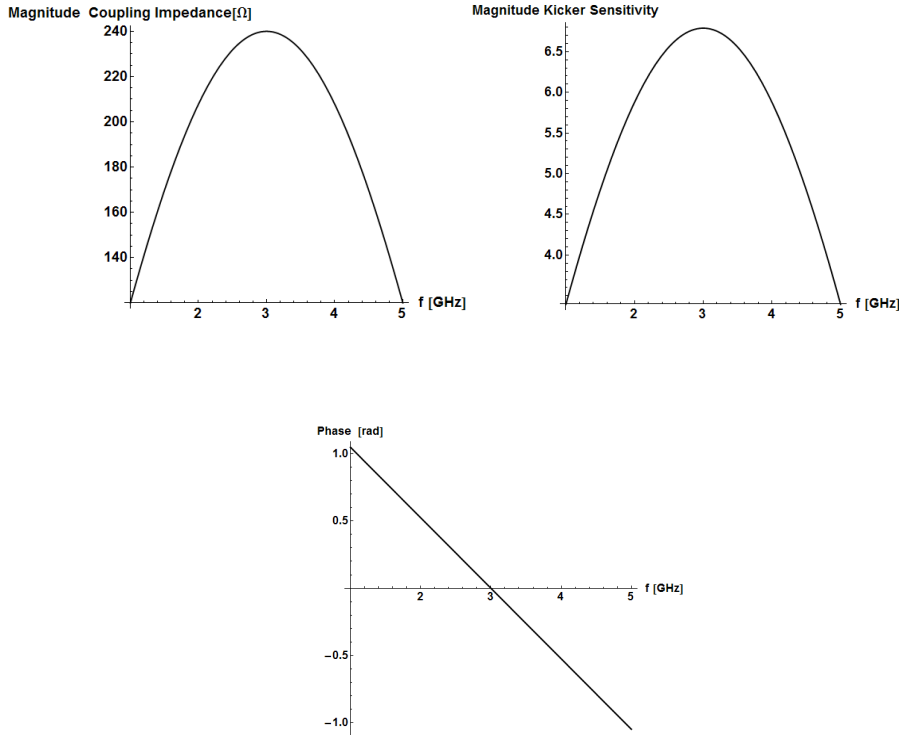


Figure 2.6: Model transfer function of the HESR pickup and kicker as used for momentum cooling in the bandwidth (2 – 4) GHz. The upper left and right figures show the magnitude of the coupling impedance and of the kicker sensitivity, respectively. The lower graph shows the phase versus frequency which is equal for pickup and kicker.

Figure 2.6 shows the model transfer functions for the pickup coupling impedance and kicker sensitivity with the parameters listed in Table 2.1.

From Figure 2.6 one concludes that the pickup coupling impedance is between 200Ω and 240Ω in the cooling bandwidth ($2 - 4$) GHz. The kicker sensitivity covers the range 5.5 to 6.8.

Table 2.1: Basic HESR pickup and kicker impedance and sensitivity values at midband frequency as used for momentum cooling simulations in the bandwidth ($2 - 4$) GHz.

Cells	PICKUP		KICKER		TANKS
	Shunt impedance [Ω]	Coupling Impedance [Ω]	Shunt Impedance [Ω]	Sensitivity	
1	9	21.2	36	0.85	
64			2304	6.8	1
128	1152	240			2
	Distance pickup to kicker			≈ 200 m	
	Installed RF power			500 W	

The intended installed RF power is 500 W per kicker tank for momentum cooling and 250 W per tank and plane for transverse stochastic cooling. Details of the transverse coupling impedance or the position sensitivity of the ring-slot couplers are outlined in chapter 3.7.

2.3.3 Notch Filter Transfer Function

The filter cooling technique was proposed by Thorndahl [1] and is routinely used in many accelerator laboratories distributed over the world [4]. The discrimination between particles with different momenta or different revolution frequencies is accomplished with a filter which is schematically depicted in Figure 2.7. We discuss the ideal case and assume that there are no frequency dependent cable losses and frequency dispersion. The input signal is denoted by $U_{in}(t)$ and is fed into a divider. As shown in the figure one branch with half the input signal is delayed by the nominal revolution period $T_0 = 2\pi/\omega_0$ and the other half is sent to the

combiner without delay. The delayed signal is subtracted at the output combiner. Thus we can write in time domain for the output voltage $U_{out}(t)$ of the filter

$$U_{out}(t) = \frac{1}{2} (U_{in}(t) - U_{in}(t - T_0)). \quad (2.26)$$

The delayed version of the input signal is $U_{in}(t - T_0)$. Performing a Fourier transform of eq. (2.26) one finds in frequency domain

$$U_{out}(\omega) = \frac{1}{2} \left\{ I - e^{-i\omega T_0} \right\} U_{in}(\omega) \quad (2.27)$$

and the transfer function $H(\omega) = \frac{U_{out}(\omega)}{U_{in}(\omega)}$ for the ideal notch filter becomes

$$H(\omega) = i \cdot \sin(\pi \frac{\omega}{\omega_0}) e^{-i\pi \frac{\omega}{\omega_0}} \quad (2.28)$$

after a simple trigonometric transformation and using $\omega_0 = \frac{2\pi}{T_0}$.

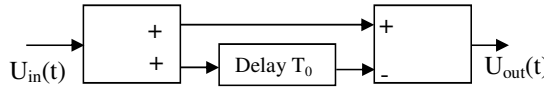


Figure 2.7: Schematic drawing of an ideal notch filter used in the cooling simulations. For an explanation see the text.

From the filter transfer function, eq. (2.28), it is apparent that the amplitude becomes zero at any revolution harmonic n , i.e. if $\omega = n \cdot \omega_0$ with any integer n . The phase makes a jump of 180 degrees around zero phase at the revolution harmonics.

Eq. (2.28) gives the frequency response for an ideal notch filter with infinite notch depth. If the notch depth is finite the frequency response of the notch filter becomes

$$H(\omega) = \frac{I}{I + a} \left\{ I - a \cdot e^{-i2\pi\omega/\omega_0} \right\} \quad (2.29)$$

with $0 \leq a \leq 1$. Eq. (2.29) equals (2.28) for $a = 1$.

The notch depth D of the filter, eq. (2.29), at the revolution harmonics $n \omega_0$ is then

$$|H(n\omega_0)| = \frac{1-a}{1+a} = D. \quad (2.30)$$

The notch depth is often expressed in Decibels: $D_{dB} = 20 \log \frac{1-a}{1+a} = 20 \log D$.

From eq. (2.28) or (2.29) we have the property $H^*(\omega) = H(-\omega)$.

Amplitude and phase response of the notch filter are visualized in Figure 2.8 for the infinite notch depth case, notch depth -30 dB and -10 dB.

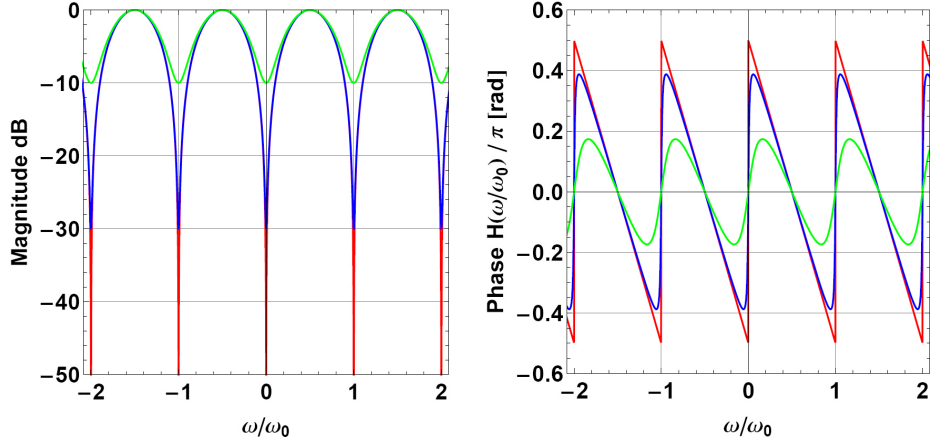


Figure 2.8: Magnitude and phase of the notch filter. The magnitude exhibits notches at the revolution harmonics which suppress particles with the nominal frequency. The phase is linearly decreasing between the notches and exhibits a phase jump of 180 degrees at the revolution harmonics for the ideal filter (red curves). Particles with frequencies which are at symmetric positions of the notches see an opposite phase. The effect of a finite notch depth is shown for -30 dB (blue) and -10 dB (green).

The notch filter discussed above is also called one-turn delay filter. It is also possible to construct two-turn delay notch filters by cascading two one-turn filters. They provide a smoother cooling in the core and result in a stronger cooling of the tails of the beam distribution [34].

2.4 TOF and Filter Cooling

2.4.1 Coherent Beam Response

In a continuous coasting beam (DC-beam) with N ions the azimuth Θ of a circulating particle with angular frequency ω is given at time t by

$$\Theta(t) = \omega t + \Theta_0 \quad (2.31)$$

with a random phase Θ_0 uniformly distributed in $[0, 2\pi]$. The revolution period of a particle is $T = 2\pi/\omega$.

The longitudinal current $I(t)$ of N ions with charge Ze measured at the pickup is then

$$I(t) = Ze \sum_{r=1}^N \omega_r \sum_{n=-\infty}^{\infty} \delta(\Theta_r(t) - \Theta_p - 2\pi n) \quad (2.32)$$

with $\delta(\cdot)$ denoting the delta function, see Appendix A. Expanding the periodic delta function into a Fourier series one obtains

$$I(t) = Ze \sum_{r=1}^N \frac{\omega_r}{2\pi} \sum_{n=-\infty}^{\infty} e^{in(\Theta_r(t) - \Theta_p)} . \quad (2.33)$$

Using the orbits, eq. (2.31), for the DC beam in eq. (2.33) one finds

$$I(t) = Ze \sum_{r=1}^N \frac{\omega_r}{2\pi} \sum_{n=-\infty}^{\infty} e^{in(\omega_r t - \Theta_p + \Theta_0^r)} \quad (2.34)$$

as the longitudinal current of the ion beam measured at the pickup. Due to the random phase it is a fluctuating current. If we average over all particle phases Θ_0^r in eq. (2.34) only the harmonic number $n = 0$ contributes and we find the DC-current is $I_{DC} = Ze f_o N$ where the mean revolution frequency $\omega_0 = 2\pi f_o = \frac{1}{N} \sum_{r=1}^N \frac{\omega_r}{2\pi}$ has been introduced. The Schottky fluctuating current is $\delta I(t) = I(t) - I_{DC}$. The Fourier Transform $I(\omega)$ (see Appendix A) of the beam current provides the frequency content of the beam. The frequency spectrum is

$$I_b(\omega) = Ze \sum_{r=1}^N \omega_r \sum_{n=-\infty}^{\infty} e^{-in(\Theta_p - \Theta_0^r)} \delta(\omega - n\omega_r) \quad (2.35)$$

and consists for each individual particle of a periodic and infinite line spectrum centered at the revolution harmonics $n\omega_r$ with strength $Ze\omega_r$.

The energy change at the kicker in time domain is found if we take into account the transfer function of the cooling system from pickup to kicker, eqs. (2.10) and (2.11). An inverse Fourier Transform (Appendix A) then yields

$$\Delta E(t) = Ze \sum_{r=1}^N \frac{\omega_r}{2\pi} \sum_{n=-\infty}^{\infty} T(n\omega_r) e^{in(\omega_r t - \Theta_p + \Theta_0^r)} \quad (2.36)$$

which creates fluctuating energy changes with zero mean since, according to the assumption of the frequency range of the amplifier, eq. (2.9), the harmonic with $n = 0$ does not contribute.

We now consider an ion that circulates with angular frequency ω_s in the ring. It samples the random energy changes $\Delta E(t)$ at the kicker at time $t = t_p^s + T_F^s + mT_s$ and thus receives energy changes per time when it passes the kicker according to

$$\Delta E_S(t) = \Delta E(t) \cdot \sum_{m=-\infty}^{\infty} \delta(t - t_p^s - T_F^s - mT_s) = \Delta E(t) \cdot \frac{\omega_s}{2\pi} \sum_{m=-\infty}^{\infty} e^{im(\omega_s t - \Theta_p - \omega_s T_F^s + \Theta_0^s)} \quad (2.37)$$

Inserting eq. (2.36) into eq. (2.37) then gives the result

$$\Delta E_S(t) = Ze \cdot \frac{\omega_s}{2\pi} \sum_{r=1}^N \frac{\omega_r}{2\pi} \sum_{n=-\infty}^{\infty} \sum_{m=-\infty}^{\infty} T(n\omega_r) e^{in(\omega_r t - \Theta_p + \Theta_0^r)} e^{im(\omega_s t - \Theta_p - \omega_s T_F^s + \Theta_0^s)} \quad (2.38)$$

for the random energy change per time when the particle passes the kicker.

The *coherent energy change F per time* a particle with angular revolution frequency ω_s experiences at the kicker follows from eq. (2.38) when averaging over all random phases Θ_0^r and Θ_0^s . The amplifier, eq. (2.9), excludes harmonic number zero (the terms $n = m = 0$) hence, following the arguments as used in [35], only those terms in the double sum survive for which $n\Theta_0^r + m\Theta_0^s = 0$ or $n/m = -\Theta_0^s/\Theta_0^r$. Since n/m is a rational number and $-\Theta_0^s/\Theta_0^r$ is a real number both ratios can only be equal for $r = s$ and $m = -n$ (The probability that two different

particles $r \neq s$ have the same phases $\Theta_0^s = \Theta_0^r$ is very small. These cases are therefore neglected here.). Averaging results therefore in the expression for the drift term of the test particle with angular frequency ω_s

$$F = \langle \Delta E_s \rangle = Ze \left(\frac{\omega_s}{2\pi} \right)^2 \sum_{n=-\infty}^{\infty} T(n\omega_s) e^{in\omega_s T_F^s}. \quad (2.39)$$

Inserting the cooling transfer function, eq. (2.11) leads to the coherent energy change per time at the kicker

$$F = \frac{\omega_s}{2\pi} \cdot \Delta E_C \approx \frac{\omega_0}{2\pi} \cdot \Delta E_C \quad (2.40)$$

where

$$\Delta E_C = \frac{(Ze)^2}{A} \frac{\omega_s}{2\pi} \sum_{n=-\infty}^{\infty} K_{||}(n\omega_s) G_A H(n\omega_s) Z_{PL}(n\omega_s) P(n\omega_s) e^{in\omega_s (T_F + \Delta T_F - T_D)} \quad (2.41)$$

constitutes the coherent energy change per nucleon and per turn. The time of flight of the particle has been replaced by $T_F^s = T_F + \Delta T_F$ where T_F is the nominal flight time. The quantity F is the drift term in the Fokker-Planck equation.

Equation (2.41) describes the energy change per nucleon at the kicker per turn which a considered particle with angular frequency $\omega_s = \omega_0(\Delta E)$ receives.

For a particle with angular frequency $\omega_s = \omega_0 + \Delta\omega$ slightly differing in the amount $\Delta\omega$ from the nominal angular revolution frequency ω_0 and with the corresponding momentum $p_s = p_0 + \Delta p$ the relation

$$\frac{\Delta T_F}{T_F} = -\eta_{PK} \frac{\Delta p}{p_0} \quad (2.42)$$

holds where η_{PK} denotes the frequency slip factor from pickup to kicker. It is given by

$$\eta_{PK} = \frac{I}{\gamma^2} - \alpha_{PK} \quad (2.43)$$

with the momentum compaction factor from pickup to kicker

$$\alpha_{PK} = \frac{I}{s_{PK}} \int_0^{s_{PK}} \frac{D(s)}{\rho(s)} ds. \quad (2.44)$$

The distance between pickup and kicker is s_{PK} . The lattice dispersion is denoted by $D(s)$ and the radius of curvature is $\rho(s)$. The frequency spread of the beam is related to the relative momentum spread in the beam by

$$\frac{\Delta\omega}{\omega_0} = \eta \frac{\Delta p}{p_0} \ll 1 \quad (2.45)$$

where the frequency slip factor for the whole ring is

$$\eta = \frac{I}{\gamma^2} - \alpha. \quad (2.46)$$

The momentum compaction factor for the whole ring with circumference L is

$$\alpha = \frac{I}{L} \int_0^L \frac{D(s)}{\rho(s)} ds. \quad (2.47)$$

The frequency dispersion vanishes if $\eta = 0$, i.e. at $\gamma = \gamma_{tr}$ with $\gamma_{tr} = \sqrt{\alpha}$.

The relative energy deviation $\frac{\Delta E}{E}$ is related to the relative momentum deviation by

$$\frac{\Delta E}{E} = \beta^2 \frac{\Delta p}{p_0} \quad (2.48)$$

and therefore

$$\frac{\Delta\omega}{\omega_0} = \kappa \frac{\Delta E}{E} \quad (2.49)$$

with the definition of $\kappa = \eta/\beta^2$.

Similarly, the relation

$$\frac{\Delta T_F}{T_F} = -\kappa_{PK} \frac{\Delta E}{E} \quad \text{with} \quad \kappa_{PK} = \eta_{PK}/\beta^2 \quad (2.50)$$

for the relative time spread from pickup to kicker is introduced.

Using the eqs. (2.49) and (2.50) the phase factor $n\omega_s(T_F - T_D + \Delta T_F)$ of eq. (2.41) can be approximated as

$$n\omega_s(T_F - T_D + \Delta T_F) \approx n\omega_0(T_F - T_D + \Delta T_F) = -n \cdot \omega_0 T_F \left\{ \kappa_{PK} \frac{\Delta E}{E} + \frac{\Delta T_D}{T_F} \right\} =: \zeta(n, \Delta E) \quad (2.51)$$

where the difference in delay time $T_D = T_{amp} + T_{delay}$ and the nominal particle time of flight $\Delta T_D = T_D - T_F$ was introduced.

Combining the phase $\zeta(n, E)$ with eq. (2.41) entails the equation

$$\Delta E_C = \frac{(Ze)^2}{A} \frac{\omega_0}{2\pi} (I + \kappa \frac{\Delta E}{E}) \sum_{n=-\infty}^{\infty} K_{||}(n\omega_s) G_A H(n\omega_s) Z_{PL}(n\omega_s) P(n\omega_s) e^{i\zeta(n, \Delta E)} \quad (2.52)$$

expressing the energy change per nucleon of an ion at the kicker as a function of energy deviation ΔE at the pickup with $\omega_s = \omega_0(I + \kappa \Delta E/E)$.

We therefore conclude that all harmonics in the cooling bandwidth contribute to the coherent energy kick ΔE_C a particle with energy deviation ΔE experiences.

Since the cooling bandwidth is limited by the amplifier, eq. (2.9), to harmonics $I \ll n_j \leq |n| \leq n_2$ and the transfer function satisfies the rule $T^*(n\omega) = T(-n\omega)$ one finally finds for the coherent energy change per turn for a DC-beam

$$\Delta E_C = 2 \cdot \frac{(Ze)^2}{A} \frac{\omega_0}{2\pi} (I + \kappa \frac{\Delta E}{E}) \sum_{n=n_j}^{n_2} \operatorname{Re} \left\{ K_{||}(n\omega_s) G_A H(n\omega_s) Z_{PL}(n\omega_s) P(n\omega_s) e^{i\zeta(n, \Delta E)} \right\} \quad (2.53)$$

which shows that the energy change at the kicker is real as expected. The unit of the coherent energy change ΔE_C per nucleon and per turn is eV/u .

The expression in eq. (2.53) is inserted into the definition of the drift term according to eq. (2.40) which will be employed in a numerical solution of the FPE for TOF or filter cooling with the appropriate transfer functions inserted in eq. (2.53). Approximations are discussed in chapters below to highlight the most important parameters that influence the coherent cooling term and thus allow optimizing the design and the performance of the cooling system.

2.4.2 Incoherent Beam Response

We now draw attention to the incoherent heating term in the FPE. Since the kicker signals are noise signals the incoherent energy change per time at the kicker is given by the mean square energy change $\langle \Delta E_s^2 \rangle$. This contribution is always positive and thus will lead to a broadening of the energy or momentum distribution of the ion beam.

If the kicker is excited with a noise signal $\Delta E(t)$ then the particles sample the random signal once per turn and we can form the sample sequence of energy changes $\Delta E[n] = \Delta E(nT_s)$ as seen by a particle on each passage of the kicker. The revolution period of a particle is T_s and n is the turn number. The corresponding autocorrelation function $R[m]$ (Appendix A) of the sampled noise signal is given by

$$R[m] = \langle \Delta E[n] \cdot \Delta E^*[n+m] \rangle \quad (2.54)$$

and equals samples $R(mT_s)$ of the autocorrelation function $R(\tau) = \langle \Delta E(t) \cdot \Delta E^*(t+\tau) \rangle$ of the noise signal at the kicker. If the kicker is excited by a white noise source with zero mean, $\langle \Delta E(t) \rangle = 0$ and $R(\tau) \propto \delta(\tau)$ then a particle receives random energy changes $\Delta E[n]$ every turn n which, on a long-term average, have zero mean. However $R[0] = \langle (\Delta E[n])^2 \rangle$ will not be zero. This will lead to a diffusion process increasing the width of the particles' energy distribution. Instead determining the autocorrelation function of the sampled noise we consider the spectral density $S_d(\omega)$ of the discrete random series $\Delta E[n]$ which is per definition the Fourier series of the autocorrelation function

$$S_d(\omega) = \sum_{n=-\infty}^{\infty} R(nT_s) e^{-in\omega T_s}. \quad (2.55)$$

The Fourier coefficients are given by

$$R(nT_s) = \frac{I}{\omega_s} \int_{-\omega_s/2}^{+\omega_s/2} S_d(\omega) e^{in\omega T_s} d\omega. \quad (2.56)$$

Applying the Poisson formula (Appendix A) to eq. (2.55) we find with $\omega_s = 2\pi/T_s$

$$S_d(\omega) = \frac{\omega_s}{2\pi} \sum_{m=-\infty}^{\infty} S(\omega + m\omega_s) \quad (2.57)$$

which relates the spectral density $S_d(\omega)$ to the noise density $S(\Omega)$ at the kicker entrance given by $S(\Omega) = \int_{-\infty}^{\infty} R_{\Delta E}(\tau) e^{-i\Omega\tau} d\tau$. Eq. (2.57) states the important fact that the spectral density of the sampled process equals the sum of the continuous spectral density $S(\omega)$ and all its displacements at $\omega + m\omega_s$.

From eq. (2.54) we deduce with eq. (2.56) for the mean square energy change per turn

$$\langle \Delta E[n]^2 \rangle = R[0] = \frac{I}{\omega_s} \int_{-\omega_s/2}^{+\omega_s/2} S_d(\omega) d\omega \quad (2.58)$$

and therefore using eq. (2.57) one has the result

$$\langle \Delta E[n]^2 \rangle = \frac{I}{2\pi} \sum_{m=-\infty}^{\infty} \int_{-\omega_s/2}^{+\omega_s/2} S(\omega + m\omega_s) d\omega \quad (2.59)$$

which relates the mean square energy change per turn with the spectral density $S(\Omega)$ of the continuous signals $\Delta E(t)$ at the kicker. It is also visible that all beam harmonics contribute to the heating. We also notice that the square energy change per turn, eq. (2.59), does not depend on the turn number n . The variance of the beam's energy distribution thus increases linearly with number of turns (diffusion).

The integral in eq. (2.59) is approximated by $S(m\omega_s) \cdot \omega_s^1$ yielding the approximate incoherent mean square energy change per turn for a particle with angular frequency $\omega_s = \omega_s(\Delta E)$ at the kicker

¹ Strictly speaking $S(m\omega_s)$ denotes the average value of S taken in an interval $\pm\omega_s/2$ around harmonic $m\omega_s$.

$$\langle \Delta E[n]^2 \rangle = \frac{\omega_s}{2\pi} \cdot \sum_{m=-\infty}^{\infty} S(m\omega_s). \quad (2.60)$$

The mean square energy change per time at the kicker is then

$$\langle \Delta E_s^2 \rangle = \frac{\omega_0}{2\pi} \frac{\omega_s}{2\pi} \cdot \sum_{m=-\infty}^{\infty} S(m\omega_s). \quad (2.61)$$

The diffusion term in the FPE, eq. (2.4), is found as

$$D(E, t) = \frac{1}{2} \langle \Delta E_s^2 \rangle = \frac{1}{2} \frac{\omega_0}{2\pi} \langle \Delta E_{IC}^2 \rangle = \frac{1}{2} \frac{\omega_0}{2\pi} \frac{\omega_s}{2\pi} \cdot \sum_{m=-\infty}^{\infty} S(m\omega_s) \quad (2.62)$$

where we identify $\langle \Delta E_{IC}^2 \rangle$ with eq. (2.60). Note that $S(m\omega_s)$ has the unit $(eV)^2 / Hz$.

Strictly speaking, the derivation is only valid if the noise distribution is stationary. However, since the distributions are changing only slowly with time during stochastic cooling it justified to employ eq. (2.62) to predict the diffusion term induced by incoherent beam noise.

2.4.2.1 Schottky Noise

The spectral density $S(\omega)$ is found if we make use of the relation (2.10) for the energy change per nucleon at the kicker, $\Delta E(\omega) = T(\omega) \cdot I_b(\omega)$, where the Fourier Transform of the beam current is $I_b(\omega)$ as given by eq. (2.35) and the transfer function of the cooling loop is $T(\omega)$ as follows from eq. (2.11). The Fourier integral $I_b(\omega)$ of the stochastic beam current $I_b(t)$ is itself a random variable. As shown in Appendix A the autocorrelation function $\langle \Delta E(\omega) \cdot \Delta E^*(\omega') \rangle$ then possesses the property

$$\langle \Delta E(\omega) \cdot \Delta E^*(\omega') \rangle = 2\pi S(\omega) \delta(\omega - \omega') \quad (2.63)$$

where $S(\omega) = \int_{-\infty}^{\infty} R_{\Delta E}(\tau) e^{-i\omega\tau} d\tau$ is the Fourier integral of the autocorrelation function $R_{\Delta E}(\tau)$.

Forming the product $\Delta E(\omega) \cdot \Delta E^*(\omega') = T(\omega) T^*(\omega') \cdot I_b(\omega) I_b^*(\omega')$ with the expression for the beam current given in eq. (2.35) yields

$$\Delta E(\omega) \cdot \Delta E^*(\omega') = T(\omega)T^*(\omega') \cdot$$

$$(Ze)^2 \sum_{r=1}^N \sum_{s=1}^N \omega_r \omega_s \sum_{n=-\infty}^{\infty} \sum_{m=-\infty}^{\infty} e^{i(m-n)\Theta_p} e^{i(n\varphi_r - m\varphi_s)} \delta(\omega - n\omega_r) \delta(\omega' - n\omega_s).$$

When averaging over all random phases φ we apply the same arguments as used for the coherent term. Then only terms with $r = s$ and $n = m$ remain leading to

$$2\pi S(\omega) \delta(\omega - \omega') = T(\omega)T^*(\omega') \cdot (Ze)^2 \sum_{r=1}^N \omega_r^2 \sum_{n=-\infty}^{\infty} \delta(\omega - n\omega_r) \delta(\omega' - n\omega_r).$$

The spectral density $S(\omega')$ is found by integrating both sides of the last expression w.r.t. ω .

This leads to

$$S(\omega) = \frac{(Ze)^2}{2\pi} \sum_{r=1}^N \omega_r^2 \sum_{n=-\infty}^{\infty} T(n\omega_r) T^*(\omega) \delta(\omega - n\omega_r) \quad (2.64)$$

which is the desired spectral density in eq. (2.62) induced by the longitudinal DC current $I(t)$, eq. (2.34), of N ions with charge Ze measured at the pickup.

Since the beam consists of a large number N of particles with angular revolution frequencies $\omega_r > 0$ clustered around the central value ω_0 , we can proceed further in replacing the sum over discrete frequencies in eq. (2.64) by an integral over continuous frequencies,

$\sum_{r=1}^N g(\omega_r) \rightarrow \int_0^{\infty} g(\omega_r) \Psi_0(\omega_r) d\omega_r$, where the angular frequency distribution Ψ_0 is normalized

to the number of ions in the beam, $\int_0^{\infty} \Psi_0(\omega) d\omega = N$ and $1/N \cdot \int_0^{\infty} \omega \Psi_0(\omega) d\omega = \omega_0$ gives the

average angular frequency of the beam. Note that $\Psi_0(\omega) = 0$ for $\omega < 0$.

We then obtain the generalized form of eq. (2.64)

$$S(\omega) = \frac{(Ze)^2}{2\pi} \sum_{n=-\infty}^{\infty} \int_0^{\infty} \omega_r^2 T(n\omega_r) T^*(\omega) \Psi_0(\omega_r) \delta(\omega - n\omega_r) d\omega_r. \quad (2.65)$$

Evaluating the integral in eq. (2.65) we obtain the important result for the noise density experienced by the beam particles

$$S(\omega) = |T(\omega)|^2 S_b(\omega) \quad (2.66)$$

which is in general true and describes the relation between input and output noise density for a linear electronic system. Furthermore, the spectral current density (Schottky noise density, units A^2/Hz) of the DC beam current is

$$S_b(\omega) = \frac{(Ze)^2}{2\pi} \sum_{\substack{n=-\infty \\ n \neq 0}}^{\infty} \frac{I}{|n|} \left(\frac{\omega}{n} \right)^2 \Psi_o \left(\frac{\omega}{n} \right). \quad (2.67)$$

To give a first illustration of the spectral current density we write eq. (2.67) as

$$S_b(\omega) = \frac{(Ze)^2}{2\pi} \left\{ \sum_{n=1}^{\infty} \frac{I}{n} \left(\frac{\omega}{n} \right)^2 \Psi_o \left(\frac{\omega}{-n} \right) + \sum_{n=1}^{\infty} \frac{I}{n} \left(\frac{\omega}{n} \right)^2 \Psi_o \left(\frac{\omega}{n} \right) \right\}$$

and assume that the width of the angular frequency distribution $\Psi_o(\omega)$ is small. The spectral current density then consists of a series of separated bands centered around the negative frequencies $-n\omega_0$ (first sum) and the positive frequencies $n\omega_0$ (second sum).

In other words, if $\omega \approx -k\omega_0 < 0$ with $k > 0$ then

$$\begin{aligned} S_b(-k\omega_0) &= \frac{(Ze)^2}{2\pi} \left\{ \frac{I}{k} \left(\frac{k\omega_0}{k} \right)^2 \Psi_o \left(\frac{-k\omega_0}{-k} \right) + \frac{I}{k} \left(\frac{k\omega_0}{k} \right)^2 \Psi_o \left(\frac{-k\omega_0}{k} \right) \right\} \\ &= \frac{(Ze)^2}{2\pi} \frac{I}{k} \left(\frac{k\omega_0}{k} \right)^2 \Psi_o \left(\frac{k\omega_0}{k} \right) \end{aligned}$$

since $\Psi_o(\omega) = 0$ for $\omega < 0$ in the second term of the curly bracket. The same result is found if we consider $\omega \approx k\omega_0$ with $k > 0$. Thus, only one harmonic number contributes to the spectral current density in the case of non-overlapping bands. We note also that $S_b(\omega) = S_b(-\omega)$.

In general, the previous expression shows that for overlapping bands particles with different revolution frequencies can contribute through different harmonics to one frequency ω of the spectral beam density. This fact is expressed by the sum in eq. (2.67).

Considering only positive frequencies as measured by a spectrum analyzer we can write eq. (2.67) as

$$S_b(\omega) = 2 \cdot \frac{(Ze)^2}{2\pi} \sum_{n=1}^{\infty} \frac{1}{n} \left(\frac{\omega}{n} \right)^2 \Psi_0 \left(\frac{\omega}{n} \right). \quad (2.68)$$

The factor two in the expression accounts for the fact that $S_b(\omega) = S_b(-\omega)$.

The measured output power density (unit W/Hz) of the pickup with coupling impedance Z_{PL} into the line impedance Z_0 becomes then

$$S_{out}(\omega) = \frac{|Z_{PL}|^2}{Z_0} |G_A|^2 \cdot S_b(\omega) \quad (2.69)$$

including an amplification with voltage gain G_A .

The following examples shall illustrate the Schottky noise power density according to eq. (2.69) for the (2 – 4) GHz system of the HESR. The longitudinal coupling impedance of the HESR ring slot-coupler for the pickup is $Z_{PL} = 240\Omega$ in the center of the cooling bandwidth, see table 1.1. The characteristic line impedance is $Z_0 = 50\Omega$. We assume $N = 10^{10}$ antiprotons at the injection energy 3 GeV with an rms relative momentum spread $\delta_{rms} = 5 \cdot 10^{-4}$ as expected from the CR injector ring. The revolution frequency is $f_0 = 506.24 kHz$. The standard lattice with $\gamma_{tr} = 6.23$ is assumed. Hence, at 3 GeV the ring frequency slip factor is $\eta = 0.03$. The lowest harmonic number in the cooling system is 3951 (f_{low}/f_0) and the upper harmonic number f_{upper}/f_0 is 7902 at this energy. There are 3952 harmonics in the cooling bandwidth. For illustration a Gaussian beam frequency distribution is considered so that with eq. (2.69) the output power density including amplification with $G_A = 57 dB$ can be calculated from

$$S(f) = |G_A|^2 \frac{|Z_{PL}|^2}{Z_0} \sum_{n=3951}^{7902} \left\{ \frac{2N e^2}{\sqrt{2\pi} n \sigma_f} \left(\frac{f}{n} \right)^2 e^{-\frac{1}{2} \left[\frac{f-nf_0}{n\sigma_f} \right]^2} \right\}. \quad (2.70)$$

It is visible that the power density is proportional to the number of particles in the ring. This is a consequence of the fact that all the particles have random phases as outlined above and therefore the currents add up incoherently.

The frequency spread σ_f in eq. (2.70) is related with the relative momentum spread δ_{rms} by

$$\sigma_f = f_0 \eta \delta_{rms}.$$

Three examples of the power density are depicted in Figure 2.9 in the frequency range from 3.9 GHz to 3.905 GHz . The well separated band structure is clearly visible even at the high frequency end of the cooling system if the relative momentum spread is $\delta_{rms} = 5 \cdot 10^{-4}$ as expected from the CR injector ring. Filter cooling is thus possible in the whole cooling bandwidth. The situation changes if the momentum spread is increased by a factor of two. The bands become broader and decrease in height. The bands start to overlap and the signal level drops by a factor of two. The bands are no longer distinguishable so that filter cooling is no longer applicable.

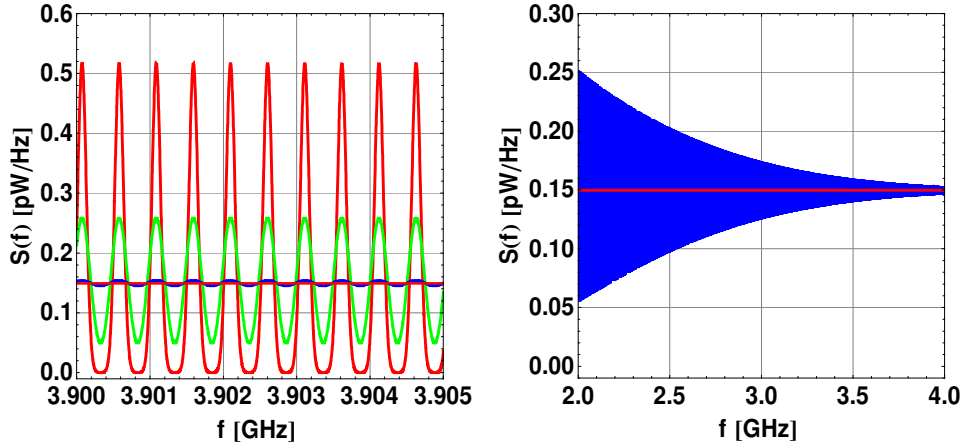


Figure 2.9: Longitudinal power spectrum at the upper range for the cooling system for different initial relative momentum spreads δ_{rms} (left plot). Red: $5 \cdot 10^{-4}$, Green: $1 \cdot 10^{-3}$ and Blue: $2 \cdot 10^{-3}$. For the latter case the bands overlap yielding a constant shot noise as indicated by the red horizontal line. The power density for $\delta_{rms} = 2 \cdot 10^{-3}$ is depicted in the whole bandwidth in the right diagram. It is visible that the height of the density is decreasing while the width is increasing yielding complete overlap at the high frequency end of the cooling bandwidth.

The extreme case arises if the momentum spread would be $\delta_{rms} = 2 \cdot 10^{-3}$. A complete band overlap is observed which results in a constant spectral power density

$S_{out}(\omega) = (\left|Z_{PL}\right|^2 / Z_0) \cdot |G_A|^2 \cdot 2N(Ze)^2 \omega_0 / 2\pi$, indicated by the red horizontal line in Figure 2.9, similar to shot noise.

The right hand side plot in Figure 2.9 shows the power density in the whole bandwidth. It is visible that the height of the density is decreasing while the width is increasing yielding complete overlap at the high frequency end of the cooling bandwidth. Increasing the momentum spread or the bandwidth does not alter the power spectrum. As will be shown below, for complete overlap the density becomes $2N(Ze)^2 \omega_0 / 2\pi$ (red horizontal line in Figure 2.9) which is the average Schottky noise current density per band if we consider only real positive frequencies.

Normalizing the current density $S_b(\omega)$ to the average Schottky density per band for non-overlapping bands yields the important quantity

$$M(\omega) = \frac{S_b(\omega)}{N(Ze)^2 \omega_0 / 2\pi} \quad (2.71)$$

which is the *mixing function (mixing factor) for unfiltered particle Schottky noise*.

Explicitly written we deduce

$$M(\omega) = \sum_{n=-\infty}^{\infty} M_n(\omega) \quad (2.72)$$

where the *mixing factor per harmonic n* is

$$M_n(\omega) = \frac{1}{\omega_0} \frac{1}{|n|} \left(\frac{\omega}{n} \right)^2 \frac{1}{N} \Psi_0 \left(\frac{\omega}{n} \right). \quad (2.73)$$

The significance of the mixing factor becomes clear if we consider the following. For low harmonic numbers the bands do not overlap and only one harmonic contributes to the Schottky density in eq. (2.68), see also Figure 2.9. Increasing the harmonic number the peak density initially decreases as $1/n$. If the bands begin to touch each other, then the width of a band is roughly $n\Delta\omega_0 \sim \omega_0$ where $\Delta\omega_0$ is the width of the beam frequency distribution. Since the correlation time of noise signals τ_{cor} is inversely proportional to the width of the noise

spectrum we have $\tau_{cor} \sim \frac{I}{n \Delta \omega_0 / 2\pi}$ and therefore $\tau_{cor} = T_0$ when the bands begin to overlap.

The fluctuating signals remain correlated over one revolution period T_0 . If we sample these fluctuating signals with the revolution period T_0 they are statistically independent and appear as white noise. This corresponds to perfect mixing $M = 1$ in the sampling picture of stochastic cooling. In the sense of sampling theory this means that a sample taken at the pickup and corrected at the kicker is renewed within one turn. With non-overlapping bands the correlation time T_{cor} becomes larger than the revolution period. Correspondingly it takes a longer time to renew the beam sample. This corresponds to *bad mixing*. In this situation the heating contribution increases due to the higher Schottky peak densities.

Similarly, if the mixing factor is $M = 1$, one concludes from eq. (2.71) that the spectral current density equals Shot noise with the density $N(Ze)^2 \omega_0 / 2\pi$ in the case the cooling chain contains no filter. The Fourier transform yields the autocorrelation function $R(\tau) = N(Ze)^2 \omega_0 / 2\pi \cdot \delta(\tau)$ which states that the noise signal is completely uncorrelated. In the frequency domain description a mixing factor $M > 1$ therefore describes to what extent the particle current density is enhanced over the Shot noise current density $N(Ze)^2 \omega_0 / 2\pi$.

For the examples outlined above Figure 2.10 illustrates the mixing factor given by eq. (2.72). In general mixing is incomplete and $M > 1$.

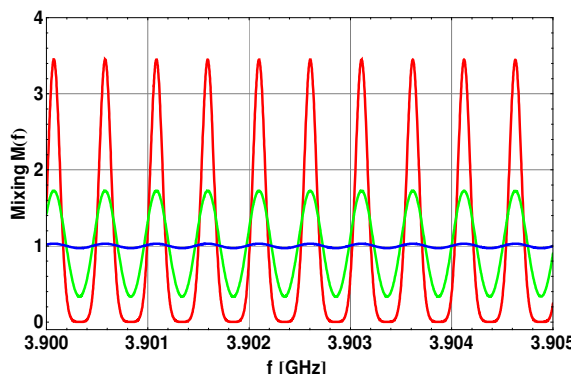


Figure 2.10: Mixing factor at the upper range for the cooling system for different initial relative momentum spreads δ_{rms} . Red: $5 \cdot 10^{-4}$, Green: $1 \cdot 10^{-3}$ and Blue: $2 \cdot 10^{-3}$. The mixing factor becomes 1, i.e., complete mixing is achieved if the momentum spread exceeds $2 \cdot 10^{-3}$.

It should be noted that for completely overlapping bands the mixing factor cannot become smaller than one. Increasing the cooling bandwidth thus will not reduce the mixing factor. Instead it will increase the unwanted mixing in the drift term at higher harmonics so that the drift term becomes non-linear. We will discuss this topic later in chapter 2.8 when we discuss the constraints on the maximal useful bandwidth of the cooling system entailed by the machine parameters.

We will show in section 2.11 how the mixing factor enters in the cooling rate equation for momentum cooling and in chapter 3 for betatron cooling.

One concludes that for filter cooling it is mandatory that $M > I$.

A practical conclusion can be drawn from Figure 2.9. For cooling system diagnostics it is preferable to work with incomplete mixing. This is demonstrated in section 2.10 for an open loop gain measurement with a network analyzer and cooling loop adjustment.

From now on well separated bands are assumed, i.e. small relative angular frequency spreads in the beam. With this assumption we can write for the spectral density of the DC-beam at harmonic number n

$$S_b(\omega) = \frac{(Ze)^2}{2\pi} \frac{I}{|n|} \left(\frac{\omega}{n} \right)^2 \Psi_o \left(\frac{\omega}{n} \right) \approx \frac{(Ze)^2 \omega_0^2}{2\pi} \frac{I}{|n|} \Psi_o \left(\frac{\omega}{n} \right) \quad (2.74)$$

for $n\Delta\omega_b \leq \omega_0$ where $\Delta\omega_b$ is the half of the total beam width.

The current density thus consists of a series of bands centred at the revolution harmonics $n\omega_0$. The frequency distribution at each harmonic is determined by the revolution frequency distribution of Ψ_o . The peak density $S_b(n\omega_0)$ decreases as n increases. The revolution frequency distribution Ψ_o is determined by the momentum distribution $\bar{\Psi}_o(\delta)$ since $\bar{\Psi}_o(\delta)d\delta = \Psi_o(\omega)d\omega$ describes the conservation of probability. The relative momentum deviation is δ and $\omega(\delta) = \omega_0(1 + \eta\delta)$.

The variance of the current density at harmonic number n is

$$\sigma_n^2 = \int (\omega - n\omega_0)^2 S_b(\omega) d\omega / \int S_b(\omega) d\omega \quad (2.75)$$

and one easily concludes with eq. (2.74) that

$$\sigma_n^2 = n^2 \sigma_\omega^2 \quad (2.76)$$

where σ_ω^2 is the variance of the particle distribution $\Psi_0(\omega)$. Thus the width σ_n of each harmonic increases linearly with harmonic number n until band overlap occurs.

The total Schottky power (Appendix A) per band at each harmonic number n (positive and negative) is however constant since

$$\frac{I}{2\pi} \int S_b(\omega) d\omega = (Zef_0)^2 N. \quad (2.77)$$

The Schottky power for real physical positive integers is then $2N(Zef_0)^2$. The average Schottky power per band is $2N(Ze)^2 \omega_0 / 2\pi$.

The incoherent energy change per time impressed to a beam particle at the kicker due to Schottky particle noise of the beam is related to the diffusion term in the FPE. With eqs. (2.62) and (2.66) the diffusion term becomes

$$D_s = \frac{I}{2} \langle \Delta E_s^2 \rangle \approx \frac{I}{2} \frac{\omega_0}{2\pi} \langle \Delta E_{IC,S}^2 \rangle \quad (2.78)$$

where the incoherent energy change per turn for a particle with $\omega_s = \omega_0(1 + \kappa \Delta E/E)$ is

$$\langle \Delta E_{IC,S}^2 \rangle = \frac{\omega_s}{2\pi} \cdot \sum_{n=-\infty}^{\infty} |T(n\omega_s)|^2 S_b(n\omega_s). \quad (2.79)$$

The probability to find a particle with frequency ω in the range $d\omega$ is equal to the probability to find the particle with energy deviation ΔE in the range $d\Delta E$. The relation between the energy deviation distribution $\Psi(E)$ and the particle angular frequency distribution $\Psi_0(\omega)$ is then $\Psi_0(\omega) = \Psi(\Delta E) \left| \frac{d\Delta E}{d\omega} \right|$. One finds $\Psi_0(\omega) = \frac{E}{|\kappa| \omega_0} \Psi(\Delta E)$ when the differential relation $d\Delta E = \frac{E}{\kappa \omega_0} d\omega$ with κ as defined in eq. (2.49) is applied.

Inserting this result into eq. (2.74) leads to $S_b(n\omega) = \frac{(Ze)^2 \omega_0}{2\pi} \frac{E}{|\kappa||n|} \Psi(\Delta E)$ where $\omega = \omega(\Delta E) = \omega_0(1 + \kappa \Delta E/E)$ is to be used (see eq. (2.49)).

The incoherent mean square energy change per turn due to Schottky particle noise is then with eq. (2.79)

$$\langle \Delta E_{IC,S}^2 \rangle = \left(\frac{Ze\omega_0}{2\pi} \right)^2 \left(1 + \kappa \frac{\Delta E}{E} \right) \cdot \frac{E}{|\kappa|} \cdot \Psi(\Delta E, t) \cdot \sum_{n=-\infty}^{\infty} \left| T(n\omega_0 \left(1 + \kappa \frac{\Delta E}{E} \right)) \right|^2 \frac{I}{|n|} \quad (2.80)$$

expressed with the energy deviation ΔE of particle. The Schottky particle noise contribution to heating depends on the beam energy distribution $\Psi(\Delta E, t)$ which changes during cooling.

Taking into account the finite bandwidth of the amplifier, eq. (2.9), and that $T^*(n\omega) = T(-n\omega)$ eq. (2.80) becomes

$$\langle \Delta E_{IC,S}^2 \rangle = 2 \cdot \left(\frac{Ze\omega_0}{2\pi} \right)^2 \left(1 + \kappa \frac{\Delta E}{E} \right) \cdot \frac{E}{|\kappa|} \cdot \Psi(\Delta E, t) \cdot \sum_{n=n_f}^{n_s} \left| T(n\omega_0 \left(1 + \kappa \frac{\Delta E}{E} \right)) \right|^2 \frac{I}{|n|}. \quad (2.81)$$

The expression according to eq. (2.81) is used in the numerical solution of the FPE for TOF or filter cooling with the appropriate transfer function inserted. Approximate expressions are discussed in chapter 2.8 below to demonstrate important parameters entering eq. (2.81) and allow optimizing the design and performance of the cooling system.

The *Schottky power at the kicker entrance* follows from

$$P_S = \frac{I}{2\pi} \int_{-\infty}^{\infty} |G_A(\omega)H(\omega)|^2 \frac{|Z_{PL}(\omega)|^2}{Z_0} S_b(\omega) d\omega \quad (2.82)$$

where the Schottky spectral (current) density $S_b(\omega)$ is given by eq. (2.67). The pickup output power density (W/Hz) is $\frac{|Z_{PL}(\omega)|^2}{Z_0} S_b(\omega)$.

2.4.2.2 Thermal Noise

Another source of noise that contributes to the diffusion is due to the electronic noise in the cooling system. It results mainly from the pickup and the first amplifier stages. If the pickup is kept on temperature T_P and the amplifier has an equivalent noise temperature T_A the additional thermal noise power density (W/Hz) is

$$S_{th}(\omega) = \frac{1}{2}k(T_A + T_R) \quad (2.83)$$

where k is the Boltzmann constant ($k = 1.38 \cdot 10^{-23} \frac{\text{J}}{\text{K}}$). The thermal noise power density

constitutes white noise extending over all positive and negative angular frequencies with a constant power density. The total noise input power to the cooling chain with characteristic impedance Z_0 in the cooling bandwidth W is

$$P = 2 \cdot \frac{1}{2\pi} \int_{\omega_l}^{\omega_u} S_{th}(\omega) d\omega = k(T_A + T_R) \frac{\omega_u - \omega_l}{2\pi} = k(T_A + T_R) W \quad (2.84)$$

where the upper and lower band angular frequencies are ω_l and ω_u , respectively.

The spectral noise density seen by the beam at the kicker is then using the general result according to eq. (2.66)

$$S(\omega) = \frac{(Ze)^2}{A^2} \left| K_{\parallel}(\omega) G_A H(\omega) \right|^2 Z_0 \frac{1}{2} k(T_A + T_R) \quad (2.85)$$

Inserting this into eq. (2.60) yields the mean square energy change per turn due to thermal noise

$$\langle \Delta E_{IC}^2 \rangle = \frac{1}{2} \frac{(Ze)^2}{A^2} \frac{\omega_0}{2\pi} \left(1 + \kappa \frac{\Delta E}{E} \right) \cdot Z_0 k(T_A + T_R) \cdot \sum_{m=-\infty}^{\infty} \left| K_{\parallel}(m\omega_s) G_A H(m\omega_s) \right|^2. \quad (2.86)$$

The finite bandwidth of the amplifier and the symmetry rule $T^*(n\omega) = T(-n\omega)$ leads then to the mean square energy change per turn due to thermal noise

$$\langle \Delta E_{IC}^2 \rangle = \frac{(Ze)^2}{A^2} \frac{\omega_0}{2\pi} \left(1 + \kappa \frac{\Delta E}{E} \right) \cdot Z_0 k(T_A + T_R) \cdot \sum_{m=n_I}^{n_2} \left| K_{\parallel}(m\omega_s) G_A H(m\omega_s) \right|^2 \quad (2.87)$$

with $\omega_s = \omega_0(1 + \kappa\Delta E/E)$. If there is no filter in the cooling chain we set $H(\omega) = I$.

The *total thermal noise power at the kicker entrance* is

$$P_{th} = \frac{I}{2\pi} \int_{-\infty}^{\infty} |G_A(\omega)H(\omega)|^2 \frac{I}{2} k(T_A + T_R) d\omega \quad (2.88)$$

The *total microwave power* is then given by the sum $P_{micro} = P_s + P_{th}$.

The electronic power that has to be installed for the stochastic cooling system is determined from the sum of the total Schottky and thermal noise power at the kicker entrance. To account for losses in the cooling chain and for the statistical nature of the cooling signals a safety factor 4 to 6 has to be included to avoid signal distortions due to e.g. amplifier non-linearities so that the necessary electronic power is $(4-6) \cdot P_{micro}$. This guarantees that the amplifiers will not be saturated and no additional heating is introduced.

If the input power $P = P_{th} + P_s$ is matched to the kicker impedance, see eq. (2.20), the required peak energy change exerted to an ion follows from $P = (\Delta E / (Ze/A))^2 / (2Z_K)$.

Instead using one high power amplifier we can distribute the power to more amplifiers which have only to deliver a correspondingly smaller power. E.g., if one uses four amplifiers with a quarter of the necessary power P one can write

$$\begin{aligned} P &= 4 \cdot \frac{I}{4} P = 4 \cdot \frac{I}{4} \frac{(\Delta E / (Ze/A))^2}{2Z_K} \\ &= 4 \cdot \frac{I}{4} \frac{4 (\Delta E / (Ze/A))^2}{2Z_K} \\ &= 4 \cdot \frac{\left(\frac{I}{4} \Delta E / (Ze/A)\right)^2}{2(Z_K / 4)} \end{aligned} \quad (2.89)$$

which shows that one can split a quarter of the necessary power to a quarter of the kicker shunt impedance. For the HESR cooling system (see Table 2.1) this means that instead using one amplifier for the kicker equipped with 64 ring-slot couplers having the shunt impedance Z_K one can form four groups with 16 ring-slot couplers each group with shunt impedance $Z_K/4$ powered with an amplifier that has only a quarter of the necessary power to be installed.

2.5 Palmer Cooling

An essentially different momentum cooling technique is the *Palmer cooling*. While for TOF and the filter cooling methods pickups and kickers are applied in sum mode, i.e. they can be built identically, the Palmer method uses a specifically designed difference pickup located at a position with large horizontal momentum dispersion D in the ring and a kicker in sum mode. At a position with a small betatron function the particle position is then mainly given by $x = D \cdot \delta$ and is thus proportional to the relative momentum deviation δ of the particle. A large dispersion is necessary to provide large position deviations x as a function of momentum spread. Consequently a wide horizontal beam pipe is mandatory. Specifically designed pickups covering a large horizontal position range are used for that purpose (Palmer pickup) [2]. Despite the different technical layout of the cooling system this method also leads to a suppression of the Schottky noise in the center of the distribution. Thermal noise is however not suppressed due to the absence of the filter in the cooling chain.

The coupling impedance of such a device is sensitive to the momentum deviation and is approximately given here as

$$Z_{PA}(\omega) = S(D\delta) \cdot Z_{PL}(\omega) \quad (2.90)$$

with the dimensionless quantity $S(D\delta) = S_0 \cdot D\delta$ and $Z_{PL}(\omega) = \sqrt{Z_p \cdot Z_0} \sin \theta(\omega) e^{i(\frac{\pi}{2} - \theta(\omega))}$.

The constant S_0 has the unit $1/m$. The output voltage of a Palmer pickup is thus proportional to the momentum or energy deviation of a particle. No 90 degree phase shifter is necessary. The transfer function $T_{PA}(\omega)$ for the Palmer method is given by

$$T_{PA}(\omega) = \frac{Ze}{A} K_{||}(\omega) G_A Z_{PL}(\omega) S_0 D \frac{I}{\eta} \frac{\Delta\omega}{\omega_0} e^{-i\omega T_D} \quad (2.91)$$

where the coupling impedance $Z_{PA}(\omega)$, eq. (2.90), has been used.

Following similar steps as for filter or TOF cooling we find the coherent energy change a particle receives at the kicker per turn due to its own energy error at the pickup.

2.5.1 Coherent Response (Palmer)

$$\Delta E_C = 2 \cdot \frac{(Ze)^2}{A} \frac{\omega_0}{2\pi} \left(I + \kappa \frac{\Delta E}{E} \right) \cdot S(D \frac{I}{\beta^2} \frac{\Delta E}{E}) \sum_{n=n_l}^{n_2} \text{Re} \left\{ K_{||}(n\omega_s) G_A Z_{PL}(n\omega_s) e^{i\zeta(n, \Delta E)} \right\} \quad (2.92)$$

with $\omega_s = \omega_0(I + \kappa \Delta E/E)$.

Similarly to TOF cooling the Palmer cooling technique provides a larger cooling acceptance compared to filter cooling as is outlined in chapter 2.9.

Similarly we derive the mean square energy change per turn at the kicker due to thermal and Schottky particle noise.

2.5.2 Incoherent Beam Response

2.5.2.1 Schottky Noise (Palmer)

$$\begin{aligned} \langle \Delta E_{IC,S}^2 \rangle &= \\ 2 \cdot \frac{(Ze)^4}{A^2} &\left(\frac{\omega_0}{2\pi} \right)^2 \left(I + \kappa \frac{\Delta E}{E} \right) \left(S(D \frac{I}{\beta^2} \frac{\Delta E}{E}) \right)^2 \cdot \frac{E}{|\kappa|} \cdot \Psi(\Delta E, t) \cdot \sum_{n=n_l}^{n_2} \left| K_{||}(n\omega_s) G_A Z_{PL}(n\omega_s) \right|^2 \frac{1}{|n|} \end{aligned} \quad (2.93)$$

with $\omega_s = \omega_0(I + \kappa E/E_0)$.

Observe that the frequency slip factor enters into the denominator. Thus heating by Schottky noise increases for bad mixing, i.e. small frequency slip factor.

Expanding the expression in brackets in eq. (2.93) shows that Palmer cooling provides a similar suppression of the Schottky noise in the center of the distribution as was found for filter cooling. However, thermal noise in the cooling loop is not suppressed due to the absence of the filter in the cooling chain as shown in the next section.

The *Schottky power at the kicker entrance* follows from

$$P_S = \frac{I}{2\pi} \int_{-\infty}^{\infty} |G_A(\omega)|^2 \frac{|Z_{PA}(\omega)|^2}{Z_0} S_b(\omega) d\omega. \quad (2.94)$$

2.5.2.2 Thermal Noise (Palmer)

$$\langle \Delta E_{IC}^2 \rangle = \frac{I}{2} \frac{(Ze)^2}{A^2} \frac{\omega_0}{2\pi} (1 + \kappa \frac{\Delta E}{E}) \cdot Z_0 k(T_A + T_R) \cdot \sum_{m=-\infty}^{\infty} |K_{||}(m\omega_s) G_A|^2 \quad (2.95)$$

with $\omega_s = \omega_0(1 + \kappa \Delta E / E)$.

We observe that the thermal noise contribution to diffusion is the same as for TOF cooling.

The *total thermal noise power at the kicker entrance* is

$$P_{th} = \frac{I}{2\pi} \int_{-\infty}^{\infty} |G_A(\omega)|^2 \frac{I}{2} k(T_A + T_R) d\omega \quad (2.96)$$

The *total microwave power* is then given by the sum $P_{micro} = P_S + P_{th}$.

It should be mentioned that in the HESR only the fast filter and/or TOF cooling techniques are applied.

In chapter 2.8 a detailed discussion of the drift and diffusion terms appearing in the different cooling methods is outlined.

2.6 Summary of Drift Terms

2.6.1 Drift Terms Filter and TOF Cooling

$$F(\Delta E, t) = 2 \cdot \frac{(Ze)^2}{A} \left(\frac{\omega_0}{2\pi} \right)^2 (1 + \kappa \frac{\Delta E}{E}) \sum_{n=n_l}^{n_2} \operatorname{Re} \left\{ K_{||}(n\omega_s) G_A H(n\omega_s) Z_{PL}(n\omega_s) P(n\omega_s) e^{i\zeta(n, \Delta E)} \right\}$$

$$\text{with } \zeta(n, \Delta E) = -n \cdot \omega_0 T_F \left\{ \kappa_{PK} \frac{\Delta E}{E} + \frac{\Delta T_D}{T_F} \right\}.$$

For TOF cooling set $H(\omega) = 1$ and change sign of the electronic gain.

The quantity $F(\Delta E, t)$ has the unit $\frac{eV/u}{s}$.

2.6.2 Drift Term Palmer Cooling

$$F(\Delta E, t) = 2 \cdot \frac{(Ze)^2}{A} \left(\frac{\omega_0}{2\pi} \right)^2 \left(1 + \kappa \frac{\Delta E}{E} \right) \cdot S(D \frac{1}{\beta^2} \frac{\Delta E}{E}) \sum_{n=n_I}^{n_2} \operatorname{Re} \left\{ K_{\parallel}(n\omega_s) G_A Z_{PL}(n\omega_s) e^{i\zeta(n, \Delta E)} \right\}$$

The quantity $F(\Delta E, t)$ has the unit $\frac{eV/u}{s}$.

2.7 Summary of Diffusion Terms and Noise Power

2.7.1 Diffusion Terms of Filter and TOF Cooling

Schottky Noise:

$$D_S(\Delta E, t) = (Ze)^2 \left(\frac{\omega_0}{2\pi} \right)^3 \left(1 + \kappa \frac{\Delta E}{E} \right) \cdot \frac{E}{|\kappa|} \cdot \Psi(\Delta E, t) \cdot \sum_{n=n_I}^{n_2} \left| T(n\omega_0 \left(1 + \kappa \frac{\Delta E}{E} \right)) \right|^2 \frac{1}{|n|}$$

where the transfer function for TOF or filter cooling has to be inserted.

The quantity $D_S(\Delta E, t)$ has the unit $\frac{(eV/u)^2}{s}$.

Schottky power at the kicker entrance:

$$P_S = \frac{I}{2\pi} \int_{-\infty}^{\infty} |G_A(\omega) H(\omega)|^2 \frac{|Z_{PL}(\omega)|^2}{Z_0} S_b(\omega) d\omega$$

Thermal Noise:

$$D_{th}(\Delta E, t) = \frac{1}{2} \frac{(Ze)^2}{A^2} \left(\frac{\omega_0}{2\pi} \right)^2 \left(1 + \kappa \frac{\Delta E}{E} \right) \cdot Z_0 k(T_A + T_R) \cdot \sum_{m=n_I}^{n_2} \left| K_{\parallel}(m\omega_s) G_A H(m\omega_s) \right|^2$$

The quantity $D_{th}(\Delta E, t)$ has the unit $\frac{(eV/u)^2}{s}$.

Thermal noise power at the kicker entrance:

$$P_{th} = \frac{1}{2\pi} \int_{-\infty}^{\infty} |G_A(\omega)H(\omega)|^2 \frac{1}{2} k(T_A + T_R) d\omega$$

Set $H(\omega) = 1$ for TOF cooling.

2.7.2 Diffusion Terms Palmer Cooling

Schottky Noise:

$$D_s(\Delta E, t) = \frac{(Ze)^4}{A^2} \left(\frac{\omega_0}{2\pi} \right)^3 \left(1 + \kappa \frac{\Delta E}{E} \right) \left(S(D \frac{1}{\beta^2} \frac{\Delta E}{E}) \right)^2 \cdot \frac{E}{|\kappa|} \cdot \Psi(\Delta E, t) \cdot \sum_{n=n_j}^{n_2} \left| K_{||}(n\omega_s) G_A Z_{PL}(n\omega_s) \right|^2 \frac{1}{|n|}$$

Thermal Noise:

$$D_{th}(\Delta E, t) = \frac{1}{2} \frac{(Ze)^2}{A^2} \left(\frac{\omega_0}{2\pi} \right)^2 \left(1 + \kappa \frac{\Delta E}{E} \right) \cdot Z_0 k(T_A + T_R) \cdot \sum_{m=n_j}^{n_2} \left| K_{||}(m\omega_s) G_A \right|^2$$

The diffusion terms have the units $\frac{(eV/u)^2}{s}$.

Thermal noise power at the kicker entrance:

$$P_{th} = \frac{1}{2\pi} \int_{-\infty}^{\infty} |G_A(\omega)|^2 \frac{1}{2} k(T_A + T_R) d\omega$$

In any cases the total microwave power at the kicker entrance is $P_{tot} = P_S + P_{th}$. To account for the fact that noise signal are amplified and the losses may occur in the cooling chain a safety factor of 4 to 6 must be included to determine the necessary electronic power that has to be installed.

2.8 Discussion of Momentum Cooling Techniques

In the following chapters we derive simplified expressions for the TOF and filter cooling methods by inspection of the drift and diffusion terms in the vicinity of zero momentum or energy spread. This allows highlighting the important quantities which determine the performance of the cooling system. Approximate expressions for the Schottky noise and thermal noise power are given to estimate the necessary electronic power which must be installed. The discussion also illustrates the limits of the cooling bandwidth that can be used for a given ring lattice design.

A detailed discussion of the Palmer cooling technique [2] is omitted here.

2.8.1 Filter Cooling

Starting with coherent energy change according to eq. (2.53) and using the transfer functions for filter cooling we derive

$$\Delta E_C = \frac{2(Ze)^2}{A} \frac{\omega_0}{2\pi} \sqrt{Z_p Z_K} (I + \eta\delta) G_A \sum_{n=n_l}^{n_2} \sin(n\pi\eta\delta) \cos(n\pi\eta\delta - n\zeta(\omega) + 2\theta(\omega)) \sin^2(\theta(n\omega)). \quad (2.97)$$

Inserting the expression $\zeta(\omega) \equiv \zeta(n, \Delta E)$ from eq. (2.51) into eq. (2.97) the argument of the cosine-function can be written as

$$n\pi(\eta + 2r\eta_{PK}) \cdot \delta + \{n\omega_0 \Delta T_D + 2\theta(n\omega)\} \approx n\pi(\eta + 2r\eta_{PK}) \cdot \delta + n\omega_0 \left\{ \Delta T_D + \frac{\pi}{\omega_C} \right\} \text{ where the ratio}$$

$r = T_F/T_0$ of the time of flight from pickup to kicker of the nominal particle and the revolution period has been introduced. To further simplify the expression, $(I + \eta\delta) \cdot \sin(n\pi\eta\delta)$ is expanded w.r.t. δ around zero resulting in $(I + \eta\delta) \cdot \sin(n\pi\eta\delta) \approx n\pi\eta\delta$.

Further $\sin^2(\theta(n\omega))$ in eq. (2.97) is replaced by one (value at the center of the cooling bandwidth).

For optimal cooling the delay time difference $\Delta T_D = T_D - T_F = (T_{amp} + T_{delay}) - T_F$ of the cooling chain is adjusted to

$$\Delta T_D = -\frac{\pi}{\omega_c}. \quad (2.98)$$

In this case the signal transit time from pickup input to kicker output equals the nominal particle travelling time from pickup to kicker, i.e., $T_F = T_{amp} + T_{delay} + \frac{\pi}{\omega_c}$. Later when we discuss examples, it is shown how the correct delay T_{delay} is adjusted by an open loop gain measurement.

The delay adjustment with eq. (2.98) then yields for the coherent energy correction per turn at the kicker in filter cooling

$$\Delta E_C = \frac{(Ze)^2}{A} \omega_0 \sqrt{Z_p Z_K} (\eta \delta) G_A \sum_{n=n_l}^{n_2} n \cdot \cos(n\pi(\eta + 2r\eta_{PK}) \cdot \delta) \quad (2.99)$$

From this result we conclude the important facts

1. Each harmonic in the cooling bandwidth contributes to cooling.
2. To first order the coherent energy change is proportional to $\eta \cdot \delta$ times the amplifier gain G_A . It increases with increasing shunt impedance of pickup and kicker.
 - a. Below transition energy $\eta > 0$ and the gain must be reversed, $G_A \rightarrow -G_A$, i.e. an additional 180 degrees phase shift must be introduced in the cooling chain to obtain cooling.
3. The deviation from linearity ($\Delta E_C \propto \eta G_A \cdot \delta$) at each harmonic is due the phase $n\pi(\eta + 2r\eta_{PK}) \cdot \delta$. This is called mixing from pickup to kicker. This is largest at the high frequency end of the cooling system.
4. In filter cooling both, the ring frequency slip factor η and the frequency slip factor η_{PK} from pickup to kicker determine the mixing and thus the deviation from linearity of the coherent energy correction. The ring slip factor η determines also the strength of the energy correction and therefore should be large. However a compromise has to be chosen to keep its influence on mixing from pickup to kicker small. As discussed below the frequency slip factor from pickup to kicker should be small as possible (the ideal case is a ring lattice with $\eta_{PK} = 0$)

5. The coherent energy change is proportional to $\sqrt{Z_p Z_K} \cdot G_A$. We will show below (eq. (2.106) that the Schottky particle power is proportional to $Z_p G_A^2$. It is therefore useful to achieve a large kicker shunt impedance Z_K in order to keep the required power in a reasonable range.

Unwanted mixing can be reduced if for each harmonic number n we have $\cos(n\pi(\eta + 2r\eta_{PK}) \cdot \delta) \approx 1$. This determines an upper limit $f_+ = n_2 \cdot f_o$ for the cooling system which follows from the requirement $n_2 \pi |\eta + 2r\eta_{PK}| \cdot |\delta| < \frac{\pi}{2}$.

The maximum useful upper harmonic n_2 of the cooling system must thus be restricted to

$$n_2 < \frac{l}{2|\eta + 2r\eta_{PK}| \cdot |\delta|} \quad (2.100)$$

where the maximum relative momentum deviation at the beginning of cooling is inserted. The relation clearly states the constraints imposed by the ring's lattice design through the ring frequency slip factor and the slip factor from pickup to kicker.

Increasing the frequency slip factor η enhances the wanted mixing from kicker to pickup. However as is visible in eq. (2.100) it also decreases the upper frequency of the cooling system.

In other words, the larger cooling bandwidth is chosen in order to receive a fast cooling rate, the smaller the momentum range where the drift term is linear will be. Beyond that the cooling force becomes non-linear. It can even cross zero leading to heating as will be shown. Cooling is only possible in a limited range of energy deviations. This defines the cooling acceptance discussed in section 2.9.

A compromise has to be chosen to allow for a high frequency limit and non-overlapping harmonics as is necessary for the filter cooling technique. It is also mandatory that for filter cooling the ring lattice should be designed such that the slip factor η_{PK} becomes almost zero.

If at each harmonic $\cos(n\pi(\eta + 2r\eta_{PK}) \cdot \delta) \approx 1$ in eq. (2.99) then, using the approximation $\sum_{n=n_l}^{n_2} n \approx \frac{\Omega_c \cdot \Omega}{\omega_0^2}$ where the center frequency of the cooling bandwidth is $f_c = \Omega_c/2\pi$ and the bandwidth is $W = \Omega/2\pi$, we deduce coherent energy change in the small energy deviation approximation

$$\Delta E_C = \frac{(Ze)^2}{A} \omega_0 \sqrt{Z_p Z_K} \frac{\Omega_c \cdot \Omega}{\omega_0^2} G_A \eta \cdot \delta = \frac{(Ze)^2}{A} \omega_0 \sqrt{Z_p Z_K} G_A \frac{\Omega_c \cdot \Omega}{\omega_0^2} \cdot \kappa \frac{\Delta E}{E}. \quad (2.101)$$

The coherent energy change is thus proportional to both, the bandwidth and the center frequency of the cooling system. High shunt impedances for pickup and kicker are useful to reduce the electronic gain G_A and thus the necessary electronic power. The drift term $F(E)$ for filter cooling according to eq. (2.5) is then found by multiplying eq. (2.101) with $\omega_0/2\pi$,

$$F(\Delta E) = \frac{1}{2\pi} \frac{(Ze)^2}{A} \sqrt{Z_p Z_K} G_A \Omega_c \cdot \Omega \cdot \kappa \frac{\Delta E}{E}. \quad (2.102)$$

In the vicinity of $\Delta E \approx 0$ the cooling force (drift term) is thus linear in the energy deviation ΔE .

It should be noted that in deriving the expression for the drift term for filter cooling, eq. (2.99), it was essential to include the 90 degree phase shifter in the signal path.

Approximation of Schottky and Thermal Noise

Inserting into eq. (2.81) the transfer function for filter cooling and using the expansion $(1 + \kappa \frac{\Delta E}{E}) \sin^2(n\pi(1 + \kappa \frac{\Delta E}{E})) \approx n^2 \pi^2 \kappa^2 \left(\frac{\Delta E}{E}\right)^2$ up to second order, then yields

$$\langle \Delta E_{IC,S}^2 \rangle = \frac{1}{2} \frac{(Ze)^4}{A^2} Z_p Z_K G_A^2 \Omega_c \cdot \Omega \frac{|\kappa|}{E} \cdot (\Delta E)^2 \Psi(\Delta E, t) \quad (2.103)$$

for the incoherent energy change per nucleon and per turn for filter cooling. Again the approximation $\sum_{n=n_l}^{n_2} n \approx \frac{\Omega_c \cdot \Omega}{\omega_0^2}$ has been used.

Schottky noise heating is proportional to the amplifier gain squared. The result demonstrates clearly the effect of the filter. In the center of the distribution Schottky noise heating is suppressed since $\langle \Delta E_{IC,S}^2 \rangle \propto (\Delta E)^2 \Psi(\Delta E, t)$. As already stated above Schottky noise is proportional to the particle distribution and thus explicitly depends on time. It is also apparent that a small ring slip factor is favored to reduce heating by Schottky noise.

Similarly an approximation for the thermal noise contribution, eq. (2.87), for filter cooling is found with the result

$$\langle \Delta E_{IC}^2 \rangle = \frac{(Ze)^2}{A^2} \frac{\omega_0}{2\pi} Z_k k(T_R + T_A) G_A^2 \left(\kappa \frac{\Delta E}{E} \right)^2 \sum_{n=n_l}^{n_2} n^2 \quad (2.104)$$

Replacing the sum by $\sum_{n=n_l}^{n_2} n^2 \approx \frac{\Omega}{\omega_0} \left(\frac{\Omega_c}{\omega_0} \right)^2$ yields

$$\langle \Delta E_{IC}^2 \rangle = \frac{(Ze)^2}{A^2} Z_k k(T_R + T_A) \frac{\Omega}{2\pi} \left(\frac{\Omega_c}{\omega_0} \right)^2 G_A^2 \left(\kappa \frac{\Delta E}{E} \right)^2 \quad (2.105)$$

Similar to Schottky noise the thermal noise contribution is suppressed at the filter frequency and a small ring slip factor is favored.

Schottky Power and Thermal Noise Power at the Kicker Entrance

Evaluating the Schottky noise power at the kicker entrance according to eq. (2.82) yields for filter cooling the expression

$$P_s = 2\pi^2 N (Ze)^2 Z_p \Omega_c^2 \frac{\Omega}{\omega_0} G_A^2 \cdot \eta^2 \delta_{rms}^2. \quad (2.106)$$

The Schottky power is determined by the number N and the squared charge state Z^2 of the ions. For heavy ions this fact can restrict the maximum cooling gain to values below the optimal case. The power is proportional to the relative rms momentum spread squared and is largest when cooling starts. During cooling the Schottky power decreases.

Similar approximations as above in this chapter have been applied to derive the Schottky power in eq. (2.106).

The thermal noise power is constant during cooling and follows from eq. (2.88)

$$P_{th} = \frac{1}{2} k(T_R + T_A) G_A^2 \frac{\Omega}{2\pi}. \quad (2.107)$$

The total microwave power at the kicker entrance is $P_{tot} = P_S + P_{th}$. To account for the fact that noise signal are amplified and that losses may occur in the cooling chain a safety factor of 5 must be included to determine the necessary installed electronic power.

2.8.2 Time-Of-Flight Cooling (TOF)

In the Time of Flight (TOF) cooling technique the filter is removed while all other components in the cooling chain remain unchanged. It is essential that the cooling path contains a 90 *degree* phase shifter that accomplishes the differentiation of the pickup signal pulses in time domain. Compiling the appropriate transfer functions in eq. (2.53) leads to the coherent energy change in TOF cooling

$$\Delta E_C = \frac{2(Ze)^2}{A} \frac{\omega_0}{2\pi} \sqrt{Z_p Z_K} (1 + \eta\delta) G_A \sum_{n=n_l}^{n_2} \sin(n\zeta(\omega) - 2\theta(n\omega)) \sin^2(\theta(n\omega)) \quad (2.108)$$

with $\omega = \omega_0(1 + \kappa E/E_0) = \omega_0(1 + \eta\delta)$ and $\zeta(\omega) \equiv \zeta(n, \Delta E)$ as given in eq. (2.51).

For the purpose of illustration we further simplify and adopt as previously the approximation $\sin^2(\theta(n\omega)) \approx 1$ in the above expression.

In TOF cooling we can apply the same delay adjustment $\Delta T_D = -\frac{\pi}{\omega_c}$ as for filter

cooling since the signal transit time of the cooling path is the same. The phase factor in eq. (2.108) then becomes

$$n\zeta(\omega) - 2\theta(n\omega) = -n\eta\delta \left\{ 2\pi r \frac{\eta_{PK}}{\eta} + \pi \frac{\omega_0}{\omega_c} \right\} \approx -n 2\pi r \eta_{PK} \delta \quad (2.109)$$

since for the HESR cooling system $\pi \frac{\omega_0}{\omega_c}$ is a small quantity.

With the approximate phase factor eq. (2.109) we expand $(1+\eta\delta)\sin(-n 2\pi r \eta_{PK}\delta)$ in eq. (2.108) w.r.t. δ up to first order yielding $(1+\eta\delta)\sin(-n 2\pi r \eta_{PK}\delta) \approx -n 2\pi r \eta_{PK}\delta$. The coherent energy change in TOF cooling for small energy deviations then further reduces to

$$\Delta E_C = -\frac{(Ze)^2}{A} \omega_0 \sqrt{Z_p Z_K} 2 r \eta_{PK} \delta G_A \sum_{n=n_l}^{n_2} n .$$

Dealing with the same approximation of the sum as applied in filter cooling entails

$$\Delta E_C = -\frac{(Ze)^2}{A} \omega_0 \sqrt{Z_p Z_K} G_A \frac{\Omega_C \cdot \Omega}{\omega_0^2} 2 r \kappa_{PK} \frac{\Delta E}{E} \quad (2.110)$$

as the coherent energy correction of an ion per turn at the kicker in TOF cooling.

The drift term for TOF cooling becomes

$$F(\Delta E) = -\frac{1}{2\pi} \frac{(Ze)^2}{A} \sqrt{Z_p Z_K} G_A \Omega_C \cdot \Omega 2 r \kappa_{PK} \frac{\Delta E}{E} . \quad (2.111)$$

In the vicinity of $\Delta E \approx 0$ the cooling force (drift term) is thus linear in the energy deviation ΔE .

The similarity of the drift term to that for filter cooling, eq. (2.102), is apparent. There are however two major differences.

1. While for filter cooling mixing from pickup to kicker should be avoided ideally by designing a magnetic lattice of the accelerator ring with $\eta_{PK} \approx 0$ TOF requires good mixing from pickup to kicker $\eta_{PK} \neq 0$. Also the ratio $r = T_F/T_o$ of particle flight time T_F from pickup to kicker and the revolution period T_o should be large.
2. The minus sign in eq. (2.111) indicates that the gain must be reversed when the cooling system is switched from filter, eq. (2.102), to the TOF cooling method.
3. If $\kappa_{PK} > 0$ cooling requires that $G_A > 0$ and vice versa.

In general the optimal lattice requirements w.r.t. mixing are not met. Even in this case satisfactory results can be achieved with both cooling methods. Moreover we can apply both cooling methods. As will be shown below the TOF cooling method obeys the larger cooling acceptance (the range of momentum spread that can be cooled). If initially the momentum

spread exceeds the cooling acceptance of filter cooling (too much mixing from pickup to kicker) one can simply start cooling with the TOF cooling method and switch to filter cooling if the momentum spread is small enough to fit into the filter cooling acceptance. This technique has been successfully applied for the first time at COSY [4] with its ($1 - 3$) GHz cooling system [8].

Approximation of Schottky and Thermal Noise

The mean squared energy change per turn at the kicker in TOF cooling by Schottky noise is found from eq. (2.81) when the filter is removed in the cooling chain (the delay path is opened). We find

$$\langle \Delta E_{IC,S}^2 \rangle = 2 \frac{(Ze)^4}{A^2} Z_p Z_K G_A^2 \left(\frac{\omega_0}{2\pi} \right)^2 \frac{\Omega}{\Omega_c} \frac{E}{|\kappa|} \Psi(\Delta E, t). \quad (2.112)$$

In the derivation of eq. (2.112) the approximation $\sum_{n=n_I}^{n_S} \frac{1}{n} \approx \ln \frac{n_S}{n_I} \approx \frac{\Omega}{\Omega_c}$ has been used.

A comparison of eq. (2.112) with the corresponding mean squared energy change per turn for filter cooling, eq.(2.103), shows that Schottky particle noise is not suppressed in the center of the distribution. Eq. (2.112) also shows that TOF cooling favors good mixing, i.e. a large κ that reduces the Schottky noise heating term. This is different for filter cooling where large mixing should be avoided, see also eqs. (2.103) and (2.105).

Evaluating the thermal noise contribution, eq. (2.87), for TOF cooling yields the approximation

$$\langle \Delta E_{IC}^2 \rangle = \frac{(Ze)^2}{A^2} Z_K k(T_R + T_A) G_A^2 \frac{\Omega}{2\pi} \quad (2.113)$$

which indicates that for TOF cooling the thermal noise contribution to the diffusion is now constant.

Schottky Power and Thermal Noise Power at the Kicker Entrance

Following the same procedure as above one finds that the Schottky power at the kicker entrance for TOF cooling equals

$$P_s = 2N(Ze)^2 \frac{\omega_0}{2\pi} Z_p G_A^2 \frac{Q}{2\pi} \quad (2.114)$$

and the thermal noise power is found to be

$$P_{th} = k(T_R + T_A)G_A^2 \frac{Q}{2\pi}. \quad (2.115)$$

The Schottky noise power is now independent of momentum spread due to the absence of the filter. Consequently the Schottky power is not reduced during cooling. The thermal noise power is now a factor of two larger as compared to filter cooling, eq. (2.107).

The total microwave power at the kicker entrance is $P_{tot} = P_s + P_{th}$. To account for the fact that noise signal are amplified and that losses may occur in the cooling chain a safety factor of 4 to 10 must be included to determine the necessary installed electronic power. The actual safety factor however depends on the amplifier layout. Intermodulation, as caused by non-linear behavior of the signal processing, adds additional frequency components which has to be avoided.

The essential difference to filter cooling is the strong Schottky noise as well as thermal noise contribution to heating in the center of the beam distribution as shown by the Equations (2.112) and (2.113). Consequently the gain has to be reduced as compared to filter cooling to avoid too much heating. In general TOF cooling is slower and leads to higher equilibrium values for the momentum spread.

2.9 Momentum Cooling Acceptance

Rearranging eq. (2.100) for filter cooling shows that the drift term is nearly linear in a range

$$|\Delta E| < \frac{\beta^2 E f_0}{2|\eta + 2r\eta_{PK}| \cdot f_+} \quad (2.116)$$

where the upper frequency of the cooling system is denoted by f_+ . If the energy spread is increased the drift term becomes non-linear and will change its sign if the energy spread is too large. The maximum energy range or range of relative momentum spread for which cooling is achieved is called *cooling acceptance*.

A similar relation as given in eq. (2.116) for filter cooling can be found for TOF cooling. The result is

$$|\Delta E| < \frac{\beta^2 E f_0}{2|2r\eta_{PK}| \cdot f_+} \quad (2.117)$$

A comparison of eqs. (2.116) and (2.117) shows that for regular lattice optics the linearity range of TOF cooling is larger as compared to filter cooling. Consequently the cooling acceptance in TOF cooling is larger.

It can be shown that Palmer cooling has a cooling acceptance likewise large as that of TOF cooling with a linearity range given by eq. (2.117).

An example for the cooling acceptance is presented in Figure 2.23 below.

2.10 Open Loop Gain and Beam Feedback

In the derivation of the drift and diffusion terms given in the previous chapters we assumed that the beam signals are measured with a pickup, amplified and fed to the kicker that produces the energy change of an ion. It was neglected so far that the electromagnetic kicker fields can coherently excite the beam at its eigen-frequencies, which subsequently introduce modulations of the beam current or the beam dipole moment which are then propagated coherently back to the pickup by the beam. This feedback from kicker back to the pickup via the beam [36] is illustrated with the feedback loop shown in Figure 2.11.

The measured beam current at the pickup output PU is the sum of the undisturbed beam current $I_i(\omega)$ as given in eq. (2.35) and the current modulation $\Delta I(\omega)$ produced by the beam feedback. The energy change per nucleon of an ion introduced by the kicker KI is therefore deduced from $\Delta E(\omega) = T(\omega) \cdot (I_i(\omega) + \Delta I(\omega))$.

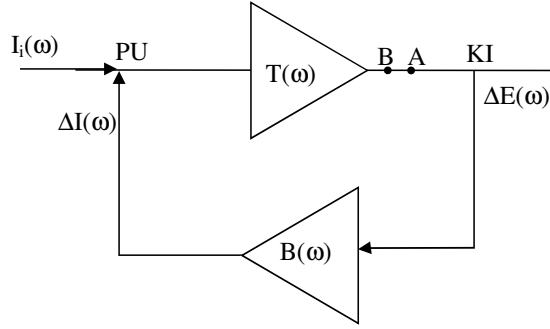


Figure 2.11: Feedback loop TOF or filter momentum cooling. The undisturbed beam current $I_i(\omega)$ is modified by addition of the modulation $\Delta I(\omega)$ introduced by the beam feedback. The loop can be opened between points A and B. A signal is then fed into the loop at point A and the response of the cooling system including the beam is measured at point B with a network analyzer. The resulting open loop gain completely determines the cooling system properties.

From Figure 2.11 we find that the current modulation is

$$\Delta I(\omega) = B(\omega) \cdot \Delta E(\omega) \quad (2.118)$$

with the beam transfer function (BTF) $B(\omega)$. Combining both equations yields for the energy change at the kicker

$$\Delta E(\omega) = \frac{T(\omega)}{1 - B(\omega)T(\omega)} \cdot I_i(\omega). \quad (2.119)$$

If we compare this with eq. (2.10) we can write the effective or *closed loop gain* of the cooling system including beam feedback as

$$G_c(\omega) = \frac{T(\omega)}{1 - B(\omega)T(\omega)}. \quad (2.120)$$

The product

$$S(\omega) = B(\omega) \cdot T(\omega) \quad (2.121)$$

in the denominator of eq. (2.120) is denoted as the *open loop gain*. The open loop gain obeys the symmetry role $S^*(\omega) = S(-\omega)$.

Explicitly, including feedback via the beam, the transfer function $T(\omega)$ of the cooling system must be replaced by the closed loop gain $G_c(\omega)$ in the equations for the drift term in the FPE. The diffusion terms must be multiplied by $1/(1 - S(\omega))^2$ [2, 36].

The open loop gain S can be measured if the cooling loop between pickup and kicker is opened at any point. A signal is then fed into point A, see Figure 2.11, and the response of the beam due to the excitation is measured at point B with a network analyzer (NA). The measurement scheme is essential the same as that used in signal analysis [37]. A device under test (DUT) is excited with the NA by a swept sine wave covering the frequency range of interest. The frequency response of the DUT is measured with the NA. The open loop or BTF measurement is an essential tool to analyze and adjust the cooling system for its best performance. Since the open loop gain S is a complex frequency dependent quantity we can consider magnitude and phase of S or the real and imaginary part of S . In general a magnitude and phase measurement at a large number of harmonics in the cooling bandwidth is carried out to adjust the gain and phase of the cooling system. Specifically, plotting the imaginary part versus the real part as a function of frequency around a revolution harmonic yields the Nyquist plot [37]. As shown below, this plot, carried out at revolution harmonics in the cooling bandwidth, provides important information on the stability margin of the cooling loop. Moreover a BTF measurement delivers important information on possible resonances that are provoked by an interaction of the beam with its environment (impedances).

A major result of signal analysis [37] is that if the real part of S equals one and the imaginary part is zero the cooling loop becomes self-oscillatory, i.e., even with zero input signal the system will oscillate. The system is unstable. Cooling is achieved if the absolute value of $1 - S$ is larger than one. An example of an open loop measurement is discussed below. The quantity $1/(1 - S)$ is called signal suppression. Optimal cooling is achieved with $S = -1$ and therefore with signal suppression 0.5.

Although there exist various original papers and books, see e.g. [1, 38, 39, 40, 41], in which the longitudinal and transverse BTF is examined in detail we adopt the description given in [42] for the general case of a coupled longitudinal and transverse phase space in this contribution. The prominent advantage of the derivation in [42] is the formal and identical treatment for both transverse and longitudinal beam transfer function. The application of modern signal analysis theory and perturbation treatment of the Vlasov equation is therefore a valuable source in the present context. So it appears useful to outline it here in more detail. Since in stochastic cooling the phase space planes are not (or should not be) coupled we present a detailed derivation for each plane separately.

Consider the longitudinal motion of a continuous coasting beam (DC beam). Then, as discussed in chapter 2.4, the orbital motion of a particle with angular frequency ω is given by

$$\Theta(t) = \omega t + \Theta_0 \quad (2.122)$$

where the phase Θ_0 is a random variable uniformly distributed in $[0, 2\pi]$.

We discuss first the case where there are no forces applied by the kicker on the particles and thus each individual particle energy $E = E_s + \Delta E$ where E_s is mean total energy per nucleon is constant. From eq. (2.122) we have that $\dot{\Theta} = \omega = \text{constant}$ and $\dot{E} = \dot{\Delta E} = 0$. The dot denotes the time derivative.

Instead using the longitudinal phase space co-ordinates (Θ, E) or $(\Theta, \Delta E)$ to describe the particle motion we use the angle-action variables (Θ, J) . The *action variable* is defined as

$$J(E) = \int_{E_s}^E \frac{dE'}{\omega(E')} \quad (2.123)$$

and has the unit $eV \cdot s/u$. For a given energy E the action $J(E)$ is the phase space area enclosed by a phase space trajectory divided by 2π . It can be shown that the space area in angle-action variables (Θ, J) or $(\Theta, \Delta J) = (\Theta, \Delta E/\omega)$ is conserved during acceleration, see chapter 6.

The action variable for the motion given by eq. (2.122) is simply $J = \frac{E}{\omega}$. From eq. (2.123) we conclude $\dot{J} = 0$ since there is no energy change, i.e., $\dot{E} = 0$. The time evolution of the orbital

motion of a particle, eq. (2.122), in angle-action variables (Θ, J) , can be derived from the Hamiltonian

$$H_0(\Theta, J) = \omega \cdot J = E(J) \quad (2.124)$$

with the canonical Hamilton's equations

$$\dot{\Theta} = \frac{\partial H_0(\Theta, J)}{\partial J} \quad \text{and} \quad j = -\frac{\partial H_0(\Theta, J)}{\partial \Theta}. \quad (2.125)$$

Since the Hamiltonian does not depend on Θ it follows $\dot{j} = 0$ as desired. The particle motion in angle action variables (Θ, J) is simply given by a straight line for given value of the $J(E)$ as depicted in Figure 2.12.

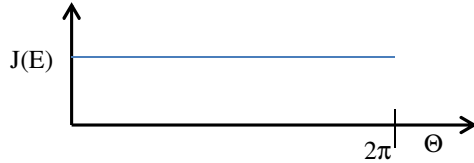


Figure 2.12: Phase space trajectory in action-angle variables.

Since the Hamiltonian does not depend on time explicitly and there are no external forces we conclude for any particle beam distribution in phase space $\Psi(\Theta, J, t)$ that the total time derivative $d\Psi/dt$ vanishes along any phase space trajectory $(\Theta(t), J(t))$ as a consequence of phase space conservation. Carrying out the total derivative of Ψ one finds the *Vlasov equation*

$$0 = \frac{d\Psi(\Theta, J, t)}{dt} = -\left(\frac{\partial H_0}{\partial \Theta} \frac{\partial \Psi}{\partial J} - \frac{\partial H_0}{\partial J} \frac{\partial \Psi}{\partial \Theta} \right) + \frac{\partial \Psi}{\partial t} =: -\{H_0, \Psi\} + \frac{\partial \Psi}{\partial t} \quad (2.126)$$

where the Hamiltonian's equations (2.125) have been used. For convenience, we also introduced the compact notion of the Poisson bracket $\{H, \Psi\}$ for two functions H and Ψ defined on phase space (Θ, J) .

From the definition of the Poisson bracket it is easily seen that $\{A, B\} = -\{B, A\}$.

Note, from eq. (2.126) $\partial\Psi/\partial t = 0$ since we assume a continuous coasting beam (DC beam) with a particle density which does not vary along the ring, $\partial\Psi/\partial\Theta = 0$, and the Hamiltonian (2.124) does not depend on azimuth. The particle density therefore only depends on J and is given by

$$\Psi(\Theta, J, t) = \frac{I}{2\pi}\Psi_o(J) \quad (2.127)$$

The particle number N in the beam is conserved and the normalization is such that

$$\int_0^{\infty} \int_0^{2\pi} \Psi(\Theta, J, t) d\Theta dJ = \int_0^{\infty} \int_0^{2\pi} \frac{I}{2\pi} \Psi_o(J) d\Theta dJ = N \quad (2.128)$$

where $\int_0^{\infty} \Psi_o(J) dJ = N$.

We now apply a voltage to the kicker, located in azimuth at Θ_K . The voltage as seen by the beam particles is denoted by $U(t, \Theta_K)$. Since the particles sample the applied voltage at the kicker location once per turn we can write for the energy change per time of a particle

$$\dot{E} = \frac{Ze}{A} \omega U(t, \Theta_K) \sum_{n=-\infty}^{\infty} \delta(\Theta(t) - \Theta_K - 2\pi n) \quad (2.129)$$

or expressed with the action variable J , eq. (2.123),

$$\dot{J} = \frac{\dot{E}}{\omega} = \frac{Ze}{A} U(t, \Theta_K) \sum_{n=-\infty}^{\infty} \delta(\Theta(t) - \Theta_K - 2\pi n). \quad (2.130)$$

In the equations the delta function appears expressing the assumption that the kicker length is considered to be short as compared to the ring length. So most of the time the particle energy E or the action J does not change, $\dot{E} = 0$ or $\dot{J} = 0$, except when the particle is at the kicker.

We assume that the energy change of a particle at the kicker is small enough so that the kicker action can be treated as a perturbation of the Hamiltonian H_o , eq. (2.124). Since the perturbation is weak the Vlasov equation (2.126) still holds for the Hamiltonian

$$H(\Theta, J, t) = H_0(J) - A(t) \cdot \mathcal{A}(\Theta, J) \quad (2.131)$$

of the perturbed particle motion. The perturbation of the Hamiltonian (2.124) is denoted by $\Delta H(\Theta, J, t) = -A(t) \cdot \mathcal{A}(\Theta, J)$. The particle number N is still conserved. The assumption is justified since for a practical cooling system the gain and phase are properly adjusted so that no particle loss occurs.

We can use the Hamiltonian' equation similar to eq. (2.125) where we replace H_0 by the Hamiltonian in eq. (2.131) to find the perturbed particle motion

$$\begin{aligned} \dot{J} &= -\frac{\partial H}{\partial \Theta} \\ &= A(t) \cdot \frac{\partial}{\partial \Theta} \mathcal{A}(\Theta, J) \\ &= \frac{Ze}{A} U(t, \Theta_K) \sum_{n=-\infty}^{\infty} \delta(\Theta(t) - \Theta_K - 2\pi n) \\ &= U(t, \Theta_K) \cdot \frac{Ze}{A} \frac{1}{2\pi} \sum_{n=-\infty}^{\infty} e^{in(\Theta(t) - \Theta_K)} \end{aligned} \quad (2.132)$$

where we have used eq. (2.130) for the derivative of the action (energy) variable. Eq. (2.132) suggests to write

$$A(t) = U(t; \Theta_K) \quad \text{and} \quad \frac{\partial}{\partial \Theta} \mathcal{A}(\Theta, J) = \frac{Ze}{A} \frac{1}{2\pi} \sum_{n=-\infty}^{\infty} e^{in(\Theta - \Theta_K)} \quad (2.133)$$

For the angle variable we derive

$$\begin{aligned} \dot{\Theta} &= \frac{\partial H}{\partial J} \\ &= \frac{\partial H_0}{\partial J} - A(t) \cdot \frac{\partial}{\partial J} \mathcal{A}(\Theta, J) \\ &= \frac{\partial H_0}{\partial J} = \omega(J) \end{aligned} \quad (2.134)$$

where in the last step we took into account that the kicker only affects the energy of a particle and not its azimuthal position, i.e. $\partial \mathcal{A}(\Theta, J) / \partial J = 0$.

From eqs. (2.132) and (2.134) it follows that we can use the unperturbed motion $\Theta(t) = \omega t + \Theta_0$ and $J(t) = J$ when considering observables along a trajectory in phase space.

The perturbed particle distribution can be written as

$$\Psi(\Theta, J, t) = \bar{\Psi}(\Theta, J) + \Delta\Psi(\Theta, J, t) \quad (2.135)$$

with the unperturbed particle distribution

$$\bar{\Psi}(\Theta, J) = \frac{I}{2\pi} \Psi_0(J) \quad (2.136)$$

and the perturbation $\Delta\Psi(\Theta, J, t)$.

Inserting the perturbed particle distribution (2.135) into the Vlasov equation (2.126) we deduce for the perturbation $\Delta\Psi(\Theta, J, t)$ the first order partial differential equation

$$\frac{\partial}{\partial t} \Delta\Psi(\Theta, J, t) = \{H_0(J), \Delta\Psi(\Theta, J, t)\} - A(t) \{\mathfrak{A}(\Theta, J), \bar{\Psi}(\Theta, J)\} \quad (2.137)$$

where again the curly brackets denote the Poisson brackets introduced with eq. (2.126).

We further simplify the differential equation by introducing the operator L_0 by the definition

$$L_0 g := i \{H_0, g\} \quad (2.138)$$

for any function on phase space $g(\Theta, J)$ with the fixed unperturbed Hamiltonian $H_0(J)$ in eq. (2.124). One easily checks that the operator L_0 is linear.

Specifically we have $L_0 \Delta\Psi = i \{H_0, \Delta\Psi\}$ for the perturbation $\Delta\Psi(\Theta, J, t)$. This is equivalent to $\{H_0, \Delta\Psi\} = -i \cdot L_0 \Delta\Psi$. Inserting this into eq. (2.137) yields the inhomogeneous partial differential equation

$$\frac{\partial}{\partial t} \Delta\Psi = -i \cdot L_0 \Delta\Psi - A(t) \cdot \{\mathfrak{A}, \bar{\Psi}\} \quad (2.139)$$

for the perturbation $\Delta\Psi(\Theta, J, t)$ with the driving term $-A(t) \cdot \{\mathfrak{A}, \bar{\Psi}\}$.

The form of the differential equation (2.139) suggests that in the absence of the perturbation, i.e., $A(t) = 0$, the homogeneous solution of eq. (2.139) can be written as

$$\Delta\Psi(\Theta, J, t) = e^{-iL_0(t-t')} \Delta\Psi(\Theta, J, t') = e^{-iL_0 t} \Delta\Psi(\Theta, J, 0) \quad (2.140)$$

since the operator L_0 for continuous coasting beams does not depend on time.

The formal solution of the inhomogeneous equation (2.139) is then given by [42]

$$\Delta\Psi(\Theta, J, t) = - \int_{-\infty}^t e^{-iL_0(t-t')} A(t') \{ \mathcal{A}(\Theta(t'), J(t')), \bar{\Psi}(\Theta(t'), J(t')) \} dt' \quad (2.141)$$

which is easily checked by taking the partial derivative w.r.t. time. Observe that $\Delta\Psi(\Theta, J, t)$ vanishes when $t \rightarrow -\infty$. This reflects the fact that the perturbation is zero in the past before the kicker is switched ON. In other words, there is no output signal before the input signal is present. The value of the perturbation at time t depends only the past values at time $t' \leq t$ of the kicker excitation (Causality principle of a physical response).

Before we continue to discuss the solution we remark that for any physical observable $B(\Theta, J)$ in phase space, which does not explicitly depend on time, the equation of motion along a phase space trajectory $(\Theta(t), J(t))$ can be written as

$$\frac{dB}{dt} = -\{H_0, B\} = i \cdot L_0 B \quad (2.142)$$

with the solution

$$B(\Theta(t), J(t)) = e^{-iL_0(t-t')} B(\Theta(t'), J(t')) = e^{-iL_0 t} B(\Theta(0), J(0)). \quad (2.143)$$

For the unperturbed particle motion the beam current at the entrance of the pickup located at azimuth Θ_p was given in eq.(2.32). We have

$$I(t; \Theta_p) = Ze \sum_{r=1}^N \omega_r \sum_{n=-\infty}^{\infty} \delta(\Theta_r(t) - \Theta_p - 2\pi n). \quad (2.144)$$

We generalize this expression as was done previously using the fact that the beam consists of a large number of particles N with angular frequencies $\omega_r > 0$ clustered around the central value ω_0 . We further use that for the continuous coasting beam Θ_r is uniformly distributed in

$[0, 2\pi]$. We then can replace the sum of the particle number in eq. (2.144) by a double integral and receive for the beam current at the pickup entrance

$$I(t; \Theta_p) = Ze \int_0^{2\pi} \int_0^\infty \omega \sum_{n=-\infty}^{\infty} \delta(\Theta(t) - \Theta_p - 2\pi n) \tilde{\Psi}(\Theta, \omega) d\Theta d\omega \quad (2.145)$$

where $\tilde{\Psi}(\Theta, \omega)$ is the unperturbed particle distribution in (Θ, ω) co-ordinate space. Using the Fourier representation of the delta function the beam current eq. (2.145) can be written as

$$\begin{aligned} I(t; \Theta_p) &= Ze \int_0^{2\pi} \int_0^\infty \frac{\omega}{2\pi} \sum_{n=-\infty}^{\infty} e^{in(\Theta(t) - \Theta_p)} \tilde{\Psi}(\Theta, \omega) d\Theta d\omega \\ &= Ze \int_0^{2\pi} \int_0^\infty \frac{\omega(J)}{2\pi} \sum_{n=-\infty}^{\infty} e^{in(\Theta(t) - \Theta_p)} \bar{\Psi}(\Theta, J) d\Theta dJ \end{aligned} \quad (2.146)$$

where in the last step the conservation of probability $\tilde{\Psi}(\Theta, \omega) d\Theta d\omega = \bar{\Psi}(\Theta, J) d\Theta dJ$ for the unperturbed particle distribution $\bar{\Psi}(\Theta, J)$ according to eq. (2.136) has been applied.

We can now calculate the current modulation $\Delta I(t; \Theta_p)$ at the pickup as the response to the kicker excitation $U(t, \Theta_K)$. With the perturbation of the particle distribution $\Delta \Psi(\Theta, J, t)$ defined in eq. (2.135) one can write for the current modulation at the pickup

$$\Delta I(t; \Theta_p) = \int_0^{2\pi} \int_0^\infty B(\Theta, J) \Delta \Psi(\Theta, J, t) d\Theta dJ. \quad (2.147)$$

where for abbreviation the pickup observable

$$B(\Theta, J) = Ze \frac{\omega(J)}{2\pi} \sum_{n=-\infty}^{\infty} e^{in(\Theta - \Theta_p)} \quad (2.148)$$

has been introduced.

Inserting the formal solution (2.141) for the perturbed beam particle distribution into eq. (2.147) leads to

$$\Delta I(t; \Theta_p) = - \int_{-\infty}^t A(t') \int_0^{2\pi} \int_0^\infty B(\Theta, J) e^{-il_\theta(t-t')} \left\{ \mathcal{A}(\Theta(t'), J(t')), \bar{\Psi}(\Theta(t'), J(t')) \right\} d\Theta dJ dt' \quad (2.149)$$

which becomes with the property (C.15) in Appendix C

$$\Delta I(t; \Theta_p) = - \int_{-\infty}^t A(t') \int_0^{2\pi} \int_0^\infty \left(e^{iL_0(t-t')} B(\Theta, J) \right) \{ \mathcal{A}(\Theta(t'), J(t')), \bar{\Psi}(\Theta(t'), J(t')) \} d\Theta dJ dt' \quad (2.150)$$

Carrying out the time propagation $B(\Theta(t-t'), J(t-t')) = e^{iL_0(t-t')} B(\Theta, J)$ according to eq. (2.143) in the integral of eq. (2.150) and using the property $\{A, B\} = -\{B, A\}$ of the Poisson bracket for any observables we obtain with the definition of the response function

$$R_{||}(t-t'; \Theta_p; \Theta_K) = \int_0^{2\pi} \int_0^\infty \{ \bar{\Psi}(\Theta(t'), J(t')), \mathcal{A}(\Theta(t'), J(t')) \} B(\Theta(t-t'), J(t-t')) d\Theta dJ \quad (2.151)$$

the current modulation

$$\Delta I(t; \Theta_p) = \int_{-\infty}^t R_{||}(t-t'; \Theta_p; \Theta_K) \cdot A(t') dt' \quad (2.152)$$

The equation describes the propagation of a disturbance $A(t') = U(t'; \Theta_K)$ applied at the kicker location Θ_K at time $t' < t$ which is subsequently observed at the pickup at location Θ_p at a later time t . The propagation of the applied energy changes at the kicker is completely determined by the response function in time domain given in eq. (2.151). The behavior of the beam is completely analog to a linear and time-invariant system described in signal processing. The output of the system $\Delta I(t; \Theta_p)$ is simply the convolution of the input to the system, $A(t') = U(t'; \Theta_K)$, with the system's response function as given in eq. (2.152).

From a Fourier transform of eq. (2.152) it follows that in angular frequency domain

$$R_{||}(\Omega; \Theta_p; \Theta_K) = \frac{\Delta I(\Omega; \Theta_p)}{U(\Omega; \Theta_K)} \quad (2.153)$$

represents the ratio of current modulation at the pickup entrance to the kicker voltage seen by the particles. The required *beam transfer function* according to the definition (2.118) is then

$$B_{\parallel}(\Omega; \Theta_p; \Theta_K) = \frac{\Delta I(\Omega; \Theta_p)}{(Ze/A)U(\Omega; \Theta_K)} = \frac{R_{\parallel}(\Omega; \Theta_p; \Theta_K)}{(Ze/A)} \quad (2.154)$$

The response function $R_{\parallel}(t-t'; \Theta_p; \Theta_K)$ in eq. (2.151) only depends on the time difference $t-t'$ since the continuous coasting beam is time-translation invariant. Eq. (2.151) then reduces to

$$R_{\parallel}(\tau; \Theta_p; \Theta_K) = \int_0^{2\pi} \left\{ \bar{\Psi}(\Theta(0), J(0)), \mathcal{A}(\Theta(0), J(0)) \right\} B(\Theta(\tau), J(\tau)) d\Theta dJ. \quad (2.155)$$

We remark that according to eq. (2.122) $\Theta(0) = \Theta_0$ and $J(0) = J$.

The evaluation of the Poisson bracket in eq. (2.155) yields

$$\left\{ \bar{\Psi}(\Theta(0), J(0)), \mathcal{A}(\Theta(0), J(0)) \right\} = -\frac{\partial \bar{\Psi}}{\partial J} \cdot \frac{Ze}{A} \frac{1}{2\pi} \sum_{m=-\infty}^{\infty} e^{im(\Theta_0 - \Theta_K)} \quad (2.156)$$

and the pickup observable $B(\Theta(\tau), J(\tau)) \approx B(\Theta(\tau), J)$ follows from eq. (2.148) with the unperturbed motion $\Theta(\tau) = \omega\tau + \Theta_0$

$$\begin{aligned} B(\Theta(\tau), J) &= Ze \frac{\omega(J)}{2\pi} \sum_{n=-\infty}^{\infty} e^{in(\Theta(\tau) - \Theta_p)} \\ &= Ze \frac{\omega(J)}{2\pi} \sum_{n=-\infty}^{\infty} e^{in(\omega\tau + \Theta_0 - \Theta_p)} \end{aligned} \quad (2.157)$$

Inserting eqs. (2.156) and (2.157) into the equation for the response function (2.155) yields

$$R_{\parallel}(\tau; \Theta_p; \Theta_K) = -\frac{I}{2\pi} \frac{(Ze)^2}{A} \int_0^{2\pi} \omega(J) \frac{\partial \bar{\Psi}}{\partial J} \sum_{n=-\infty}^{\infty} e^{in(\Theta_K - \Theta_p)} e^{in\omega(J)\tau} dJ. \quad (2.158)$$

In deriving the result the property

$$\frac{I}{2\pi} \int_0^{2\pi} e^{i(n+m)\Theta_0} d\Theta_0 = \delta_{n,-m} \quad (2.159)$$

has been used. The double sum which appears when evaluating eq. (2.155) then collapses into one sum.

The conservation of probability requires

$$\tilde{\Psi}(\Theta, \omega) d\omega = \bar{\Psi}(\Theta, J) dJ = \Psi(\Theta, E) dE$$

and we can write

$$\bar{\Psi}(\Theta, J) = \Psi(\Theta, E) \left| \frac{dE}{dJ} \right| = \omega \Psi(\Theta, E) = \omega \tilde{\Psi}(\Theta, \omega) \left| \frac{d\omega}{dE} \right| = \kappa \frac{\omega_0}{E} \omega \tilde{\Psi}(\Theta, \omega) \text{sign}(\kappa) \quad (2.160)$$

with $d\omega/dE = \kappa \omega_0/E$ and κ as given in eq. (2.49). It follows

$$\frac{\partial \bar{\Psi}(\Theta, J)}{\partial J} dJ = \kappa \cdot \text{sign}(\kappa) \frac{\omega_0}{E} \frac{\partial}{\partial \omega} (\omega \tilde{\Psi}(\Theta, \omega)) d\omega. \quad (2.161)$$

With the help of the last equation the integral (2.158) w.r.t. the action J can then be expressed as an integral w.r.t. angular frequency ω

$$R_{\parallel}(\tau; \Theta_p; \Theta_K) = -\frac{1}{2\pi} \frac{(Ze)^2}{A} \kappa \frac{\omega_0}{E} \int_0^{\infty} \omega \frac{\partial}{\partial \omega} (\omega \tilde{\Psi}(\Theta, \omega)) \sum_{n=-\infty}^{\infty} e^{in(\Theta_K - \Theta_p)} e^{in\omega\tau} d\omega. \quad (2.162)$$

The densities are normalized as $\int_0^{2\pi} \int_0^{\infty} \tilde{\Psi}(\Theta, \omega) d\Theta d\omega = \int_0^{\infty} 2\pi \tilde{\Psi}(\Theta, \omega) d\omega = N$ since the unperturbed angular frequency distribution does not depend on azimuth. It is now convenient to use the definition

$$\Psi_0(\omega) = 2\pi \tilde{\Psi}(\Theta, \omega) \quad (2.163)$$

with the particle frequency distribution $\Psi_0(\omega)$ normalized as

$$\int_0^{\infty} \Psi_0(\omega) d\omega = N. \quad (2.164)$$

Eq. (2.162) can then written as

$$R_{\parallel}(\tau; \Theta_p; \Theta_K) = -\frac{1}{2\pi} \frac{(Ze)^2}{A} \kappa \frac{\omega_0}{E} \int_0^{\infty} \omega \frac{\partial}{\partial \omega} (\omega \Psi_0(\omega)) \sum_{n=-\infty}^{\infty} e^{-in(\Theta_K - \Theta_p)} e^{-in\omega\tau} d\omega. \quad (2.165)$$

To find the frequency response to the kicker excitation we apply the Laplace transform

$$\bar{h}(s) = \int_0^\infty h(t)e^{-st}dt \text{ to eq. (2.165) with the complex frequency } s = \lambda + i\Omega. \text{ This yields}$$

$$R_{\parallel}(s; \Theta_p; \Theta_K) = -\frac{1}{2\pi} \frac{(Ze)^2}{A} \frac{\kappa \omega_0}{E} \int_0^\infty \omega \frac{\partial}{\partial \omega} (\omega \Psi_0(\omega)) \sum_{n=-\infty}^{\infty} \frac{e^{-in(\Theta_K - \Theta_p)}}{s + in\omega} d\omega. \quad (2.166)$$

The angular frequency response is found from eq. (2.166) by letting λ approach zero in $s = \lambda + i\Omega$. The sum in the integral can be performed exactly [43]

$$\lim_{\lambda \rightarrow 0+} \sum_{n=-\infty}^{\infty} \frac{e^{-in(\Theta_K - \Theta_p)}}{s + in\omega} = -\frac{\pi}{\omega} e^{i\frac{\Omega}{\omega}(\Theta_K - \Theta_p)} \left\{ 1 + i \cot(\pi \frac{\Omega}{\omega}) \right\} \quad (2.167)$$

so that the frequency response becomes

$$R_{\parallel}(\Omega; \Theta_p; \Theta_K) = \frac{1}{2} \frac{(Ze)^2}{A} \frac{\kappa \omega_0}{E} \int_0^\infty \frac{\partial}{\partial \omega} (\omega \Psi_0(\omega)) e^{i\frac{\Omega}{\omega}(\Theta_K - \Theta_p)} \left\{ 1 + i \cot(\pi \frac{\Omega}{\omega}) \right\} d\omega \quad (2.168)$$

and the beam transfer function is finally found with eq. (2.154)

$$B_{\parallel}(\Omega; \Theta_p; \Theta_K) = \frac{Ze}{2} \frac{\kappa \omega_0}{E} e^{i\Omega T_F} \int_0^\infty \frac{\partial}{\partial \omega} (\omega \Psi_0(\omega)) C(\Omega, \omega) \left\{ 1 + i \cot(\pi \frac{\Omega}{\omega}) \right\} d\omega \quad (2.169)$$

where the *mixing factor between pickup and kicker* is introduced by

$$C(\Omega, \omega) = e^{i2\pi\alpha\Omega \left(\frac{1}{\omega} - \frac{1}{\omega_0} \right)} \quad (2.170)$$

with $\alpha = (\Theta_K - \Theta_p)/2\pi$. The nominal particle travelling time from pickup to kicker is denoted by T_F .

To illustrate the essential physics contained in the beam transfer function of a stochastic cooling system as given in eq. (2.169) we assume a narrow frequency distribution so that the bands do not overlap. The mixing factor is approximated with $C(\Omega, \omega) \approx 1$. We

assume that the delay line is adjusted to the nominal particle travelling time from pickup to kicker and thus cancels the factor $e^{i\Omega T_F}$ in eq. (2.169). In this case eq. (2.169) simplifies to

$$B_{||}(\Omega; \Theta_p; \Theta_K) = \frac{Ze}{2} \frac{\kappa}{E} \frac{\omega_0}{2\pi} \int_0^\infty \frac{\partial}{\partial \omega} (\omega \Psi_o(\omega)) \left\{ 1 + i \cot(\pi \frac{\Omega}{\omega}) \right\} d\omega. \quad (2.171)$$

The only contribution to the real part of the BTF stems from the singularities of the term $\cot(\pi \frac{\Omega}{\omega})$ in the integrand since

$$\int_0^\infty \frac{\partial}{\partial \omega} (\omega \Psi_o(\omega)) d\omega = 0. \quad (2.172)$$

The singularities occur when the excitation frequency of the kicker equals $\Omega = n\omega$ where n is a revolution harmonic. The imaginary part of $1 + i \cot(\pi \frac{\Omega}{\omega})$ is nearly zero if the beam is excited in the non-overlapping region with a frequency between the revolution harmonics. In this case the resistive real part vanishes.

In the vicinity of the singularities of $\cot(\pi \Omega / \omega)$ we expand

$$\cot(\pi \frac{\Omega}{\omega}) \approx \frac{\omega}{\pi} \frac{I}{\Omega - n\omega} \quad (2.173)$$

and consider the beam transfer function according to eq. (2.171) for a small frequency spread $\Delta\omega/\omega_0$. To avoid the singularities in the integral for the beam transfer function we add a small imaginary part to the exciting frequency, $\Omega \rightarrow \Omega - i\varepsilon$, with $\varepsilon > 0$. The choice of a negative imaginary part guarantees that the response in time, eq. (2.152), vanishes in the past, i.e. $\lim_{t \rightarrow -\infty} \Delta I(t; \Theta_p) = 0$, as required for causality of the time signals (No output before input). To see this, consider the signal $B_{||}(\Omega; \Theta_p; \Theta_K) \cdot e^{i\Omega t}$ for the single frequency Ω . It is obvious that the signal lasts forever. If we make the above replacement $\Omega \rightarrow \Omega - i\varepsilon$, with $\varepsilon > 0$ then $B_{||}(\Omega - i\varepsilon; \Theta_p; \Theta_K) \cdot e^{i(\Omega-i\varepsilon)t} = B_{||}(\Omega - i\varepsilon; \Theta_p; \Theta_K) e^{i\Omega t} e^{-\varepsilon t}$ will vanish in the past as $t \rightarrow -\infty$.

With this the beam transfer function, eq. (2.171), transforms into

$$\begin{aligned}
B_{\parallel}(\Omega; \Theta_p; \Theta_K) &= \lim_{\varepsilon \rightarrow 0^+} B_{\parallel}(\Omega - i\varepsilon; \Theta_p; \Theta_K) \\
&= iZe \frac{\kappa}{E} \left(\frac{\omega_0}{2\pi} \right)^2 \lim_{\varepsilon \rightarrow 0^+} \int_0^\infty \omega \frac{\partial}{\partial \omega} \Psi_o(\omega) \frac{1}{\Omega - n\omega - i\varepsilon} d\omega.
\end{aligned} \tag{2.174}$$

The limit in eq. (2.174) can be evaluated with the formula (B.14), Appendix B,

$$\lim_{\varepsilon \rightarrow 0^+} \int \frac{\varphi(x)}{y - x \pm i\varepsilon} dx = \mp i\pi \varphi(y) + P \int \frac{\varphi(x)}{y - x} dx \tag{2.175}$$

where P stands for the principal value part of the integral.

For non-overlapping, well separated revolution harmonics we obtain the beam transfer function

$$B_{\parallel}(\Omega; \Theta_p; \Theta_K) = -\frac{Ze}{2} \left(\frac{\kappa \omega_0}{E} \right) \frac{\omega_0}{2\pi} \left\{ \Omega \frac{\partial}{\partial \Omega} \Psi(\Omega) - \frac{i}{\pi} P \int \frac{\omega \frac{\partial}{\partial \omega} \Psi_o(\omega)}{\Omega - n\omega} d\omega \right\} \tag{2.176}$$

where for one revolution harmonic n the density is given by $\Psi(\Omega) = \frac{1}{|n|} \Psi_o\left(\frac{\Omega}{n}\right)$.

If more than one band contributes to an exciting frequency Ω we have to add up all contributing harmonics in the frequency range of interest. The total density $\Psi(\Omega)$ in the real part of the BTF for overlapping bands is then according to eq. (2.74) given by

$$\Psi(\Omega) = \sum_{\substack{n=-\infty \\ n \neq 0}}^{\infty} \frac{1}{|n|} \Psi_o\left(\frac{\Omega}{n}\right) \tag{2.177}$$

for small total spread in $\Delta\omega$ ($\Delta\omega/\omega_0 < 1$).

For non-overlapping, well separated revolution harmonics the beam transfer function, eq. (2.176), can be simplified to give for one harmonic n

$$\begin{aligned}
B_{\parallel}(\Omega; \Theta_p; \Theta_K) &= -\frac{Ze}{2} \left(\frac{\kappa \omega_0}{E} \right) \frac{\omega_0^2}{2\pi |n|} \left\{ \frac{\partial}{\partial \omega} \Psi_o\left(\frac{\Omega}{n}\right) - \text{sign}(n) \frac{i}{\pi} P \int \frac{\frac{\partial}{\partial \omega} \Psi_o(\omega)}{\Omega/n - \omega} d\omega \right\} \\
&
\end{aligned} \tag{2.178}$$

with $\Omega = n\omega_0(1 + \Delta\omega/\omega_0)$.

A direct consequence of the causality of the time domain response of the beam is that the real and imaginary parts of the beam transfer function cannot be independent from each other. Indeed, causality implies that the imaginary and real parts of the beam transfer function satisfy the *Kramers-Kronig relations* [42, 44]

$$\text{Im}[B_{||}(\Omega; \Theta_p; \Theta_K)] = \frac{1}{\pi} P \int_{-\infty}^{\infty} \frac{\text{Re}[B_{||}(\Omega'; \Theta_p; \Theta_K)]}{\Omega - \Omega'} d\Omega' \quad (2.179)$$

and

$$\text{Re}[B_{||}(\Omega; \Theta_p; \Theta_K)] = -\frac{1}{\pi} P \int_{-\infty}^{\infty} \frac{\text{Im}[B_{||}(\Omega'; \Theta_p; \Theta_K)]}{\Omega - \Omega'} d\Omega' \quad (2.180)$$

where again P stands for the principle value part of the integral (see Appendix B).

These equations imply that the knowledge of one component (imaginary or real part) implies the knowledge of the other and thus the full complex and analytical BTF.

Furthermore, from the Kramers-Kronig relation we can conclude the interesting fact that the beam response cannot be purely resistive, i.e., $\text{Im}[B_{||}(\Omega; \Theta_p; \Theta_K)] = 0$ for all frequencies Ω because this would also require $\text{Re}[B_{||}(\Omega; \Theta_p; \Theta_K)] = 0$ for all frequencies Ω .

In chapter 2.4.2.1 it was shown that the Schottky noise density becomes constant for high harmonics and wide bands (see Figure 2.9 and Figure 2.10). For complete overlap in the cooling bandwidth the total density $\Psi(\Omega)$ in the BTF becomes constant. Equivalently the mixing factor $M(\Omega)$ equals one, indicating perfect mixing. From eq. (2.176) one concludes that the real part of the BTF vanishes for all frequencies in the cooling bandwidth. Consequently according to eq. (2.179) the imaginary part of the BTF vanishes in the cooling bandwidth. Hence, for perfect mixing the beam transfer function is zero in the cooling bandwidth. Beam feedback does not play a significant role when mixing is sufficiently high.

However as outlined previously the situation of perfect mixing has to be avoided if the filter cooling technique shall be applied for momentum cooling.

Open loop gain measurements are an essential and routine tool to explore the stability margin of a stochastic cooling feedback loop. The stability margins have been investigated numerically and analytically for the HESR momentum and betatron cooling systems. A numerical example illustrating the longitudinal beam transfer function at harmonic number 5927 according to eq. (2.178) is shown in Figure 2.13 for an antiproton beam in the HESR with $N = 10^{10}$ particles at $3.8 \text{ GeV}/c$. The frequency slip factor is $\eta = 0.03$ ($\gamma < \gamma_{tr}$) and a Gaussian momentum distribution is assumed with a relative momentum spread $\delta_{rms} = 2 \cdot 10^{-4}$. In the right panel of Figure 2.13 the imaginary part is plotted versus the real part of the BTF as a function of frequency deviation Δf (Nyquist plot, see also below for a more detailed discussion). The arrows point in the direction of increasing frequency.

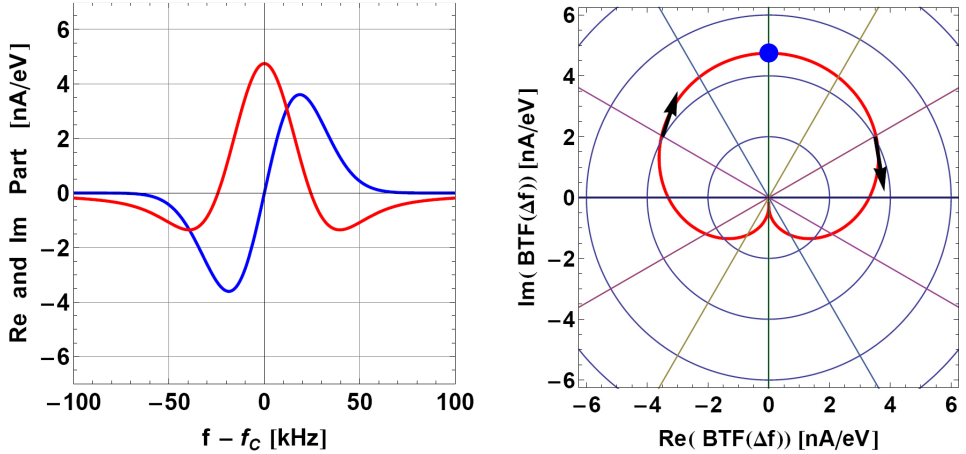


Figure 2.13: Real (blue) and imaginary (red) part of the longitudinal BTF (left panel). A Nyquist diagram of the BTF is shown in the right panel.

The corresponding magnitude and phase of the BTF is displayed in Figure 2.14.

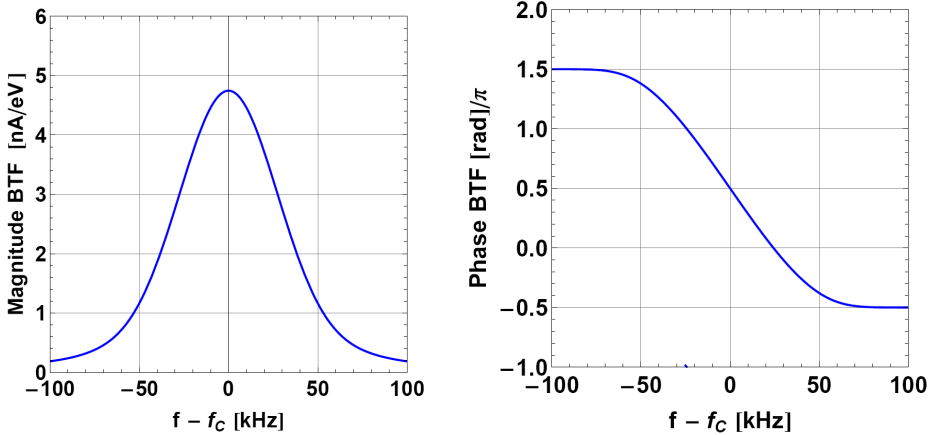


Figure 2.14: Magnitude (left) and phase (right) of the longitudinal BTF around harmonic number 5927.

Note that the real and imaginary part change sign above transition energy according to eq. (2.178). This corresponds to a phase shift in the BTF of 180 degrees.

Observe that the relation $B^*(\Omega) = B(-\Omega)$ holds as desired.

In the Fokker-Planck equation (2.4) we deal with the energy deviation per nucleon ΔE of an ion from the total mean energy per nucleon $E = \gamma E_0$. It is therefore useful to express the beam transfer function in the variable ΔE by using the transformation between energy deviation and angular frequency $\omega(\Delta E) = \omega_0 + d\omega/dE \cdot \Delta E = \omega_0 + \kappa \omega_0/E \cdot \Delta E$. Then the following relations hold, $\Omega - n\omega = n \kappa \omega_0/E (\Delta E^* - \Delta E)$ and $\Omega - n\omega_0 = n \kappa \omega_0/E \Delta E^*$. Taking into account that the integration limits depend on the sign of κ the beam transfer function in energy space in the vicinity of the revolution harmonic n , eq. (2.178), transforms to

$$\tilde{B}(\Delta E^*) = -Ze \left(\frac{\omega_0}{2\pi} \right)^2 \frac{1}{|n|} \left\{ \frac{\pi}{|\kappa \omega_0/E|} \frac{d\Psi_0}{d\Delta E} (\Delta E^*) + \text{sign}(n) \cdot \frac{i}{\kappa \omega_0/E} \cdot P \int_{-\infty}^{\infty} \frac{d\Psi_0}{d\Delta E} \frac{1}{\Delta E^* - \Delta E} d\Delta E \right\}. \quad (2.181)$$

The open loop gain $S(\Omega)$ according to eq. (2.121) at harmonic number n is then obtained with the BTF given in eq. (2.176) and the transfer function of the cooling system

$$T(\Omega) = \frac{Ze}{A} K_{\parallel}(\Omega) G_A H(\Omega) P(\Omega) Z_{PL}(\Omega) e^{-i\Omega(T_F + \Delta T_D)} \text{ as given in eq. (2.11) where } \Delta T_D = T_D - T_F$$

denotes the difference of the delay time of the delay line and the nominal particle flight time from pickup to kicker. Note the unit $[T(\Omega)] = (eV/u)/A$.

The open loop gain for each harmonic in the cooling bandwidth is measured with a network analyzer. The scanned frequency range for harmonic number n is $\Omega = n \omega_0 (1 + \Delta\omega/\omega_0)$ with $|\Delta\omega/\omega_0| < 1$. The cooling system can then be adjusted for optimal cooling harmonic by harmonic [41]. An example will be discussed below.

We conclude the essential facts:

- The open loop gain is proportional to the ion charge squared.
- The open loop gain is proportional to the number of ions. The electronic gain should be decreased if the particle number is increased to avoid instabilities of the cooling loop.
- the open loop gain depends on the gradient of the beam frequency distribution. It becomes large at the edge of the distribution which can result in loop instabilities specifically at the edge of the beam distribution.
- the cooling loop may become unstable during cooling when the beam distribution gets too small and stiff. In other words, during momentum cooling the momentum spread is reduced which leads to less mixing from kicker to pickup. A gain reduction can avoid this. Additional heating of the beam distribution as introduced by intrabeam scattering or an internal target can help to stabilize the cooling loop.
- In chapter 2.4.1, eq. (2.53), it was shown that in the electronic transfer function $T(\Omega)$ of the cooling system a 180 degrees phase shift must be introduced when the working point of the machine is changed from below transition to above transition energy. From eq. (2.176) it is apparent that the BTF in frequency space changes its sign in going from below to above transition energy. Hence, the open loop gain retains its sign. The sign change of the BTF in frequency space is equivalent to a change of the sign of the imaginary part of the BTF, eq. (2.181), in energy space.
- Increasing the absolute value of frequency slip factor reduces the beam transfer function, eq. (2.181). For large values of the frequency slip factor the open loop gain

becomes very small so that the feedback effect may be negligible. This is due to the fact that for large values of the slip factor and large momentum spreads the current modulations induced by the kicker die out before they reach the pickup.

- In chapter 2.4 und 2.5 it was outlined that each harmonic in the cooling bandwidth contributes to the drift and diffusion terms in the Fokker-Planck equation (2.4). In [41] it is shown that momentum cooling can be optimized by maximizing the flux (in frequency range) at each harmonic in the cooling bandwidth when the bands do not overlap and thermal noise plays no significant role. Fastest cooling is then achieved if the open loop gain at every harmonic number is $S = -I$ over the whole beam distribution. As a consequence the signal suppression is 0.5 in this case. In praxis however this requires a sophisticated amplifier response. Here we use a flat amplifier response in the cooling bandwidth so that the optimal signal suppression is not everywhere equal to 0.5. For filter cooling the open loop gain exhibits a sudden phase jump around zero while for TOF cooling the phase is zero in the center of the distribution.
- For $\theta_p = \theta_k$ the BTF is called full ring BTF.

Figure 2.15 illustrates the open loop gain $S(\Omega)$, eq. (2.121), at harmonic number 5927 for HESR filter cooling with parameters as given above for the BTF and an electronic gain of 122 dB. The notch depth is assumed to be 40 dB.

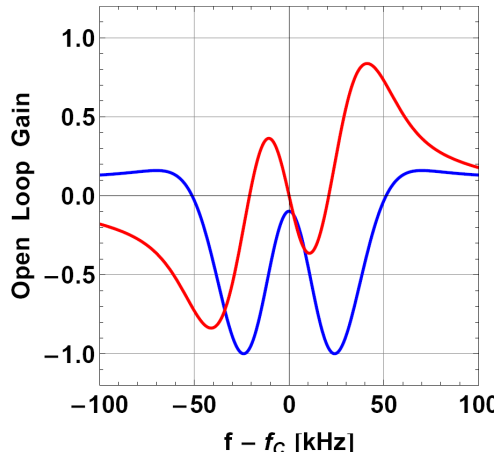


Figure 2.15: Open loop gain for optimized filter cooling. The real part is given in blue, the imaginary part is in red.

The stability of the cooling loop is investigated with the Nyquist diagram [37] depicted in Figure 2.16 at harmonic number 5927. A Nyquist plot is a parametric plot of the open loop gain. The angular frequency is swept as a parameter resulting in a plot as a function of frequency. The loop would be unstable if the curve encircles the point (1,0) (Nyquist criterion) [37]. In this example the electrical delay of the system is adjusted to the travelling time of the nominal particle from pickup to kicker. The gain is 122 dB so that $\text{Re } S \approx -1$ and $\text{Im } S = 0$ in the Nyquist diagram (see blue arrow) for optimal cooling. The open loop phase is then 180° . The black arrows indicate the direction in which the loops in the Nyquist diagram are passed through when the frequency is swept from left to right in the magnitude plot shown in figure. The blue dot is the center of the notch in the magnitude plot. The cooling loop is stable since the curve in the Nyquist diagram does not surround the point (1,0).

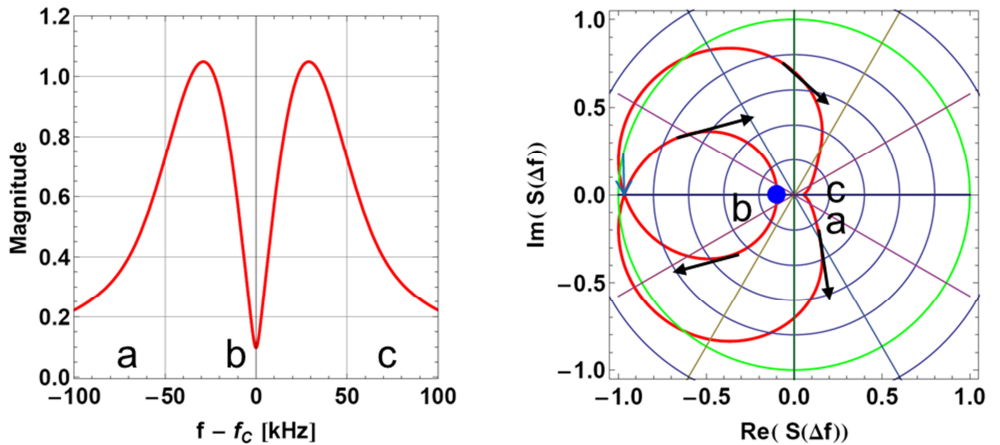


Figure 2.16: Magnitude (left) of the open loop gain and Nyquist stability diagram for filter cooling. The arrows in the Nyquist diagram indicate the direction in which the curve is traversed when the frequency is swept from a over b to c.

The signal suppression $1/(1-S(\Omega))$ is drawn in Figure 2.17. The effect of the signal suppression on the spectral density when the cooling loop is closed is shown for the case when thermal noise is negligible. For optimal cooling the signal suppression should be ideally 0.5 (-6 dB). But this is not achievable over the whole distribution since the magnitude response of the amplifier is constant, see Figure 2.17. The spectral power density at a harmonic number

changes from $S_b(\Omega)$ to $S_b(\Omega)/|1-S(\Omega)|^2$ when the cooling loop is closed, Figure 2.17 right. The open loop gain measurement is an essential and practical method to analyze and optimize the cooling system. By comparing open and closed loop spectral power densities at many harmonics in the cooling bandwidth the system can be optimized.

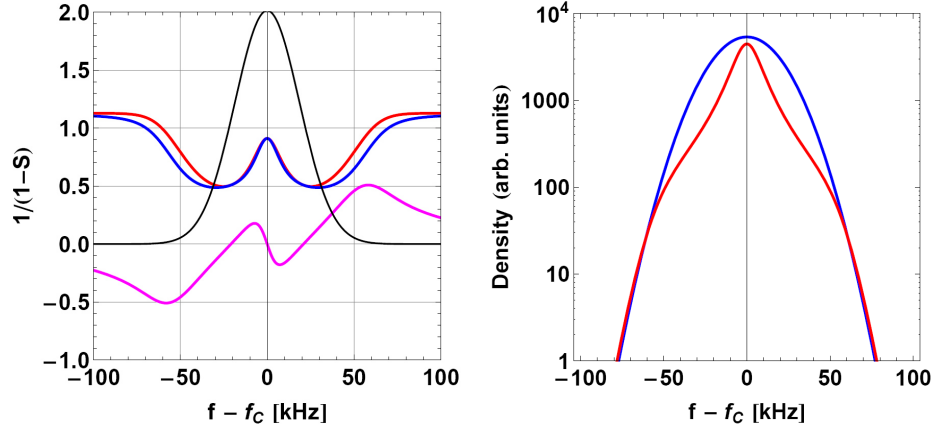


Figure 2.17: Signal suppression at harmonic number 5927 for filter cooling in the HESR (left panel). Magnitude: red, real part: blue, Imaginary part: magenta. The frequency distribution (arb. Units) is shown in black. The right panel shows the frequency distribution when the loop is open (blue) and when the loop is closed (red).

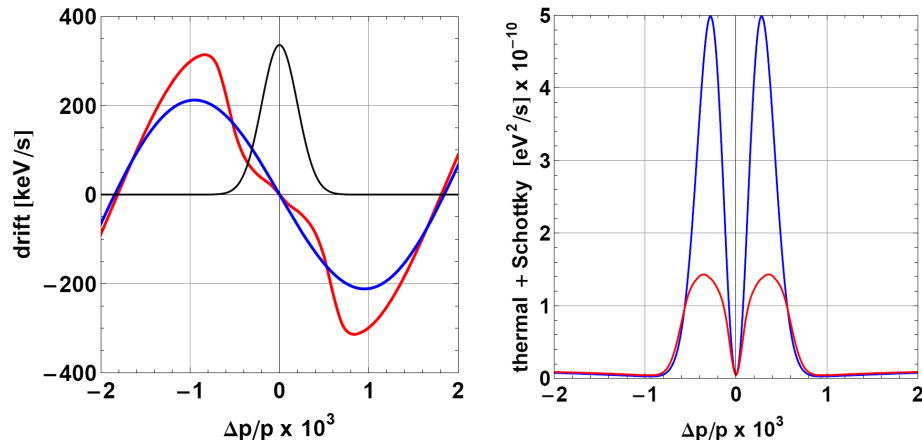


Figure 2.18: Drift term (left) with (red) and without (blue) signal suppression. The momentum distribution (arb. Units) is shown in black. The thermal and Schottky noise with (red) and without (blue) signal suppression is shown in the right panel for filter cooling.

The signal suppression $I/(I-S(\Delta\omega/\omega))$ affects both, the cooling force as well as the Schottky and the thermal noise contributions. The effect on the drift and diffusion terms for filter cooling is illustrated in Figure 2.18. The figure of the drift term shows that cooling is less affected in the center of the distribution. The cooling force is slightly reduced for tail particles. The major effect of signal suppression is visible for the noise contribution, Figure 2.18 right. Here, including the feedback via the beam leads to a reduction of beam and thermal noise.

A measured open loop gain for bunched beam cooling in the Relativistic Heavy Ion Collider (RHIC) at the Brookhaven National Laboratory (BNL) is presented in [45]. The measured open loop gain agrees well with that predicted in Figure 2.15. The measured signal suppression measured in ref. [45] resembles the simulation depicted in Figure 2.17.

A measurement of the Nyquist stability diagram for filter cooling of a proton beam at $2.4 \text{ GeV}/c$ in COSY using the $(1.8 - 3) \text{ GHz}$ bandwidth is shown in Figure 2.19. The measurement renders the simulation shown in Figure 2.16.

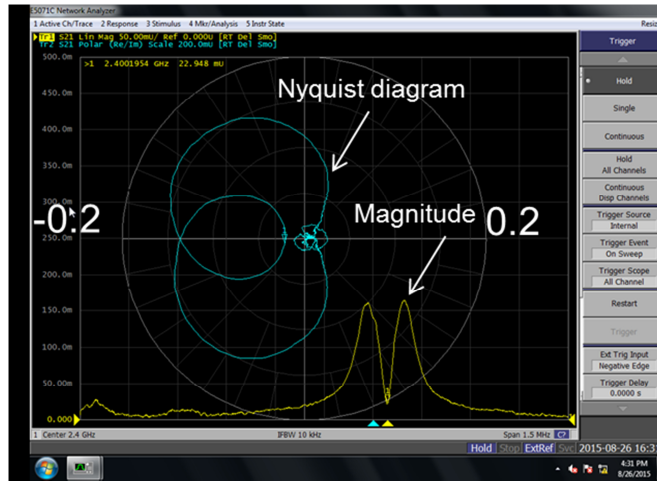


Figure 2.19: Magnitude (yellow trace) and Nyquist stability diagram (blue) for filter cooling of a proton beam in COSY at $2.4 \text{ GeV}/c$.

As discussed in the previous sections TOF cooling is achieved if in the filter cooling chain the filter is set to $H(\omega)=1$ and an additional phase shift of 180 degrees is introduced in the cooling chain to obtain a negative slope for the drift term in the FPE that provides cooling, see also the approximate expression for the drift term eq. (2.102) for filter and eq. (2.111) for TOF cooling. Note that the 90 degree phase shifter still remains in the signal path.

Figure 2.20 illustrates the open loop gain prediction and the measurement results for TOF cooling in COSY at harmonic number $n = 1367$ with a $2.6 \text{ GeV}/c$ beam containing $N = 10^9$ protons. The COSY cooling bandwidth is $(1.8 - 3) \text{ GHz}$. The full ring frequency slip factor was measured to be $\eta = -0.1$ and the rms relative momentum spread of the beam is $\delta_{rms} = 1.5 \cdot 10^{-4}$. In the simulation an electronic gain of 90 dB is assumed. The predictions fairly well reproduce the measured open loop gain as well as the measured stability diagram. In the stability diagram one observes that the open loop phase is now 0° which is attained in the center of the distribution (blue dot in Figure 2.20).

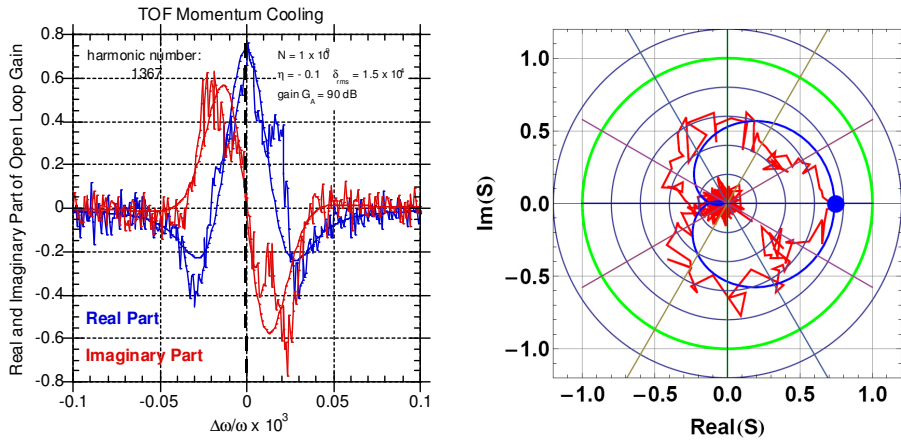


Figure 2.20: Open loop gain for TOF cooling at COSY, left panel. The model prediction is drawn as lines. The right panel presents the Nyquist stability diagram.

Increasing the gain would result in a shift of this point towards the stability limit $(1, 0)$. The same would happen in the course of cooling so that the cooling loop may become unstable when the real part of the open loop gain exceeds one, $Re S > 1$. To avoid instabilities the initial gain should be kept sufficiently small during cooling. Obviously TOF cooling provides slower cooling than the filter technique, however with the advantage of larger cooling acceptances as outlined in chapter 2.9.

From the Nyquist plot one concludes that the shielding factor $1/(1-S(\omega))$ is larger than one in the center of the distribution indicating an enhancement of the drift and diffusion terms in the FPE.

Beam experiments at COSY verify the prediction that TOF cooling is stable if the initial momentum spread is large and the gain is chosen appropriately. TOF cooling is therefore a suitable method to pre-cool the beam when the momentum spread initially exceeds the cooling acceptance for filter cooling.

To conclude the chapter it is remarked that the open loop gain $S(\omega) = B(\omega)T(\omega)$ remains unchanged when the machine's working point is moved from below to above transition energy since the beam transfer function $B(\omega)$ as well as the cooling system transfer function $T(\omega)$ change sign according to chapters 2.4, 2.5 and 2.8.

The open loop gain for Palmer cooling is essentially similar as for filter cooling. It is obtained with the beam transfer function $B(\omega)$, eq. (2.176), and the system transfer function for Palmer cooling $T_{PA}(\omega)$, eq. (2.91).

The thermal noise from pickup and amplifiers is not suppressed in the center of the distribution due to the absence of the notch filter in the cooling signal path.

2.11 Rate Equation for Momentum Cooling

The solution of the FPE (2.4) provides the time development of the beam distribution as a whole with time during cooling. Since the drift and diffusion terms in general depend on ΔE , t and the instant beam distribution $\Psi(\Delta E, t)$ itself, as has been outlined in the previous sections, a solution of the FPE can only be found numerically. Only in simple cases the FPE is accessible for an analytical solution. In the following consideration we include the beam-target interaction as outlined in chapter 4. It consists of a mean energy loss per turn ε which affects the beam as a whole and contributes to the drift term in the FPE. Furthermore, energy loss straggling accounts for an additional energy and time independent diffusion term.

As an example we treat TOF cooling (a similar treatment can be carried out for Palmer cooling) analytically for the case of the linear cooling force (linear drift) approximation as given by eq. (2.111)

$$F(\Delta E) = -F_0 \cdot \Delta E + \varepsilon f_0 \quad (2.182)$$

with

$$F_0 = \frac{1}{2\pi} \frac{(Ze)^2}{A} \sqrt{Z_p Z_K} G_A Q_C \cdot Q \frac{2r \kappa_{PK}}{E} .$$

We include an additional constant drift $\varepsilon f_0 < 0$ which describes the mean energy loss per nucleon and second a particle with revolution frequency f_0 suffers due to the beam-target interaction as outlined in chapter 4.

We assume that thermal noise dominates and neglect the Schottky noise contribution in the diffusion term of the FPE. The diffusion term in the FPE is then given by eq. (2.113) plus an additional energy and time independent diffusion D_T induced by the beam-target interaction

$$D(\Delta E, t) = D_{th} + D_T \quad (2.183)$$

$$\text{with the thermal noise contribution } D_{th} = \frac{1}{2} \frac{\omega_b}{2\pi} \frac{(Ze)^2}{A^2} Z_K k(T_R + T_A) G_A^2 \frac{\Omega}{2\pi}.$$

Since the diffusion term does not vary with energy, the FPE, eq. (2.4), simplifies to

$$\frac{\partial}{\partial t} \Psi(\Delta E, t) = -\frac{\partial}{\partial \Delta E} ((-F_0 \Delta E + \varepsilon f_0) \Psi(\Delta E, t)) + D \cdot \frac{\partial^2}{\partial (\Delta E)^2} \Psi(\Delta E, t) \quad (2.184)$$

The mean energy deviation (beam center) $\mu(t) = \frac{1}{N} \int \Delta E \Psi(\Delta E, t) d\Delta E$ and the variance of the beam $\sigma_{\Delta E}^2(t) = \frac{1}{N} \int (\Delta E - \mu(t))^2 \Psi(\Delta E, t) d\Delta E$ will be determined from the FPE as a function of time during cooling including the beam-target interaction. The beam distributions are normalized to the particle number N and vanish at infinity.

We derive an analytical solution of the FPE for the *initial conditions* $\mu(0) = \mu_0$ and $\sigma(0) = \sigma_0$.

The time evolution of the beam center follows from the simple differential equation

$$\frac{d\mu(t)}{dt} = \frac{1}{N} \int \Delta E \frac{\partial \Psi(\Delta E, t)}{\partial t} d\Delta E = -F_0 \mu(t) + \varepsilon f_0 \quad (2.185)$$

where in the last step the FPE eq. (2.184) has been inserted. Partial integration and the fact that the distributions and their derivatives vanish at infinity have been applied.

The solution for the time evolution of the beam center, taking into account the initial condition $\mu(0) = \mu_0$, is

$$\mu(t) = (\mu_0 - \varepsilon f_0 / F_0) e^{-F_0 t} + \varepsilon f_0 / F_0 \quad (2.186)$$

which shows that the drift term moves the center of gravity of the initial distribution exponentially towards an equilibrium value $\mu(\infty)$ determined by the mean energy loss and the cooling force

$$\mu(\infty) = \varepsilon f_0 / F_0 < 0 \quad (2.187)$$

In a similar way we find with the FPE the time evolution of the beam variance from the first order differential equation

$$\frac{d\sigma^2(t)}{dt} = -2F_0\sigma^2(t) + 2D \quad (2.188)$$

with the solution

$$\sigma^2(t) = \left(\sigma_0^2 - \frac{D}{F_0} \right) e^{-2F_0 t} + \frac{D}{F_0} \quad (2.189)$$

which states that the beam variance is exponentially cooled to an equilibrium value

$$\sigma^2(\infty) = \frac{D}{F_0} = \frac{D_h + D_T}{F_0} \quad (2.190)$$

determined by both the drift *and* diffusion terms of the thermal noise in the cooling loop and the diffusion induced by the beam-target interaction.

The general solution of the FPE for thermal noise dominated TOF cooling with the initial condition $\Psi(\Delta E, 0) = \frac{N}{\sqrt{2\pi}\sigma_0} e^{-\frac{I(\Delta E - \mu_0)^2}{2\sigma_0^2}}$ is finally

$$\Psi(\Delta E, t) = \frac{N}{\sqrt{2\pi}\sigma(t)} e^{-\frac{I(\Delta E - \mu(t))^2}{2\sigma(t)^2}} \quad (2.191)$$

where the time dependent mean $\mu(t)$ and variance $\sigma(t)$ are determined from eqs. (2.186) and (2.189).

From eq. (2.187) one would conclude that a large electronic gain G_A would help to limit the shift in the mean energy $\mu(\infty)$ imposed by the mean energy loss due to the target. However by inspecting eq. (2.190) with the explicit expressions for the drift F_0 , eq. (2.182), and for the diffusion term $D = D_{th} + D_T$, eq. (2.183), we see that the contribution from thermal noise in the cooling system to the beam equilibrium is proportional to the electronic gain. Thus the gain is limited if the equilibrium beam energy spread should be small. Low noise amplifiers and thermal cooling the pickup structures help to reduce the thermal noise contribution. However, cooling cannot fully compensate the mean energy loss, specifically for large target thicknesses. As outlined later, a barrier cavity is used in COSY and the HESR to compensate the mean energy loss.

Albeit the FPE cannot be solved analytically for filter cooling it is worthwhile to try an approximate solution. The result is useful if a quick overview on the cooling process, specifically when the beam-target interaction is included, is necessary without numerically solving the FPE. Also, a handy formula is derived which gives an estimate of the necessary electronic gain. We assume that the mean energy loss is compensated and include only the additional diffusion D_T due to the target.

We consider again the drift term in the linear approximation for the filter cooling technique

$$F(\Delta E) = -F_0 \cdot \Delta E \quad (2.192)$$

as given in eq.(2.102). The constant is $F_0 = \frac{1}{2\pi} \frac{(Ze)^2}{A} \sqrt{Z_p Z_k} G_A \Omega_C \cdot \Omega \cdot \frac{\kappa}{E}$, $G_A > 0$, $\kappa > 0$.

We treat a Schottky noise dominated beam and therefore neglect thermal noise in the diffusion term of the FPE which, according to eqs. (2.103) and (2.6), can be written as

$$D_s(\Delta E, t) = D_0 \cdot \Delta E^2 \Psi(\Delta E, t) + D_T \quad (2.193)$$

with the abbreviation $D_0 = \frac{1}{4} \frac{(Ze)^4}{A^2} Z_p Z_k G_A^2 \Omega_C^2 \cdot \Omega^2 \frac{|\kappa|}{E} \frac{\omega_0}{2\pi}$.

The additional energy and time independent diffusion induced by the beam-target interaction is given by D_T .

The FPE can then be transformed into

$$\begin{aligned} \frac{\partial}{\partial t} \Psi(\Delta E, t) = & F_0 \cdot \frac{\partial}{\partial \Delta E} (\Delta E \Psi(\Delta E, t)) + D_0 \cdot \frac{\partial}{\partial \Delta E} \left\{ \Delta E^2 \Psi(\Delta E, t) \frac{\partial}{\partial \Delta E} \Psi(\Delta E, t) \right\} \\ & + D_T \frac{\partial^2}{\partial \Delta E^2} \Psi(\Delta E, t) \end{aligned} \quad (2.194)$$

It is visible that in this case the diffusion term explicitly depends on energy and the beam distribution itself.

The time evolution of the beam variance of the energy distribution for a centered beam is found if we differentiate both sides w.r.t. time and use the FPE. Partial integration and taking into account that the distributions vanish at infinity then yields the first order differential equation for the beam variance

$$\frac{d\sigma^2(t)}{dt} = -2F_0 \cdot \sigma^2(t) + 2D_T - 2\frac{D_0}{N} \int \Delta E^3 \Psi(\Delta E, t) \frac{\partial}{\partial \Delta E} \Psi(\Delta E, t) d\Delta E \quad (2.195)$$

which contains the unknown beam distribution. We further evaluate the integral with partial integration and by applying the identity $\frac{\partial \Psi^2}{\partial \Delta E} = 2\Psi \frac{\partial \Psi}{\partial \Delta E}$ which leads to

$$\frac{d\sigma^2(t)}{dt} = -2F_0 \cdot \sigma^2(t) + 2D_T + 3\frac{D_0}{N} \int \Delta E^2 \Psi^2(\Delta E, t) d\Delta E \quad (2.196)$$

The last integral still comprises the unknown energy distribution and consequently cannot be solved exactly for the beam variance.

Albeit the shape of the distribution will change during cooling we proceed with the rough assumption that an initial centered Gaussian beam distribution stays nearly Gaussian during cooling. We then approximate the integral by $\int \Delta E^2 \Psi^2(\Delta E, t) d\Delta E \approx \sigma(t) \frac{N^2}{3\sqrt{2\pi}}$.

Inserting this result into eq. (2.195) leads to the approximate rate equation for the beam variance

$$\frac{I}{\tau} = \frac{1}{\sigma^2} \frac{d\sigma^2}{dt} = -2F_0 + \frac{I}{\sqrt{2\pi}} D_0 N \frac{I}{\sigma} + \frac{2D_T}{\sigma^2} \quad (2.197)$$

in filter cooling dominated by Schottky noise. Inspecting the coefficients F_0 as well as D_0 and collecting terms we finally end up with the rate equation for the relative momentum spread $\delta_{rms} = \sigma / (\beta^2 E)$

$$\frac{I}{\tau} = \frac{1}{\delta_{rms}^2} \frac{d\delta_{rms}^2}{dt} = -2 \frac{W}{N} \{ 2g - g^2 M(\delta_{rms}) \} + \frac{2D_T}{(\beta^2 E)^2 \delta_{rms}^2} \quad (2.198)$$

including the diffusion caused by the beam-target interaction. The bandwidth is $W = \Omega/2\pi$ and the dimensionless gain g is defined as

$$g = \frac{N(Ze)^2}{2A} \sqrt{Z_p Z_K} \Omega_c \cdot \frac{\kappa}{E} G_A \quad (2.199)$$

The *mixing factor* M is introduced as

$$M(\delta_{rms}) = \frac{I}{2\sqrt{2\pi}} \frac{f_0}{|\eta| \delta_{rms} \cdot W} \frac{W}{f_c} \quad (2.200)$$

with $f_0 = \omega_0/2\pi$, $f_c = \Omega_c/2\pi$ and the relative rms momentum spread of the beam is δ_{rms} (standard deviation of the momentum distribution).

Eq. (2.198) with $D_T = 0$ is the well-known and celebrated rate equation for stochastic momentum cooling as derived with the statistical concept of sampling by D. Möhl [1, 2, 3].

Cooling is described by the first term in the curly bracket of eq. (2.198). It is proportional to the gain g . The second term is proportional to g^2 and results in heating by Schottky noise of the beam. The mixing factor increases the heating term if mixing is incomplete, $M > 1$. In section 2.4.2.1 it was outlined that $M > 1$ implies that the Schottky density is large and therefore an intensified heating by particle noise occurs.

Optimal cooling without target is achieved in eq. (2.198) if $g = 1/M$. The necessary electronic gain G_A follows from eq. (2.199). The optimal cooling rate is then

$$\frac{I}{\tau} = \frac{I}{\delta_{rms}^2} \frac{d\delta_{rms}^2}{dt} = -2 \frac{W}{N} \frac{I}{M} \quad (2.201)$$

The equation again shows that a large bandwidth is required for fast cooling. The cooling rate decreases with an increasing particle number. Good mixing is requested. However as stated previously a compromise in mixing must be made for the filter momentum cooling technique. From eq. (2.199) we conclude that the pickup and kicker shunt impedances Z_p , Z_k should be large so that the electronic gain attains practical values, i.e., that the electronic power can be kept on a moderate level. The equation demonstrates that the electronic gain G_A must be decreased if the particle number N increases and the optimal cooling rate, eq. (2.201) should be attained.

Note that the optimal cooling rate does not depend on the ion specie if the thermal noise is negligible. It is only proportional to the bandwidth W and inversely proportional to the particle number N as well as the mixing factor M .

By setting $d\delta_{rms}/dt$ equal to zero in eq. (2.198) and taking into account that the mixing factor, eq. (2.200), depends on the relative momentum spread we find a quadratic equation for the equilibrium value in cooling with internal target. The solution is

$$\delta_{eq}(x) = \frac{x}{4} \pm \frac{I}{2} \sqrt{\left(\frac{x}{2}\right)^2 + \frac{a}{x}} \quad (2.202)$$

with the abbreviations $x = g \cdot f_0 / (2\sqrt{2\pi}|\eta|f_c)$ and $a = N f_0 D_T / (\sqrt{2\pi}|\eta|f_c W (\beta^2 E)^2)$.

The result thus depends on the cooling gain through x and the minimum equilibrium value is found by solving $d\delta_{eq}/dx$ for x . Only the positive sign in eq. (2.202) leads to a real and positive value of the equilibrium momentum spread. The optimal gain yielding the minimum equilibrium value is then given by $x_{opt} = (a/2)^{1/3}$. Inserting x_{opt} into eq. (2.202) gives

$$\delta_{eq} = \left(\frac{N}{2\sqrt{2\pi} |\eta| W f_c} \frac{f_0}{(\beta^2 E)^2} \frac{D_T}{f_c} \right)^{1/3} \quad (2.203)$$

for the smallest relative momentum spread of the beam including the beam-target interaction if it is assumed that the mean energy loss is compensated.

The necessary optimal electronic gain is deduced from eq. (2.199)

$$G_A = \frac{4}{\sqrt{2\pi}} \frac{A \beta^2 E}{N(Ze)^2 f_0 \sqrt{Z_p Z_K}} \delta_{eq} \quad (2.204)$$

with δ_{eq} given in eq. (2.203).

Eq. (2.203) shows that a large frequency slip factor is favored if the equilibrium momentum spread should be small. However, as already pointed out, a compromise has to be chosen if filter cooling should be practical. The bandwidth and center frequency should be large to achieve a small equilibrium value. Again, practical values are restricted due to mixing from pickup to kicker which is neglected in the linear approach of the drift term eq. (2.192).

As an example we consider an antiproton beam in the HESR at 3 GeV kinetic energy with $N = 10^{10}$ particles. We use the standard lattice with $\gamma_r = 6.23$. The kinematic values are $\beta = 0.971$, $\gamma = 4.197$, and the revolution frequency is $f_0 = 506 \text{ kHz}$. The ring frequency slip factor at this energy is $\eta = 0.03$. The stochastic cooling system has the bandwidth $W = 2 \text{ GHz}$ and the center frequency $f_c = 3 \text{ GHz}$. From Table 2.1 the pickup and kicker shunt impedances of the HESR cooling system are $Z_p = 1152 \Omega$ and $Z_K = 2304 \Omega$, respectively. A hydrogen target with thickness $N_T = 4 \cdot 10^{15} \text{ cm}^{-2}$ yields the diffusion term $D_T = 1.4 \cdot 10^9 (\text{eV})^2/\text{s}$ (see chapter 4).

Inserting these values into eq. (2.203) we expect for the relative rms momentum spread in equilibrium $\delta_{eq} \approx 8 \cdot 10^{-5}$. The necessary electronic voltage gain then follows from eq. (2.204) which yields $G_A = 3.7 \cdot 10^5$ or in the technical log-scale $G_A = 20 \log(3.7 \cdot 10^5) = 111 \text{ dB}$. The prediction agrees quite well with the result found by a numerically solution of the FPE presented in the next chapter.

The result represents a first order estimate of the equilibrium energy or momentum spread that can be reached if we assume a compensation of the mean energy loss. The formula (2.204) offers a recommendation for the necessary electronic gain. However it should be clearly stated that a full description, describing the time evolution of the beam distribution, can

only be found by solving the Fokker-Planck equation including the beam-target interaction or by particle tracking simulations including the synchrotron motion if e.g. a barrier bucket cavity is applied to compensate the mean energy loss due to the beam-target interaction.

2.12 Example Antiproton Cooling in the HESR

In this chapter we present an example and illustrate the difference in the cooling acceptance of the TOF and filter cooling method by means of a numerical solution of the FPE for momentum cooling formalism as outlined above. The simulation predicts the cooling properties of a 3 GeV antiproton beam with the $(2 - 4)\text{ GHz}$ cooling system in the HESR. The pickup and kicker shunt impedances are listed in Table 2.1. The frequency slip factor of the standard lattice with $\gamma_{tr} = 6.23$ is $\eta = 0.03$. Figure 2.21 depicts the 3D time development of the beam momentum distribution in filter momentum cooling of 10^{10} antiprotons with an internal hydrogen target with thickness $N_T = 4 \cdot 10^{15}\text{ cm}^{-2}$. It is assumed that the mean energy loss due to the target is compensated. The beam with an initial relative momentum spread $\delta_{rms} = 5 \cdot 10^{-4}$ is cooled to an equilibrium value with target operation. The equilibrium relative momentum spread $\delta_{rms} = 8 \cdot 10^{-5}$ is attained in approximately 200 s . The proposed momentum cooling system therefore fulfils the condition of the high resolution mode of the HESR where a momentum resolution in the order of $\delta_{rms} \approx 5 \cdot 10^{-5}$ is required in the PANDA internal target experiment.

The electronic gain is 110 dB . The thermal noise power is 0.1 W and the Schottky particle power is 5 W for filter cooling according to eqs. (2.106) and (2.107). Due to the statistical nature of the cooling signals a saturation of the amplifier may occur which effectively result in an additional beam heating. This is avoided if the installed electronic power includes a safety factor in the order of ten. The installed power should then be 50 W . This value does not exceed the envisaged RF power of 500 W .

The beam feedback effects are included in this simulation.

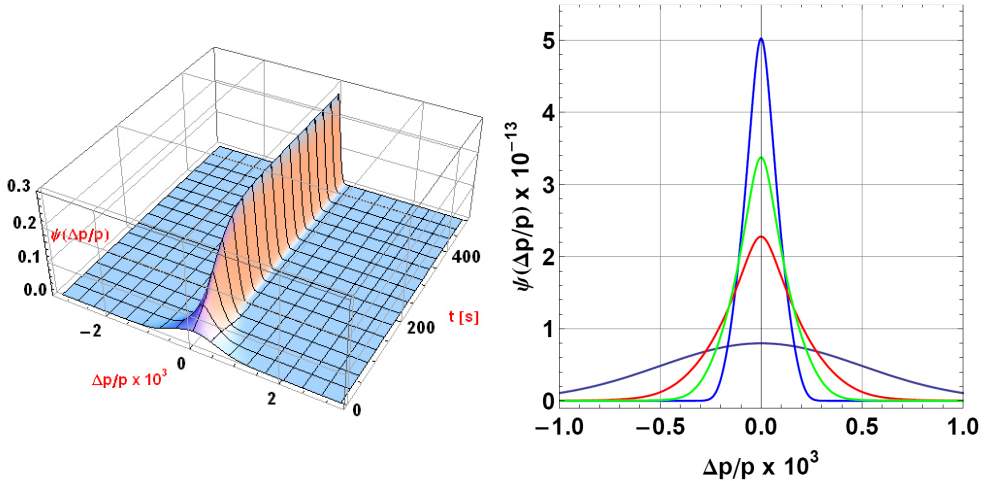


Figure 2.21: Time evolution of the momentum distribution in filter cooling of a 3 GeV antiproton beam in the HESR with hydrogen target operation. The right figure shows the momentum distribution normalized to one at time 0 s (black), 80 s (red), 100 s (green) and in equilibrium at 500 s (blue). In 200 s the antiproton beam attains an equilibrium with $\delta_{rms} = 8 \cdot 10^{-5}$.

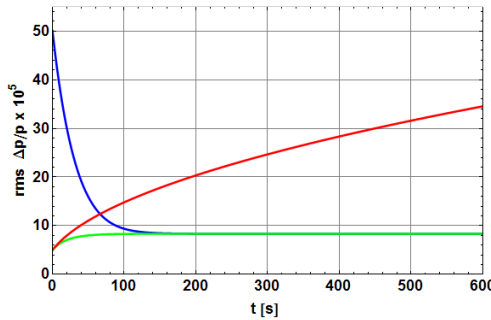


Figure 2.22: Time evolution of the rms relative momentum spread in filter cooling of a 3 GeV antiproton beam in the HESR with hydrogen target operation. In 200 s the beam attains an equilibrium with $\delta_{rms} = 8 \cdot 10^{-5}$. The figure shows that the equilibrium value is independent from the initial value (blue and green curve). The beam momentum spread increases due to the beam-target interaction (red curve) if cooling is off.

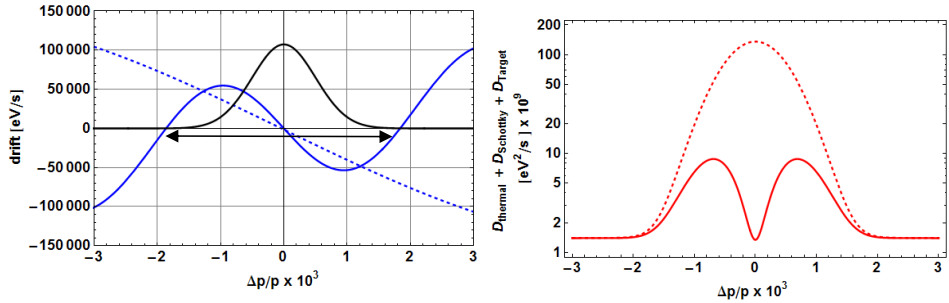


Figure 2.23: The left figure shows the drift (cooling) term for TOF (dotted) and filter cooling. The right figure displays the diffusion contributions due to thermal noise, Schottky particle noise and beam-target interaction. Thermal and Schottky noise contributions are suppressed in the center of the distribution due to the notch filter in the signal path. The electronic gain is 110 dB. The cooling acceptance $\pm 1.8 \cdot 10^{-3}$ for filter cooling is indicated as an arrow. The larger cooling acceptance for TOF cooling is visible. The initial momentum distribution with $\delta_{rms} = 5 \cdot 10^{-4}$ is drawn in black.

The time evolution of the relative momentum spread is shown in Figure 2.22 for filter cooling. The figure shows that the equilibrium value is independent from the initial value (blue and green curve). If cooling is switched off the beam momentum spread increases due to the beam-target interaction (red curve).

The cooling force is displayed in Figure 2.23 for TOF and filter cooling.

The non-linear behaviour is apparent for filter cooling, see chapter 2.6. The drift term becomes zero at $\pm 1.8 \cdot 10^{-3}$. Beyond these limits, the system changes from cooling to heating. For comparison the initial beam distribution is drawn. It just fits into the acceptance limit of the filter cooling system. The cooling acceptance $\pm 1.8 \cdot 10^{-3}$ is indicated as arrow for filter cooling.

The larger cooling acceptance for TOF cooling is clearly visible in Figure 2.23. It is seen that the momentum range where the cooling force is nearly linear, i.e. where eq. (2.111) is a good approximation of the drift term, is much larger. The same electronic gain 110 dB is used. It is also observed that as compared with filter cooling the diffusion is not suppressed in

the center of the beam distribution. The Schottky noise power and thermal noise power according to eqs. (2.114) and (2.115) amounts here 60 W and 0.2 W, respectively. The necessary RF power is about 600 W. Furthermore the beam equilibrium would be larger. The circumstance that thermal noise and Schottky noise are not suppressed leads to a longer cooling time and a larger equilibrium value for the momentum spread. TOF cooling thus does not fulfill the experimental request for a low momentum spread.

Figure 2.24 shows the open loop gain at the end of filter cooling. The cooling loop is stable as is visible in the Nyquist diagram.

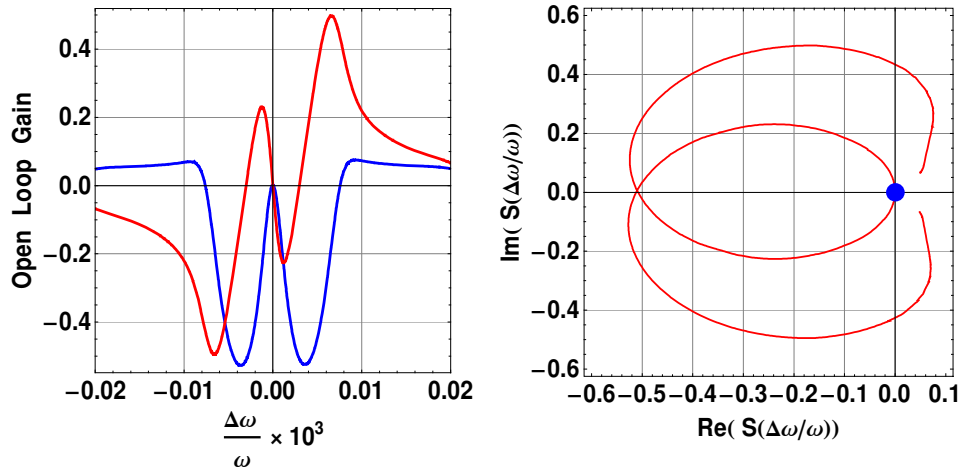


Figure 2.24: The left figure shows the open loop gain S for the filter method (real part blue, imaginary part red) at the end of cooling. The right figure displays the Nyquist stability diagram. The cooling loop is stable.

The signal suppression at the end of cooling is depicted in Figure 2.25.

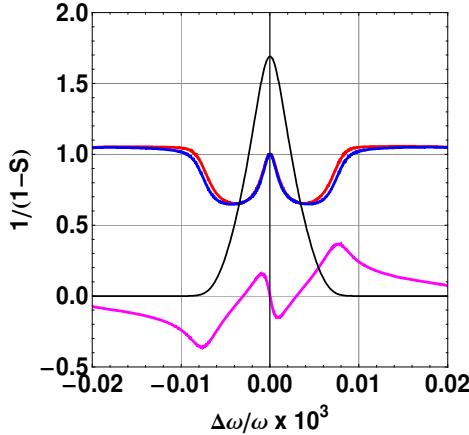


Figure 2.25: Signal suppression at the end of filter cooling at the center of the cooling bandwidth. Real part blue, imaginary part magenta, magnitude red. The signal suppression is almost real. The beam frequency distribution at the end of cooling is shown in black.

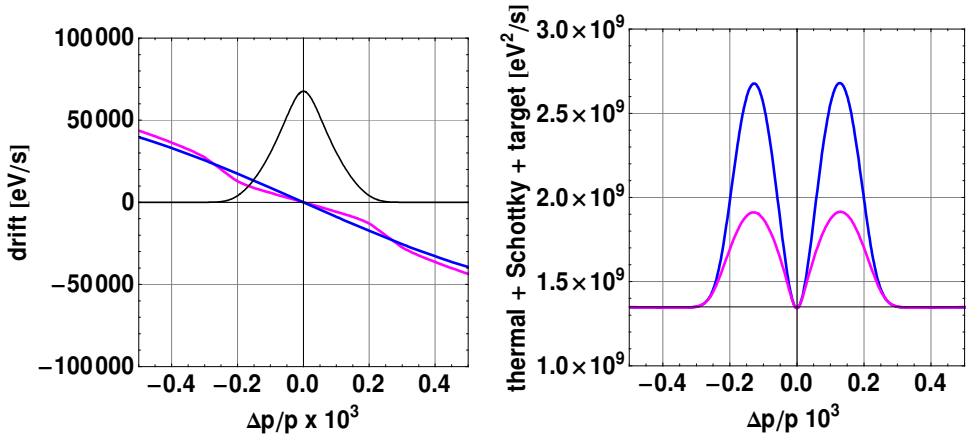


Figure 2.26: Left figure: The drift term neglecting feedback via the beam (blue) and including feedback (magenta) at the end of filter cooling. The drift term is almost not altered when beam feedback is included. Right figure: Including signal suppression the diffusion due to thermal and Schottky noise becomes reduced.

In Figure 2.26 one observes that beam feedback does not alter the drift term significantly. It has therefore been neglected in the cooling simulations. Including beam feedback affects cooling benefits from a reduced diffusion due to thermal and Schottky noise.

3 Stochastic Betatron Cooling

In this section we consider transverse stochastic cooling. The aim of transverse cooling is not only to reduce the beam size but also to reduce the angle deviation of the beam particles. Thus the aim of transverse cooling is to reduce the phase space which is occupied by the beam particles. We assume that the reader is already familiar with the basic concepts of stochastic cooling [1, 2, 3] so that an introduction to transverse cooling and a description of betatron motion of particles in circular accelerator is omitted here.

The outline presented here is essentially that as elucidated in detail in [35]. However, the description given here follows the same concept of ensemble averaging as applied in section 2.4 for momentum cooling. Similarly, the mathematics of random signals and Fourier transforms is adopted. Beam spectra are derived from autocorrelation functions [31]. The derivation of the cooling formula contains the pickup and kicker transfer function for the HESR. The pickup and kicker are now operated in difference mode. For transverse cooling the pickup senses the beam dipole moment which is the product of beam current times beam position at the pickup.

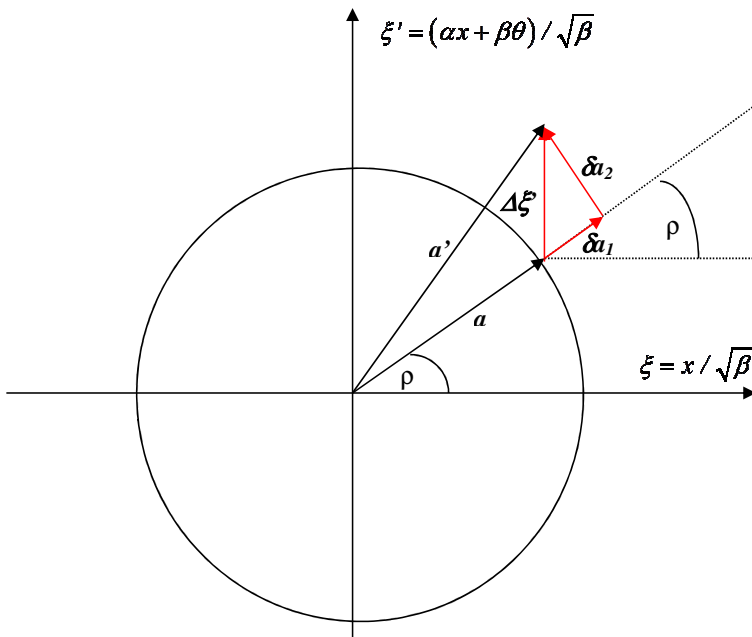


Figure 3.1: Normalized phase space at the kicker [35]. The quantities are explained in the text.

Operated in difference mode the kicker now can exert transverse deflections to a beam particle to correct its position error measured at the pickup.

The presented theory explicitly includes beam feedback via the beam.

We consider the particle betatron motion in normalized phase space as depicted in Figure 3.1 and discuss the impact of a transverse deflection given to a particle on the beam emittance.

The *emittance* ε of the beam is given by

$$\varepsilon = a^2 = (\xi')^2 + \xi^2 = \left(\frac{\alpha x + \beta \theta}{\sqrt{\beta}} \right)^2 + \left(\frac{x}{\sqrt{\beta}} \right)^2 \quad (3.1)$$

and the *phase space area* is

$$F = \pi \varepsilon. \quad (3.2)$$

The unit of the emittance is *mm mrad* and that of the phase space area is $\pi \text{ mm mrad}$. The usual TWISS parameters are α and β at the kicker location. Position and angle in unnormalized phase space are given by x and θ , respectively.

If a kick $\Delta\theta$ applied to a particle at the kicker does not alter the position of the particle then the change of ξ' in normalized phase space is given by

$$\Delta\xi' = \sqrt{\beta} \Delta\theta \quad (3.3)$$

The kick $\Delta\xi'$ is the sum of the component along the vector a , δa_1 , which follows from the geometry in the Figure 3.1 and is given by

$$\delta a_1 = -\Delta\xi' \cdot \sin \rho \quad (3.4)$$

and the component perpendicular to the vector a , δa_2 , is

$$\delta a_2 = \Delta\xi' \cdot \cos \rho \quad (3.5)$$

After the kick the betatron amplitude has changed from a to a' .

The *emittance change* $\Delta\epsilon = \epsilon(\theta + \Delta\theta) - \epsilon(\theta)$ becomes up to second order

$$\Delta\epsilon = 2\sqrt{\beta}\sqrt{\epsilon} \cdot \sin\rho \cdot \Delta\theta + \beta(\Delta\theta)^2 \quad (3.6)$$

or using eqs. (3.4) and (3.5)

$$\Delta\epsilon = 2\sqrt{\beta}\sqrt{\epsilon} \cdot \sin\rho \cdot \Delta\theta + \beta(\Delta\theta \sin\rho)^2 + \beta(\Delta\theta \cos\rho)^2 \quad (3.7)$$

If $\Theta(t)$ denotes the particle's azimuth in the ring at time t , then

$$\Theta(t) = \omega t + \Theta_0 \quad (3.8)$$

where $\omega = 2\pi/T$ with the revolution period T . The distribution of the initial phase Θ_0 is uniform in $[0, 2\pi]$ for the DC beam.

Let Θ_p the location of the pickup and Θ_K the distance between pickup and kicker.

A particle is at the kicker if

$$\Theta(t) = \omega t + \Theta_0 = \Theta_p + \Theta_K + 2\pi n, \quad n \in \mathbb{Z} \quad (3.9)$$

Then

$$t = t_p + t_K + nT \quad (3.10)$$

with $t_p = \frac{\Theta_p}{\omega} - \frac{\Theta_0}{\omega}$ the time of the particle at the pickup and $t_K = \frac{\Theta_K}{\omega}$ the particle travelling time from pickup to kicker.

At time t the betatron phase ρ (see Figure 3.1) is given by

$$\rho(t) = \omega Q \cdot (t - t_K) + \mu + \phi \quad (3.11)$$

where Q is the particle's tune, μ the betatron phase advance from pickup to kicker and $\phi \in [0, 2\pi]$ is a uniformly distributed random phase. The particle travelling time from pickup to kicker is t_K . The angular frequency of the betatron motion is ωQ .

A particle that starts at time t_p at the pickup arrives at the kicker at the time $t = t_p + t_k$. The betatron phase at the kicker is then $\rho(t_p + t_k) = \omega Q \cdot t_p + \phi + \mu$. That is, the betatron phase at the kicker is just the betatron phase at the pickup plus the phase advance μ from pickup to kicker.

3.1 Coherent Emittance Change

The kicker signals at the kicker are sampled by the particles once per turn. The emittance change per time at the kicker for a given *test particle* j is then with eq. (3.6)

$$\begin{aligned} \frac{\Delta\epsilon_j}{\Delta t} &= 2\sqrt{\epsilon_j}\sqrt{\beta_k} \sin(Q_j\omega_j(t - t_k^j) + \mu + \phi_0^j) \cdot \Delta\theta(t) \\ &\quad \cdot \omega_j \sum_{n=-\infty}^{\infty} \delta(\Theta_j(t) - \Theta_p - \Theta_k - 2\pi n) \end{aligned} \quad (3.12)$$

where the second order kick contribution in eq. (3.6) can be neglected.

Equivalently the emittance change per time can be written as

$$\begin{aligned} \frac{\Delta\epsilon_j}{\Delta t} &= 2\sqrt{\epsilon_j}\sqrt{\beta_k} \sin(Q_j\omega_j(t - t_k^j) + \mu + \phi_0^j) \cdot \Delta\theta(t) \\ &\quad \cdot \frac{\omega_j}{2\pi} \sum_{n=-\infty}^{\infty} e^{in\omega_j(t - t_p^j - t_k^j)} \end{aligned} \quad (3.13)$$

when the periodic delta functions in eq. (3.12) is expanded into a Fourier series.

The deflection $\Delta\theta(t)$ the test particle receives at the kicker is derived from the beam dipole moment $d(t)$ made up by all beam particles which is measured with the pickup in difference mode. It is given by the convolution of the system response function $\Delta\theta(t) = \int T(t - \tau)d(\tau)d\tau$ or equivalently in frequency domain $\Delta\theta(\omega) = T(\omega)d(\omega)$ where $T(\omega)$ is the electronic transfer function from pickup to kicker. Similar to longitudinal cooling it contains the pickup and kicker transfer function as well as the electronic gain. It is again assumed that the amplifier response is limited to the finite bandwidth of the cooling system.

In chapter 3.7 it will be shown that the deflection can be written as

$$\Delta\theta = \frac{\Delta p_\perp}{p} = K_\perp \frac{ZeU_k}{\beta pc} \quad (3.14)$$

where the dimensionless quantity $K_{\perp}(\omega)$ is the kicker sensitivity and $U_K(\omega)$ is the kicker input voltage. If $G_A(\omega)$ denotes voltage gain of the cooling system (possible filters, etc. are included) and $Z'_{PL}(\omega)$ denotes the position sensitive pickup coupling impedance (unit Ω/m) then

$$\Delta\theta(\omega) = \frac{Ze}{\beta pc} K_{\perp}(\omega) G_A(\omega) Z'_{PL}(\omega) \cdot d(\omega). \quad (3.15)$$

The *cooling system transfer function* is thus given by

$$T(\omega) = \frac{Ze}{\beta pc} K_{\perp}(\omega) G_A(\omega) Z'_{PL}(\omega). \quad (3.16)$$

A description of the pickup and kicker transfer functions is outlined in section 3.7.

The dipole moment of particle r at the pickup is

$$d_r^P(t) = x_r^P(t) \cdot i_r^P(t) \quad (3.17)$$

with the betatron motion $x_r^P(t) = \sqrt{\epsilon_r} \sqrt{\beta_p} \cos(\omega_r Q_r t + \phi_0^r)$ and $i_r^P(t) = \frac{Ze\omega_r}{2\pi} \sum_{n=-\infty}^{\infty} e^{in\omega_r(t-t_p^r)}$ the beam current of particle r with charge Ze at the pickup.

The dipole moment of N beam particles is then the sum over all beam particles

$$d(t) = \sum_{r=1}^N d_r^P(t). \quad (3.18)$$

The Fourier Transform of the particle's dipole moment yields the frequency content of the transverse betatron motion as measured with a spectrum analyser

$$d_r^P(\omega) = \frac{\sqrt{\epsilon_r} \sqrt{\beta_p}}{2} Ze\omega_r \cdot \sum_{k=-\infty}^{\infty} \left\{ \delta((k+Q_r)\omega_r - \omega) e^{i\phi_0^r} + \delta((k-Q_r)\omega_r - \omega) e^{-i\phi_0^r} \right\} e^{-ik\chi_0^r}. \quad (3.19)$$

The appearance of the delta function is the result of sampling the betatron motion with a pickup once per turn. Only the betatron sideband frequencies $(k \pm Q_r)\omega_r$ occur in the spectrum. Note that the magnitude of the Fourier transform possesses the symmetry

$|d_r^P(\omega)| = |d_r^P(-\omega)|$ since the particle dipole moment, eq. (3.17), is a real valued signal. The Fourier transform of the beam's dipole moment is a random quantity due to the random phases $\chi_0^r = \omega_r t_p^r = \Theta_p - \Theta_0^r$ and ϕ_0^r (see eq. (3.10)). The random nature of the Fourier transform of the particle's dipole moment leads to the transverse power spectrum of the beam. We present the detailed derivation later in section 3.4.

The kick function $\Delta\theta(t)$ in time domain is determined with the inverse Fourier transform

$$\Delta\theta(t) = \frac{1}{2\pi} \int T(\omega) d(\omega) e^{i\omega t} d\omega = \frac{1}{2\pi} \sum_{r=1}^N \int T(\omega) d_r^P(\omega) e^{i\omega t} d\omega \quad (3.20)$$

resulting in

$$\begin{aligned} \Delta\theta(t) &= \frac{1}{2\pi} \frac{\sqrt{\beta_p}}{2} (Ze) \sum_{r=1}^N \sqrt{\varepsilon_r} \omega_r \\ &\cdot \sum_{k=-\infty}^{\infty} \left\{ T((k+Q_r)\omega_r) e^{i\phi_r^r} e^{i(k+Q_r)\omega_r t} + T((k-Q_r)\omega_r) e^{-i\phi_r^r} e^{i(k-Q_r)\omega_r t} \right\} e^{-ik\chi_0^r}. \end{aligned} \quad (3.21)$$

The deflection $\Delta\theta(t)$ is inserted into eq. (3.13) to calculate the *emittance change of particle j per time*. It is visible that all particles contribute to the deflection with different random phases. A useful quantity to describe cooling is thus found by averaging over all random phases in eq. (3.13). One finds with similar arguments as used in section 2.4 for momentum cooling that in the sum in eq. (3.21) over the particle number none of the particles contribute except the particle $r = j$. The double sum in n and k which appears in eq. (3.13) when eq. (3.21) is inserted collapses into one sum with the same arguments as used in section 2.4. The average emittance change for particle j is therefore the sum over all betatron sideband frequencies $(k \pm Q_j)\omega_j$ of the considered test particle j itself. In other words, the average emittance change per time of particle j is due to its own position error at the pickup. Including the property $T^*(\omega) = T(-\omega)$ of the transfer function results in

$$\left\langle \frac{\Delta\varepsilon_j(t)}{\Delta t} \right\rangle = \varepsilon_j \sqrt{\beta_p \beta_k} (Ze) \left(\frac{\omega_j}{2\pi} \right)^2 \sum_{n=-\infty}^{\infty} 2 \operatorname{Re} \left\{ e^{i[(n+Q_j)\omega_j t + \frac{\pi}{2} - \mu]} T((n+Q_j)\omega_j) \right\}. \quad (3.22)$$

Each betatron sideband of particle j in the cooling bandwidth contributes to cooling. As will be outlined below each harmonic can be adjusted to yield optimal cooling. Observe that the emittance change per time for the test particle j depends on the phase advance μ as well as the particle travelling time t_K^j from pickup to kicker. If both are properly adjusted the emittance of the test particles is reduced with time. Before treating eq. (3.22) in detail the competing incoherent contribution to the emittance change is investigated.

3.2 Incoherent Emittance Change

The random kicks at the kicker derived from the beam particles at the pickup have the statistical properties of zero mean

$$\langle \Delta\theta(t) \rangle = 0 \quad (3.23)$$

since the beam dipole moment has zero mean if the beam is centered at the pickup. Consequently the average change in emittance due to random deflections at the kicker follows from eq. (3.7)

$$\langle \Delta\epsilon \rangle = \left\langle \beta (\Delta\theta \sin \rho)^2 \right\rangle + \left\langle \beta (\Delta\theta \cos \rho)^2 \right\rangle = \left\langle (\delta a_1)^2 \right\rangle + \left\langle (\delta a_2)^2 \right\rangle \quad (3.24)$$

as the sum of the averages of the squared random and uncorrelated components δa_1 and δa_2 .

The random noise source $\Delta\theta(t)$ is a continuous time signal at the kicker. It is sampled by the particles once per revolution when they pass the kicker. Therefore the effect of sampling in the calculation of the incoherent emittance change has to be included. First the time continuous process is treated and subsequently the sampled version is derived.

First the autocorrelation function of the two independent time continuous random components

$$\delta a_1(t) = -\sqrt{\beta_K} \sin(Q_j \omega_j(t - t_K^j) + \mu + \phi_0^j) \cdot \Delta\theta(t) \quad (3.25)$$

and

$$\delta a_2(t) = \sqrt{\beta_K} \cos(Q_j \omega_j(t - t_K^j) + \mu + \phi_0^j) \cdot \Delta\theta(t) \quad (3.26)$$

are considered. Writing $\delta a_i(t)$ as

$$\delta a_i(t) = \frac{\sqrt{\beta_K}}{2i} \left(e^{i(\xi_j(t) + \phi_0^j)} - e^{-i(\xi_j(t) + \phi_0^j)} \right) \Delta\theta(t) \quad (3.27)$$

with the phase $\xi_j(t) = Q_j \omega_j(t - t_K^j) + \mu$ yields the product

$$\begin{aligned} \delta a_i(t) \cdot \delta a_i^*(t + \tau) = \\ \frac{\beta_K}{4} \left\{ e^{iQ_j \omega_j \tau} + e^{-iQ_j \omega_j \tau} - e^{-i(\xi_j(t) + \xi_j(t + \tau))} e^{-i2\phi_0^j} - e^{i(\xi_j(t) + \xi_j(t + \tau))} e^{i2\phi_0^j} \right\} \cdot \Delta\theta(t) \cdot \Delta\theta^*(t + \tau). \end{aligned}$$

Averaging both sides yields the autocorrelation function [31]

$$R_{\delta a_i}(\tau) = \langle \delta a_i(t) \cdot \delta a_i^*(t + \tau) \rangle = \frac{\beta_K}{2} \cos(Q_j \omega_j \tau) \cdot R_{\Delta\theta}(\tau) \quad (3.28)$$

for the random variable δa_i determined by the autocorrelation function of the random deflecting kicks $R_{\Delta\theta}(\tau) = \langle \Delta\theta(t) \cdot \Delta\theta^*(t + \tau) \rangle$.

Similarly one finds the autocorrelation function for the random component $\delta a_2(t)$

$$R_{\delta a_2}(\tau) = \frac{\beta_K}{2} \cos(Q_j \omega_j \tau) \cdot R_{\Delta\theta}(\tau). \quad (3.29)$$

The sum of both autocorrelation functions gives in the autocorrelation function of the sum $\delta a_i + \delta a_2$ of the two independent random variables which we call

$$R_{\sqrt{\Delta\epsilon}}(\tau) = \beta_K \cos(Q_j \omega_j \tau) \cdot R_{\Delta\theta}(\tau). \quad (3.30)$$

The *spectral density* is the Fourier transform of the autocorrelation function [31]

$$S_{\sqrt{\Delta\epsilon}}(\omega) = \int R_{\sqrt{\Delta\epsilon}}(\tau) e^{-i\omega\tau} d\tau. \quad (3.31)$$

Since the signals are real they obey the symmetry relations

$$R_{\Delta\theta}(-\tau) = R_{\Delta\theta}(\tau) \quad \text{and} \quad S_{\Delta\theta}(-\omega) = S_{\Delta\theta}(\omega). \quad (3.32)$$

The spectral density of the autocorrelation function in eq. (3.30) can be written as

$$S_{\sqrt{\Delta\epsilon}}(\omega) = \frac{\beta_K}{2} \{ S_{\Delta\theta}(\omega - Q_j\omega_j) + S_{\Delta\theta}(\omega + Q_j\omega_j) \}. \quad (3.33)$$

It is now taken into account that the random signals $\sqrt{\Delta\epsilon}$ or $\Delta\theta$ are sampled by a particle at the kicker once per turn. The sequence of discrete kicks $\Delta\theta[n] = \Delta\theta(nT_j)$ where T_j is the revolution period of particle j can then be formed. The discrete autocorrelation is the sampled version $R_{\Delta\theta}[n] = R_{\Delta\theta}(nT_j)$ or $R_{\sqrt{\Delta\epsilon}}[n] = R_{\sqrt{\Delta\epsilon}}(nT_j)$. The appropriate spectral density [31] is therefore deduced from

$$S_{\sqrt{\Delta\epsilon_s}}(\omega) = \sum_{m=-\infty}^{\infty} R_{\sqrt{\Delta\epsilon_s}}[m] e^{-im\omega T_j} \quad (3.34)$$

with

$$R_{\sqrt{\Delta\epsilon_s}}[m] = \frac{I}{\omega_j} \int_{-\omega_j/2}^{\omega_j/2} S_{\sqrt{\Delta\epsilon_s}}(\omega) e^{im\omega T_j} d\omega. \quad (3.35)$$

The Poisson formula [31] is applied to show that the spectral density of the sampled process is determined from

$$S_{\sqrt{\Delta\epsilon_s}}(\omega) = \frac{\omega_j}{2\pi} \sum_{n=-\infty}^{\infty} S_{\sqrt{\Delta\epsilon}}(\omega + n\omega_j) \quad (3.36)$$

where $S_{\sqrt{\Delta\epsilon}}(\omega)$ is the power density of the continuous process given in eq. (3.33).

Hence, the power spectrum of the sampled process is the sum of $S_{\sqrt{\Delta\epsilon}}(\omega)$ and all its displacements with $n\omega_j$.

The incoherent emittance change per turn is now evaluated from the autocorrelation function $R_{\sqrt{\Delta\epsilon_s}}[\tau]$ at $\tau=0$. We apply the same steps as in chapter 2.4.2 and take into account eqs. (3.34), (3.35) and (3.36) to find the incoherent emittance change per turn

$$\langle \Delta\epsilon \rangle \approx \frac{\omega_j}{2\pi} \sum_{n=-\infty}^{\infty} S_{\sqrt{\Delta\epsilon}}(n\omega_j). \quad (3.37)$$

Observe that $R_{\sqrt{\Delta\epsilon}}(\tau)$ in eq. (3.30) has the unit $[R_{\sqrt{\Delta\epsilon}}(\tau)] = m$. The spectral density $S_{\sqrt{\Delta\epsilon}}(\omega)$ defined in eq. (3.31) has therefore the unit $[S_{\sqrt{\Delta\epsilon}}(\omega)] = m/\text{Hz}$ so that $[\langle \Delta\epsilon \rangle] = m$.

The final result for the incoherent emittance change is found if we employ the spectral density $S_{\sqrt{\Delta\epsilon}}(\omega)$ as given in eq. (3.33) in the eq. (3.37). The incoherent emittance change per turn

$$\begin{aligned}\langle \Delta\epsilon \rangle &= \frac{\beta_K}{2} \frac{\omega_j}{2\pi} \sum_{n=-\infty}^{\infty} \{ S_{\Delta\theta}((n - Q_j)\omega_j) + S_{\Delta\theta}((n + Q_j)\omega_j) \} \\ &= \beta_K \frac{\omega_j}{2\pi} \sum_{n=-\infty}^{\infty} S_{\Delta\theta}((n + Q_j)\omega_j)\end{aligned}\quad (3.38)$$

is a sum over all sideband frequencies. In the last step the relation given in eq. (3.32) has been applied.

Eq. (3.38) states the important conclusion that the beam responses only if the noise source $S_{\Delta\theta}$ contains the side band frequencies $(n + Q_j)\omega_j$ of the beam.

The spectral density $S_{\Delta\theta}(\omega)$ of the random variable $\Delta\theta$ is composed of the input particle noise (Schottky noise) to the cooling system and by thermal noise inherent in the cooling loop.

If $S_d(\omega)$ denotes the Schottky spectral density (Schottky dipole density, unit $(Am)^2/\text{Hz}$) at the pickup (see section 3.4) and $S_{th}(\omega)$ is the thermal noise density into the cooling chain it is convenient to de-compose the spectral noise density $S_{\Delta\theta}(\omega)$ of the random variable $\Delta\theta$ into two parts

$$S_{\Delta\theta}(\omega) = |T(\omega)|^2 S_d(\omega) + |H(\omega)|^2 Z_0 S_{th}(\omega) \quad (3.39)$$

where Z_0 is the characteristic line impedance and the system transfer function $T(\omega)$ introduced in eq. (3.16) is

$$T(\omega) = \frac{Ze}{\beta pc} K_{\perp}(\omega) G(\omega) Z'_{pl}(\omega) \quad (3.40)$$

and

$$H(\omega) = T(\omega) / Z'_{PL}(\omega) \quad (3.41)$$

similarly defined as in longitudinal cooling has been introduced. At the moment we omit details of its constituents which we will outline in chapter 3.7.

To further proceed in the evaluation of eq. (3.38) for the incoherent emittance change we introduce the *mixing factor* and the *noise-to-signal ratio*. An explicit discussion of these quantities is given in sections 3.4 and 3.5.

The ***mixing factor*** as a function of frequency is defined as

$$M(\Omega) = \frac{S_d(\Omega)}{S_0} = \frac{\text{Schottky dipole density}}{\text{average density per harmonic}}. \quad (3.42)$$

The ***noise-to-signal ratio*** is introduced by

$$U(\Omega) = \frac{S_n(\Omega)}{\left|Z'_{PL}(\Omega)\right|^2 / Z_0} = \frac{\text{Thermal noise power density}}{\text{Schottky power density at the PU output}}. \quad (3.43)$$

In both expressions the average Schottky noise density per harmonic S_0 derived in section 3.4

$$S_0 = \frac{N}{2} (Ze)^2 \frac{\omega_j}{2\pi} \epsilon \beta_p \approx \frac{N}{2} (Ze)^2 \frac{\omega_0}{2\pi} \epsilon \beta_p \quad (3.44)$$

enters.

Rearranging eq. (3.38) with eq. (3.39) and inserting the mixing factor as well as the noise-to-signal ratio finally yields the *incoherent emittance change per second*

$$\frac{\langle \Delta\epsilon \rangle}{\Delta t} = \frac{\epsilon}{2N} \frac{\omega_j}{2\pi} \sum_{n=-\infty}^{\infty} |g((n+Q_j)\omega_j)|^2 \{M((n+Q_j)\omega_j) + U((n+Q_j)\omega_j)\}. \quad (3.45)$$

as a sum over the mixing factor and noise-to-signal ratio at each betatron sideband in the cooling bandwidth. The dimensionless gain function $g(\Omega)$ has been defined as

$$g(\Omega) = N(Ze) \frac{\omega_j}{2\pi} \sqrt{\beta_p \beta_K} \cdot T(\Omega). \quad (3.46)$$

In section 3.4 the Schottky noise density is derived and discussed in detail. It will be shown that in the case of overlapping sidebands many harmonics can contribute at a given frequency $(n+Q_j)\omega_j$. Consequently the mixing factor at frequency $(n+Q_j)\omega_j$ in eq. (3.45) itself can be a sum over many harmonics. This will be outlined in section 3.5.

3.3 Emittance Cooling Rate Equation

Introducing the dimensionless gain also in the expression for the coherent emittance change according to eq. (3.22) finally yields the well-known

Emittance Cooling Rate equation

$$\frac{1}{\varepsilon_j} \frac{d\varepsilon_j}{dt} = \frac{1}{2N} \frac{\omega_j}{2\pi} \left\{ \sum_{n=-\infty}^{\infty} 2 \operatorname{Re} \left[e^{i[(n+Q_j)\omega_j t_k^j + \frac{\pi}{2} - \mu]} g((n+Q_j)\omega_j) \right] \right. \\ \left. + \sum_{n=-\infty}^{\infty} |g((n+Q_j)\omega_j)|^2 \{M((n+Q_j)\omega_j) + U((n+Q_j)\omega_j)\} \right\}. \quad (3.47)$$

The sum appearing in the cooling rate actually runs over all harmonics in the finite cooling bandwidth. The rate equation involves two contributions. The first part in the curly brackets contributes to cooling if the amplifier gain as well as mixing from pickup to kicker and cooling system delay is properly adjusted. The second part being proportional to the amplifier gain squared always contributes to heating and is determined by the mixing factor as well as the noise to-signal ratio. A good signal-to-noise ratio ($U \ll 1$) as well as a mixing factor $M \approx 1$ is recommended if the heating contribution should be small.

Eq. (3.47) leads to the well-known cooling formula given in. To show this, assume that the gain is

$$g(\omega) = -(-1)^k |g(\omega)| e^{-i\omega t_d} \quad (3.48)$$

with the electronic delay t_d adjusted to the nominal particle transit time from pickup to kicker, $t_d = T_{PK}$. For an off-momentum particle the travelling time from pickup to kicker is

$t_K^j = T_{PK} + \Delta T_{PK}$ with $\Delta T_{PK} = -T_{PK} \eta_{PK} \frac{\Delta p}{p}$. If the betatron phase advance μ is an odd multiple

of a quarter betatron wave length, i.e., $\mu = (2k+1)\pi/2$, where k is a positive integer, the coherent term in eq. (3.47) becomes

$$\frac{I}{\varepsilon} \frac{d\varepsilon}{dt} = -\frac{I}{2N} \frac{\omega_0}{2\pi} \sum_{n=-\infty}^{\infty} 2 \cos((n+Q_0)\omega_0 \Delta T_{PK}) |g((n+Q_0)\omega_0)|$$

for particles in the center of the distribution, i.e. $\omega_j = \omega_0$.

If the time spread from pickup to kicker is very small, $\Delta T_{PK} \approx 0$, then $\cos((n+Q_0)\omega_0 \Delta T_{PK}) \approx 1$. The coherent term is then negative and cooling is achieved. The result shows that the gain depends on whether k is an even or odd integer. A 180 degree phase shifter is needed in the cooling chain to achieve cooling.

For large harmonic numbers $|g((n+Q_0)\omega_0)| \approx |g(n\omega_0)| =: g_n$ etc. the cooling rate equation and assuming the correct sign of the gain, eq. (3.47) reduces in the center of the distribution ($\omega_j = \omega_0 = 2\pi f_0$) to

$$\begin{aligned} \frac{I}{\varepsilon} \frac{d\varepsilon}{dt} &= -\frac{I}{2N} \frac{\omega_0}{2\pi} \sum_{n=-\infty}^{\infty} \left\{ 2g_n \cos(n\omega_0 \Delta T_{PK}) - g_n^2 (M_n + U_n) \right\} \\ &= -\frac{f_0}{N} \sum_{n=n_l}^{n_2} \left\{ 2g_n \cos(n\omega_0 \Delta T_{PK}) - g_n^2 (M_n + U_n) \right\} \end{aligned} \quad (3.49)$$

where the finite bandwidth is $W = (n_2 - n_l)f_0$ and the sum runs only over positive frequencies (giving a factor of two since $g_n = g_{-n}$ etc.).

Eq. (3.49) demonstrates that each harmonic in the cooling bandwidth contributes to cooling and that the cooling system can be optimized harmonic by harmonic.

For a constant gain $g = g_n$ the usual well known cooling formula [1, 3, 2] is found

$$\frac{I}{\varepsilon} \frac{d\varepsilon}{dt} = -\frac{W}{N} \left\{ 2gM^* - g^2(M + U) \right\} \quad (3.50)$$

where the *average mixing factor*

$$M = \frac{f_0}{W} \sum_{n=n_l}^{n_2} M_n \quad (3.51)$$

and the *average noise-to-signal ratio*

$$U = \frac{f_0}{W} \sum_{n=n_l}^{n_2} U_n \quad (3.52)$$

as well as *mixing from pickup to kicker*

$$M^* = \frac{f_0}{W} \sum_{n=n_l}^{n_2} \cos(n\omega_0 \Delta T_{PK}) \quad (3.53)$$

have been introduced.

M^* can be considered as the pickup signal, which is sent to the kicker, processed by the bandpass system, similarly as discussed in chapter 2.3.1, page 16. Eq. (3.53) shows that the nominal particle with $\Delta T_{PK} = 0$ receives the full correction at the kicker since $M^* = 1$. A particle passing the kicker too early ($\Delta T_{PK} < 0$) or too late ($\Delta T_{PK} > 0$) experiences an incomplete correction only, or will be even heated if M^* becomes negative. Thus mixing from pickup to kicker is bad and means *unwanted mixing*. An approximation of M^* is given by the parabola $M^* = 1 - \left(\frac{\Delta T_{PK}}{T_s/2} \right)^2$ when the time deviation of a particle is in the range of $|\Delta T_{PK}| \leq T_s/2$, where the sampling time is $T_s = 1/2W$. The quantity $M^+ = (T_s/2)/\Delta T_{PK}$ is the *mixing factor from pickup to kicker* introduced in [2].

In section 3.5 it is shown that if all sidebands overlap then $M_n = 1$ for all n and from eq. (3.51) it follows that the average mixing factor becomes $M = 1$.

If the phase error should be less than $\pm 60^\circ$ ($\cos(.) > 0.5$) in each term then $\omega_{max} T_{PK} |\eta_{PK}| |\delta_{max}| < \frac{1}{3}\pi$ and the upper frequency of the cooling system is limited to

$$f_{max} < \frac{1}{6T_{PK} |\eta_{PK}| |\delta_{max}|} \quad (3.54)$$

The cooling rate, eq. (3.49), can be maximized by optimizing the rate at each betatron harmonic. For $\Delta T_{PK} \ll T_{PK}$ the *optimum gain* for each betatron harmonic, which maximize the cooling rate, is

$$g_n^{opt} = \frac{I}{M_n + U_n} \quad (3.55)$$

Inserting this into eq. (3.49) yields the *optimal cooling rate*

$$\left(\frac{1}{\varepsilon} \frac{d\varepsilon}{dt} \right)_{opt} = -\frac{f_0}{N} \sum_{n=n_f}^{n_s} \frac{1}{M_n + U_n} \rightarrow -\frac{W}{N} \cdot \frac{1}{M + U} \quad (3.56)$$

Notice that the cooling rate is proportional to the bandwidth W and that it decreases with increasing particle number N . The optimal value is found if $M + U = 1$, i.e. the mixing factor should be $M = 1$ and no thermal noise, $U = 0$.

The rate equation (3.47) represents a first order differential equation for the beam emittance. The equation is solved to predict the time evolution of the emittance during cooling including the beam-target interaction which adds an additional emittance growth rate to the rate equation (3.47) as is outlined in chapter 4.

3.4 Schottky Noise Density

In chapter 3.1 the particle's transverse dipole moment in frequency domain was deduced

$$\hat{d}_r(\omega) = \frac{\sqrt{\epsilon_r} \sqrt{\beta_p}}{2} Z e \omega_r \cdot \sum_{k=-\infty}^{\infty} \left\{ \delta((k + Q_r) \omega_r - \omega) e^{i\phi_r^r} + \delta((k - Q_r) \omega_r - \omega) e^{-i\phi_r^r} \right\} e^{-ik\chi_r^r} \quad (3.57)$$

which when summed up for all beam particles N yields the total transverse dipole moment of the beam

$$\hat{d}(\omega) = \sum_{r=1}^N \hat{d}_r(\omega) \quad (3.58)$$

which is a random quantity where for each particle the phases ϕ_r^r and χ_r^r are uniformly distributed in $[0, 2\pi[$ for a DC beam. It is therefore not well defined. A well-defined quantity is the spectral density that can be measured with a spectrum analyzer.

We can find the spectral density by forming $\hat{d}(\omega) \cdot \hat{d}^*(\omega')$ using eq. (3.57) and (3.58). As outlined in Appendix A the autocorrelation function $\langle \hat{d}(\omega) \cdot \hat{d}^*(\omega') \rangle$ possesses the property

$\langle \hat{d}(\omega) \cdot \hat{d}^*(\omega') \rangle = 2\pi \delta(\omega - \omega') \cdot S(\omega)$ which allows us to derive the spectral density once the Fourier transform of the dipole moment is known.

Averaging over the phases and using the arguments as in chapter 2.4.2.1 we arrive at

$$\begin{aligned} \langle \hat{d}(\omega) \cdot \hat{d}^*(\omega') \rangle &= \sum_{r=1}^N \sum_{k=-\infty}^{\infty} \frac{\epsilon_r \beta_p}{4} (Ze)^2 \omega_r^2 \cdot \\ &\quad \{ \delta(\omega - (k + Q_r) \omega_r) \delta(\omega' - (k + Q_r) \omega_r) \\ &\quad + \delta(\omega - (k - Q_r) \omega_r) \delta(\omega' - (k - Q_r) \omega_r) \} \\ &= 2\pi \delta(\omega - \omega') \cdot S(\omega). \end{aligned} \quad (3.59)$$

Integrating both sides w.r.t. ω leads to the expression for the spectral density

$$S_d(\omega) = \frac{(Ze)^2}{4 \cdot 2\pi} \sum_{r=1}^N \sum_{k=-\infty}^{\infty} \sum_{\pm} \omega_r^2 (\epsilon_r \beta_p) \delta(\omega - (k \pm Q_r) \omega_r). \quad (3.60)$$

Since a large number N of particles with angular revolution frequencies $\omega_r > 0$ clustered around the central value ω_0 is involved, we can proceed further in replacing the sum over discrete frequencies and particle emittances ϵ_r in eq. (3.60) by an integral,

$$\sum_{r=1}^N g(\omega_r, \epsilon_r) \rightarrow \int_0^\infty \int_0^\infty g(\omega_r, \epsilon_r) \Psi_0(\omega_r) \rho(\epsilon_r) d\omega_r d\epsilon_r, \text{ where the angular frequency distribution}$$

Ψ_0 is normalized to the number of Ions in the beam, $\int_0^\infty \Psi_0(\omega) d\omega = N$ and

$$I/N \cdot \int_0^\infty \omega \Psi_0(\omega) d\omega = \omega_0.$$

Note the essential fact that per definition

$$\Psi_0(\omega) = 0 \quad \text{for } \omega < 0. \quad (3.61)$$

The angular frequencies and the particle emittances are assumed to be independently distributed. The density for the emittances is normalized such that $\int_0^\infty \rho(\epsilon_r) d\epsilon_r = 1$.

The spectral dipole beam density is then given by

$$S_d(\omega) = \frac{(Ze)^2 \epsilon \beta_p}{4 \cdot 2\pi} \sum_{k=-\infty}^{\infty} \sum_{\pm} \int_0^{\infty} Q^2 \Psi_o(Q) \delta(\omega - (k \pm Q)Q) dQ. \quad (3.62)$$

Evaluating the integral results in the final transverse spectral density of the DC-beam, called Schottky dipole density

$$S_d(\omega) = \frac{(Ze)^2 \epsilon \beta_p}{4 \cdot 2\pi} \sum_{k=-\infty}^{\infty} \sum_{\pm} \left(\frac{\omega}{k \pm Q} \right)^2 \Psi_o \left(\frac{\omega}{k \pm Q} \right) \frac{1}{|k \pm Q|} \quad (3.63)$$

as the sum over all sideband angular frequencies $(k \pm Q)\omega_0$. The spectral density of the beam has the unit $(Am)^2/Hz$. Note that the current density possesses the symmetry $S_d(\omega) = S_d(-\omega)$. This is guaranteed by the appearance of the sum over $(k \pm Q)\omega_0$. If the Schottky dipole density is evaluated according to eq. (3.63) one has to account for the fact that $\Psi_o(Q) = 0$ for $Q < 0$.

The Schottky dipole density is proportional to the beam emittance ϵ and the beta function β_p at the pickup. It increases with the number of particles in the ring. It is important to note that the dipole density is proportional to the charge of the circulating particles squared. This has a direct impact on the necessary electronic power that has to be installed for the cooling system as will be discussed below.

The spectral dipole density is measured with a pickup operated in difference mode. It has a position sensitive complex coupling impedance $Z'_{pl}(\omega)$ with the unit Q/m . The pickup output power density is then

$$S_p(\omega) = \frac{|Z'_{pl}(\omega)|^2}{Z_0} S_d(\omega) \quad (3.64)$$

where Z_0 is the characteristic line impedance usually 50Ω . By inspection of the units it is seen that the power density has the unit W/Hz .

From eq. (3.63) it follows that contribution of the $k \pm Q$ harmonic to the total spectral density at angular frequency ω is given by

$$S_d^\pm(\omega) = \frac{I}{4} \frac{(Ze)^2}{2\pi} \epsilon \beta_p \left(\frac{\omega}{k \pm Q} \right)^2 \frac{1}{|k \pm Q|} \Psi_o \left(\frac{\omega}{k \pm Q} \right) \quad (3.65)$$

It is determined by the beam frequency distribution $\Psi_o(\omega)$ with $\int_0^\infty \Psi_o(\omega) d\omega = N$. The shape of the sideband is thus predefined by the momentum distribution.

Eq. (3.63) represents the general expression for the Schottky dipole moment for negative and positive angular frequencies. The tune Q is decomposed in the sum of its integer part $\|Q\|$ and its fractional part q , $Q = \|Q\| + q$. Then, $k \pm Q = (k \pm \|Q\|) \pm q = n \pm q$.

In general the tune $Q(\delta)$ depends on the relative momentum spread δ in the beam. The resulting tune spread $\Delta Q = \Delta q = Q' \cdot \delta$ is determined by the machine chromaticity Q' . Together with the frequency spread $\Delta\omega = \eta\omega_0\delta$ the spread of the sideband frequencies becomes $\Delta\omega_\pm = \{(n \pm q)\eta \pm Q'\}\omega_0\delta$, see appendix D. Since the stochastic cooling system is operated at high harmonic numbers one can however neglect chromatic effects to first order and assume in the following that the sideband frequency spread is determined solely by the spread in revolution frequencies $\Delta\omega = \eta\omega_0\delta$. An extension that includes chromaticity in the description of the transverse dipole density of the DC-beam is outlined in the appendix D.

From eq. (3.63) one concludes that in the real positive frequencies domain, which is measured by a spectrum analyzer, the spectrum reads

$$S_d(\omega) = \left\{ \sum_{n=1}^{\infty} S_d^-(\omega, n) + \sum_{n=0}^{\infty} S_d^+(\omega, n) \right\} \quad (3.66)$$

with the *lower ($n - q$) sideband*

$$S_d^-(\omega, n) = \frac{(Ze)^2 \epsilon \beta_p}{2 \cdot 2\pi} \left(\frac{\omega}{n - q} \right)^2 \Psi_o \left(\frac{\omega}{n - q} \right) \frac{1}{|n - q|}, \quad n = 1, 2, 3, 4, \dots \quad (3.67)$$

and the *upper ($n + q$) betatron sideband*

$$S_d^+(\omega, n) = \frac{(Ze)^2 \epsilon \beta_p}{2 \cdot 2\pi} \left(\frac{\omega}{n + q} \right)^2 \Psi_o \left(\frac{\omega}{n + q} \right) \frac{1}{|n + q|}, \quad n = 0, 1, 2, 3, 4, \dots \quad (3.68)$$

Thus, in the real positive frequency domain to every revolution harmonic n two sidebands belong, the lower ($n - q$) and the upper ($n + q$) betatron sideband. The shape of the sideband distribution is determined by the frequency distribution $\Psi_0(\omega)$ or by the beam's momentum distribution.

If the single sidebands do not overlap only one harmonic contributes to the spectral density at frequency ω and the *Schottky power per betatron sideband* is deduced from

$$P_n^\pm = \frac{I}{2\pi} \int S_d^\pm(\omega, n) d\omega. \quad (3.69)$$

Inserting eq. (3.67) or (3.68) yields approximately

$$P_n^\pm \approx \frac{N}{2} \left(\frac{\omega_0}{2\pi} \right)^2 (Ze)^2 \epsilon \beta_p \quad (3.70)$$

which shows that the Schottky power per band is independent from the harmonic number.

The *Schottky power per harmonic* as measured with a spectrum analyzer is calculated from

$$P_n = P_n^- + P_n^+ = N \left(\frac{\omega_0}{2\pi} \right)^2 (Ze)^2 \epsilon \beta_p. \quad (3.71)$$

The *total transverse Schottky power* of the DC-beam in the cooling bandwidth W containing W/f_0 harmonics is consequently

$$P = \frac{W}{f_0} \cdot N \left(\frac{\omega_0}{2\pi} \right)^2 (Ze)^2 \epsilon \beta_p. \quad (3.72)$$

The *average Schottky power density* S_0 *per harmonic* appearing in the mixing factor eq. (3.42) and the noise-to-signal eq. (3.43) is with eq. (3.63) given by

$$\begin{aligned} S_0 &= \frac{I}{\omega_0} \int \{S_d^+(\Omega) + S_d^-(\Omega)\} d\Omega \\ &= \frac{N}{2} (Ze)^2 \left(\frac{\omega_0}{2\pi} \right) \epsilon \beta_p. \end{aligned} \quad (3.73)$$

The *total Schottky power* P_S delivered by the beam to the kicker entrance via the cooling chain follows from

$$P_S = \frac{I}{2\pi} \int |G_A(\omega) Z'_{PL}(\omega)|^2 \frac{S_d(\omega)}{Z_0} d\omega. \quad (3.74)$$

The integral runs actually only over the finite bandwidth W . Amplifier, filters etc. are included in $G_A(\omega)$.

The *total thermal noise power* at the kicker P_{th} entrance amounts

$$P_{th} = \frac{I}{2\pi} \int |G_A(\omega)|^2 S_{th} d\omega. \quad (3.75)$$

Approximate expressions for the power contributions are found if we assume a flat pickup and gain response $Z'_{PL} \approx Z'_{PL}(\omega_C)$, $G_A \approx G_A(\omega_C)$ where ω_C is the center angular frequency of the cooling system.

For the case that the sidebands do not overlap eq. (3.74) yields for the total transverse Schottky power in the cooling bandwidth W at the kicker entrance

$$P_S = N(Ze)^2 \frac{\omega_0}{2\pi} \frac{|Z'_{PL}|^2}{Z_0} |G_A|^2 \cdot W \cdot \epsilon \beta_p. \quad (3.76)$$

In designing a cooling system one has to determine the maximum electronic RF power which has to be installed for the cooling system. Eq. (3.76) tells that the Schottky particle output power at the kicker entrance is proportional to the particle number and the particle's charge squared. It is proportional to the amplifier gain squared and increases with bandwidth. It is largest at the beginning of cooling when the uncooled beam size at the pickup, $\sqrt{\epsilon \beta_p}$, is largest. In the estimation of the power consumption one has also to account for the total thermal noise power in the cooling bandwidth W which is according to eq. (3.75) given by

$$P_{th} = k(T_A + T_R) |G_A|^2 W. \quad (3.77)$$

The Boltzmann constant is $k = 1.38 \cdot 10^{-23} W/K$. The equivalent noise temperature of the amplifier is T_A and the noise temperature of the pickup is T_R . The thermal noise power is again proportional to the amplifier gain squared.

Thus the total power is the sum of both Schottky power and noise power. For the total power that has to be installed for transverse cooling (horizontal and vertical) a safety factor ≈ 5 has to be included due to the fact that noise signals are amplified and an overload of the amplifier, which would lead to an additional heating, has to be avoided.

An example shall illustrate the order of magnitude of the installed power. It is assumed that $N = 10^{10}$ antiprotons are stored in the HESR. With two tanks for the pickup, equipped with 64 ring slot coupler each, we achieve a coupling impedance of $Z'_{PL} \approx 5 k\Omega/m$ in the center of the cooling bandwidth (2 – 4) GHz, see Table 1.2 and Table 3.1 as well as details in chapter 3.7. The characteristic line impedance is $Z_0 = 50 \Omega$. The bandwidth is 2 GHz. A typical gain is 120 dB which corresponds to $G_A = 1 \cdot 10^6$. The revolution frequency at 3 GeV is $\omega_0/2\pi = 506 \text{ kHz}$. Take a betatron function at the pickup with $\beta_p = 10 m$. The total emittance is $\epsilon = 6 \cdot \epsilon_{rms} = 16 \text{ mm mrad}$. With these values the Schottky power e.g. for horizontal cooling, in the cooling bandwidth W amounts $P_s \approx 20 W$. The thermal noise power is with low noise amplifiers and cryogenically cooled pickup structures, $T_A + T_R \approx 40 K$, $P_{th} \approx 1 W$. Thus the total power is $P_{tot} \approx 21 W$. Including a safety factor 5 the power that has to be installed for one cooling plane amounts to $P_{installed} = 105 W$. In the HESR one kicker tank with 250 W per transverse plane is available.

Note that at the beginning of cooling the required power is largest and decreases when the emittance is reduced.

As was outlined at the end of the previous chapter 2.4.2.2, eq. (2.89), the necessary power can be distributed to different power amplifiers by grouping the ring slot couplers.

3.5 Mixing Factor and Noise-to-Signal Ratio

The definition of the *mixing factor* M is similar as for momentum cooling. We re-write eq. (3.63) equivalently as

$$S_d(\Omega) = \frac{N}{2} (Ze)^2 \epsilon \beta_p \frac{\omega_0}{2\pi} \cdot M(\Omega) \quad (3.78)$$

where the *mixing factor* $M(\Omega)$ is defined for positive and negative angular frequencies Ω as

$$M(\Omega) = \sum_{k=-\infty}^{\infty} \{M_k^-(\Omega) + M_k^+(\Omega)\} \quad (3.79)$$

with

$$M_k^\pm(\Omega) = \frac{1}{2\omega_0 N} \left(\frac{\Omega}{k \pm Q} \right)^2 \Psi_o \left(\frac{\Omega}{k \pm Q} \right) \frac{1}{|k \pm Q|}. \quad (3.80)$$

Or, using the fractional tune q

$$M_n^\pm(\Omega) = \frac{1}{2\omega_0 N} \left(\frac{\Omega}{n \pm q} \right)^2 \Psi_o \left(\frac{\Omega}{n \pm q} \right) \frac{1}{|n \pm q|}. \quad (3.81)$$

Eq. (3.78) is in agreement with the definition for the mixing factor, eq. (3.42), given in section 3.2. For well separated sidebands only one mixing factor $M_k^\pm(\Omega)$ contributes to the total mixing factor $M(\Omega)$. If the harmonic number becomes large so that $n > q$ the mixing factor

becomes at each harmonic $M_n^\pm(\Omega) = \frac{1}{\omega_0 N} \left(\frac{\Omega}{n} \right)^2 \Psi_o \left(\frac{\Omega}{n} \right) \frac{1}{|n|}$, i.e., the two adjacent sidebands

add up. The mixing factor is then the same as that for momentum cooling given by eq. (2.73), chapter 2.4.2.1.

For fully overlapping sidebands the mixing factor in eq. (3.79) becomes $M(\Omega) = 1$ independently from frequency as will be shown in an example below. Therefore $M_n = M((n+Q)\omega_j)) = 1$ for all harmonics n and the average mixing factor in eq. (3.51) equals one.

Similarly as for momentum cooling, we conclude from eq. (3.78) that the spectral beam dipole density (transverse Schottky noise density) equals white noise with the frequency independent density $\frac{N}{2}(Ze)^2\epsilon\beta_p\frac{\omega_0}{2\pi}$ if the mixing factor is $M = 1$. Performing the Fourier transform of the constant density one finds the autocorrelation function

$$R(\tau) = \frac{N}{2}(Ze)^2\epsilon\beta_p\frac{\omega_0}{2\pi} \cdot \frac{1}{2\pi} \int_{-\infty}^{\infty} e^{i\Omega\tau} d\Omega = \frac{N}{2}(Ze)^2\epsilon\beta_p\frac{\omega_0}{2\pi} \cdot \delta(\tau)$$

which states that the noise signal is completely uncorrelated, i.e., uncorrelated samples in the time domain description. In the frequency domain description a mixing factor $M > 1$ describes to what extent the Schottky particle dipole density is enhanced over the white noise density and thus contributes to a stronger incoherent emittance increase.

The one-to-one relation between spectral density (frequency domain) and autocorrelation function (time domain) allows the important and consistent interpretation of the mixing factor either in time domain, i.e. uncorrelated samples for best cooling if $M = 1$ or equivalently in the frequency domain description where the spectral beam density is then essentially white noise for $M = 1$ which similarly leads to the best cooling condition.

The mixing factor is illustrated for antiprotons in the HESR at 3 GeV kinetic energy. The same parameters that have been applied in section 2.4.2.1 to discuss the mixing in momentum cooling are utilized. The lattice with $\gamma_{tr} = 6.23$ has a fractional betatron tune $q = 0.62$ in the horizontal and vertical phase space plane.

For a beam with a relative momentum spread $\delta_{rms} = 1 \cdot 10^{-4}$ the bands are well separated, Figure 3.2.

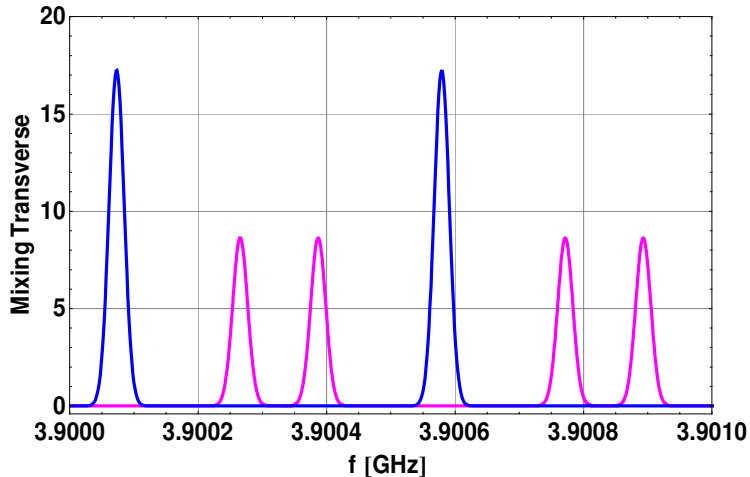


Figure 3.2: Transverse (magenta) and longitudinal mixing at the upper range of the cooling system for $\delta_{rms} = 1 \cdot 10^{-4}$. The bands are well separated.

The longitudinal sidebands are still well separated when the momentum spread is increased to $\delta_{rms} = 5 \cdot 10^{-4}$. The transverse betatron sidebands however partly overlap yielding good wanted mixing for betatron cooling, Figure 3.3. If we compare Figure 3.2 with the right image in Figure 3.3 we notice that the mixing factor is reduced by nearly a factor of five.

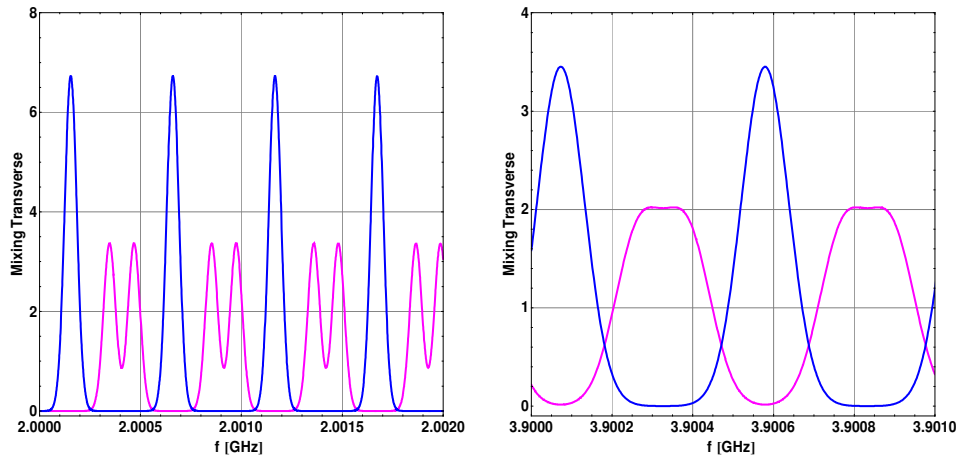


Figure 3.3: Transverse (magenta) and longitudinal mixing at the lower (left) and upper range (right) of the cooling system for $\delta_{rms} = 5 \cdot 10^{-4}$. The sidebands partly overlap. The mixing factors decrease.

It should be mentioned that for diagnostic reasons the bands should not completely overlap. This will be discussed below when we deal with the open loop gain of a transverse cooling system.

The average transverse wanted mixing factor is $M = \frac{1}{2\pi W} \int_{bandwidth} M(\Omega) d\Omega \approx 3$ for the case $\delta_{rms} = 5 \cdot 10^{-4}$.

Increasing the momentum spread further leads to a complete overlap of the sidebands. The mixing factor becomes $M = 1$ as is shown in Figure 3.4.

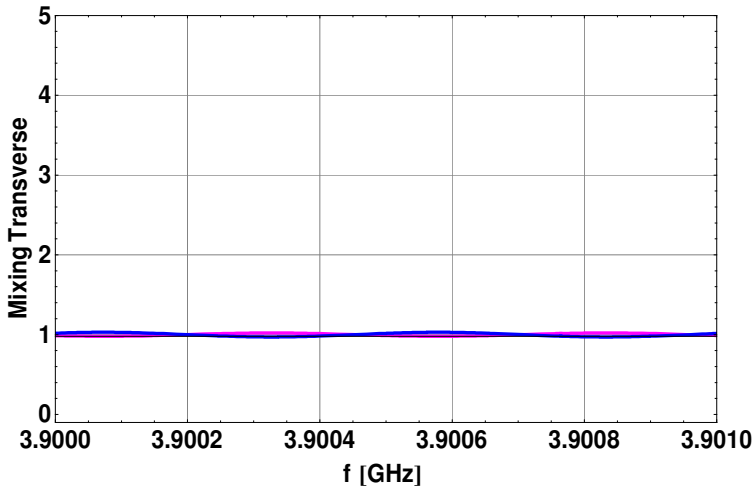


Figure 3.4: Transverse (magenta) and longitudinal mixing at the upper range of the cooling system for $\delta_{rms} = 2 \cdot 10^{-3}$. Complete overlap of the transverse and longitudinal Schottky bands. The mixing factor is $M = 1$.

With $\Omega = (n \pm Q)\omega$ the mixing factor, eq. (3.80), is approximately given by

$$M^\pm((n \pm Q)\omega) \approx \frac{\omega}{2N|n \pm Q|} \Psi_o(\omega) \quad (3.82)$$

if the bands do not overlap.

Average mixing factor

In the centre of the distribution $\omega = \omega_0$ and for large harmonic numbers n but still well separated bands the mixing factor becomes approximately $M(n\omega_0) \approx \frac{\omega_0}{2|n|} \frac{I}{N} \Psi_0(\omega_0)$.

Under this assumption the average mixing factor M according to eq. (3.51) is estimated to be

$$M = \frac{1}{2N} \frac{\omega_0^2 \Psi_0(\omega_0)}{2\pi W} \ln \frac{n_2}{n_1} \approx \frac{1}{2N} \frac{\omega_0^2 \Psi_0(\omega_0)}{2\pi W} \cdot \frac{W}{f_c} \quad (3.83)$$

where f_c is the center frequency of the cooling system. In the last step the approximation $\ln(n_2/n_1) \approx W/f_c$ for an octave bandwidth has been applied.

Eq. (3.83) can be used to estimate the average mixing factor for different beam distributions. For a Gaussian beam one finds the average mixing factor

$$M = \frac{f_0^2}{2\sqrt{2\pi} \sigma_f W} \cdot \ln \frac{f_+}{f_-} \quad (3.84)$$

where the revolution frequency is f_0 and the standard deviation of the beam frequency distribution is σ_f . The upper and lower frequency of the cooling system is f_+ and f_- , respectively. The bandwidth is $W = f_+ - f_-$.

Signal-To-Noise Ratio

The noise-to-signal ratio has been defined in eq. (3.43). It can be written as

$$U^\pm(\Omega) = \frac{S_{th}^\pm(\Omega)}{\left(|Z'_{PL}(\Omega)|^2 / Z_0 \right) \cdot S_0} = \frac{\frac{I}{2} k(T_R + T_A)}{\frac{N}{2} (Ze)^2 \frac{\omega_0}{2\pi} \frac{|Z'_{PL}|^2}{Z_0} \epsilon \beta_p}$$

and equals the ratio

$$U^\pm(\Omega) = \frac{k(T_R + T_A) \cdot |G_A|^2 W}{N(Ze)^2 \frac{\omega_0}{2\pi} \frac{|Z'_{PL}|^2}{Z_0} \epsilon \beta_p \cdot |G_A|^2 W} \quad (3.85)$$

of the thermal noise power in the cooling bandwidth at the kicker entrance to the Schottky particle power in the cooling bandwidth at the kicker entrance.

3.6 Open Loop Gain and Beam Feedback

We now continue to include the transverse feedback in the cooling equations for betatron cooling as was similar done for momentum cooling. Figure 3.5 sketches the loop.

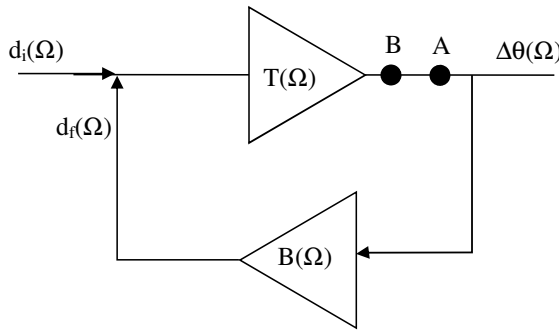


Figure 3.5: Feedback for transverse cooling. The undisturbed beam dipole moment $d_i(\Omega)$ is modified by addition of the dipole moment modulation $d_f(\Omega)$ introduced by the beam feedback. The loop can be opened between points A and B. A signal is then fed into the loop at point A and the transverse response of the cooling system including the beam is measured at point B with a network analyzer. The resulting open loop gain completely determines the transverse cooling system properties.

The *transverse beam feedback function* describes the response of the beam's dipole moment at the pickup upon a time depended deflection $\Delta\theta(t)$ at the kicker.

The complex beam transfer function $B(\Omega)$ is defined as the ratio

$$B(\Omega) = \frac{d_f(\Omega)}{\Delta\theta(\Omega)} \quad (3.86)$$

where the deflection at the kicker in frequency domain is $\Delta\theta(\Omega)$ and $d_f(\Omega)$ is the dipole moment modulation of the beam at the pickup input. The undisturbed dipole moment of the beam at the pickup is $d_i(\Omega)$.

The resulting deflection at the kicker is

$$\Delta\theta(\Omega) = T(\Omega) \cdot (d_i(\Omega) + d_f(\Omega)) \quad (3.87)$$

with the system transfer function $T(\Omega)$.

Inserting the beam transfer function, eq. (3.86), yields the closed loop gain

$$\frac{\Delta\theta(\Omega)}{d_i(\Omega)} = \frac{T(\Omega)}{1 - B(\Omega)T(\Omega)} \quad (3.88)$$

Thus the system transfer function has to be modified according to eq. (3.88) if the beam transfer function is taken into account.

The *closed loop gain* is then similar to longitudinal cooling given by

$$G_c(\Omega) = \frac{T(\Omega)}{1 - B(\Omega)T(\Omega)} \quad (3.89)$$

and the *open loop gain* is denoted by

$$S(\Omega) = B(\Omega)T(\Omega). \quad (3.90)$$

The system will be stable if $\text{Re}[B(\Omega)T(\Omega)] < 1$. It can be shown (see below) that if mixing from kicker to pickup is small, i.e., the mixing factor M is large and thermal noise is negligible, the optimum open loop gain becomes $S(\Omega) = -I$ in the centre of the distribution ($\omega = \omega_0$). According to eq. (3.89) the closed loop gain is reduced by a factor of two (signal suppression). On the other hand, if mixing is small or amplifier noise (U) becomes important, then $S(\Omega)$ tends to zero and no signal suppression occurs.

With beam feedback the input dipole current density changes to $S_d(\Omega) / |1 - S(\Omega)|^2$. If the open loop gain is optimal, $S(\Omega) = -I$, one observes a signal suppression of 0.5 in the

cooling bandwidth or equivalently, a reduction of the power density by 6 dB, see also Figure 3.7 for an example.

It will be elucidated below with examples that the cooling system can be analyzed and optimized by measuring the open loop gain $S(\Omega)$ with a network analyzer.

The beam transfer function, eq. (3.86), has the units Am. A dimensionless beam transfer function is defined by

$$B_{\perp}(\Omega) = \frac{B(\Omega)}{Ze f_0 \sqrt{\beta_p \beta_k}} \quad (3.91)$$

The closed loop gain can be written as

$$\frac{\Delta\theta(\Omega)}{d_i(\Omega)} = \frac{T(\Omega)}{1 - \frac{B(\Omega)}{N(Ze)f_0\sqrt{\beta_p\beta_k}} \cdot N(Ze)f_0\sqrt{\beta_p\beta_k}T(\Omega)} \quad (3.92)$$

and therefore with eq. (3.91)

$$\frac{\Delta\theta(\Omega)}{d_i(\Omega)} = \frac{T(\Omega)}{1 - \frac{1}{N} B_{\perp}(\Omega) \cdot g(\Omega)} \quad (3.93)$$

with $g(\Omega)$ as given in eq. (3.46).

Taking the signal suppression into account the cooling rate for the emittance, eq. (3.47), is modified to include beam feedback.

3.6.1 Emittance Cooling Rate Including Beam Feedback

$$\begin{aligned} \frac{1}{\varepsilon_j} \frac{d\varepsilon_j}{dt} &= \frac{1}{2N} \frac{\omega_j}{2\pi} \left\{ \sum_{n=-\infty}^{\infty} 2 \operatorname{Re} \left\{ e^{i[\Omega_j t^K + \frac{\pi}{2} - \mu]} \frac{g(\Omega_j)}{1 - \frac{1}{N} B_{\perp}(\Omega_j) \cdot g(\Omega_j)} \right\} \right. \\ &\quad \left. + \sum_{n=-\infty}^{\infty} \left| \frac{g(\Omega_j)}{1 - \frac{1}{N} B_{\perp}(\Omega_j) \cdot g(\Omega_j)} \right|^2 \{M(\Omega_j) + U(\Omega_j)\} \right\} \end{aligned} \quad (3.94)$$

where $\Omega_j = (n + Q_j)\omega_j$.

3.6.2 Transverse Beam Transfer Function

The transverse beam transfer function is derived similarly with the approach as outlined in chapter 2.10 for the longitudinal BTF. The only complication which is now added is that besides the longitudinal motion we have to consider the betatron motion. In the following we give the major steps.

We assume the sinusoidal approximation of the betatron motion and write as depicted in Figure 3.1

$$\xi(\phi, I) = \sqrt{2I} \cos \phi \quad (3.95)$$

where the action I has been introduced which is the phase space area divided by 2π . A comparison with eq. (3.2) yields the relation of the action and the emittance ϵ

$$I = \frac{\epsilon}{2}. \quad (3.96)$$

The phase angle of a particle in eq. (3.95) is similarly defined as in eq. (3.11) and is given by

$$\phi(t) = Q\omega t + \phi_0 \quad (3.97)$$

where the betatron tune is Q and ϕ_0 is a random phase uniformly distributed in $[0, 2\pi]$.

The phase space is now four-dimensional with co-ordinates (ϕ, I, Θ, J) in which the longitudinal angle action variables have been introduced in chapter 2.10. We assume that the transverse phase space is de-coupled from the longitudinal phase space and that the pickups and kickers are located in dispersion free regions in the ring. The following discussion is either for the horizontal or vertical BTF. The general case of possible coupling is outlined in [42].

The Hamiltonian of the unperturbed motion is then simply given by

$$H_0(\phi, I, \Theta, J) = \omega \cdot (J + QI) \quad (3.98)$$

from which the equation of motion follow with

$$\dot{\phi} = \frac{\partial H_0}{\partial I} = Q\omega \quad \dot{I} = -\frac{\partial H_0}{\partial \phi} = 0 \quad (3.99)$$

and

$$\dot{\Theta} = \frac{\partial H_0}{\partial J} = \omega \quad \dot{J} = -\frac{\partial H_0}{\partial \Theta} = 0. \quad (3.100)$$

The unperturbed particle distribution is

$$\bar{\Psi}_0(\phi, I, \Theta, J) = \frac{1}{2\pi} \rho(I) \cdot \frac{1}{2\pi} \Psi_0(J) \quad (3.101)$$

with the normalization

$$\int_0^{2\pi} \int_0^{\infty} \int_0^{2\pi} \int_0^{\infty} \bar{\Psi}_0(\phi, I, \Theta, J) d\phi dJ d\Theta dI = \int_0^{2\pi} \int_0^{\infty} \frac{1}{2\pi} \rho(I) d\phi dI \cdot \int_0^{2\pi} \int_0^{\infty} \frac{1}{2\pi} \Psi_0(J) d\Theta dJ = N \quad (3.102)$$

and $\int_0^{\infty} \rho(I) dI = 1$ as well $\int_0^{\infty} \Psi_0(J) dJ = N$.

Similarly as outlined in chapter 2.10 a particle distribution $\bar{\Psi}(\phi, I, \Theta, J, t)$ satisfies the Vlasov equation

$$\frac{\partial \bar{\Psi}}{\partial t} = \{H_0, \bar{\Psi}\} = -iL_0 \bar{\Psi} \quad (3.103)$$

where the Poisson brackets are now defined as

$$\{f, g\} = \left(\frac{\partial f}{\partial \phi} \frac{\partial g}{\partial I} - \frac{\partial f}{\partial I} \frac{\partial g}{\partial \phi} \right) + \left(\frac{\partial f}{\partial \Theta} \frac{\partial g}{\partial J} - \frac{\partial f}{\partial J} \frac{\partial g}{\partial \Theta} \right) \quad (3.104)$$

for any two functions f and g defined on the phase space (ϕ, I, Θ, J) . The linear operator in eq. (3.103) is given by $L_0 g = i\{H_0, g\}$.

We now apply a time dependent deflection $\Delta\theta(t, \Theta_K)$ at the kicker located at Θ_K . The kicker deflection will be sampled by a circulating particle once per turn. The single particle action change per time, \dot{I} , due to the deflection is then given similar as in eq. (3.12)

$$\dot{I} = \frac{\dot{\epsilon}}{2} = \sqrt{2I\beta_K} \sin(Q\omega t + \phi_0) \cdot \omega \sum_{n=-\infty}^{\infty} \delta(\Theta(t) - \Theta_K - 2\pi n) \cdot \Delta\theta(t; \Theta_K) \quad (3.105)$$

assuming as before that the position of a particle is not altered by the deflection.

For weak kicker deflections we can treat the kicker action as a perturbation of the Hamiltonian in eq. (3.98) and write for the resulting Hamiltonian

$$H(\phi, I, \Theta, J, t) = H_0(I, J) - A(t) \cdot \mathcal{A}(\phi, I, \Theta, J) \quad (3.106)$$

with the perturbation part

$$\Delta H = -A(t) \cdot \mathcal{A}(\phi, I, \Theta, J). \quad (3.107)$$

The particle motion then follows with the Hamiltonian eq. (3.106)

$$\begin{aligned} \dot{I} &= -\frac{\partial H}{\partial \phi} \\ &= A(t) \cdot \frac{\partial}{\partial \phi} \mathcal{A}(\phi, I, \Theta, J) \\ &= \Delta\theta(t; \Theta_K) \cdot \sqrt{2I\beta_K} \sin(Q\omega t + \phi_0) \cdot \omega \sum_{n=-\infty}^{\infty} \delta(\Theta(t) - \Theta_K - 2\pi n). \end{aligned} \quad (3.108)$$

Comparing the second and third line in the equation we can identify for the perturbation

$$A(t) = \Delta\theta(t; \Theta_K) \quad \text{and} \quad \frac{\partial \mathcal{A}(\phi, I, \Theta, J)}{\partial \phi} = \sqrt{2I\beta_K} \sin(\phi) \cdot \omega \sum_{n=-\infty}^{\infty} \delta(\Theta - \Theta_K - 2\pi n) \quad (3.109)$$

Since we assume a decoupled motion the deflection does not change the longitudinal motion so that we have

$$\dot{\Theta} = \frac{\partial H}{\partial J} = \omega \quad \dot{J} = -\frac{\partial H}{\partial \Theta} = 0. \quad (3.110)$$

As a conclusion we find that in the presence of the perturbation the betatron phase is given by $\phi(t) = Q\omega t + \phi_0$ as well as the longitudinal motion is $\Theta(t) = \omega t + \Theta_0$ and the action (energy) is $J(t) = J = \text{constant}$.

The perturbed particle density can be written as

$$\Psi(\phi, I, \Theta, J, t) = \bar{\Psi}_o(I, J) + \Delta\Psi(\phi, I, \Theta, J, t) \quad (3.111)$$

where the perturbation is $\Delta\Psi(\phi, I, \Theta, J, t)$ and the unperturbed particle distribution $\bar{\Psi}_o(I, J)$ is given in eq. (3.101).

The Vlasov equation for the perturbation $\Delta\Psi(\phi, I, \Theta, J, t)$ merges, similarly as described in chapter 2.10, in the inhomogeneous partial differential equation

$$\frac{\partial}{\partial t} \Delta\Psi = -i \cdot L_o \Delta\Psi - A(t) \cdot \{\mathfrak{A}, \bar{\Psi}_o\}. \quad (3.112)$$

with the driving term $-A(t) \cdot \{\mathfrak{A}, \bar{\Psi}_o\}$ determined by eq. (3.109). Performing the Poisson bracket $\{\mathfrak{A}, \bar{\Psi}_o\}$ defined in eq. (3.104) yields

$$\{\mathfrak{A}, \bar{\Psi}_o\} = \frac{\partial \mathfrak{A}}{\partial \phi} \cdot \frac{\partial \bar{\Psi}_o}{\partial I}. \quad (3.113)$$

with $\partial \mathfrak{A} / \partial \phi$ given in eq. (3.109). In the derivation the properties have been considered that the unperturbed particle distribution $\bar{\Psi}_o(I, J)$ does not depend on ϕ and Θ as well as that the kicker deflection does not change the particle energy and therefore $\partial \mathfrak{A} / \partial \Theta = 0$.

The formal solution of the partial differential equation (3.112) is given by

$$\Delta\Psi(\phi, I, \Theta, J, t) = - \int_{-\infty}^t e^{-iL_o(t-t')} A(t') \{\mathfrak{A}(\phi(t'), I(t'), \Theta(t'), J(t')), \bar{\Psi}_o(I(t'), J(t'))\}. \quad (3.114)$$

Observe that the perturbation $\Delta\Psi(\Theta, J, t)$ in the particle density vanishes when $t \rightarrow -\infty$. This reflects the fact that the perturbation is zero in the past before the kicker is switched ON. In other words, no output signal before the input signal is present.

The dipole moment of a single particle observed at the pickup entrance (see also eq. (3.17)) is given by

$$d(t; \Theta_p) = \sqrt{2I\beta_p} \cos(\phi(t)) Ze\omega(J) \sum_{m=-\infty}^{\infty} \delta(\Theta(t) - \Theta_p - 2\pi m). \quad (3.115)$$

We now carry out the same steps as in chapter 2.10 for the longitudinal BTF when proceeding from eq. (2.141) to eq. (2.151) to find the dipole momentum modulation of the beam at the pickup $\Delta d(t; \Theta_p)$ as a result of the kicker action

$$\Delta d(t; \Theta_p) = \int_{-\infty}^t R_{\perp}(t-t'; \Theta_p; \Theta_K) \cdot A(t') dt' \quad (3.116)$$

with the response function given as

$$R_{\perp}(\tau; \Theta_p; \Theta_K) = \int \{\bar{\Psi}(X(0)), \mathcal{A}(X(0)\} B(X(\tau)) d^4 X. \quad (3.117)$$

For abbreviation the phase space variables $X = (\phi, I, \Theta, J)$ and the volume element $d^4 X = d\phi dI d\Theta dJ$ are introduced.

The observable $B(X)$ in the integral of eq. (3.117) is that as given in eq. (3.115)

$$B(X) = B(\phi, I, \Theta, J) = \sqrt{2I\beta_p} \cos(\phi) Z e \omega(J) \sum_{m=-\infty}^{\infty} \delta(\Theta - \Theta_p - 2\pi m). \quad (3.118)$$

Equation (3.116) is completely similar to that derived for the longitudinal BTF in chapter 2.10 which underlines the identical formal treatment of the BTF either for the longitudinal or transverse phase space using perturbation theory.

The propagation of the deflection $A(t') = \Delta \theta(t'; \Theta_K)$ applied by the kicker at location Θ_K at times $t' < t$ resulting in a dipole moment modulation $\Delta d(t; \Theta_p)$ at time t at the pickup located at azimuth Θ_p is a convolution of the deflection and the beam's response function in time domain $R_{\perp}(\tau; \Theta_p; \Theta_K)$. A Fourier transform then delivers the transverse beam transfer function $R_{\perp}(\Omega; \Theta_p; \Theta_K)$ according to the definition given in eq. (3.86).

Replacing the cos-term by a complex exponential and using the Fourier expansion of the delta-function in eq. (3.118) yields

$$B(X(\tau)) = Z e \frac{\omega(J)}{2\pi} \sqrt{\frac{\beta_p I}{2}} \cdot \sum_{m=-\infty}^{\infty} \left\{ e^{i[(m+Q)\omega(J)\tau - m(\Theta_p - \Theta_0) + \phi_0]} + e^{-i[(m+Q)\omega(J)\tau - m(\Theta_p - \Theta_0) + \phi_0]}\right\}. \quad (3.119)$$

Inserting eq. (3.119) and the explicit expression of the Poisson bracket $\{\bar{\Psi}(X(0)), \mathfrak{A}(X(0))\}$ according to eqs. (3.113) and (3.109) in the equation for the response function (3.117) gives after some straight forward calculations

$$R_{\perp}(\tau; \Theta_p; \Theta_K) = -i(Ze) \frac{\sqrt{\beta_p \beta_K}}{2} \frac{1}{(2\pi)^2} \cdot \left\{ e^{i\mu} \int_0^{\infty} \omega^2 \Psi_0(\omega) \sum_{n=-\infty}^{\infty} e^{-i[(n+Q)\omega\tau + (n+Q)(\Theta_K - \Theta_p)]} d\omega \right. \\ \left. - e^{-i\mu} \int_0^{\infty} \omega^2 \Psi_0(\omega) \sum_{n=-\infty}^{\infty} e^{i[(n+Q)\omega\tau + (n+Q)(\Theta_K - \Theta_p)]} d\omega \right\}. \quad (3.120)$$

The betatron phase advance from pickup to kicker is $\mu = Q \cdot (\Theta_K - \Theta_p)$. The frequency response is found with a Laplace transformation and evaluating the sum as outlined in [43]. Following the steps as performed in chapter 2.10 leads to the transverse beam transfer function as defined by eq. (3.86)

$$R_{\perp}(\Omega; \Theta_p; \Theta_K) = \frac{i}{4} (Ze) \sqrt{\beta_p \beta_K} \frac{1}{2\pi} e^{i\Omega T_{PK}} \cdot \left\{ e^{i\mu} \int_0^{\infty} \omega C(\Omega, \omega) \Psi_0(\omega) \left[1 + i \cot(\pi(\frac{\Omega}{\omega} + Q)) \right] d\omega \right. \\ \left. - e^{-i\mu} \int_0^{\infty} \omega C(\Omega, \omega) \Psi_0(\omega) \left[1 + i \cot(\pi(\frac{\Omega}{\omega} - Q)) \right] d\omega \right\} \quad (3.121)$$

where the mixing factor $C(\Omega, \omega)$ is the same as for the longitudinal case, eq. (2.170), chapter 2.10, and the particle travelling time from pickup to kicker is denoted by T_{PK} .

In the further discussion we assume that $C(\Omega, \omega) \approx 1$ and that in the vicinity of a singularity $\Omega = (n \pm Q)\omega$ we can expand

$$\cot(\pi(\frac{\Omega}{\omega} \pm Q)) \approx \frac{\omega}{\pi} \frac{1}{\Omega - (n \mp Q)\omega}. \quad (3.122)$$

The transverse beam transfer function is then given by

$$\begin{aligned}
R_{\perp}(\Omega; \Theta_p; \Theta_K) = & -\frac{N}{4} (Ze) \sqrt{\beta_p \beta_K} \frac{\omega_0}{2\pi} e^{i\Omega T_{PK}} \cdot \\
& \left\{ 2 \sin \mu + e^{i\mu} \frac{1}{\pi} \frac{1}{\omega_0 N} \int_0^\infty \frac{\omega^2 \Psi_o(\omega)}{\Omega - (n-Q)\omega} d\omega - e^{-i\mu} \frac{1}{\pi} \frac{1}{\omega_0 N} \int_0^\infty \frac{\omega^2 \Psi_o(\omega)}{\Omega - (n+Q)\omega} d\omega \right\}.
\end{aligned} \tag{3.123}$$

The integrals are evaluated as discussed in chapter 2.10 by adding a small imaginary part $i\varepsilon$ with $\varepsilon > 0$ in the denominator of the integrands to attain causality of the signals. In the limit of $\varepsilon \rightarrow 0$ we then find for the *normalized transverse beam transfer function* according to the definition eq. (3.91)

$$\begin{aligned}
B_{\perp}(\Omega; \Theta_p; \Theta_K) = & -\frac{N}{4} e^{i\Omega T_{PK}} \cdot \\
& \left\{ 2 \sin \mu + ie^{i\mu} \frac{1}{\omega_0 N} \left[\left(\frac{\Omega}{n-Q} \right)^2 \frac{1}{|n-Q|} \Psi_o \left(\frac{\Omega}{n-Q} \right) - \frac{i}{\pi} P \int_0^\infty \frac{\omega^2 \Psi_o(\omega)}{\Omega - (n-Q)\omega} d\omega \right] \right. \\
& \left. - ie^{-i\mu} \frac{1}{\omega_0 N} \left[\left(\frac{\Omega}{n+Q} \right)^2 \frac{1}{|n+Q|} \Psi_o \left(\frac{\Omega}{n+Q} \right) - \frac{i}{\pi} P \int_0^\infty \frac{\omega^2 \Psi_o(\omega)}{\Omega - (n+Q)\omega} d\omega \right] \right\}
\end{aligned} \tag{3.124}$$

where the principal part of the integral in eq. (3.123) is indicated with P .

We now discuss the beam transfer function for the specific case when the betatron phase advance is adjusted for optimal cooling, $\mu = (2k+1)\pi/2$ with non-negative integer k as discussed in chapter 3.3. We then have $e^{i\mu} = i \cdot (-1)^k$, $e^{-i\mu} = -i \cdot (-1)^k$ and $\sin \mu = (-1)^k$. Inserting this into eq. (3.124) leads to

$$\begin{aligned}
B_{\perp}(\Omega; \Theta_p; \Theta_K) = & -(-1)^k N e^{i\Omega T_{PK}} \cdot \\
& \frac{1}{2} \left\{ 1 - \left[\frac{1}{2\omega_0 N} \left(\frac{\Omega}{n-Q} \right)^2 \frac{1}{|n-Q|} \Psi_o \left(\frac{\Omega}{n-Q} \right) + \frac{1}{2\omega_0 N} \left(\frac{\Omega}{n+Q} \right)^2 \frac{1}{|n+Q|} \Psi_o \left(\frac{\Omega}{n+Q} \right) \right] \right\} \\
& + \frac{i}{4\omega_0 N} \left[\frac{1}{\pi} P \int_0^\infty \frac{\omega^2 \Psi_o(\omega)}{\Omega - (n-Q)\omega} d\omega + \frac{1}{\pi} P \int_0^\infty \frac{\omega^2 \Psi_o(\omega)}{\Omega - (n+Q)\omega} d\omega \right].
\end{aligned} \tag{3.125}$$

If the system delay is adjusted to the particle transit time from pickup to kicker the real part of the BTF can be written as

$$Re[B_{\perp}(\Omega; \Theta_p; \Theta_K)] = -(-1)^k N \cdot \frac{I}{2} \{ I - [M_n^-(\Omega) + M_n^+(\Omega)] \} \quad (3.126)$$

where we have used the mixing factors defined by eq. (3.80) in chapter 3.5.

If many overlapping bands contribute to a single frequency Ω the real part of the BTF, eq. (3.126), has to be modified to

$$Re[B_{\perp}(\Omega; \Theta_p; \Theta_K)] = -(-1)^k N \cdot \frac{I}{2} \{ I - M(\Omega) \}. \quad (3.127)$$

The real part now contains the mixing factor

$$M(\Omega) = \sum_{k=-\infty}^{\infty} \{ M_k^-(\Omega) + M_k^+(\Omega) \} \quad (3.128)$$

for overlapping betatron sidebands as defined in chapter 3.5.

From eq. (3.127) we conclude that for perfect mixing $M(\Omega) = 1$ as outlined in chapter 3.5 the real part of the BTF vanishes. The causality of the beam signals entails that the real and imaginary part of the BTF are not independent from each other. The knowledge of one implies the knowledge of the other and thus the full complex and analytical BTF. This fact follows from the *Kramers-Kronig dispersion relations* for causal systems [42, 44] which are given by

$$Im[B_{\perp}(\Omega; \Theta_p; \Theta_K)] = \frac{I}{\pi} P \int_{-\infty}^{\infty} \frac{Re[B_{\perp}(\Omega'; \Theta_p; \Theta_K)]}{\Omega - \Omega'} d\Omega' \quad (3.129)$$

and

$$Re[B_{\perp}(\Omega; \Theta_p; \Theta_K)] = -\frac{I}{\pi} P \int_{-\infty}^{\infty} \frac{Im[B_{\perp}(\Omega'; \Theta_p; \Theta_K)]}{\Omega - \Omega'} d\Omega' \quad (3.130)$$

where P stands again for the principal value part of the integral.

Hence, for perfect mixing with $M(\Omega) = 1$, eq. (3.129) implies that the imaginary part also vanishes and consequently that the full BTF becomes zero. As a result any perturbation imposed on the beam particles at the kicker will vanish before it reaches the pickup. Beam feedback then plays no role in the cooling rate equation. This is consistent with the conclusion

drawn in chapter 3.5 that for perfect mixing the beam is completely uncorrelated for perfect mixing.

As previously pointed out it is not convenient for cooling system diagnostics and optimization to operate the cooling system in a regime where all bands overlap. In the next chapter we discuss the cooling properties for a beam in which the bands are narrow and the tune value is such the bands are well separated. Consequences of partly overlapping bands are discussed in [41].

3.6.3 Core Cooling Formula

Suppose the phase advance between pickup und kicker is $\mu = (2k+1)\frac{\pi}{2}$ where k is an integer, $k = 0, 1, 2, \dots$. The gain is $g(\omega) = -(-1)^k |g(\omega)| e^{-i\omega\tau_d}$. We assume that mixing from pickup to kicker is negligible, $C(Q, \omega) \approx 1$, and that the electronic delay is adjusted to the nominal particle travelling time from pickup to kicker, $\tau_d = T_{PK}$.

For non-overlapping bands we consider a single harmonic for which the real part of the BTF in the center of a symmetric distribution at $Q = (n \pm Q)\omega_0$ is given according to eq. (3.126) by

$$Re[B_\perp((n \pm Q)\omega_0; \Theta_p; \Theta_K)] = -(-1)^k N \cdot \frac{I}{2} \{1 - M((n \pm Q)\omega_0)\} \quad (3.131)$$

with the mixing factor in the center of the distribution

$$M((n \pm Q)\omega_0) = \frac{I}{2N} \omega_0 \frac{1}{|n \pm Q|} \Psi_0(\omega_0) \gg 1 \quad (3.132)$$

for narrow bands (see eq. (3.81) and Figure 3.2).

It should be noted that for a symmetric distribution the imaginary part of the BTF vanishes in the center of the distribution since the principal value in eq. (3.125) is an odd function of frequency in this case according to the Kramers-Kronig relation eq. (3.129).

We then have approximately for the *signal suppression factor* in the core cooling rate according to eq. (3.94)

$$\begin{aligned}\Gamma((n \pm Q)\omega_0) &= \frac{I}{I - \frac{1}{N} B_{\perp}((n \pm Q)\omega_0) \cdot g((n \pm Q)\omega_0)} \\ &= \frac{I}{I - S((n \pm Q)\omega_0)}\end{aligned}\quad (3.133)$$

with the open loop gain

$$S((n \pm Q)\omega_0) = -\frac{M((n \pm Q)\omega_0)}{2} |g((n \pm Q)\omega_0)| \quad (3.134)$$

To simplify the core cooling rate equation (3.94) for the emittance of the beam we introduce the abbreviations for the open loop gain in the center of the distribution

$$S_n = -S((n+Q)\omega_0) = \frac{M((n+Q)\omega_0)}{2} |g((n+Q)\omega_0)| = \frac{M_n}{2} g_n \text{ and for the signal suppression}$$

$\Gamma_n = \Gamma((n \pm Q)\omega_0)$. The noise-to-signal ration is abbreviated by $U_n = U((n+Q)\omega_0)$.

Inserting this in eq. (3.94) we obtain the betatron core cooling rate equation for non-overlapping betatron sidebands including beam feedback (see also [2, 3])

$$\frac{1}{\tau} = \frac{1}{\varepsilon} \frac{d\varepsilon}{dt} = -\frac{f_0}{2N} \left\{ \sum_{n=-\infty}^{\infty} \frac{2g_n}{I + S_n} - \sum_{n=-\infty}^{\infty} \left(\frac{g_n}{I + S_n} \right)^2 \{M_n + U_n\} \right\}. \quad (3.135)$$

The cooling rate can now be optimized by adjusting the gain and phase harmonic by harmonic in the cooling bandwidth. Optimum cooling is then found if for all harmonics in the cooling bandwidth the condition

$$\Gamma_n \cdot g_n (U_n + M_n) = I \quad (3.136)$$

is fulfilled.

The optimum gain is

$$(g_n)_{opt} = \frac{I}{U_n + \frac{M_n}{2}} \quad (3.137)$$

in the center of the distribution and the optimum cooling rate is found from eq. (3.135) which yields

$$\frac{I}{\tau} = -\frac{f_0}{2N} \sum_{n=-\infty}^{\infty} \frac{I}{M_n + U_n} \quad (3.138)$$

In the limiting case of negligible thermal noise ($U_n \ll M_n/2$) in the cooling system the signal suppression corresponding to eqs. (3.136) and (3.137) when the cooling loop is closed is given by

$$\Gamma_n = \frac{I}{2}. \quad (3.139)$$

In this case the optimal cooling rate is achieved if at each harmonic involved in the cooling bandwidth the gain is given by

$$(g_n)_{opt} = \frac{2}{M_n}. \quad (3.140)$$

This value is twice as large as in eq.(3.55) for the case when beam feedback is neglected.

Thus in the case of negligible amplifier noise we have an adjustment criterion for optimal cooling: By comparing open and closed loop Schottky noise densities the electronic gain can be adjusted harmonic by harmonic at all involved bands in the cooling bandwidth for optimal cooling. If at all harmonics in the cooling bandwidth a signal suppression of an half is observed cooling will be optimal.

When thermal noise in the cooling system dominates ($U_n \gg M_n/2$) the optimal cooling rate is found from eq. (3.137) which in this case is $(g_n)_{opt} = I/U_n$ at all bands involved. The signal suppression when the loop is closed becomes $\Gamma_n = I$ and no signal suppression can be observed when the cooling loop is closed.

Equivalently optimum cooling at each harmonic is attained for negligible thermal noise if the magnitude of the open loop gain and the open loop phase satisfy

$$|S((n \pm Q)\omega_0)| = 1 \quad \text{and} \quad \varphi((n \pm Q)\omega_0) = \pi \quad (3.141)$$

i.e., an open loop magnitude one in the center of the distribution and phase of 180 degrees is required at all harmonics in the cooling bandwidth.

The emittance core cooling rate, eq. (3.135), is equivalent to a first order differential equation for the beam emittance. This equation will be solved to predict the time evolution of the emittance during stochastic cooling including the beam-target interaction in COSY or HESR. More details are presented in chapter 4 where the beam-target interaction will be outlined.

The open loop gain measurement is an essential practical method to analyze and to optimize a transverse cooling system [35]. This is illustrated with an example for horizontal betatron cooling of $N = 10^{10}$ stored antiprotons with momentum $3.8 \text{ GeV}/c$ at the HESR where thermal noise in the cooling loop is negligible (Schottky noise dominates). In this case the optimal normalized gain is given by eq. (3.140) and eq. (3.141) determines the conditions for optimal cooling. Two tanks are used for the pickup, equipped with 64 ring slot coupler each and one tank equipped with 64 ring slot coupler is used as kicker. The shunt impedance of the pickup is $Z_p = 1152 \Omega$ and that of the kicker $Z_k = 2304 \Omega$, see Table 2.1. In this example the normalized gain $g(\Omega)$ according to eq. (3.46) at the center of the cooling bandwidth with

$$|g(\omega_c)| = N(Ze)^2 \frac{\omega_0}{2\pi} \sqrt{\beta_p \beta_k} \sqrt{Z_p Z_k} (S_{pu})^2 \frac{c}{\omega_c p_0 c} G_A \quad (3.142)$$

is used. It is assumed that $g(\Omega)$ is constant and real over the bandwidth ($2 - 4$) GHz. The electrical delay of the cooling system is adjusted to the nominal particle travelling time from pickup to kicker. The position sensitivity is S_{pu} .

The revolution frequency at $3.8 \text{ GeV}/c$ is $\omega_0/2\pi = 506 \text{ kHz}$.

As outlined in the chapter 3.7 the position sensitivity of the ring slot couplers amounts $S_{pu} \approx 20/m$. The beta function at the pickup and kicker for the standard lattice with $\gamma_{tr} = 6.23$ are 166 m and 15 m , respectively. The distance between pickup and kicker is 201 m . The horizontal betatron phase advance between pickup and kicker is $\mu_{pk} = 13 \cdot \pi/2$ and the fractional tune is $q = 0.62$. The full ring frequency slip factor is $\eta = 0.03$.

The open loop gain $S(\Omega) = \frac{I}{N} B_{\perp}(\Omega) \cdot g(\Omega)$ is calculated with the beam transfer function given in eq. (3.125) for a Gaussian beam momentum distribution with a relative momentum spread $\delta_{rms} = 1 \cdot 10^{-4}$. The electronic voltage gain is set to $G_A = 115 dB$.

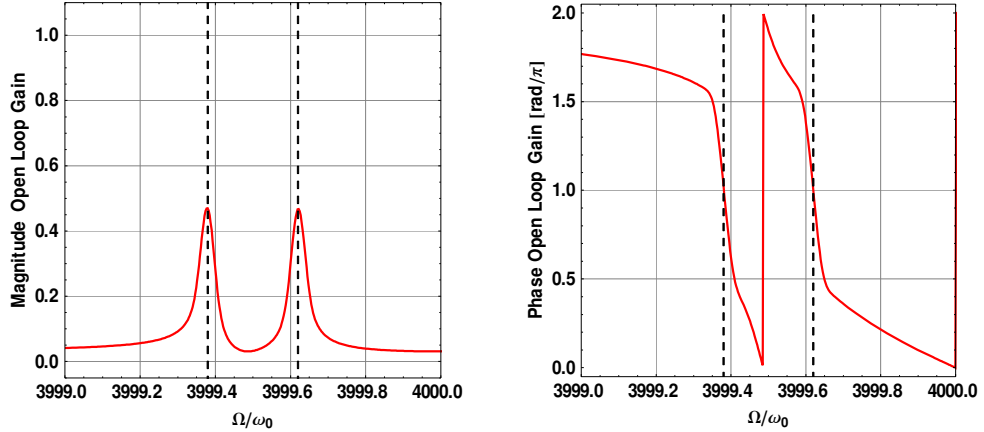


Figure 3.6: Simulation of the open loop gain. Magnitude (left) and phase response (right) between harmonic number 3999 and 4000. The betatron sidebands $(4000 - 0.62)\omega_0$ and $(3999 + 0.62)\omega_0$ are visible. The signal delay is set to the nominal particle travelling time from pickup to kicker. The phase in the center of the distribution (dotted lines) is 180 degrees for the desired betatron phase advance from pickup to kicker $\mu_{PK} = 13 \cdot \pi/2$ for optimal cooling, eq. (2.99). The gain 115 dB is however not the optimal gain. The magnitude of the open loop gain indicates that increasing it by 6 dB would lead to optimal cooling at these harmonics.

Figure 3.6 shows the simulation result for an open loop gain between harmonic number 3999 and 4000 in the cooling bandwidth. The open loop gain is real in the center of the sidebands since the phase is 180 degrees. The graphic indicates that the gain is too small. Increasing it by 6 dB would lead to the optimal open loop gain magnitude $|S| = 1$ required for optimal cooling according to eq. (3.141).

The signal suppression, Figure 3.7, would then be equal 0.5 in the center of the sidebands instead ≈ 0.25 for 115 dB gain. The open loop phase shows a rapid change of 180 degrees across each sideband. In the center the phase is 180 degrees as desired by eq. (3.141) for optimal cooling at this harmonic in the cooling bandwidth.

In Figure 3.8 the Nyquist stability diagram is displayed. It consists of two loops corresponding to the two betatron sidebands in the harmonic range between 3999 and 4000. The loops are traversed with increasing frequency as indicated by arrows in the figure. If the betatron phase advance and the signal delay are set correctly the loops of the betatron sidebands are centered around the negative real axis as shown in the right graph of Figure 3.8. The cooling loop is stable since $\text{Re}(S) < 1$ in the diagram. A phase error in the electronics would become noticeable by a simply rotation of the loops around the origin. If one loop in the Nyquist stability diagram encloses the point (1,0) the cooling loop becomes unstable.

Next, an artificial betatron phase advance error of 45 degrees ($\mu_{PK} = 13.5 \cdot \pi/2$) is introduced. The gain is increased to the optimal gain 121 dB. The loops in the Nyquist diagram are now clearly separated.

Figure 3.9 shows that the difference in the open loop phase at the center of the two sidebands equals twice the error $\Delta\mu$ in betatron phase advance.

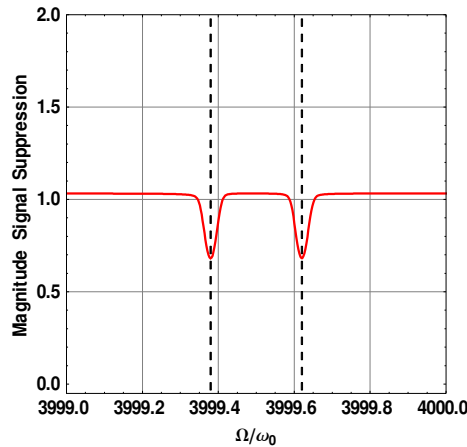


Figure 3.7: Simulation of the signal suppression magnitude at harmonic number between harmonic number 3999 and 4000. The gain is not optimal. The signal suppression in the center of the distribution becomes 0.5 as desired when the gain is increased by 6 dB gain.

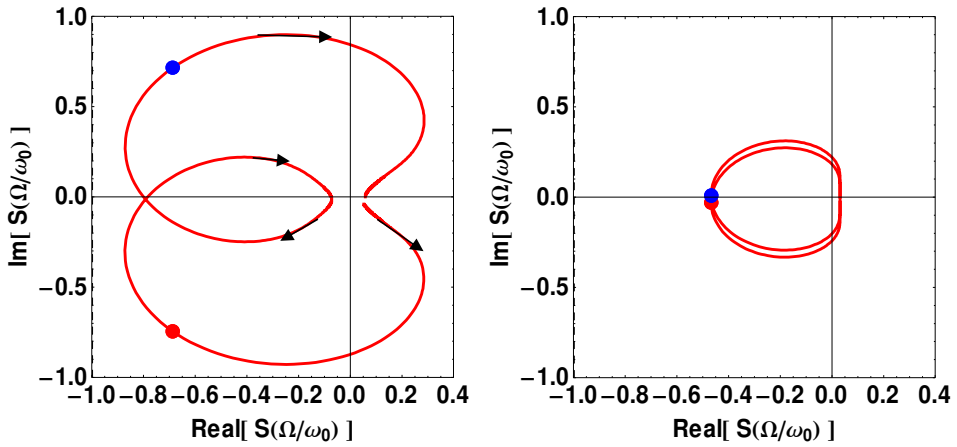


Figure 3.8: Nyquist stability diagram. If the betatron phase advance is correct the loops of the betatron sidebands are centred about the negative real axis (right graph). The center of the sidebands is marked with a dot. It is seen that the open loop gain is real in the center of the sidebands. Red: lower sideband, blue: upper sideband. The direction of the frequency sweep is indicated by arrows. The left graph shows the case when the betatron phase advance from pickup to kicker deviates from the optimal value $\mu_{PK} = 13 \cdot \pi/2$ by 45 degrees. The signal delay is as required. Any phase (delay) error in the electronics will rotate the loops around the origin.

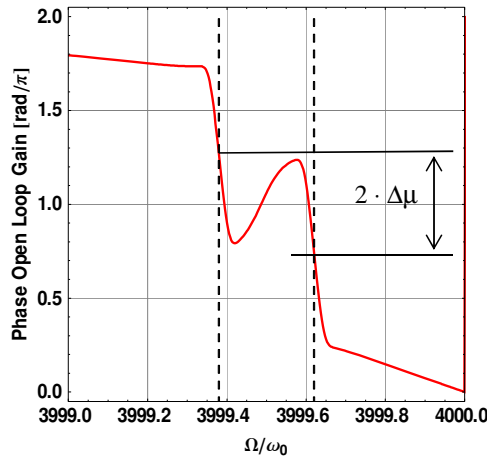


Figure 3.9: Open loop phase of the two sidebands for a betatron phase advance $\mu_{PK} = 13.5 \cdot \pi/2$. The difference in the open loop phase at the center of the two sidebands equals twice the error $\Delta\mu = 0.25\pi$ in the betatron phase advance.

Optimal cooling is achieved if for each betatron sideband in the cooling bandwidth gain and phase (*180* degrees at the center of the sidebands) are optimized by means of an open loop gain measurement. In practice however it is sufficient to scan some *100* Schottky sidebands in the cooling bandwidth.

A deeper discussion of the open loop gain measurement as a diagnostic tool to optimize the cooling system can be found in [35].

3.7 Transverse Pickup Impedance and Kicker Sensitivity

The main stochastic cooling system of the HESR operates in the frequency range of *2 - 4 GHz*. The beam coupling structure is based on ring slot couplers [11, 33] surrounding the whole beam thus covering the total image current, Figure 3.10. The left image of the figure shows a single ring divided in an octagonal arrangement of eight 50Ω electrodes. The signals can be summed up to create the longitudinal beam signals or they can be subtracted to produce the beam position signals for transverse cooling. The rings with a thickness of *9 mm* can be stacked as shown in the right image of Figure 3.10 to increase the shunt impedance. The inner diameter of each ring is *90 mm*. It was shown by simulations that these structures yield a significantly higher longitudinal shunt impedance as compared to a $\lambda/4$ structure. Additionally, the structures have the great advantage that they can be simultaneously used in all three cooling planes (horizontal, vertical and longitudinal). Due to the high sensitivity of the new ring slot couplers no movable parts in the vacuum are needed to obtain a good signal to noise ratio.

According to the Lorentz reciprocity theorem [30] the same electrode configuration as used for a pickup can work as a kicker device.

In a small test-tank the new structures were successfully operated in the synchrotron COSY [11] as pickup only and in a small version of *16* rings, as pickup and kicker in the Nuclotron in Dubna. This small cooling system acts as test-bench for the NICA project [12].

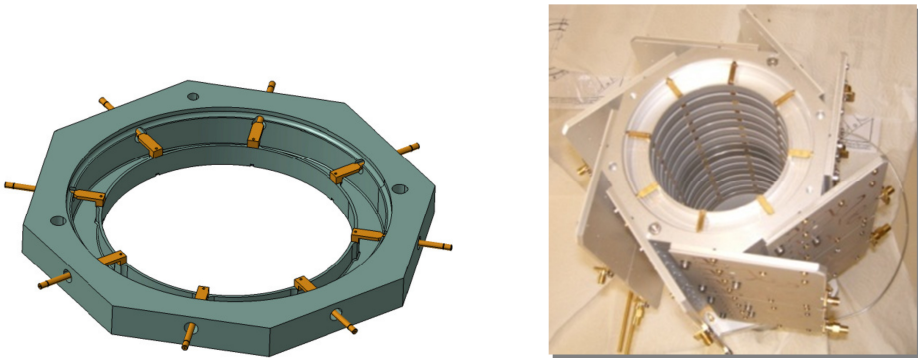


Figure 3.10: Left, drawing of one ring slot coupler cell with eight electrodes 22.5 degrees apart. The cells of thickness 9 mm can be stacked to increase the sensitivity of the pickup/kicker as shown in the right image. In the picture the stack consists of 16 cells. The figure also shows the boards for signal combining of the electrodes.

As outlined in chapter 2.3.2 each ring has a *shunt impedance* of 36Ω when driven as longitudinal kicker. According to the reciprocity theorem [30] the *pickup shunt impedance* is found from $Z_p = Z_k/4$. This yields for one cell 9Ω . In the HESR the kicker tank for momentum and betatron cooling contains 64 cells which results in a total shunt impedance for the kicker $Z_k = 64 \cdot 36 \Omega = 2304 \Omega$. There are two pickup tanks each equipped with 64 cells yielding a total pickup shunt impedance of $Z_p = 2 \cdot 64 \cdot 9 \Omega = 1152 \Omega$. Three kicker tanks will be installed one for momentum cooling and two for transverse cooling. Two pickup tanks are installed which simultaneously deliver longitudinal and transverse signals. See also Figure 1.1.

For transverse cooling the *transverse shunt or coupling impedance* is necessary. It is defined as the derivative of the impedance with respect to the transverse position of the particle in the pickup. We applied the analytical method of image charges [46] and the numerical boundary element method (BEM) [47]. The latter method can be applied for arbitrarily shaped electrodes to determine the transverse coupling impedance of the ring slot coupler pickup. The drawing in Figure 3.10 suggests to compare the results with those derived in an approach that describes the position sensitivity for a round pickup [48]. The structure can be used either for pickups or for kickers. The Panofsky-Wenzel theorem [30] relates the energy change induced by the kicker to the reflection it exerts to a particle. The theorem will

be used here to determine the transverse kicker sensitivity once the pickup sensitivity is known.

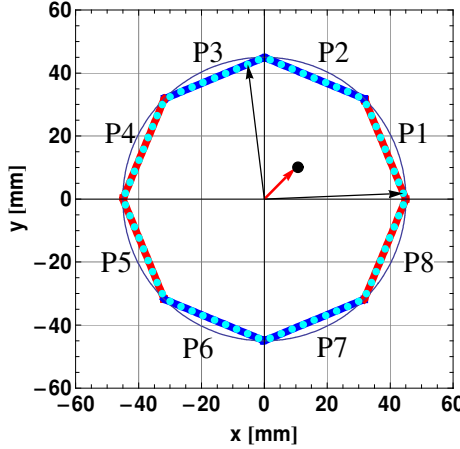


Figure 3.11: Electrode model for the ring slot couplers. The eight electrodes are labelled with P1 to P8. The red arrow indicates the beam position \vec{r}_0 . The black arrows indicate the position in the segments \vec{r}'_j and the node position \vec{r}_i (light blue dots) for the BEM calculation. The charge difference of the upper and lower electrodes (blue) $(P2 + P3) - (P6 + P7)$ gives the vertical beam position. Similarly, with the left right electrodes (red) difference of $(P1 + P8) - (P4 + P5)$ yields the horizontal beam position. The sum of the charge of all electrodes gives the image charge of the beam.

In both methods the ring slot couplers are modeled as sketched in Figure 3.11. Eight electrodes with a length of 34.44 mm are placed 22.5 degrees apart as shown in the figure to form an octagon. For highly relativistic beams, the electric near fields of a beam particle are disk-shaped in the longitudinal direction and the pickup sensitivity can be calculated using electrostatic field models in the plane.

From Green's theorem [49] it follows that in the electrostatic problem the potential $\Psi(\vec{r})$ at any point \vec{r} in 3D space is found from

$$\Psi(\vec{r}) = -4\pi \int_V G(\vec{r}, \vec{r}') \rho(\vec{r}') d^3 r - 4\pi \int_{\partial V} G(\vec{r}, \vec{r}') \sigma(\vec{r}') d\sigma \quad (3.143)$$

where $\rho(\vec{r}')$ is the charge density of the beam inside the volume V enclosed by the pickup electrode surface ∂V . The charge density induced by the beam on the electrodes is denoted by $\sigma(\vec{r}')$. The potential $\Psi(\vec{r})$ satisfies the Poisson equation $\Delta\Psi(\vec{r})=-4\pi\rho(\vec{r})$ and the Green's function fulfills $\Delta G(\vec{r},\vec{r}')=-\delta(\vec{r}-\vec{r}')$.

Considering eq. (3.143) in the plane, $\Gamma=\partial V$ is the curve formed by the pickup plates that encloses the area V . Inserting the Green function in the plane $G(\vec{r},\vec{r}')=\frac{I}{2\pi}\ln(|\vec{r}-\vec{r}'|)$ [49] into eq. (3.143) yields for a point like beam $\rho(\vec{r})=Q\delta(\vec{r}-\vec{r}_0)$ with charge Q located at position \vec{r}_0 inside the pickup

$$\Psi(\vec{r})=-2Qe\ln(|\vec{r}-\vec{r}_0|)-2\int_{\Gamma}\sigma(\vec{r}')\ln|\vec{r}-\vec{r}'|d\Gamma. \quad (3.144)$$

In eq. (3.144) the surface integral in eq. (3.143) is now a line integral along the closed path Γ formed by the pickup electrodes P1 to P8 in Figure 3.11. We solve the equation for points \vec{r} on the electrodes. Thus the potential $\Psi(\vec{r})$ is zero for points on the boundary. To solve eq. (3.144) for the charge line density $\sigma(\vec{r}')$ induced by the beam on the electrodes each electrode is divided in straight line segments $\Gamma_j, j = 1, 2, \dots, N$. The middle (node) of each line segment is $\vec{r}=\vec{r}_i, i = 1, 2, \dots, N$. If we assume that the charge line density $\sigma(\vec{r}_j')$ is constant on each line segment eq. (3.144) reduces to the matrix equation

$$G_{i0} = \sum_{j=1}^N G_{ij} \sigma_j \quad i = 1, 2, 3, \dots, N \quad (3.145)$$

With

$$G_{i0} = Qe \ln |\vec{r}_i - \vec{r}_0| \quad (3.146)$$

$$G_{ij} = \int_{\Gamma_j} \ln \frac{I}{|\vec{r}_i - \vec{r}_j'|} d\Gamma_j \quad (3.147)$$

and $\sigma_j = \sigma(\vec{r}_j'), j = 1, 2, 3, \dots, N$ the constant charge density on line segment j .

The $N \times N$ matrix $[G_{ij}]$ in eq. (3.145) can be inverted to find the charge density on the boundary Γ ,

$$[\sigma_i] = [G_{ij}]^{-1} [G_{io}]. \quad (3.148)$$

For the numerical simulation each electrode in Figure 3.11 is divided into nine segments. Thus, for eight electrodes the matrix eq. (3.147) consists of 5184 matrix elements.

A solution of the matrix equation (3.148) then delivers the horizontal (H) or vertical (V) normalized charge (voltage) differences as a function of position in the pickup by comparing the induced charges (or the voltages) on the eight electrodes P1, P2,, P8.

The *vertical normalized charge difference* is found from the expression

$$V = \frac{(P2 + P3) - (P6 + P7)}{P1 + P2 + P3 + P4 + P5 + P6 + P7 + P8} = \frac{\Delta_V}{\Sigma} \quad (3.149)$$

while the same pickup also delivers the *horizontal normalized charge difference* which is determined from

$$H = \frac{(P1 + P8) - (P4 + P5)}{P1 + P2 + P3 + P4 + P5 + P6 + P7 + P8} = \frac{\Delta_H}{\Sigma} \quad (3.150)$$

The horizontal and vertical position sensitivities, $S_x = \partial H / \partial x$, $S_y = \partial H / \partial y$, then follows from the derivatives of H and V w.r.t. the horizontal position or vertical beam position x and y , respectively.

In Figure 3.12 the numerical result of the vertical pickup sensitivity for a beam that is horizontally centered in the pickup is shown.

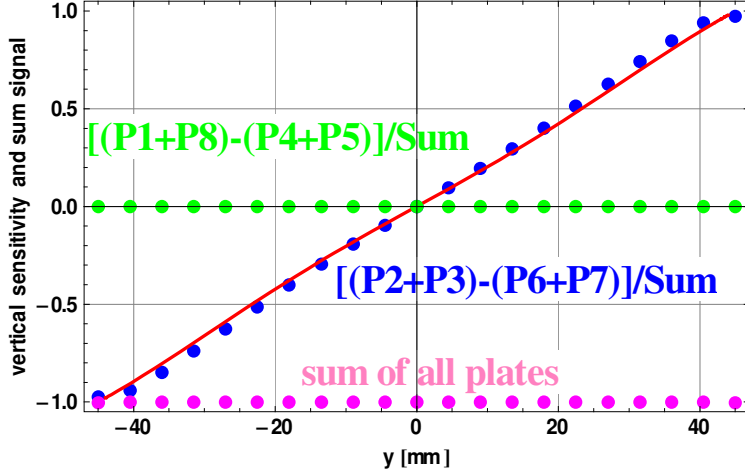


Figure 3.12: Normalized vertical (blue) and horizontal (green) charge differences for beam that is horizontally on axis. The red curve is the charge difference found with an analytical formula for a round pickup. The slope gives the vertical position sensitivity $S_y = 20/m$.

The blue dots in Figure 3.12 give the vertical normalized charge difference V versus vertical beam position y . The derivative w.r.t. y gives the position sensitivity $S_y = 20/m$. For comparison the analytical result using the image charge method [46] is displayed in black. It yields a similar value for the sensitivity $S_y = 18/m$. The green points represent the left - right difference for a beam that is centered on the horizontal axis. The sum of all electrodes yields the total image charge (magenta). The symmetry of the pickup structure leads to the same sensitivity in the horizontal plane.

For comparison the figure we included the result for a round pickup [48] as described by the induced normalized charge density at azimuth ϕ

$$\sigma(\phi) = -\frac{I}{2\pi} \frac{b^2 - r^2}{b^2 + r^2 - 2br \cos(\phi - \varphi)} \quad (3.151)$$

where b is the beam pipe radius, $b = 45\text{ mm}$ for the HESR. The particle position in polar coordinates is $\vec{r}_0 = r(\cos(\varphi), \sin(\varphi))$. We choose for a vertical pickup the angle $\phi \in [\pi/4, 3\pi/4]$ for the upper electrodes while $\phi \in [5\pi/4, 7\pi/4]$ for the lower electrodes. The

left electrodes cover the azimuthal angles $\phi \in [3\pi/4, 5\pi/4]$ and the right electrodes cover the range $\phi \in [7\pi/4, \pi/4]$.

In Figure 3.12 we find a good agreement between this analytical approach and the numerical BEM.

From Figure 3.12 it follows that $\Delta_y = S(y)\Sigma_y \propto S(y)Z_{PL} \cdot (iy)$ where Z_{PL} is the longitudinal coupling impedance, eq. (2.22), introduced in chapter 2.3.2. Similarly, one finds for the horizontal plane $\Delta_x = S(x)\Sigma_x \propto S(x)Z_{PL} \cdot (ix)$. The *transverse coupling impedance* $Z'_{PL}(\omega)$ either in the horizontal or vertical plane of two pickup tanks is then found to be

$$Z'_{PL}(\omega) = S_{x,y} \sqrt{Z_p Z_0} e^{i(\pi/2 - \theta(\omega))} \sin \theta(\omega) \quad (3.152)$$

which has the same frequency response as the longitudinal pickup. The position sensitivity is $S_{x,y} = 20/m$ either for the horizontal or vertical plane. The shunt impedance of the two pickup tanks is $Z_p = 1152 \Omega$ and the characteristic impedance is $Z_0 = 50 \Omega$. The frequency dependent phase θ is $\theta(\omega) = \frac{\pi}{2} \frac{\omega}{\omega_c}$ where ω_c is the center angular frequency of the cooling system. Thus, in the center of the cooling bandwidth the pickup coupling impedance of the two tanks amounts $Z'_{PL}(\omega_c) = 4.8 k\Omega/m$.

The *transverse kicker sensitivity* is defined as

$$K_\perp = \frac{\Delta p_\perp \beta c}{Ze \cdot U_K} \quad (3.153)$$

where Δp_\perp is the transverse momentum change executed to the beam by the kicker when it is driven by the kicker input voltage U_K .

We calculate the transverse kicker sensitivity by a determination of the longitudinal energy change ΔE a particle receives when the kicker is operated in difference mode. This means e.g. that the electrode pairs (P2+P3) and (P6+P7) are driven by equal but opposite voltages. Then, with the similar definition as in eq. (2.20), we find

$$K'_{\parallel} = \frac{\Delta E / Ze}{U_K} \quad (3.154)$$

as the longitudinal kicker sensitivity when the kicker is driven in difference mode. The longitudinal kicker sensitivity in the difference mode operation is to first order $K'_{\parallel} = K_{\parallel} \cdot S \cdot y$ where S is the position sensitivity determined above for the pickup and y is the (horizontal or vertical) position of a particle in the kicker. The longitudinal kicker sensitivity K_{\parallel} for sum mode operation (electrodes are supplied with voltages of the same sign) has been given in eq. (2.23). According to eq. (3.154) the energy change ΔE now depends of the particle position y in the pickup. It vanishes for particles that are on axis in the kicker.

The *transverse momentum change* Δp_{\perp} is related with the energy variation ΔE induced by the kicker according to the Panofsky-Wenzel theorem [30]

$$\Delta p_{\perp} = \frac{i}{\omega} \frac{\partial(\Delta E)}{\partial y}. \quad (3.155)$$

The derivative of the energy change is taken either in the horizontal or vertical direction. Inserting eq. (3.155) into eq. (3.153) and using in eq. (3.154) $K'_{\parallel} = K_{\parallel} \cdot S \cdot y$ with the longitudinal kicker sensitivity given in eq. (2.23) we obtain finally for the *transverse kicker sensitivity*

$$K_{\perp}(\omega) = S \cdot \sqrt{\frac{Z_K}{Z_0}} e^{-i\theta(\omega)} \sin \theta(\omega) \frac{\beta c}{\omega}. \quad (3.156)$$

The kicker shunt impedance for one tank is $Z_K = 2304 \Omega$ and $S = 20/m$. Equation (3.156) shows that the kicker response is largest when $\omega = 0$.

The magnitude of the kicker response of one tank is shown at the momentum $3.8 \text{ GeV}/c$ ($\beta = 0.97$) in Figure 3.13.

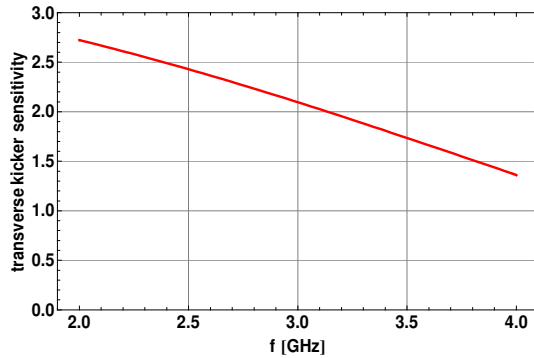


Figure 3.13: Magnitude of the transverse kicker sensitivity for one tank containing a stack of 64 ring slot couplers.

In the center of the cooling bandwidth the kicker sensitivity is $|K_{\perp}(\omega_c)| \approx 2$.

Table 3.1: Transverse pickup and kicker properties in the HESR

Transverse cooling		
Pickup:		
Number of tanks	2	
Number of ring-slot coupler per tank	64	
Transverse coupling impedance	4.8	kΩ/m
Kicker:		
Number of tanks	1 horizontal, 1 vertical	
Number of ring-slot coupler per tank	64	
Transverse kicker sensitivity per tank	≈ 2	
Installed power:		
Horizontal	250	W
Vertical	250	W
Distance pickup to kicker	≈ 200	m

4 Beam-Target Interaction

The beam-target interaction described in detail by [50] consists essentially of a mean energy loss and a mean squared momentum deviation per turn. Furthermore, the periodical Coulomb collisions of the ions with target atoms lead to small angle kicks that result in an emittance increase with time. If β_T denotes the betatron function at the target, D and D' the position and angle dispersion at the target, respectively, then the emittance growth $d\epsilon/dt$ due to the beam-target interaction is given by the rate

$$\frac{d\epsilon}{dt} = \frac{f_0}{2} \left\{ \beta_T \theta_{rms}^2 + \frac{D^2}{\beta_T} \delta_{loss}^2 + \beta_T D'^2 \delta_{loss}^2 \right\} \quad (4.1)$$

where θ_{rms}^2 is the mean square scattering angle per target traversal and δ_{loss}^2 is the mean square momentum deviation per target traversal (see below). Eq. (4.1) shows that a non-zero position and angle dispersion at the target location introduces a coupling between the transverse and longitudinal phase space. The emittance change $d\epsilon/dt$ thus also depends on the energy loss straggling in the target. To avoid this, the (PANDA) target is at a location with zero position and angle dispersion. The lattice optics optimized for the PANDA experiment is shown in chapter 5. This is the condition we assume in the following.

The emittance increase of an $^{238}U^{92+}$ ion beam in the HESR due to the beam-target interaction is quite small in the case of a hydrogen target with $N_T = 4 \cdot 10^{15} \text{ atoms/cm}^2$ as considered here. This is due to the low revolution frequency and that the beta function at the target amounts to $\beta_T = 1 \text{ m}$.

Table 4.1: Transverse emittance increase due to beam-target interaction for bare uranium

T [GeV/u]	$d\epsilon/dt$ [mm mrad/s]	θ_{rms}^2 [mrad 2]
3	$0.5 \cdot 10^{-4}$	$2 \cdot 10^{-10}$
0.74	$5 \cdot 10^{-4}$	$2 \cdot 10^{-9}$

The *mean energy loss* ε per turn [51] of an ion with charge Ze is calculated from the Bethe-Bloch equation

$$\varepsilon = -K Z^2 Z_T \frac{N_T}{N_A} \frac{I}{\beta^2} \left[\frac{1}{2} \ln \left(\frac{2m_e c^2 \beta^2 \gamma^2 E_{max}}{I^2} \right) - \frac{\beta^2}{2} \left(1 + \frac{E_{max}}{T_{max}} \right) \right]. \quad (4.2)$$

The target with charge number Z_T has the density N_T in units *atoms/cm²*. The electron mass is given by m_e . The mean excitation energy is I , for gaseous hydrogen $I = 19.2$ eV. The ionization constant is approximately given by $I \approx 16 \cdot Z_T^{0.9}$ eV for $Z_T > 1$. $K = 0.307075$ MeV cm²/mol. The Avogadro number is $N_A = 6.023 \cdot 10^{23}$ mol⁻¹. The mean energy loss of an ion has the unit MeV.

The mean energy loss leads to an additional drift term in the Fokker-Planck equation when the beam-target interaction is included in the model.

We deduce the maximum kinetic energy T_{max} [50] which can be imparted from the ion to a free electron in a single collision from

$$T_{max} = \frac{2m_e c^2 \beta^2 \gamma^2}{I + 2\gamma m_e / M + (m_e / M)^2} \quad (4.3)$$

for an ion with momentum $p = M \gamma \beta c$, $M = A \cdot m_r$.

To account for the finite momentum acceptance δ_{acc} of the machine, for the HESR $\delta_{acc} = \pm 2.5 \cdot 10^{-3}$, the Bethe-Bloch equation (4.2) contains E_{max} which is the maximum energy loss an ion can suffer by the beam-target interaction without being lost at the acceptance limit. We determine the maximum energy from

$$E_{max} = \text{Min}\{T_{max}, T_{cut}\} \quad (4.4)$$

with the maximum kinetic energy as allowed by the momentum acceptance limit of the machine

$$T_{cut} = \delta_{acc} \frac{\gamma + 1}{\gamma} T_0. \quad (4.5)$$

In the case of heavy ions discussed here $E_{max} = T_{max} < T_{cut}$ (or $\delta_{max} < \delta_{acc}$) so that the finite momentum acceptance constitutes no restriction. For antiprotons in the HESR this is in general not true. Here the maximum energy loss is restricted to T_{cut} . While eq. (4.2) describes the mean energy loss of the ions which affects the beam distribution as a whole the *mean squared momentum deviation* per target traversal δ_{loss}^2 [50] for an ion with kinetic energy $T_0 = (\gamma - 1) \cdot A \cdot E_r$ ($E_r = 931.5 \text{ MeV}$) which we determine from

$$\delta_{loss}^2 = \left(\frac{\gamma}{\gamma + 1} \frac{1}{T_0} \right)^2 \xi E_{max} \left(1 - \frac{\beta^2}{2} \right) \quad (4.6)$$

contributes to a broadening of the beam distribution. Here ξ is a measure of the effective target thickness [50] which is given by

$$\xi = 0.1535 \cdot Z^2 \cdot Z_T \cdot N_T \frac{I}{\beta^2 N_A} \text{ MeV} . \quad (4.7)$$

To compare the beam-target interaction for different ion species we can apply the following scaling laws. Observing that $T_{max} \approx 2m_e c^2 \beta^2 \gamma^2$ for the considered energy range (including antiprotons) we conclude from eqs. (4.6) and (4.7) that the mean squared momentum deviation per target traversal scales with charge and mass number as

$$\delta_{loss}^2 \sim \left(\frac{Z}{A} \right)^2 . \quad (4.8)$$

The *diffusion in energy space* of an ion with kinetic energy $T_0 = (\gamma - 1) \cdot A \cdot E_r$ and revolution frequency f_0 due to the beam-target interaction is determined from

$$D_{target} = \frac{f_0}{2} \left(\frac{1 + \gamma T_0}{\gamma A} \right)^2 \delta_{loss}^2 = \frac{f_0}{2} \frac{I}{A^2} \xi E_{max} \left(1 - \frac{\beta^2}{2} \right) \quad (4.9)$$

with units $(eV/u)^2 / s$ and therefore the scaling law for the charge to mass ratio $D_{target} \sim \left(\frac{Z}{A} \right)^2$.

The diffusion induced by the target is added to the diffusion term in the Fokker-Planck equation.

The mean energy loss per nucleon, ε / A , scales as Z^2 / A .

In Table 4.2 we summarize ionization constants for three different target materials.

Ionization constants:

Table 4.2: Ionization constants for three target materials

<i>target material</i>	$I [eV]$
gaseous H_2	19.2
$^{134}Xe^{54}$	579.8
Hydrogen	19.2

We note that the ionization constant has a strong impact on the mean energy loss.

4.1 Beam-Target Interaction of an Ion Beam

4.1.1 Hydrogen Target

The following Figure 4.1 and Figure 4.2 show the beam-target interaction for a hydrogen target of thickness $N_T = 4 \cdot 10^{15} \text{ atoms/cm}^2$ located at the PANDA position, Figure 5.1 and Figure 1.1, (no dispersion) in the energy range 500 MeV/u to 3 GeV/u .

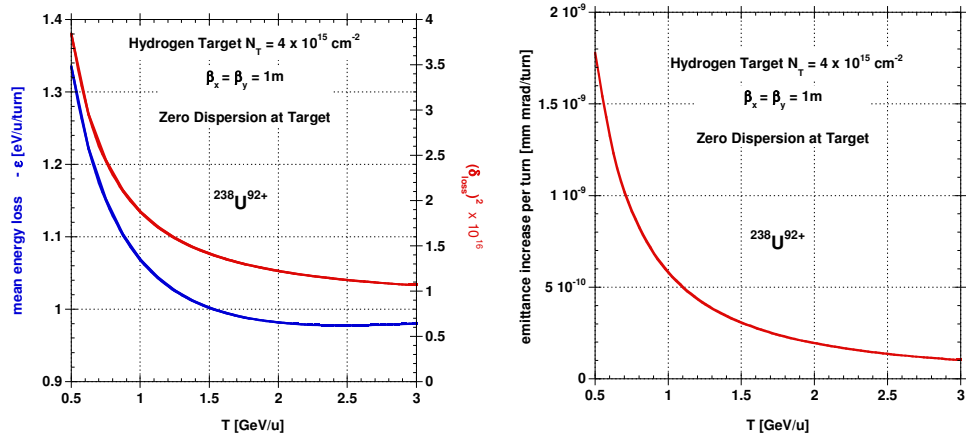


Figure 4.1: Mean energy loss and mean squared momentum deviation (left plot) and emittance increase per turn (right plot) due to the beam-target interaction for the stable $^{238}\text{U}^{92+}$ ion beam.

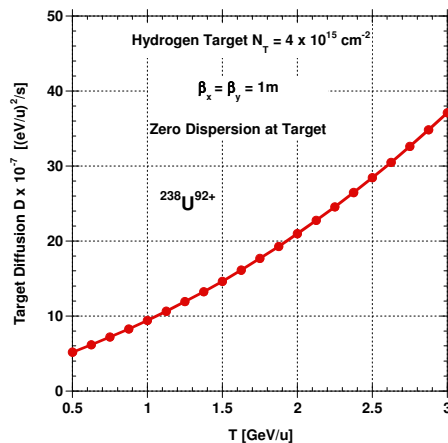


Figure 4.2: Target diffusion versus energy per nucleon for $^{238}\text{U}^{92+}$

4.1.2 Xenon Target

The following Figure 4.3 and Figure 4.4 show the mean energy loss, mean square momentum deviation and emittance increase per turn for a $^{134}\text{Xe}^{54}$ target with density $N_T = 1 \cdot 10^{13} \text{ atoms/cm}^2$.

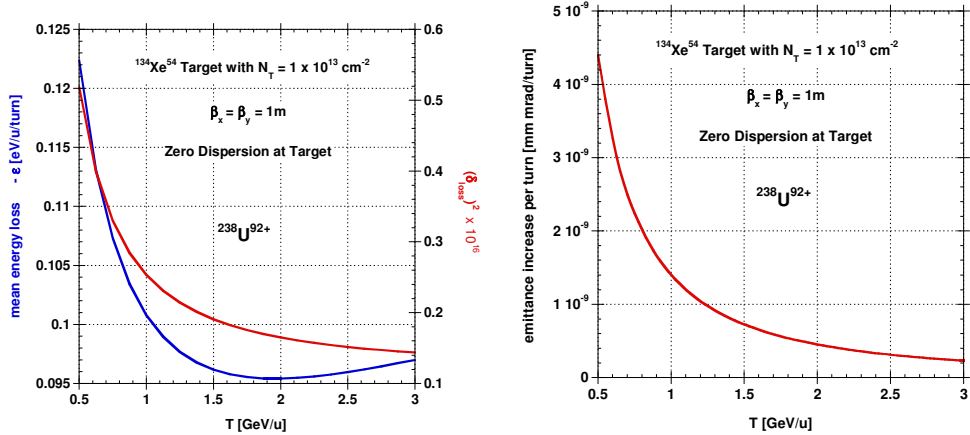


Figure 4.3: Mean energy loss and mean squared momentum deviation (left plot) and emittance increase per turn (right plot) due to the beam-target interaction for the stable $^{238}\text{U}^{92+}$ ion beam and $^{134}\text{Xe}^{54}$ target.

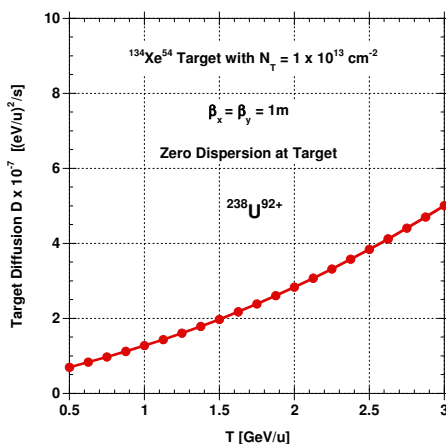


Figure 4.4: Target diffusion versus energy per nucleon for a $^{238}\text{U}^{92+}$ beam and $^{134}\text{Xe}^{54}$ target

From the scaling laws above we conclude that in the case of an $^{132}\text{Sn}^{50+}$ ion beam the mean squared momentum deviation δ_{loss}^2 and correspondingly the target diffusion term is nearly the same since the ratios Z/A of both ion species are nearly the same. The mean energy loss per nucleon is in the case of an $^{132}\text{Sn}^{50+}$ ion beam nearly a factor of two smaller.

4.2 Beam-Target Interaction of an Antiproton Beam

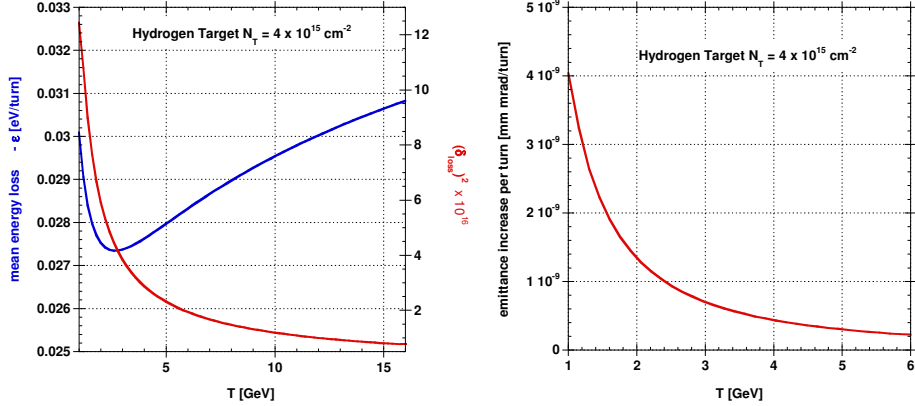


Figure 4.5: Mean energy loss and mean squared momentum deviation (left plot) and emittance increase per turn (right plot) due to the beam-target interaction an antiproton beam and a hydrogen target.

Figure 4.5 displays the beam-target interaction of an antiproton beam with a hydrogen target of thickness $N_T = 4 \cdot 10^{15} \text{ atoms/cm}^2$.

5 Intrabeam Scattering

Intrabeam scattering (IBS) [52, 53] caused by small-angle Coulomb scattering in a charged beam becomes an important issue specifically for heavy ions since the growth rates are proportional to Z^4 / A^2 . IBS effects increases for lower energies as $1/\beta^3\gamma^4$ and grows with the number of ions N stored in the ring. It also rises with a reduction in emittance as $\sim 1/(\epsilon_x\epsilon_y)$. If the beam is bunched the IBS rates also increase with decreasing bunch length σ_s . It is shown below that IBS is the dominating heating mechanism that dictates the limit of the equilibrium energy or momentum spread of an ion beam as long as the strong mean energy

loss is compensated with a barrier bucket cavity. IBS may become a severe limitation when the ion beam is cooled in all planes simultaneously.

In our simulations we adopt the Martini model [52, 53] for IBS predictions which includes the variation of the TWISS parameters around the ring. We assume that the transverse phase space motion is not coupled. In this case the growth rates which strongly depend on the optics lattice structure of the ring can be obtained at any location in the machine. The actual growth rates observed over a time long compared with the revolution period are found by averaging the individual growth rates over the circumference of the ring.

We utilized the HESR lattice as shown in Figure 5.1 with $\gamma_{tr} = 6.23$ and the tune value $Q_x = Q_y = 7.2$. The lattice is optimized for the beta function at the PANDA location, $\beta_x = \beta_y = 1m$. The dispersion in the long straights is zero for optimal target operation and stochastic cooling application.

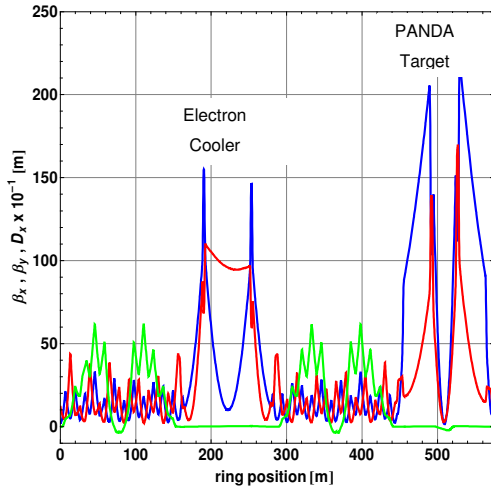


Figure 5.1: HESR lattice with $\gamma_{tr} = 6.23$ and $Q_x = Q_y = 7.2$. The Dispersion function (green) is multiplied with 10. The dispersion is zero in the long straights and at the PANDA location $\beta_x = \beta_y = 1m$. Red: Vertical betatron function, Blue: Horizontal betatron function

The following IBS growth rates are determined from

$$\text{Momentum spread growth rate} \quad \frac{I}{\tau_p} = \frac{1}{\sigma_p^2} \frac{d\sigma_p^2}{dt} \quad (5.1)$$

$$\text{Emittance growth rate} \quad \frac{I}{\tau_{\epsilon_{x,y}}} = \frac{1}{\epsilon_{x,y}} \frac{d\epsilon_{x,y}}{dt} \quad (5.2)$$

where x, y denote the horizontal and vertical plane, respectively. The relative momentum spread is $\sigma_p = \Delta p / p$.

We obtain the corresponding momentum spread diffusion rate from

$$D_{\sigma_p^2} = \frac{I}{2} \frac{d\sigma_p^2}{dt} = \frac{1}{2} \sigma_p^2 \frac{I}{\tau_p} \quad (5.3)$$

and the diffusion rate in energy space is evaluated from

$$D_{\Delta E^2} = (\beta^2 E)^2 \frac{1}{2} \sigma_p^2 \frac{I}{\tau_p} \quad (5.4)$$

with the unit $(eV/u)^2 / s$.

Figure 5.2 and Figure 5.3 present the IBS calculations for a $^{238}U^{92+}$ DC-beam with $N = 10^8$ ions for the two energies 740 MeV/u and 3 GeV/u below transition energy. It is assumed that the initial rms emittances $\epsilon_x = \epsilon_y = 0.125 \text{ mm mrad}$ at 740 MeV/u injection energy can be scaled including 25% dilution when the beam is accelerated to 3 GeV/u . The beam emittance is cooled such that it is kept almost unchanged during cooling.

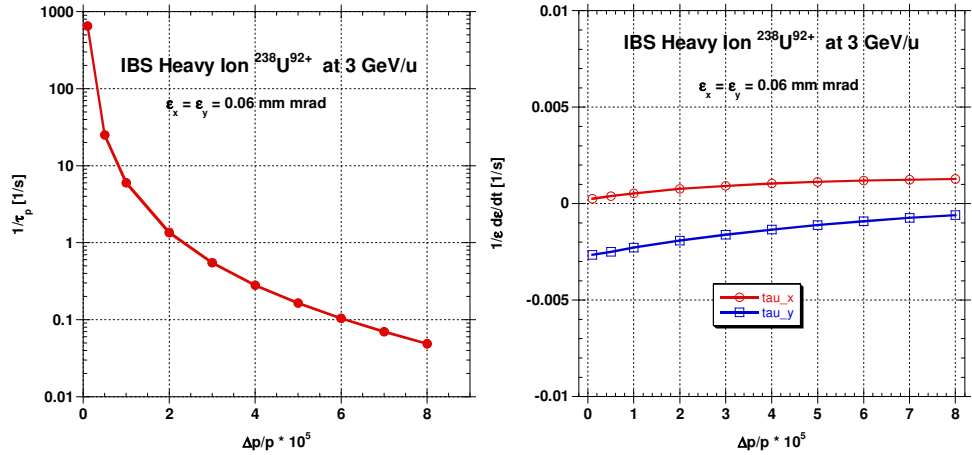


Figure 5.2: IBS momentum growth rate as described in the text (left) and emittance (red: horizontal, blue: vertical) growth rates (right) as a function of relative momentum spread. The initial emittance is kept fixed at $\epsilon_{x,y} = 0.06 \text{ mm mrad}$ (rms). The ion number is $N = 10^8$.

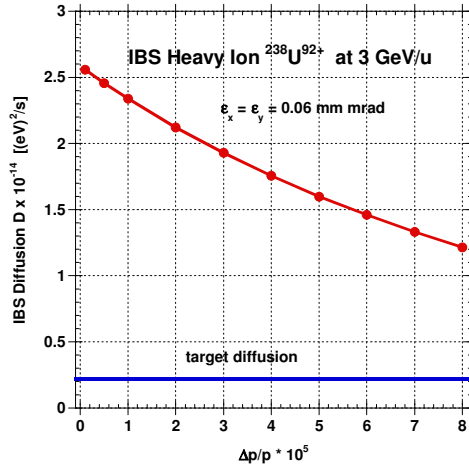


Figure 5.3: The diffusion rate in energy space in comparison with the target diffusion. Note the rates are multiplied with mass number squared. The ion number is $N = 10^8$.

Figure 5.2 illustrates that the emittance increase per turn is negligible in case of IBS as long as the emittance is kept fixed (not cooled) at $\epsilon_{x,y} = 0.06 \text{ mm mrad}$. Figure 5.3 demonstrates that the IBS diffusion rate prevails the target diffusion rate in the heavy ion beam cooling.

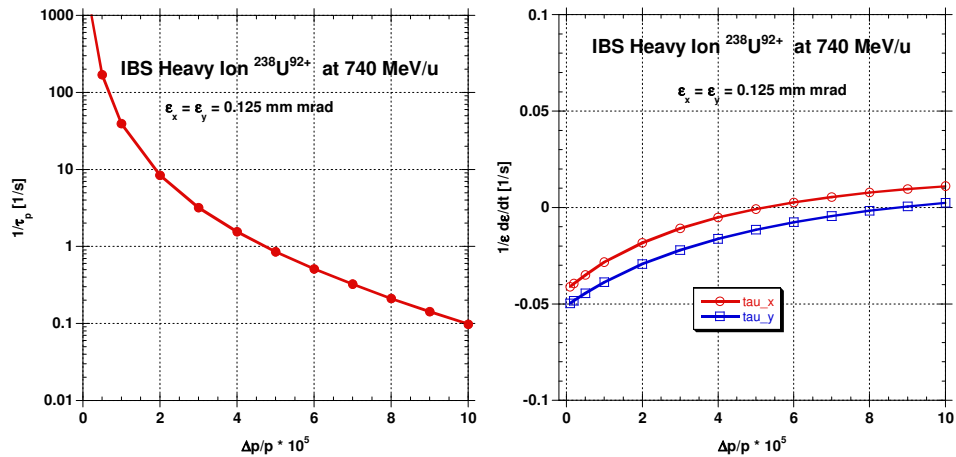


Figure 5.4: IBS momentum growth rate as described in the text (left) and emittance growth rates (right) as a function of relative momentum spread at 740 MeV/u. The initial emittance is kept fixed at $\epsilon_{x,y} = 0.125 \text{ mm mrad}$ (rms). The ion number is $N = 10^8$

The IBS simulation results at 740 MeV/u are shown in Figure 5.4 and Figure 5.5.

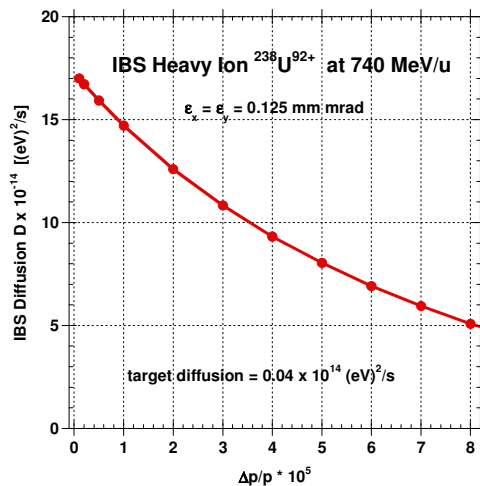


Figure 5.5: The diffusion rate in energy space in comparison with the target diffusion. Note the rates are multiplied with mass number squared. The ion number is $N = 10^8$.

As expected the IBS rates are increased at the lower energy albeit the emittance is larger due to the strong energy dependency. Nevertheless the emittance rate is small and negligible for the considered cooling rates. Also in this case we observe that the diffusion induced by the beam-target interaction is much smaller than the diffusion due to IBS.

It is interesting to note that the IBS theory predicts a negative growth rate for the vertical emittance, Figure 5.2, leading to vertical cooling while heating is visible in the other two planes. This is due to the fact that below transition energy the six-dimensional phase space is conserved and the inter-particle Coulomb collisions lead only to an exchange of energy in the phase space planes. In our example this effect is especially pronounced if the momentum growth rate becomes large as this is the case for 740 MeV/u , see Figure 5.4. Here, we observe cooling in the transverse planes if the momentum growth rate is increasing.

The IBS growth rates for a beam of 10^{10} antiprotons at 3 GeV injection energy are shown in Figure 5.6. As expected the growth rates are smaller for the smaller charge state of the beam.

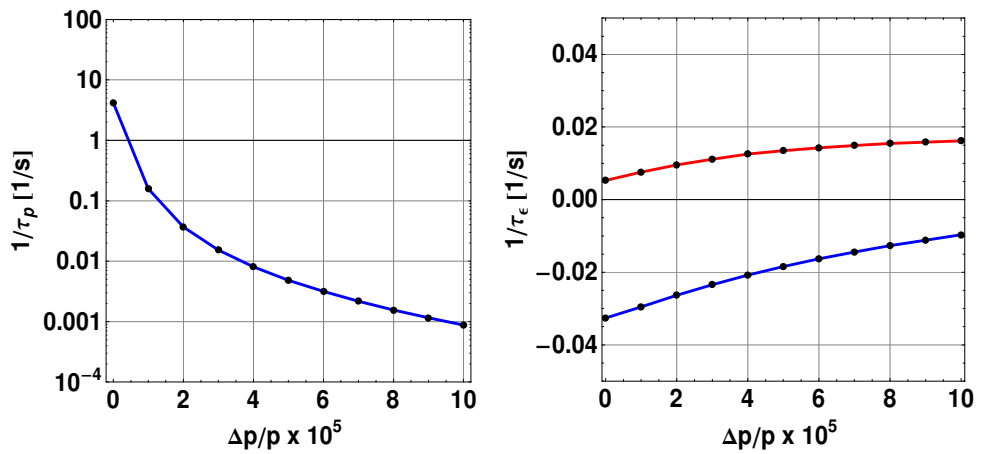


Figure 5.6: Intrabeam scattering rates for a beam with $N = 10^{10}$ antiprotons at 3 GeV and a fixed emittance $\epsilon_x = \epsilon_y = 0.125 \text{ mm mrad}$. Left: Momentum spread growth rate. Right: Horizontal (red) and vertical (blue) emittance growth rate multiplied by 1000.

6 Synchrotron Phase Space Motion

In this chapter we briefly describe the synchrotron motion of charged particles subject to rf fields introduced by the cavities installed in the accelerator ring [54] with the emphasis on the motion in barrier buckets.

We consider a particle with nominal momentum p_0 (reference particle) which has the angular revolution frequency ω_0 and assume that the particle is in the middle of the accelerating gap of the cavity at time t_0 . At the middle of the cavity gap we assume that the path length s is zero, $s(t_0)=0$. At the time $t=s/v+t_0$ the particle with velocity v reaches the position s in the ring. If R is the average machine radius then $\theta=s/R$ is the azimuth of the particle at position s . With $\omega_0=d\theta_0/dt=v/R$ for the nominal particle we can calculate the time the particle arrives the azimuth θ_0 as $t=\theta_0/\omega_0+t_0$. Therefore, the nominal particle possesses in the accelerating gap the rf phase $\omega_{rf}t_0=\omega_{rf}t-h\theta_0$ where ω_{rf} is the angular frequency of the cavity. We assume that the angular frequency of the cavity is an integer multiple h of the angular revolution frequency ω_0 , i.e., $h=\omega_{rf}/\omega_0$.

The rf phase ϕ at the accelerating gap for an arbitrary particle is therefore

$$\phi(t) = \omega_{rf} t - h\theta(t) \quad (6.1)$$

For the reference particle with momentum p_0 the accelerating phase is kept constant at ϕ_0 from turn to turn since for $d\theta_0/dt=\omega_0$ and $h=\omega_{rf}/\omega_0$ we conclude that the change of the synchronous phase ϕ_0 with time is $d\phi_0/dt=\omega_{rf}-hd\theta_0/dt=\omega_{rf}-h\omega_0=0$. The rate of change of the relative phase $\phi-\phi_0$ with time for an arbitrary particle is then

$$\begin{aligned} \frac{d\phi}{dt} &= \frac{d}{dt}(\phi-\phi_0) = -h\left(\frac{d\theta}{dt} - \frac{d\theta_0}{dt}\right) = -(\omega - \omega_0) \\ &= -h\omega_0 \frac{\eta}{\beta^2 E} \Delta E \end{aligned} \quad (6.2)$$

where we have used the relations (2.45) and (2.48) with the definition of the ring frequency slip factor $\eta=I/\gamma^2 - I/\gamma_{tr}^2$. The total energy per nucleon of a reference ion is denoted by E .

The energy change per nucleon of an arbitrary particle w.r.t the reference particle with charge Ze and mass number A obeys the equation

$$\frac{d}{dt}(\Delta E - \Delta E_0) = \frac{Z}{A} e \frac{\omega_0}{2\pi} (U(\phi) - U(\phi_0)). \quad (6.3)$$

The cavity voltage is $U(\phi)$ which is periodically, $U(\phi) = U(\phi + 2\pi)$, must satisfy the condition $\int_0^{2\pi} U(\phi) d\phi = 0$.

Both equations (6.2) and (6.3) together describe the particle motion in longitudinal synchrotron phase space with co-ordinates $(\phi, \Delta E)$.

Before discussing the equation of motion particularly for barrier cavities we introduce the Hamiltonian of the synchrotron motion as is similarly done in classical mechanics. This generalization allows a detailed discussion of the phase space motion.

The *Hamiltonian* [54] in phase space co-ordinates $(\phi, \Delta E/h\omega_0)$ corresponding to the equation of motion (6.2) and (6.3) reads

$$H(\phi, \frac{\Delta E}{h\omega_0}) = -\frac{1}{2} (h\omega_0)^2 \frac{\eta}{\beta^2 E} \left(\frac{\Delta E}{h\omega_0} \right)^2 + Ze \frac{1}{2\pi h} U_0 [\Gamma\phi + \Pi(\phi)] \quad (6.4)$$

where $\Gamma = g(\phi_s)$ and the integrated voltage shape is $\Pi(\phi) = -\int_0^\phi g(\tilde{\phi}) d\tilde{\phi}$. The arbitrary cavity

voltage is $U(\phi) = U_0 \cdot g(\phi)$ with the same conditions as required in eq. (6.3). The shape of the voltage is given by $g(\phi)$ and the peak voltage is U_0 .

The time evolution of the particles in phase space is uniquely determined by the system of Hamilton's equations [54]

$$\frac{d\phi}{dt} = \frac{\partial H}{\partial(\Delta E/h\omega_0)} \quad \text{and} \quad \frac{d(\Delta E/h\omega_0)}{dt} = -\frac{\partial H}{\partial\phi} \quad (6.5)$$

from which we deduce the equations of motion (6.2) and (6.3).

The co-ordinate pair $(\phi, \Delta E/h\omega_0)$ should be applied for acceleration treatment since in these coordinates the phase space $[eV \cdot s/u]$ is invariant during acceleration.

The solution of Hamilton's equations (6.5) describes curves in phase space which we discuss for a barrier bucket cavity below.

The case of a sinusoidal voltage $U(\phi) = U_0 \sin(\phi)$ used for particle acceleration is outlined in detail in [54, 55]. Here we only summarize important quantities.

The *bucket half height* ΔE_b per nucleon is the maximum available height of the stable area (bounded motion) that is separated from the unbounded motion by the separatrix. The bucket half height per nucleon is given by

$$\Delta E_b = \sqrt{\frac{2\beta^2 E |ZeU_0|}{A\pi h |\eta|}} \cdot Y(\phi_0) \quad (6.6)$$

where the bucket height factor

$$Y(\phi_0) = \left| \cos \phi_0 - \frac{\pi - 2\phi_0}{2} \sin \phi_0 \right|^{1/2} \quad (6.7)$$

determines the ratio of the maximum bucket height to the height of the stationary bucket ($\phi_0 = 0$).

The *bucket area* \mathfrak{A}_b per nucleon $[eV \cdot s/u]$ (of the stable motion) is obtained from

$$\mathfrak{A}_b = \frac{16\beta}{\omega_0} \cdot \sqrt{\frac{E |ZeU_0|}{2\pi Ah |\eta|}} \cdot \alpha(\phi_0) \quad (6.8)$$

where $\alpha(\phi_0)$ denotes the ratio of the accelerating bucket area to the stationary bucket area. It is approximately given by [55]

$$\alpha(\phi_0) \approx \frac{1 - \sin \phi_0}{1 + \sin \phi_0}. \quad (6.9)$$

The synchrotron motion with a stationary barrier bucket is usually discussed in the phase space $(\tau, \Delta E)$ where the time in the bunch is defined as $\tau := \phi/\omega_0$. The Hamiltonian (6.4) becomes then using $h = I$ and $\phi_0 = 0$

$$H(\tau, \Delta E) = -\frac{I}{2} \frac{\eta}{\beta^2 E} (\Delta E)^2 + V(\tau) \quad (6.10)$$

with the rf potential

$$V(\tau) = Ze \frac{\omega_0}{2\pi} U_0 \Pi(\tau) \quad (6.11)$$

where the integrated voltage shape is

$$\Pi(\tau) = -\int_0^\tau g(\tilde{\tau}) d\tilde{\tau}. \quad (6.12)$$

The barrier voltage is given by $U_0 \cdot g(\tau)$. Note that the rf potential is only determined up to an arbitrary additive constant.

With the corresponding Hamilton's equations (6.5) the synchrotron motion follows from

$$\frac{d}{dt} \tau = -\frac{\eta}{\beta^2 E} \Delta E \quad \text{and} \quad \frac{d}{dt} \Delta E = \frac{Ze}{A} \frac{\omega_0}{2\pi} U_0 g(\tau). \quad (6.13)$$

Since the Hamiltonian (6.10) is time independent, i.e., $dH/dt = 0$, the Hamiltonian is a constant of motion, $H(\tau, \Delta E) = K$. The solution of eq. (6.13) is a motion of a phase point $(\tau(t), \Delta E(t))$ in the phase space. Its image is a curve $(\tau(t), \Delta E(t))$ in which $\Delta E(t)$ follows from eq. (6.10) and is given by

$$\Delta E = \pm \sqrt{\frac{2\beta^2 E}{\eta} [V(\tau) - K]} \quad (6.14)$$

We can distinguish two cases

$$1.) \quad \eta > 0 \quad (\gamma < \gamma_r) \quad \text{then} \quad V(\tau) > K \quad (6.15)$$

$$2.) \quad \eta < 0 \quad (\gamma > \gamma_{tr}) \quad \text{then} \quad V(\tau) < K \quad (6.16)$$

If the charge state changes its sign then the barrier voltage must be reversed.

Since the Hamiltonian is time independent there is one and only one phase space curve $(\tau(t), \Delta E(t))$ passing through every phase space point. I.e., phase space curves for different levels K cannot cross. To each point on a phase space curve we can assign the phase velocity vector $(d\tau(t)/dt, d\Delta E(t)/dt)$, eq. (6.13), which is a tangent at each phase space point $(\tau(t), \Delta E(t))$ and represents the direction of the phase space flow. Below transition, $\eta > 0$, and the flow is to the left for $\Delta E > 0$, since $d\tau(t)/dt < 0$. In the lower half plane where $\Delta E < 0$, the flow is to the right. A particle is at rest when $\Delta E = 0$. Above transition, $\eta < 0$, the motion is clockwise.

In the following we consider as illustration an example for an antiproton beam ($Z = -1$) in the HESR at $3.8 \text{ GeV}/c$. The ring frequency slip factor is $\eta = 0.03$, i.e., the working point is below transition energy. The revolution period is $T_0 = 1.971 \mu\text{s}$ and $\beta = 0.971$. For a half sine-wave barrier the voltage consists of two sinusoidal half waves of length $T_l = 100 \text{ ns}$ each, $U(\tau) = U_0 \sin(2\pi \frac{\tau}{2T_l})$. The barrier peak voltage is $U_0 = 2 \text{ kV}$. The gap (distance) between the two barrier pulses is chosen to be $T_g = 500 \text{ ns}$ in this example. The barrier voltage and the potential $V(\tau) = Ze \frac{\omega_0}{2\pi} U_0 \Pi(\tau)$ are shown in Figure 6.1.

A plot of the phase space in the co-ordinates $(\tau, \Delta p/p)$ where $\Delta p/p = \Delta E/(\beta^2 E)$ is the relative momentum spread is shown in Figure 6.2. According to case 1, eq. 5.15, the motion can be bounded or unbounded for $0 < K \leq 64 \text{ eV}/u$. For $K < 0$ the motion is unbounded, see Figure 6.1.

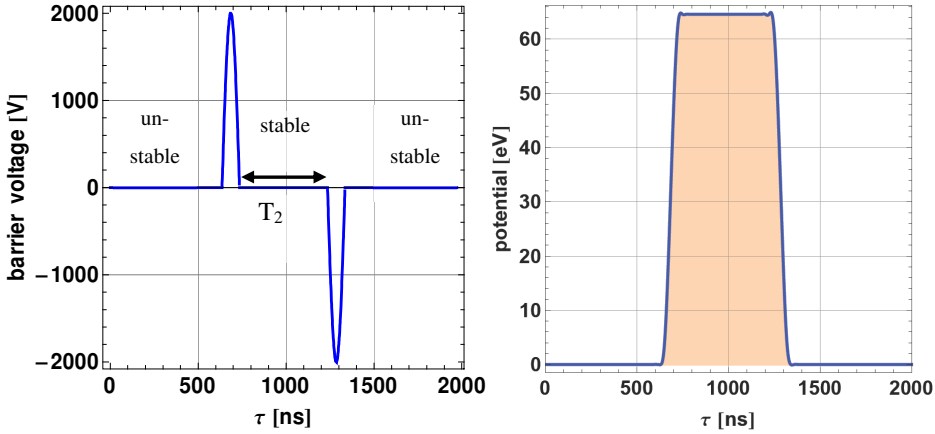


Figure 6.1: Left figure: barrier voltage plotted versus time in the bunch $0 \leq \tau \leq T_0$. Each pulse has a length of $T_1 = 100 \text{ ns}$. The distance (gap) of the two pulses is $T_2 = 500 \text{ ns}$. The right part of the figure shows the potential in the Hamiltonian (6.10). The stable (bounded) area is indicated as the shaded region.

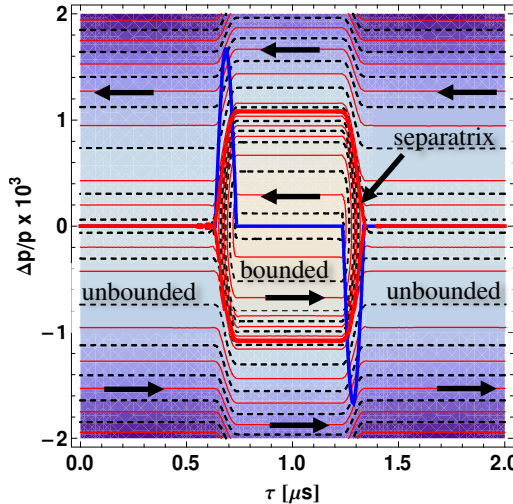


Figure 6.2: Phase space portrait of the synchrotron motion in the barrier shown in Figure 6.1. For three phase space curves arrows indicate the direction of synchrotron motion. The separatrix is drawn in bold red. The phase space curves do not cross each other since the Hamiltonian is constant along each curve. Particles inside the separatrix have two turning points in the potential where they are reflected. Their motions are closed and periodic curves (libration). If the amplitude gets large the motion outside the separatrix is no longer bounded.

The voltage shape is drawn in blue. Within the separatrix (depicted in red), i.e. the curve given by $H(\tau, \Delta p/p) = K = 0$, the synchrotron motion has two turning points in the rf potential (shaded area in Figure 6.1, right panel) so that the phase space curves are closed (bounded motion). They represent a periodic motion (libration). The area enclosed by the separatrix is the *stable bucket*.

In the following example we consider a barrier made up by two full one wave length barrier voltages, $U(\tau) = U_0 \sin(2\pi \frac{\tau}{2T_l})$ with $T_l = 100\text{ ns}$, as shown in Figure 6.3. The barrier pulse length is now $2T_l = 200\text{ ns}$ each or barrier frequency $f_{BB} = 5\text{ MHz}$. The barrier peak voltage is $U_0 = 2\text{ kV}$. Barriers of such kind where the gap length can be increased from zero up to a certain length by moving the barrier voltages will be applied for the antiproton accumulation process as outlined in detail in the first part of the book. The antiproton beam bunch delivered by the collector ring CR will be injected into the middle gap of the barriers every ten seconds. The already stored beam will be accumulated in the (stable) accumulation area as shown in Figure 6.3. A full description of the accumulation process of antiprotons in the HESR is presented in a later chapter.

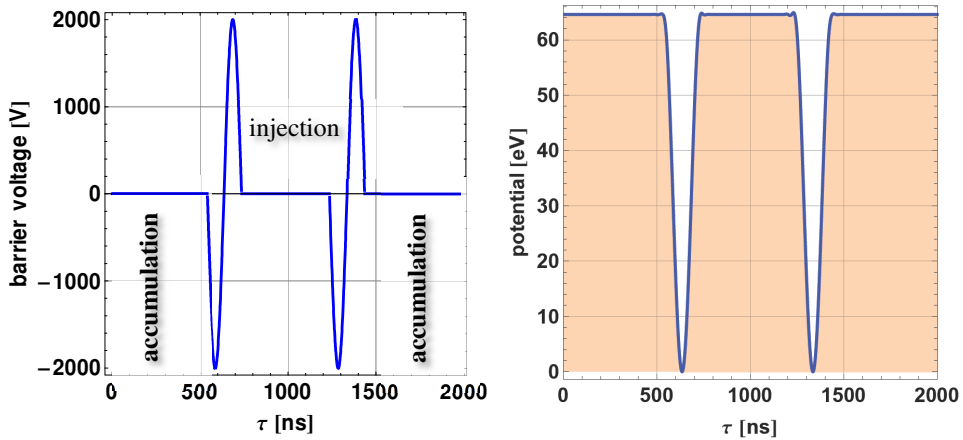


Figure 6.3: Left figure: barrier voltage plotted versus time in the bunch $0 \leq \tau \leq T_0$. Each pulse has a length of $2T_l = 200\text{ ns}$. The gap between the two barriers amounts 500 ns . The right part of the figure shows the potential in the Hamiltonian (6.10). The stable (bounded) area is indicated as the shaded region.

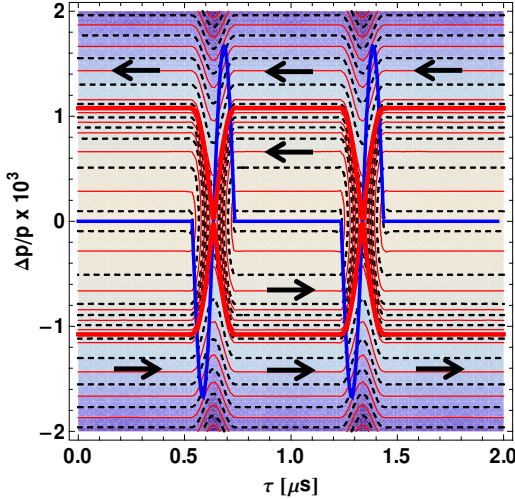


Figure 6.4: Phase space portrait of the synchrotron motion in the rf field of the barriers shown in figure 5.3. The separatrix is drawn in bold red. For three phase space curves arrows indicate the direction of synchrotron motion.

The important difference between the barriers depicted in the Figure 6.3 and Figure 6.1 is that the barriers shown in Figure 6.3 now provide two stable areas. The gap in the middle ($0.65 \mu s \leq \tau \leq 1.35 \mu s$) and the one in the range $0.0 \mu s \leq \tau \leq 0.65 \mu s$ as well as $1.35 \mu s \leq \tau \leq T_0$ are shown in the phase space plot of Figure 6..

The *half barrier height per nucleon* ΔE_b of the stable area in a barrier bucket with voltage $U(\tau) = U_0 \sin(2\pi \frac{\tau}{2T_l})$ can be derived from the Hamiltonian (6.10) with the potential eq. (6.11) for the sine wave pulse. We obtain

$$\Delta E_b = \sqrt{\varepsilon \frac{2\beta^2 E e U_0}{\pi |\eta|} \frac{2T_l}{T_0}} \quad (6.17)$$

where the charge-to-mass ratio is $\varepsilon = |Z/A|$.

If the gap between the barriers is zero, $T_2 = 0$, and the barrier period equals the revolution period, $2T_l = T_0$, eq. (6.17) reduces to the stationary bucket height for a $h = 1$ cavity voltage, eq. (6.6).

The synchrotron motion inside the separatrix is a periodic motion. Its period can be deduced from the Hamilton's equations (6.5). The *synchrotron period* $T_s(W)$ or the *synchrotron frequency* $f_s(W) = 1/T_s(W)$ of the stable motion in the barrier bucket depends on the penetration depth W with $0 \leq W \leq T_l$ into the barrier bucket pulse of length T_l as illustrated in Figure 6.5 for antiprotons below transition energy [55]. It is found to be

$$T_s(W) = 2 \frac{T_2}{|\eta|} \frac{\beta^2 E}{|\Delta E(W)|} + 4T_C(W). \quad (6.18)$$

The first term in the equation results from the contribution in the upper and lower half plane when the particles move on straight lines outside the barrier pulses and therefore depends on the gap T_2 between the two barrier pulses as well as on the energy deviation $\Delta E(W)$ which in turn is determined by the penetration depth W .

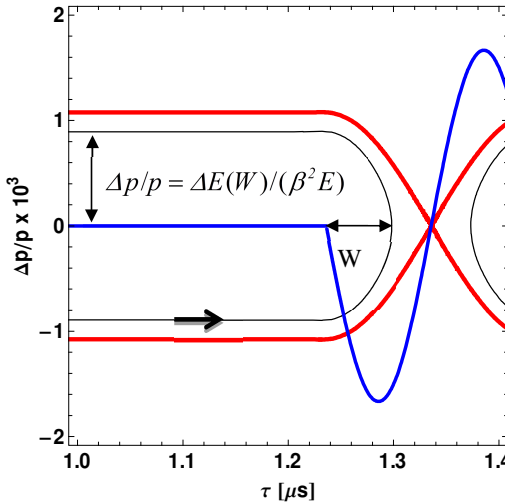


Figure 6.5: The synchrotron period of a particle moving in the stable area of the bucket depends on the penetration depth W with $0 \leq W \leq T_l$ into the barrier pulse. For a positive ring slip factor ($\gamma < \gamma_{re}$) an antiproton with a negative energy deviation moves to the right and is bended by the negative barrier voltage into the upper half plane. The path through the barrier consists of two half bends.

The second term [55] accounts for the contribution of four half bends of the phase space curve when the particle moves with a penetration depth W through the two barrier pulses. The time needed by an ion that penetrates into the barrier pulse with time W to pass one quarter bend is obtained from the quantity

$$T_c(W) = \sqrt{\frac{1}{\epsilon} \frac{\pi}{2} \frac{\beta^2 E}{|\eta| e U_0} \frac{T_0}{T_l}} \cdot \int_0^W \frac{d\tau}{\sqrt{\cos(\pi \frac{\tau}{T_l}) - \cos(\pi \frac{W}{T_l})}}. \quad (6.19)$$

The energy deviation $\Delta E(W)$ as a function of the penetration depth W into the barrier which appears in eq. (6.19) is deduced from the Hamiltonian (6.10) for the sine wave pulse

$$\Delta E(W) = \Delta E_b \cdot \sqrt{\frac{1}{2} \cdot \left\{ 1 - \cos\left(\pi \frac{W}{T_l}\right) \right\}} \quad (6.20)$$

with the half barrier bucket height ΔE_b given in eq. (6.17).

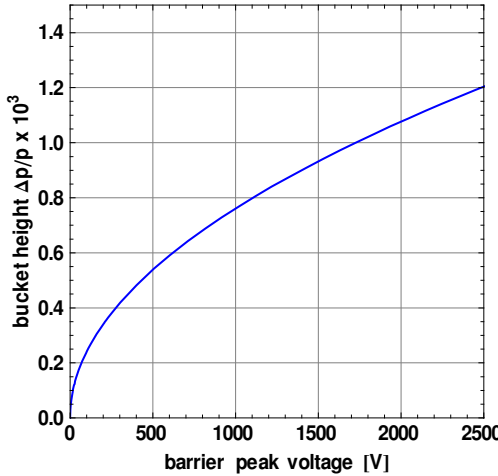


Figure 6.6: Bucket height $\Delta p/p$ times 10^3 versus barrier peak voltage.

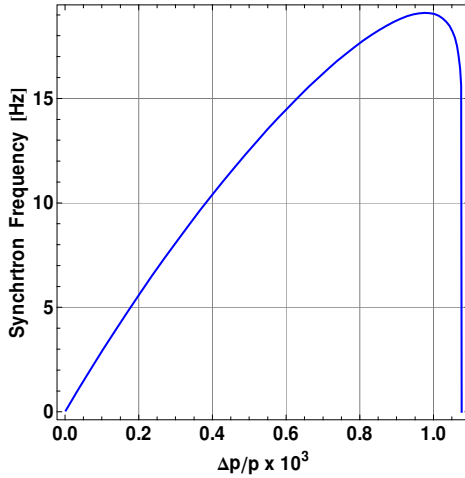


Figure 6.7: Synchrotron frequency versus $\Delta p/p$ times 10^3 . At the boundary (separatrix) the synchrotron motion becomes zero.

The stable bucket area \mathfrak{A}_b per nucleon between two sine-wave barrier pulses is easily deduced from eq. (6.20) which yields

$$\mathfrak{A}_b = \left(\frac{8}{\pi} T_1 + 2T_2 \right) \Delta E_b. \quad (6.21)$$

In Figure 6.6 we show the barrier half height $\Delta p/p = \Delta E/(\beta^2 E)$ as a function from the barrier peak voltage U_0 for the barriers with the pulse length $T_1 = 100\text{ ns}$.

The synchrotron frequency versus relative momentum deviation is plotted in Figure 6.7 for the barriers with a gap of $T_2 = 500\text{ ns}$. The synchrotron frequency increases linearly from zero with the momentum deviation and becomes again zero on the separatrix.

Appendix A Autocorrelation Function and Power Density

In this chapter some useful formulae and rules are given. For details the reader is referred to the literature [31].

The Fourier Transform of a function $w(t)$ is defined as

$$\hat{w}(\omega) = \int_{-\infty}^{\infty} w(t) e^{-i\omega t} dt \quad (\text{A.1})$$

with the inverse

$$w(t) = \frac{1}{2\pi} \int_{-\infty}^{\infty} \hat{w}(\omega) e^{i\omega t} d\omega \quad (\text{A.2})$$

For random variables $w(t)$ we define the autocorrelation function $R(t, t')$ by the average of $R(t, t') = \langle w(t) \cdot w^*(t') \rangle$. The Fourier Transform of the autocorrelation function gives

$$\Gamma(\omega, \omega') = \iint R_x(t_1, t_2) e^{-i(\omega t_1 + \omega' t_2)} dt_1 dt_2. \quad (\text{A.3})$$

If the random process is quasi stationary, i.e. the autocorrelation function depends only on the time difference, $R_x(t_1, t_2) = R_x(t_2 - t_1)$, one finds the relation

$$\Gamma(\omega, \omega') = 2\pi \delta(\omega + \omega') \cdot S(\omega) \quad (\text{A.4})$$

where the power density $S(\omega)$ is the Fourier transform of the autocorrelation function $S(\omega) = \int R_x(\tau) e^{-i\omega\tau} d\tau$. For the definition of the delta function $\delta(\omega)$ see below.

Using the definition of the Fourier Transform, (A.1), the autocorrelation function is given by

$$R(\tau) = \frac{1}{2\pi} \int S(\omega) e^{i\omega\tau} d\omega \quad (\text{A.5})$$

and

$$R_x(0) = \frac{1}{2\pi} \int S(\omega) d\omega = \int S(\omega) \frac{d\omega}{2\pi} = \int S(2\pi f) df \quad (\text{A.6})$$

gives the power. The angular frequency is $\omega = 2\pi f$. The spectral density as measured with a spectrum analyzer at frequency f is given by $\tilde{S}(f) = S(2\pi f)$.

If $\hat{x}(\omega)$ denotes the Fourier transform of the signal x (or of one of its realisation) then

$$\hat{x}(\omega) \cdot \hat{x}^*(\omega') = \iint x(t_1) \cdot x^*(t_2) e^{-i(\omega t_1 - \omega' t_2)} dt_1 dt_2. \quad (\text{A.7})$$

Taking the average on both sides of eq. (A.7) yields with eq. (A.3) the important lemma

$$\langle \hat{x}(\omega) \cdot \hat{x}^*(\omega') \rangle = \Gamma(\omega, -\omega') \quad (\text{A.8})$$

or with eq. (A.4)

$$\langle \hat{x}(\omega) \cdot \hat{x}^*(\omega') \rangle = 2\pi \delta(\omega - \omega') \cdot S(\omega). \quad (\text{A.9})$$

Integrating both sides w.r.t. ω yields the power density $S(\omega')$. This allows us to derive the spectral power density once the Fourier transform of the signal is known.

The autocorrelation function of a stationary process has the property that $\lim_{\tau \rightarrow \infty} R(\tau) = \langle x \rangle^2$ where the average of the random variable is given by $\langle x \rangle$. The spectral density then contains a delta pulse at zero frequency, $S(\omega) = \tilde{S}(\omega) + 2\pi \langle x \rangle^2 \delta(\omega)$ with $\tilde{S}(\omega)$ denoting the random process where the mean $\langle x \rangle$ has been removed.

Appendix B Distributions

In this chapter some basic distributions and their properties which are frequently applied in this book are discussed. For a comprehensive and rigorous discussion see e.g. [56]. In the following we consider real valued and indefinitely differentiable functions $\varphi(t)$ which vanish outside an interval $[-R, R]$. These functions are necessarily continuous. The set of these functions is called S .

Consider the function

$$w_\varepsilon(t) = \frac{1}{\pi} \frac{\varepsilon}{t^2 + \varepsilon^2} \quad (\text{B.1})$$

with positive parameter $\varepsilon > 0$. For every $\varepsilon > 0$ the functions are symmetric w.r.t. zero, are positive and vanish as $|t|$ tends to infinity. The functions are bell-shaped and centered around zero. The peak value increases while the width decreases as ε approaches zero. However, it is easy to see that the area is constant, $\int_{-\infty}^{\infty} w_\varepsilon(t) dt = 1$, for every ε .

We then evaluate the integral for every $\varphi \in S$

$$\int_{-\infty}^{\infty} w_\varepsilon(t) \varphi(t) dt = \int_{-\infty}^{\infty} w_\varepsilon(t) (\varphi(t) - \varphi(0)) dt + \varphi(0) \int_{-\infty}^{\infty} w_\varepsilon(t) dt \quad (\text{B.2})$$

Since, per definition, φ is continuous, i.e., $\varphi(x) \rightarrow \varphi(0)$ when $x \rightarrow 0$, the first integral on the right hand side of eq. (B.2) vanishes as ε approaches zero one finds

$$\lim_{\varepsilon \rightarrow 0+} \int_{-\infty}^{\infty} w_\varepsilon(t) \varphi(t) dt = \varphi(0). \quad (\text{B.3})$$

We then define the *delta distribution* $\delta(t)$ as

$$\lim_{\varepsilon \rightarrow 0+} \int_{-\infty}^{\infty} w_\varepsilon(t) \varphi(t) dt = \int_{-\infty}^{\infty} \delta(t) \varphi(t) dt = \varphi(0) \quad (\text{B.4})$$

or symbolically written

$$\lim_{\varepsilon \rightarrow 0+} w_\varepsilon(t) = \delta(t). \quad (\text{B.5})$$

From eq. (B.4) it is obvious that the delta distribution $\delta(t)$ is a linear mapping which associates to every function φ of S the real image value $\varphi(0)$. Inserting in eq. (B.4) the identity mapping one finds the property of the delta distribution

$$\lim_{\varepsilon \rightarrow 0+} \int_{-\infty}^{\infty} w_\varepsilon(t) dt = \int_{-\infty}^{\infty} \delta(t) dt = 1 \quad (\text{B.6})$$

which means that the area of the delta “function” taken over a small range around zero is equal to unity.

From eq. (B.4) one deduces that the delta function $\delta(t)$ obeys the scaling rule

$$\delta(at) = \frac{1}{|a|} \delta(t) \quad (\text{B.7})$$

for the non-vanishing scaling parameter a . With $a = -1$ we see that the delta function is an even “function”, $\delta(t) = \delta(-t)$.

Eq. (B.4) can be generalized to

$$\lim_{\varepsilon \rightarrow 0+} \int_{-\infty}^{\infty} w_{\varepsilon}(t-\tau) \varphi(t) dt = \int_{-\infty}^{\infty} \delta(t-\tau) \varphi(t) dt = \varphi(\tau). \quad (\text{B.8})$$

The Fourier Transform of the delta function is $\hat{\delta}(\omega) = \int \delta(t) e^{-i\omega t} dt$ and, due to the fact that for any function $h(t)$ the relation $\delta(t)h(t) = \delta(t)h(0)$ is valid according to (B.4), one has $\hat{\delta}(\omega) = 1$.

An inverse Fourier Transform according to (A.2) then shows

$$\delta(t) = \frac{1}{2\pi} \int_{-\infty}^{\infty} e^{i\omega t} d\omega \quad \text{and similarly} \quad \delta(\omega) = \frac{1}{2\pi} \int_{-\infty}^{\infty} e^{i\omega t} dt \quad (\text{B.9})$$

The next important distribution is the *Cauchy Principal Value*. It is defined by

$$P \int_{-\infty}^{\infty} \frac{\varphi(x)}{x} dx = \lim_{\varepsilon \rightarrow 0+} \left(\int_{-\infty}^{-\varepsilon} \frac{\varphi(x)}{x} dx + \int_{\varepsilon}^{\infty} \frac{\varphi(x)}{x} dx \right) \quad (\text{B.10})$$

where the singularity at $x = 0$ is excluded with the small interval $[-\varepsilon, \varepsilon]$.

We now consider the distribution $\int_{-\infty}^{\infty} \frac{\varphi(x)}{x \pm i\varepsilon} dx$.

The integral can be written as

$$\begin{aligned}
\int_{-\infty}^{\infty} \frac{\varphi(x)}{x \pm i\varepsilon} dx &= \int_{-\infty}^{\infty} \varphi(x) \frac{x \mp i\varepsilon}{x^2 + \varepsilon^2} dx \\
&= \int_{-\infty}^{\infty} \varphi(x) \frac{x}{x^2 + \varepsilon^2} dx \mp i \int_{-\infty}^{\infty} \varphi(x) \frac{\varepsilon}{x^2 + \varepsilon^2} dx \\
&= \int_{-\infty}^{\infty} \varphi(x) \frac{x}{x^2 + \varepsilon^2} dx \mp i\pi \int_{-\infty}^{\infty} \varphi(x) \left(\frac{1}{\pi} \frac{\varepsilon}{x^2 + \varepsilon^2} \right) dx.
\end{aligned} \tag{B.11}$$

Taking the limit for $\varepsilon \rightarrow 0+$ on both sides yields the formula

$$\lim_{\varepsilon \rightarrow 0+} \int_{-\infty}^{\infty} \frac{\varphi(x)}{x \pm i\varepsilon} dx = P \int_{-\infty}^{\infty} \frac{\varphi(x)}{x} dx \mp i\pi\varphi(0) \tag{B.12}$$

where eqs. (B.10) and (B.4) have been applied. More generally one deduces

$$\lim_{\varepsilon \rightarrow 0+} \int_{-\infty}^{\infty} \frac{\varphi(x)}{x - y \pm i\varepsilon} dx = P \int_{-\infty}^{\infty} \frac{\varphi(x)}{x - y} dx \mp i\pi\varphi(y) \tag{B.13}$$

Symbolically this is frequently written as

$$\lim_{\varepsilon \rightarrow 0+} \frac{1}{x - y \pm i\varepsilon} = P \left(\frac{1}{x - y} \right) \mp i\pi\delta(x - y). \tag{B.14}$$

The *Poisson formula*

If the Fourier Transform is given by (A.1) then for any number T the relation [31]

$$\sum_{n=-\infty}^{\infty} w(t + nT) = \frac{\omega_0}{2\pi} \sum_{n=-\infty}^{\infty} \hat{w}(n\omega_0) e^{in\omega_0 t} \tag{B.15}$$

holds with $\omega_0 = 2\pi/T$.

Appendix C Liouville Operator and Time Evolution

A general discussion of the Liouville operator, its properties and relation to the time-evolution operator is found in the literature. Here we concentrate on the major features as used in the book.

In chapter 2.10 the Liouville operator associated with the unperturbed Hamiltonian H_0 was defined as

$$L_0 g = i \{ H_0, g \} \quad (\text{C.1})$$

for any real or complex-valued function g defined on phase space $\vec{x} := (\Theta, J)$. Using the Poisson bracket one finds

$$L_0 g = i \left(\frac{\partial H_0}{\partial \Theta} \frac{\partial g}{\partial J} - \frac{\partial H_0}{\partial J} \frac{\partial g}{\partial \Theta} \right) = -i \frac{\partial H_0}{\partial J} \frac{\partial g}{\partial \Theta} \quad (\text{C.2})$$

since the Hamiltonian H_0 does not depend on azimuth in the accelerator ring.

The scalar product of any two phase space functions (real or complex-valued) which vanish sufficiently rapid at infinity is defined as

$$(f, g) = \int f^*(x) \cdot g(x) d^2 x. \quad (\text{C.3})$$

We define the *adjoint* operator A^\dagger of an operator A by the relation

$$(A^\dagger f, g) = (f, A g). \quad (\text{C.4})$$

(Note: the adjoint operator corresponds to the complex-conjugate of a complex number.)

Using the Liouville operator given in eq. (C.2) one finds

$$(L_0 f, g) = (f, L_0 g) \quad (\text{C.5})$$

which shows that the Liouville operator is self-adjoint (Hermitian)

$$L_0^\dagger = L_0. \quad (\text{C.6})$$

In chapter 2.10 it was found that for time-invariant Hamiltonian systems the equation of motion of an observable B along a phase space trajectory $\vec{x}(t) := (\Theta(t), J(t))$ is governed by

$$\frac{dB}{dt} = -\{H_0, B\} = i \cdot L_0 B \quad (\text{C.7})$$

with the solution

$$B(\vec{x}(t)) = U(t, t_0)B(\vec{x}(t_0)) \quad (\text{C.8})$$

in which the time-evolution operator is

$$U(t, t_0) = e^{-i(t-t_0)L_0}. \quad (\text{C.9})$$

For time-independent systems the time-evolution operator depends only on the time difference $t - t_0$ and not on a specific instant.

The adjoint operator is given by

$$U^\dagger(t, t_0) = e^{i(t-t_0)L_0^\dagger} = e^{i(t-t_0)L_0} \quad (\text{C.10})$$

where in the last step the property that the Liouville operator is Hermitian, eq. (C.6), has been applied. Combining eqs. (C.9) and (C.10) shows that the time evolution operator has the unitarity property

$$U^\dagger(t, t_0)U(t, t_0) = I \quad (\text{C.11})$$

where I is the unity operator. From eq. (C.11) one concludes that the inverse of the time evolution operator $U^{-1}(t, t_0)$, describing the backwards motion in time, is given by

$$U^{-1}(t, t_0) = U^\dagger(t, t_0). \quad (\text{C.12})$$

From property (C.11) it is deduced that

$$(f, g) = (U^\dagger U f, U^\dagger U g) = (U U^\dagger U f, U g) = (U f, U g) \quad (\text{C.13})$$

which shows that the time-evolution operator conserves the scalar product. Considering an observable A defined on phase space the average value is given by $\bar{A} = (A, \rho)$ with the

distribution function ρ normalized to unity. From eq. (C.13) it follows that the time-evolution operator preserves the average value of the observable A .

Furthermore from eq. (C.13) one has the important feature

$$(f, Ug) = (U^\dagger f, U^\dagger Ug) = (U^\dagger f, g). \quad (\text{C.14})$$

which is explicitly written for real-valued functions f and g as

$$\int f(x) \left(e^{-i(t-t_0)L_0} g(x) \right) dx = \int \left(e^{i(t-t_0)L_0} f(x) \right) g(x) dx \quad (\text{C.15})$$

This property has been applied in chapter 2.10 in the step from eq. (2.149) to eq. (2.150).

The same treatment as just carried out can be generalized to higher order integrals in (C.3) as they appear for the transverse BTF in chapter 3.6.

Appendix D Transverse Dipole Density with Chromaticity

The transverse dipole density (transverse Schottky noise density) has been deduced in chapter 3.4 assuming a negligible tune dependence on momentum spread of the beam. In this chapter we consider the tune as a function of momentum spread or equivalently as a function of frequency to include chromatic effects into the description of the transverse Schottky noise density. We then consider the integral in eq. (3.62)

$$\int_0^\infty \Omega^2 \Psi_0(\Omega) \delta(\omega - (k \pm Q(\Omega)) \cdot \Omega) d\Omega \quad (\text{D.1})$$

where now the tune $Q(\Omega)$ depends on angular frequency Ω . Assuming a linear behavior around the nominal frequency ω_0 we can expand $(k \pm Q(\Omega)) \cdot \Omega$ in eq. (D.1) as

$$(k \pm Q(\Omega)) \cdot \Omega \approx (k \pm Q_0 \pm \omega_0 \dot{Q}) \cdot \Omega \neq \omega_0^2 \dot{Q} \quad (\text{D.2})$$

where the average tune is given by $Q_0 = Q(\omega_0)$ and \dot{Q} is the derivative at ω_0

$$\dot{Q} = \frac{dQ}{d\Omega}(\omega_0) \quad (\text{D.3})$$

which is related to the chromaticity $\xi = (dQ/Q_0)/(dp/p_0)$ by

$$\dot{Q} = \frac{\xi}{\eta} \frac{Q_0}{\omega_0}. \quad (\text{D.4})$$

The frequency slip factor η of the ring is given in chapter 2.4. Sometimes $Q' = \xi \cdot Q_0$ is denoted as chromaticity.

Inserting (D.2) into eq. (D.1) and applying the property $\delta(a \cdot x) = \delta(x)/|a|$ of the delta function one finds the sideband frequency distributions at harmonic number k of the beam according to eq. (3.62)

$$S_d^\pm(\omega) = \frac{1}{4} \frac{(Ze)^2}{2\pi} \epsilon \beta_p \left(\frac{\omega \pm \omega_0^2 \dot{Q}}{k \pm Q_0 \pm \omega_0 \dot{Q}} \right)^2 \frac{1}{|k \pm Q_0 \pm \omega_0 \dot{Q}|} \Psi_o \left(\frac{\omega \pm \omega_0^2 \dot{Q}}{k \pm Q_0 \pm \omega_0 \dot{Q}} \right). \quad (\text{D.5})$$

Note that for zero chromaticity $\dot{Q} = 0$ the expression reduces to that given in eq. (3.65).

The sideband frequency distributions peak at

$$\omega^\pm = (k \pm Q_0) \omega_0 = (n + q_0) \omega_0. \quad (\text{D.6})$$

The tune Q_0 is decomposed in the sum of its integer part $\|Q_0\|$ and its fractional part q_0 , $Q_0 = \|Q_0\| + q_0$. Then, $k \pm Q_0 = (k \pm \|Q_0\|) \pm q_0 = n \pm q_0$.

The peak value

$$S_d^\pm(\omega^\pm) = \frac{1}{4} \frac{(Ze)^2}{2\pi} \epsilon \beta_p \omega_0^2 \frac{\Psi_o(\omega_0)}{|k \pm Q_0 \pm \omega_0 \dot{Q}|} \quad (\text{D.7})$$

is found if ω^\pm is inserted into eq. (D.5).

For narrow non-overlapping sidebands the width is deduced from the variance of the distribution

$$\sigma_\pm^2 = \int (\omega - \omega_\pm)^2 S_d^\pm(\omega) d\omega / \int S_d^\pm(\omega) d\omega. \quad (\text{D.8})$$

Using the approximation $\frac{\omega \pm \omega_0^2 \dot{Q}}{k \pm Q_0 \pm \omega_0 \dot{Q}} \approx \omega_0$ for narrow bands one deduces the width (standard deviation) of a sideband at harmonic number k including chromaticity

$$\begin{aligned}\sigma_{\pm} &= |n \pm q_0 \pm \omega_0 \dot{Q}| \sigma_{\omega} \\ &= |(n \pm q_0) \eta \pm \xi Q_0| \omega_0 \delta\end{aligned}\tag{D.9}$$

where the relation (D.4) and $\sigma_{\omega} = \omega_0 \eta \delta$ have been used.

Eq. (D.9) demonstrates that the finite width of each Schottky sideband results from the spread of revolution frequencies and the spread of betatron frequencies. Due to chromaticity the two sidebands $n \pm q_0$ have different widths. Assuming that the machine chromaticity is the only source of a tune spread dQ a comparison of the width of the two sidebands $n \pm q_0$ allows to determine the chromaticity.

List of Figures

Figure 1.1: Schematic view of the HESR	2
Figure 1.2: Floor plane of the Cooler Synchrotron COSY. Internal and external experiment stations and installations as in the year 2014 are shown. The diagonal signal paths of the stochastic cooling system across the ring from pickup to kicker are visible.	5
Figure 2.1: Sketch of cooling when the drift term is proportional to the momentum deviation. The flux as shown in the middle of the right hand side is simply proportional to the product of the initial beam distribution (red curve) at time t with $-\delta$. Below the flux its derivative is shown. One clearly sees in which regions the density is increased or decreased. If this curve is added to the initial distribution with an appropriate weight (gain) the beam distribution at time $t + \Delta t$ is found (blue curve). The peak density is increased and the width is reduced.	10
Figure 2.2: Electronic setup for filter cooling. The output signal of the sum-pickup is pre-amplified and after filtering and amplification the signal is fed to the kicker in sum mode. The filtering is accomplished with the notch filter. A 90 degree phase shifter is essential for the correct sign of the momentum correction signal at the kicker. The variable delay in the chain is used to adjust the electronic transit time to the arrival time of the reference particle at the kicker.....	13
Figure 2.3: Electronic setup for TOF cooling. The output signal of the sum-pickup is first pre-amplified. The delay-path of the notch filter is opened and the 90 degree phase shifter is used to differentiate the pickup output pulse of a particle which is then sent after power amplification to the kicker in sum mode. For the correct sign of the momentum correction signal at the kicker an additional 180 degrees phase shift is applied. The variable delay in the chain is used to adjust the electronic transit time and thereby the zero crossing time of the differentiated pules to the arrival time of the reference particle at the kicker.....	14
Figure 2.4: Setup for Palmer cooling. A specifically designed horizontal-position-sensitive pickup (Palmer pickup) located in the ring at a large dispersion is used to measure the momentum deviation of a particle.....	14
Figure 2.5: The pickup output signal after processing with a bandpass system of bandwidth W , left panel. The output of a 90 degree phase shifter, right panel, provides a signal which is similar to the derivative of the input pulse. As discussed in the chapter for TOF cooling the output signal allows to discriminate between particles of different energy deviations and provides the correct phase to correct it at the kicker.....	18
Figure 2.6: Model transfer function of the HESR pickup and kicker as used for momentum cooling in the bandwidth (2 – 4) GHz. The upper left and right figures show the magnitude of the coupling impedance and of the kicker sensitivity, respectively. The lower graph shows the phase versus frequency which is equal for pickup and kicker.	21
Figure 2.7: Schematic drawing of an ideal notch filter used in the cooling simulations. For an explanation see the text.	23
Figure 2.8: Magnitude and phase of the notch filter. The magnitude exhibits notches at the revolution harmonics which suppress particles with the nominal frequency. The phase is linearly decreasing between the notches and exhibits a phase jump of 180 degrees at the revolution harmonics for the ideal filter (red curves). Particles with frequencies which are at symmetric positions of the notches see an opposite phase. The effect of a finite notch depth is shown for -30 dB (blue) and -10 dB (green).	24

Figure 2.9: Longitudinal power spectrum at the upper range for the cooling system for different initial relative momentum spreads δ_{rms} (left plot). Red: $5 \cdot 10^{-4}$, Green: $1 \cdot 10^{-3}$ and Blue: $2 \cdot 10^{-3}$. For the latter case the bands overlap yielding a constant shot noise as indicated by the red horizontal line. The power density for $\delta_{rms} = 2 \cdot 10^{-3}$ is depicted in the whole bandwidth in the right diagram. It is visible that the height of the density is decreasing while the width is increasing yielding complete overlap at the high frequency end of the cooling bandwidth. 36

Figure 2.10: Mixing factor at the upper range for the cooling system for different initial relative momentum spreads δ_{rms} . Red: $5 \cdot 10^{-4}$, Green: $1 \cdot 10^{-3}$ and Blue: $2 \cdot 10^{-3}$. The mixing factor becomes 1, i.e., complete mixing is achieved if the momentum spread exceeds $2 \cdot 10^{-3}$ 38

Figure 2.11: Feedback loop TOF or filter momentum cooling. The undisturbed beam current $I_i(\omega)$ is modified by addition of the modulation $\Delta I(\omega)$ introduced by the beam feedback. The loop can be opened between points A and B. A signal is then fed into the loop at point A and the response of the cooling system including the beam is measured at point B with a network analyzer. The resulting open loop gain completely determines the cooling system properties. 59

Figure 2.12: Phase space trajectory in action-angle variables. 62

Figure 2.13: Real (blue) and imaginary (red) part of the longitudinal BTF (left panel). A Nyquist diagram of the BTF is shown in the right panel. 75

Figure 2.14: Magnitude (left) and phase (right) of the longitudinal BTF around harmonic number 5927. 76

Figure 2.15: Open loop gain for optimized filter cooling. The real part is given in blue, the imaginary part is in red. 78

Figure 2.16: Magnitude (left) of the open loop gain and Nyquist stability diagram for filter cooling. The arrows in the Nyquist diagram indicate the direction in which the curve is traversed when the frequency is swept from a over b to c. 79

Figure 2.17: Signal suppression at harmonic number 5927 for filter cooling in the HESR (left panel). Magnitude: red, real part: blue, Imaginary part: magenta. The frequency distribution (arb. Units) is shown in black. The right panel shows the frequency distribution when the loop is open (blue) and when the loop is closed (red). 80

Figure 2.18: Drift term (left) with (red) and without (blue) signal suppression. The momentum distribution (arb. Units) is shown in black. The thermal and Schottky noise with (red) and without (blue) signal suppression is shown in the right panel for filter cooling. 80

Figure 2.19: Magnitude (yellow trace) and Nyquist stability diagram (blue) for filter cooling of a proton beam in COSY at 2.4 GeV/c. 81

Figure 2.20: Open loop gain for TOF cooling at COSY, left panel. The model prediction is drawn as lines. The right panel presents the Nyquist stability diagram. 82

Figure 2.21: Time evolution of the momentum distribution in filter cooling of a 3 GeV antiproton beam in the HESR with hydrogen target operation. The right figure shows the momentum distribution normalized to one at time 0 s (black), 80 s (red), 100 s (green) and in equilibrium at 500 s (blue). In 200 s the antiproton beam attains an equilibrium with $\delta_{rms} = 8 \cdot 10^{-5}$ 92

Figure 2.22: Time evolution of the rms relative momentum spread in filter cooling of a 3 GeV antiproton beam in the HESR with hydrogen target operation. In 200 s the beam attains an equilibrium with $\delta_{rms} = 8 \cdot 10^{-5}$. The figure shows that the equilibrium value is independent from the initial value (blue and green curve). The beam momentum spread increases due to the beam-target interaction (red curve) if cooling is off.	92
Figure 2.23: The left figure shows the drift (cooling) term for TOF (dotted) and filter cooling. The right figure displays the diffusion contributions due to thermal noise, Schottky particle noise and beam-target interaction. Thermal and Schottky noise contributions are suppressed in the center of the distribution due to the notch filter in the signal path. The electronic gain is 110 dB. The cooling acceptance $\pm 1.8 \cdot 10^{-3}$ for filter cooling is indicated as an arrow. The larger cooling acceptance for TOF cooling is visible. The initial momentum distribution with $\delta_{rms} = 5 \cdot 10^{-4}$ is drawn in black.....	93
Figure 2.24: The left figure shows the open loop gain S for the filter method (real part blue, imaginary part red) at the end of cooling. The right figure displays the Nyquist stability diagram. The cooling loop is stable.	94
Figure 2.25: Signal suppression at the end of filter cooling at the center of the cooling bandwidth. Real part blue, imaginary part magenta, magnitude red. The signal suppression is almost real. The beam frequency distribution at the end of cooling is shown in black.	95
Figure 2.26: Left figure: The drift term neglecting feedback via the beam (blue) and including feedback (magenta) at the end of filter cooling. The drift term is almost not altered when beam feedback is included. Right figure: Including signal suppression the diffusion due to thermal and Schottky noise becomes reduced.....	95
Figure 3.1: Normalized phase space at the kicker [35]. The quantities are explained in the text.	96
Figure 3.2: Transverse (magenta) and longitudinal mixing at the upper range of the cooling system for $\delta_{rms} = 1 \cdot 10^{-4}$. The bands are well separated.	119
Figure 3.3: Transverse (magenta) and longitudinal mixing at the lower (left) and upper range (right) of the cooling system for $\delta_{rms} = 5 \cdot 10^{-4}$. The sidebands partly overlap. The mixing factors decrease.	119
Figure 3.4: Transverse (magenta) and longitudinal mixing at the upper range of the cooling system for $\delta_{rms} = 2 \cdot 10^{-3}$. Complete overlap of the transverse and longitudinal Schottky bands. The mixing factor is $M = 1$	120
Figure 3.5: Feedback for transverse cooling. The undisturbed beam dipole moment $d_i(\Omega)$ is modified by addition of the dipole moment modulation $d_f(\Omega)$ introduced by the beam feedback. The loop can be opened between points A and B. A signal is then fed into the loop at point A and the transverse response of the cooling system including the beam is measured at point B with a network analyzer. The resulting open loop gain completely determines the transverse cooling system properties.....	122
Figure 3.6: Simulation of the open loop gain. Magnitude (left) and phase response (right) between harmonic number 3999 and 4000. The betatron sidebands $(4000 - 0.62)\omega_0$ and $(3999 + 0.62)\omega_0$ are visible. The signal delay is set to the nominal particle travelling time from pickup to kicker. The phase in the center of the distribution (dotted lines) is 180 degrees	

for the desired betatron phase advance from pickup to kicker $\mu_{PK} = 13 \cdot \pi/2$ for optimal cooling, eq. (2.99). The gain 115 dB is however not the optimal gain. The magnitude of the open loop gain indicates that increasing it by 6 dB would lead to optimal cooling at these harmonics 137

Figure 3.7: Simulation of the signal suppression magnitude at harmonic number between harmonic number 3999 and 4000. The gain is not optimal. The signal suppression in the center of the distribution becomes 0.5 as desired when the gain is increased by 6 dB gain..... 138

Figure 3.8: Nyquist stability diagram. If the betatron phase advance is correct the loops of the betatron sidebands are centred about the negative real axis (right graph). The center of the sidebands is marked with a dot. It is seen that the open loop gain is real in the center of the sidebands. Red: lower sideband, blue: upper sideband. The direction of the frequency sweep is indicated by arrows. The left graph shows the case when the betatron phase advance from pickup to kicker deviates from the optimal value $\mu_{PK} = 13 \cdot \pi/2$ by 45 degrees. The signal delay is as required. Any phase (delay) error in the electronics will rotate the loops around the origin. 139

Figure 3.9: Open loop phase of the two sidebands for a betatron phase advance $\mu_{PK} = 13.5 \cdot \pi/2$. The difference in the open loop phase at the center of the two sidebands equals twice the error $\Delta\mu = 0.25\pi$ in the betatron phase advance. 139

Figure 3.10: Left, drawing of one ring slot coupler cell with eight electrodes 22.5 degrees apart. The cells of thickness 9 mm can be stacked to increase the sensitivity of the pickup/kicker as shown in the right image. In the picture the stack consists of 16 cells. The figure also shows the boards for signal combining of the electrodes..... 141

Figure 3.11: Electrode model for the ring slot couplers. The eight electrodes are labelled with P1 to P8. The red arrow indicates the beam position \vec{r}_0 . The black arrows indicate the position in the segments \vec{r}'_j and the node position \vec{r}_i (light blue dots) for the BEM calculation. The charge difference of the upper and lower electrodes (blue) (P2 + P3) – (P6 + P7) gives the vertical beam position. Similarly, with the left right electrodes (red) difference of (P1 + P8) – (P4 + P5) yields the horizontal beam position. The sum of the charge of all electrodes gives the image charge of the beam..... 142

Figure 3.12: Normalized vertical (blue) and horizontal (green) charge differences for beam that is horizontally on axis. The red curve is the charge difference found with an analytical formula for a round pickup. The slope gives the vertical position sensitivity $S_y = 20/m$ 145

Figure 3.13: Magnitude of the transverse kicker sensitivity for one tank containing a stack of 64 ring slot couplers. 148

Figure 4.1: Mean energy loss and mean squared momentum deviation (left plot) and emittance increase per turn (right plot) due to the beam-target interaction for the stable $^{238}U^{92+}$ ion beam. 153

Figure 4.2: Target diffusion versus energy per nucleon for $^{238}U^{92+}$ 153

Figure 4.3: Mean energy loss and mean squared momentum deviation (left plot) and emittance increase per turn (right plot) due to the beam-target interaction for the stable $^{238}U^{92+}$ ion beam and $^{134}Xe^{54}$ target. 154

Figure 4.4: Target diffusion versus energy per nucleon for a $^{238}U^{92+}$ beam and $^{134}Xe^{54}$ target	154
Figure 4.5: Mean energy loss and mean squared momentum deviation (left plot) and emittance increase per turn (right plot) due to the beam-target interaction an antiproton beam and a hydrogen target.....	155
Figure 5.1: HESR lattice with $\gamma_r = 6.23$ and $Q_x = Q_y = 7.2$. The Dispersion function (green) is multiplied with 10. The dispersion is zero in the long straights and at the PANDA location $\beta_x = \beta_y = 1m$. Red: Vertical betatron function, Blue: Horizontal betatron function.....	156
Figure 5.2: IBS momentum growth rate as described in the text (left) and emittance (red: horizontal, blue: vertical) growth rates (right) as a function of relative momentum spread. The initial emittance is kept fixed at $\varepsilon_{x,y} = 0.06 \text{ mm mrad}$ (rms). The ion number is $N = 10^8$	158
Figure 5.3: The diffusion rate in energy space in comparison with the target diffusion. Note the rates are multiplied with mass number squared. The ion number is $N = 10^8$	158
Figure 5.4: IBS momentum growth rate as described in the text (left) and emittance growth rates (right) as a function of relative momentum spread at 740 MeV/u. The initial emittance is kept fixed at $\varepsilon_{x,y} = 0.125 \text{ mm mrad}$ (rms). The ion number is $N = 10^8$	159
Figure 5.5: The diffusion rate in energy space in comparison with the target diffusion. Note the rates are multiplied with mass number squared. The ion number is $N = 10^8$	159
Figure 5.6: Intrabeam scattering rates for a beam with $N = 10^{10}$ antiprotons at 3 GeV and a fixed emittance $\varepsilon_x = \varepsilon_y = 0.125 \text{ mm mrad}$. Left: Momentum spread growth rate. Right: Horizontal (red) and vertical (blue) emittance growth rate multiplied by 1000.	160
Figure 6.1: Left figure: barrier voltage plotted versus time in the bunch $0 \leq \tau \leq T_0$. Each pulse has a length of $T_1 = 100 \text{ ns}$. The distance (gap) of the two pulses is $T_2 = 500 \text{ ns}$. The right part of the figure shows the potential in the Hamiltonian (6.10). The stable (bounded) area is indicated as the shaded region.....	166
Figure 6.2: Phase space portrait of the synchrotron motion in the barrier shown in Figure 6.1. For three phase space curves arrows indicate the direction of synchrotron motion. The separatrix is drawn in bold red. The phase space curves do not cross each other since the Hamiltonian is constant along each curve. Particles inside the separatrix have two turning points in the potential where they are reflected. There motions are closed and periodic curves (libration). If the amplitude gets large the motion outside the separatrix is no longer bounded.	166
Figure 6.3: Left figure: barrier voltage plotted versus time in the bunch $0 \leq \tau \leq T_0$. Each pulse has a length of $2T_1 = 200 \text{ ns}$. The gap between the two barriers amounts 500 ns. The right part of the figure shows the potential in the Hamiltonian (6.10). The stable (bounded) area is indicated as the shaded region.....	167
Figure 6.4: Phase space portrait of the synchrotron motion in the rf field of the barriers shown in figure 5.3. The separatrix is drawn in bold red. For three phase space curves arrows indicate the direction of synchrotron motion.....	168
Figure 6.5: The synchrotron period of a particle moving in the stable area of the bucket depends on the penetration depth W with $0 \leq W \leq T_1$ into the barrier pulse. For a positive ring	

slip factor ($\gamma < \gamma_{re}$) an antiproton with a negative energy deviation moves to the right and is bended by the negative barrier voltage into the upper half plane. The path through the barrier consists of two half bends.	169
Figure 6.6: Bucket height $\Delta p/p$ times 10^3 versus barrier peak voltage.	170
Figure 6.7: Synchrotron frequency versus $\Delta p/p$ times 10^3 . At the boundary (separatrix) the synchrotron motion becomes zero.....	171

List of Tables

Table 1.1: Main HESR and CAVITY parameters	3
Table 1.2: Number of loop couplers and cooling bandwidth used for stochastic cooling.	6
Table 2.1: Basic HESR pickup and kicker impedance and sensitivity values at midband frequency as used for momentum cooling simulations in the bandwidth (2 – 4) GHz.....	22
Table 3.1: Transverse pickup and kicker properties in the HESR	148
Table 4.1: Transverse emittance increase due to beam-target interaction for bare uranium...	149
Table 4.2: Ionization constants for three target materials	152

References

- [1] D. Möhl, G. Petrucci, L. Thorndahl and S. van der Meer, Phys. Rep. Vol. 58, No.2, Feb. 1980.
- [2] D. Möhl, *Stochastic Cooling of Particle Beams*, Lecture Notes in Physics 866, Springer Verlag, 2013, ISBN 978-3-642-34978-2.
- [3] D. Möhl, CERN Accelerator School, CAS , CERN 87-03, Vol. 2, p. 453.
- [4] F. Caspers and D. Möhl, Eur. Phys. J. H, 36,4, 2012, 601-632.
- [5] R. Maier, Proc. of PAC'11, New York, March 2011.
- [6] *FAIR - Facility for Antiproton and Ion Research*, Green Paper - The Modularized Start Version, October 2009.
- [7] PANDA, arxiv.org/pdf/0903.3905.
- [8] H. Stockhorst, T. Katayama, B. Lorentz, R. Maier, D. Prasuhn and R. Stassen, ICFA Beam Dynamics Newsletter No. 64, August 2014, 121 -132.
- [9] F. Etzkorn, R. Stassen, R. Greven, T. Katayama, R. Maier, G. Schug and H. Stockhorst, Proc. of IPAC`14, Dresden, Germany, June 15 – 20, 2014.
- [10] R. Stassen, F.-J. Etzkorn, G. Schug, H. Stockhorst, T. Katayama and L. Thorndahl, *RF and Stochastic Cooling System of the HESR*, Proc. of the 3rd Int. Part. Acc. Conference IPAC12, New Orleans, Louisiana, USA, May 20-25, 2012.
- [11] R. Stassen, F. Etzkorn, R. Maier, D. Prasuhn, H. Stockhorst and L. Thorndahl, *COSY as Ideal Test Facility for HESR RF and Stochastic Cooling Hardware*, Proc. of. the 23rd Particle Accelerator Conference, 4 – 8 May 2009, Vancouver, British Columbia, Canada.
- [12] G. Trubnikov et al., *NICA Project at JINR*, Proc. of IPAC13, Shanghai, China, 12-17 May 2013.

- [13] *Technical Design Report (TDR) Collector Ring (CR)*, GSI, Darmstadt, February 2014.
- [14] C. Dimopoulou, ICFA Beam Dynamics Newsletter No. 64, August 2014, 108 - 121.
- [15] T. Katayama et al., *Beam Accumulation with Barrier Voltage and Stochastic Cooling*, Proc. of IPAC'10, Kyoto, Japan, 837 (2010).
- [16] M. Steck, C. Dimopoulou, B. Franzke, O. Gorda, T. Katayama, F. Nolden, G. Schreiber, D. Möhl, R. Stassen, H. Stockhorst, I. N. Meshkov, A. O. Sidorin and G. Trubnikov, *Demonstration of Longitudinal Stacking in the ESR*, COOL'11 Workshop on Beam Cooling and Related Topics, September 12-16, 2011, Alushta, Ukraine.
- [17] T. Stöhlker et al., Phys. Scr. T156 (2013) 014085.
- [18] H. Stockhorst, T. Katayama, A. Lehrach, B. Lorentz, R. Maier, D. Prasuhn und R. Stassen, *Heavy ion storage and acceleration in the HESR with stochastic cooling and internal target*, Phys. Scr. to be published.
- [19] R. Stassen, G. Schug, H. Stockhorst, T. Katayama and L. Thorndahl, *The Stochastic Cooling System of HESR*, COOL'11 Workshop on Beam Cooling and Related Topics, September 12-16, 2011, Alushta, Ukraine.
- [20] R. Maier, Nucl. Instr. Meth. A390, 1 (1997).
- [21] H. Stockhorst et al., *Progress and Developments at the Cooler Synchrotron Cosy*, Proc. of the European Accelerator Conference EPAC 2002, Paris, 629 (2002).
- [22] H. J. Stein, D. Prasuhn, H. Stockhorst, J. Dietrich, K. Fan, V. Kamerdjiev, R. Maier, I. Meshkov, A. Sidorin and V. Parkhomchuk, *Present Performance of Electron Cooling at COSY-Jülich*, Proc. of the XVIII Conf. on Charged Particle Accelerators RUPAC 2002, Obminsk (2002).
- [23] P. Brittner, H. Hacker, R. Maier, U. Pfister, D. Prasuhn, H. Singer, W. Spieß, R. Stassen, H. Stockborst and A. Zumloh, *The Stochastic Cooling System of COSY*, Proc. of the 3rd European Particle Accelerator Conference (EPAC 92), Berlin, Germany, 24 -28 March 1992.

- [24] N. Alinovski et al., *2 MeV Electron Cooler for COSY and HESR - First Results*, Proc. of IPAC`14, Dresden, Germany, June 15 – 20, 2014..
- [25] A. Lehrach et al., *Acceleration of the Polarized Proton Beam in the Cooler Synchrotron COSY*, Proc. of the 1999 Particle Accelerator Conference, New York, USA, 1999.
- [26] A. Lehrach, *Strahl- und Spindynamik von Hadronenstrahlen in Mittelenergie-Ringbeschleunigern*, Schriften des Forschungszentrums Jülich, Reihe Schlüsseltechnologien Band 8, 2008, ISBN 978-3-89336-548-7.
- [27] K. Bongardt, D. Dinev, S. Martin, P. Meads, D. Prasuhn, H. Stockhorst and R. Wagner, *The COSY Lattice*, Proc. of the 2nd European Particle Accelerator Conference (EPAC 90), Nice, France, 12 - 16 June, 1990.
- [28] W. Kells, *Filterless Fast Momentum Cooling*, Proc. of the 11th Int. Conf. on High-Energy Accelerators, Geneva, Switzerland, July 7-11, 1980, p. 777.
- [29] T. Katayama and N. Tokuda, Particle Accelerators, 1987, Vol. 21, p. 99.
- [30] G. Lambertson, “*Dynamic Devices – Pickup and Kickers*, AIP Conf. Proc. 153, p. 1413.
- [31] A. Papoulis, *Probability, Random Variables and Stochastic Processes*, McGraw-Hill, 1984, ISBN 0-07-048468-6.
- [32] H. D. Lüke, *Signal-Übertragung*, Springer Verlag, 1990, ISBN 3-540-52177.
- [33] L. Thorndahl, *Numerical Studies of Longitudinal Filter Cooling for the HESR*, internal report, Forschungszentrum Juelich GmbH, 2009.
- [34] J. M. Brennan and M. Blaskiewicz, *Bunched Beam Stochastic Cooling at RHIC*, Proc. of COOL07, Bad Kreuznach, Germany, Sept. 10-14, 2007.
- [35] J. Mariner and D. McGinnis, AIP Conf. Proc. 249 (1992) 693 – 761.
- [36] F. J. Sacherer, CERN/ISR-TH/78-11 (1978).
- [37] D. R. Choudhury, *Network and Systems*, John Wiley & Sons, Inc., 1988.

- [38] J. Borer, G. Guignard, A. Hofman, E. Peschardt, F. Sacherer and B.Zotter, IEEE Transactions on Nuclear Science, Vol. NS-26, No. 3, June 1979.
- [39] S. v. d. Meer, *A different formulation of the longitudinal and transverse beam response*, CERN/PS/AA/80-4, January 1980.
- [40] P. J. Chou and G. Jackson, *Beam transfer function and impedance measurements in the Fermilab Main Ring*, Proc. of the 1995 Part. Acc. Conf., 1995.
- [41] S. v. d. Meer, *Optimum Gain and Phase for Stochastic Cooling Systems*, CERN 84-15, 1984, p. 183.
- [42] S. Chattopadhyay, *Some fundamental aspects of fluctuations and coherence in charged-particle beams in storage rings*, CERN 84-11, SPS devision, October 1984.
- [43] B. Zotter, *On the Summation of Infinite Algebraic and Fourier Series*, CERN/ISR-TH/78-9, April 1978.
- [44] S. J. Orfanidis, *Electromagnetic Waves and Antennas*, published on WorldWideWeb under www.ece.rutgers.edu/~orfanidi/ewa, 2010.
- [45] M. Blaskiewicz and J. M. Brennan, Phys. Rev. ST Accel. Beam 10, 061001 (2007).
- [46] T. Katayama, *Transverse Coupling Impedance of PU & Kicker Developed at Julich*, (Ver. 2), Internal Report Forschungszentrum Juelich, 2011 July.
- [47] T. Shintake et al., Nucl. Instr. Meth. A254 (1987) 146.
- [48] R. E. Shafer, *Beam Position Monitoring*, AIP 1992.
- [49] J. D. Jackson, *Classical Electrodynamics*, John Wiley & Sons, Inc. New York, 1963.
- [50] F. Hinterberger, *Beam-Target Interaction and Intrabeam Scattering in the HESR Ring*, 2006, J  l-4206, ISSN 0944-2952.
- [51] K. Hagiwara et al., *Passage of Particles through Matters*, Physical Review D66, 2002.
- [52] M. Martini, *Intrabeam Scattering in the ACOL-AA Machines*, CERN PS/84-9 (AA), 1984

- .
- [53] J. Wei, *Evolution of Hadron Beams under Intrabeam Scattering*, Proc. of Particle Conference PAC 93, Washington, DC, 17-20 May 1993.
- [54] G. Dôme, CERN Accelerator School, CERN, Geneva, Switzerland, 11-21 October 1983, CAS CERN 84-15, p. 215.
- [55] S. Y. Lee, *Accelerator Physics*, World Scientific, 1999, ISBN 981-02-3709-X.
- [56] H. J. Weaver, *Theory of Discrete and Continuous Fourier Analysis*, John Wiley & Sons, Inc., 1989, ISBN 0-471-62872-7.

Schriften des Forschungszentrums Jülich
Reihe Schlüsseltechnologien / Key Technologies

Band / Volume 107

Neutron Scattering

Experimental Manuals of the JCNS Laboratory Course held at
Forschungszentrum Jülich and at the Heinz-Maier-Leibnitz Zentrum Garching
edited by Th. Brückel, D. Richter, G. Roth, A. Wischnewski and R. Zorn (2015),
ca 150 pp

ISBN: 978-3-95806-056-2

Band / Volume 108

STM-based quantum transport through molecular wires

N. Fournier (2015), ix, 295 pp

ISBN: 978-3-95806-059-3

Band / Volume 109

**Study on the electroforming and resistive switching behaviour
of nickel oxide thin films for non-volatile memory applications**

R. Weng (2015), xxi, 159 pp

ISBN: 978-3-95806-062-3

Band / Volume 110

Microswimmers – From Single Particle Motion to Collective Behaviour

Lecture Notes of the DFG SPP Summer School 2015

edited by G. Gompper, C. Bechinger, S. Herminghaus, R. E. Isele-Holder,
U.B. Kaupp, H. Löwen, H. Stark, R. G. Winkler (2015)

ISBN: 978-3-95806-083-8

Band / Volume 111

Long range order in 3D nanoparticle assemblies

E. Josten (2015), 238 pp

ISBN: 978-3-95806-087-6

Band / Volume 112

Silicon nanowire structures for neuronal cell interfacing

S. Pud (2015), 153 pp

ISBN: 978-3-95806-089-0

Band / Volume 113

Memristive Phenomena -

From Fundamental Physics to Neuromorphic Computing

Lecture Notes of the 47th IFF Spring School 2016

22 February – 04 March 2016, Jülich, Germany

ed. by R. Waser and M. Wuttig (2016), ca 1000 pp

ISBN: 978-3-95806-091-3

Band / Volume 114

**Single-Cell Analysis of Microbial Production Strains
in Microfluidic Bioreactors**

A. M. Grünberger (2015), XIX, 225 pp
ISBN: 978-3-95806-092-0

Band / Volume 115

**Magnetic order and spin dynamics in the
extended kagome system $\text{CaBaCo}_2\text{Fe}_2\text{O}_7$**

J. Reim (2015), viii, 144 pp
ISBN: 978-3-95806-097-5

Band / Volume 116

**Structural and electronic investigations on homo- and hetero-organic
layers involving CuPc on silver single crystal surfaces**

K. M. Schönauer (2015), x, 148 pp
ISBN: 978-3-95806-112-5

Band / Volume 117

**First-principles investigation of inelastic magnetic excitations
in nanostructures deposited on surfaces**

B. J. Schweißinghaus (2016), v, 204 pp
ISBN: 978-3-95806-115-6

Band / Volume 118

Magnetic, structural, and electronic properties of NiFe_2O_4 ultrathin films

M. Hoppe (2016), vii, 118 pp
ISBN: 978-3-95806-122-4

Band / Volume 119

First-principle investigation of displacive response in complex solids

D. A. Klüppelberg (2016), xi, 179 pp
ISBN: 978-3-95806-123-1

Band / Volume 120

**Beam Cooling at COSY and HESR - Theory and Simulation -
Part 1 Theory**

H. Stockhorst, T. Katayama and R. Maier (2016), v, 192 pp
ISBN: 978-3-95806-127-9

Schlüsseltechnologien /
Key Technologies
Band / Volume 120
ISBN 978-3-95806-127-9

